STATISTICAL METHODS FOR RECONSTRUCTION OF ENTRY, DESCENT, AND LANDING PERFORMANCE WITH APPLICATION TO VEHICLE DESIGN

A Thesis
Presented to
The Academic Faculty

by

Soumyo Dutta

In Partial Fulfillment
of the Requirements for the Degree
Doctor of Philosophy in the
Daniel Guggenheim School of Aerospace Engineering

Georgia Institute of Technology
December 2013

STATISTICAL METHODS FOR RECONSTRUCTION OF ENTRY, DESCENT, AND LANDING PERFORMANCE WITH APPLICATION TO VEHICLE DESIGN

Approved by:

Dr. Robert D. Braun, Advisor
Daniel Guggenheim School of
Aerospace Engineering
Georgia Institute of Technology

Dr. Brian J. German
Daniel Guggenheim School of
Aerospace Engineering
Georgia Institute of Technology

Dr. Marcus J. Holzinger
Daniel Guggenheim School of
Aerospace Engineering
Georgia Institute of Technology

Dr. Ryan P. Russell
Department of Aerospace Engineering
and Engineering Mechanics
The University of Texas at Austin

Mr. Mark Schoenenberger
Atmospheric Flight and Entry
Systems Branch
NASA Langley Research Center

Date Approved: October 17, 2013

To Bappa, Maa

and

Nicole

ACKNOWLEDGEMENTS

There are numerous people without whom I would not have been able complete this Ph.D. Foremost, I would like to thank my advisor, Prof. Bobby Braun, who introduced me to the area that eventually became my Ph.D. topic the first time I met him during my visit to GT as a prospective graduate student. His advice and continued support has made me strive harder and has made me a better engineer today. I would also like to thank my Ph.D. committee who dedicated their time and effort and whose advice tremendously improved the quality of this work.

Of course, the effort to complete this Ph.D. was made all the more memorable and enjoyable due to the company of my fellow students in the Space Systems Design Laboratory. Countless hours spent discussing various topics, poring over equations and illegible drawings on white boards, and bonding over poker and trivia has made the last five years fly by in a flash. I would like to especially thank Zarrin Chua, Chris Cordell, Cole Kazemba, Milad Mahzari, Ian Meginnis, Richard Otero, Zach Putnam, and Brad Steinfeldt. I would also like to thank the mentors I have had during my time in graduate school - Ian Clark at JPL and Chris Karlgaard at AMA - who have helped me both academically and professionally. Thank you everyone!

Ultimately, it was the support of my family that gave me the chance to reach for my dreams. Nicole, you happily went along with all of my whims and tolerated the many interruptions to dates and weekends together to finish a homework assignment or run a case on the computer. You have a lot of patience to accept these things and I know that I am so lucky to have you in my life! And Bappa and Maa, you did most of the work for me by giving me the opportunity to come to this country and allowing me to try whatever I set my mind to. This is your achievement as much as it is mine!

TABLE OF CONTENTS

LIST OF TABLES

LIST OF FIGURES

NOMENCLATURE

Acronyms

AFE	Aeroassist Flight Experiment
CFD	Computational Fluid Dynamics
DGB	Disk-gap Band
EDL	Entry, Descent, and Landing
EI	Entry Interface
EKF	Extended Kalman Filter
FADS	Flush Atmospheric Data System
FSW	Flight Software
GA	Genetic Algorithm
GRAM	Global Reference Atmospheric Models
HI-FADS	High angle of attack flush air data system
IMU	Inertial Measurement Unit
KF	Kalman Filter
MER	Mars Exploration Rovers
MGCM	NASA Ames Mars General Circulation Model
MMM5	Mars Mesoscale Model 5
MPF	Mars Pathfinder

MRAMS	Mars Regional Atmospheric Modeling System
MSL	Mars Science Laboratory
NASA	National Aeronautics and Space Administration
NSGA-II	Non-dominated Sorting Genetic Algorithm-II
PD/ADS	Pressure Distribution/Air Data System
POST2	Program to Optimize Simulated Trajectories II
RMS	Root-mean-square
SCLK	Spacecraft Clock Time
SEADS	Shuttle Entry Air Data System
TPS	Thermal Protection System
UKF	Unscented Kalman Filter

Subscripts

∞	Freestream condition
A	Axial force
b	Backward pass
D	Drag force
DS, b	Descent Stage frame to body frame
DS, IMU	Descent Stage frame to IMU frame
f	Forward pass
J, DS	J2000 frame to Descent Stage frame

$J, MCMF$ J2000 frame to Mars Centered Mars Fixed frame

k Time index

L Lift force

l Rolling moment

m Pitching moment

$MCMF, LH$ Mars Centered Mars Fixed frame to Local Horizontal frame

N Normal force

n Yawing moment

p Pressure

$stag$ Stagnation point

T Tangential force

t Total condition

u UKF parameters

Superscripts

$+$ Best estimate (post-measurement update)

$-$ Nominal estimate (pre-measurement update)

$\tilde{}$ Deviation

a State and covariance post-unscented transformation

b State and covariance pre-unscented transformation

i Sigma point index for the UKF

$\hat{}$	Estimated quantity	

Symbols

α	Angle of attack	rad
β	Sideslip angle	rad
$\delta\theta$	Change in angle	rad
δh	Step size for measurement Jacobian calculation	
δV	Change in velocity	m/s
η	Cone angle	rad
γ	Flight path angle	rad
$\lambda_u, \alpha_u, \beta_u, \kappa_u$	UKF tuning parameters	
$\mathbf{e}$	Deviation of the state estimate from the truth	
$\mathbf{q}$	Quaternion	
$\mathbf{v}$	Measurement noise vector	
$\mathbf{w}$	State noise vector	
$\mathbf{x}$	State vector	
$\mathbf{y}$	Measurement value	
ν	Bank angle	rad
ω	Planet rotation rate	rad/s
ω_x, ω_y, and ω_z	Angular rates in body frame	rad/s
ϕ	Planet-centric latitude	rad

ψ	Heading angle	rad
ρ	Density	$\mathrm{kg/m^3}$
σ	Uncertainty	
θ	Longitude	rad
ζ	Clock angle	rad
A	Process equation Jacobian w.r.t. state vector	
a	Speed of sound	m/s
a_x, a_y, a_z	Accelerations in body frame	$\mathrm{m/s^2}$
B	Process equation Jacobian w.r.t. state noise	
C	Coefficient (see subscripts for more description)	
$C_{m_q} + C_{m_{\dot{\alpha}}}$	Pitch damping sum	
F	Force	N
G	Number of measurement points used for filter tuning	
g	Gravitational acceleration	$\mathrm{m/s^2}$
H	Measurement equation Jacobian w.r.t. state vector	
h	Measurement equation	
I	Identity matrix	
J	Objective function	
j	Imaginary unit (i.e. $\sqrt{-1}$)	
K	Kalman gain	

k	Specific heat ratio	
L	Batch size to calculate $\mathbf{v}$	
M	Mach number	
N	Batch size to calculate $\mathbf{w}$	
n	Number of state elements	
P	State covariance	
p	Pressure	Pa.
Q	Process noise covariance	
R	Gas constant	J/K-kg
R	Measurement noise covariance	
r	Planet-centric radius	m
$R_{v,b}$	Rotation matrix (local horizontal to body frame)	
S	Reference area	m^2
T	Temperature	K, $^\circ$ C
t	Time	s
u, v, w	Body-frame velocity components	m/s
V	Velocity	m/s
W	Sigma point weighting for the UKF	

SUMMARY

There is significant uncertainty in our knowledge of the Martian atmosphere and the aerodynamics of the Mars entry, descent, and landing (EDL) systems. Designing for these uncertainties lead to higher system masses and conservative performance predictions. Data from flight instrumentation on-board Mars EDL systems can be used to quantify these uncertainties; however, the existing data set is sparse and many parameters of interest have not been previously observable. A majority of the flight reconstructions performed in the past have been deterministic in nature, neither utilizing statistical information about the uncertainty of the measured data nor quantifying uncertainty of the estimated parameters. Statistical estimation methods blend together disparate data types to improve the reconstruction of parameters of interest for the vehicle. For example, integrating data obtained from aeroshell-mounted pressure transducers (also known as flush atmospheric data systems), inertial measurement unit, and radar altimeter can improve the estimates of the trajectory, atmospheric profile, and aerodynamic coefficients, while also quantifying the uncertainty in these estimates. Moreover, the statistical methods can be leveraged to improve current engineering models in order to reduce conservatism in future EDL vehicle design.

The work in this thesis presents a comprehensive methodology for parameter reconstruction and uncertainty quantification while blending dissimilar Mars EDL data sets. Statistical estimation methods applied include the Extended Kalman filter, Unscented Kalman filter, and Adaptive filter to improve parameter estimation and uncertainty quantification over traditional EDL reconstruction techniques. The estimators are applied in a manner in which the observability of the parameters of interest

is maximized while using the sparse, disparate EDL data set. The methodology is validated with simulated Mars EDL data and then applied to actual flight data from the 2012 Mars Science Laboratory. Reconstructed performance of all three estimators are compared with each other and to independent estimations, where applicable.

The reconstruction methodology is also used as a tool for improving vehicle design and reducing design conservatism. A method of optimizing the design of future EDL flush atmospheric data systems is presented by utilizing the reconstruction methodology in the objective function. In one method, a residual-based optimization procedure is demonstrated where the accuracy of the estimates drives the design and placement of the flush atmospheric data system sensor suite. In another method, an observability-based optimization procedure is implemented where the uncertainties of the parameters of interest are minimized. Both cases provide means to optimize FADS sensor layouts and to tailor them for a given trajectory and mission operation, something hitherto ignored in practice. The methods also identify the point of diminishing returns in the number of sensors needed, an important quantity to know with limited bandwidth on flight computers.

Ultimately, the impact of the estimation methodology on aerodynamic and atmospheric engineering models is studied. Aerodynamic uncertainties can be estimated from past flight data; however, some of the flight measurements introduce assumptions and uncertainties that dilute the impact of these measurements and do not rationalize reductions in aerodynamic database uncertainties. Direct measurement of some targeted atmospheric parameters on future missions combined with a statistical estimation methodology can yield significant improvement in aerodynamic uncertainty quantification and lead to reductions in conservatism present in design models. Reconstructed atmospheric profiles using the estimation methodology do not show as great of a promise in decreasing uncertainties in atmospheric models, since EDL missions only provide data for a vertical profile of the atmosphere at one time

period. However, if reconstructed atmospheric profiles and uncertainties are combined with continuous data from orbiters or ground meteorological stations, one could make great improvements in the atmospheric models used for EDL vehicle design.

CHAPTER I

INTRODUCTION

Mars has captivated the the human imagination for centuries as it has shined brightly in the night sky. Humans have been sending spacecraft to Mars for several decades; however, the red planet's thin atmosphere and rough terrain present challenges to the exploration of the planet's surface. The entry, descent, and landing (EDL) sequence has challenged vehicle designers since the spacecraft has to slow down from interplanetary speeds using an atmosphere that is only about $\frac{1}{100}$th as dense as Earth's atmosphere, but is still thick enough that the landing sequence cannot be done solely by propulsion in a mass efficient manner. The surface is also strewn with rocks and craters that create hazards for safe landing. Finally, the conditions for Mars EDL are difficult to replicate on Earth, creating a challenge for verification and validation of spacecraft design [1].

The United States has landed seven successful missions on the surface of Mars. The design of the entry and descent systems for these missions have been remarkably similar, with the each using a 70 deg. sphere-cone shaped rigid aeroshell for the hypersonic entry phase and a disk-gap band (DGB) type of supersonic parachute for the descent portion of the sequence. The terminal landing system has varied. Vikings 1 and 2 and Phoenix landed using subsonic propulsion and crushable legs, Mars Pathfinder (MPF) and the two Mars Exploration Rovers (MER) used air bag systems, and Mars Science Laboratory (MSL) utilized a propulsive system called the Sky Crane [1, 2, 3]. Figure 1 shows the EDL sequence for MSL [4].

Despite the similarity between these spacecraft (see Fig. 2 [5]), there remains large uncertainties in the engineering models, leading to design conservatism and a

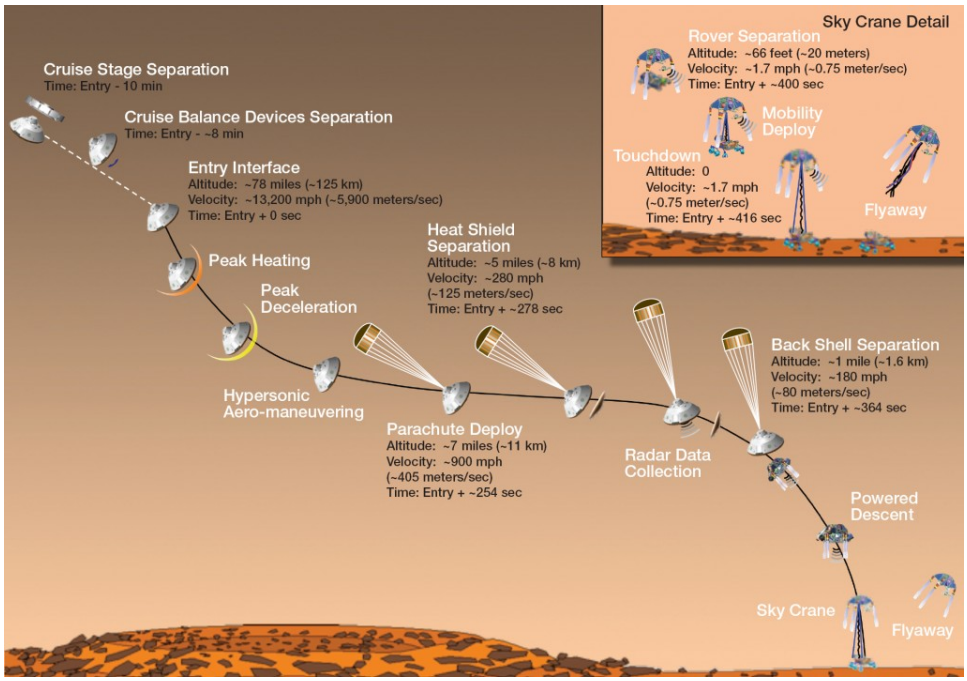

Figure 1: Mars Science Laboratory entry, descent, and landing sequence.

higher EDL system mass. Flight data from EDL spacecraft can be used to reconstruct trajectory, atmosphere, and vehicle aerodynamic coefficients and thus allow for the quantification of the uncertainties in the vehicle performance and the Martian environment.

This thesis will demonstrate a comprehensive methodology to utilize flight data from sensors on-board Mars EDL vehicles to statistically reconstruct both the parameters of interest and their uncertainties. The methodology will focus on reconstructing an EDL vehicle's trajectory, aerodynamic coefficients, and the atmosphere on the day of flight. Additionally, the reconstruction tools will be leveraged towards design of future EDL instrumentation and improvement in modeling tools to reduce design margins in future missions.

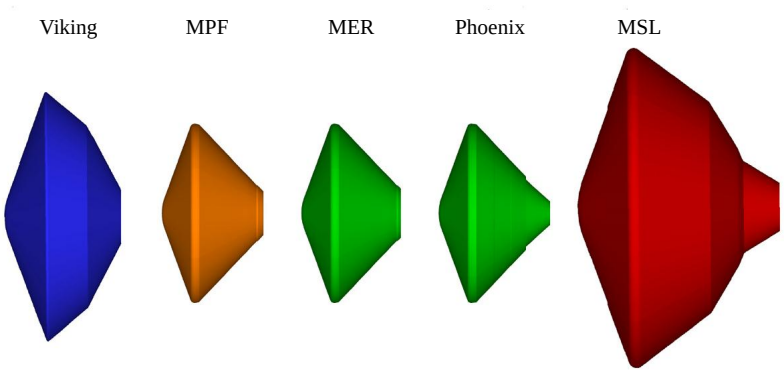

(a) U.S. Mars aeroshells to size [5].

Parameter	Viking	MPF	MER	Phoenix	MSL
Forebody Geometry	70 deg. sphere-cone				
Aeroshell Diameter (m)	3.5	2.65	2.65	2.65	4.5
DGB Parachute Diameter (m)	16.15	12.4	15.09	11.5	19.7

(b) Comparison of U.S. Mars EDL missions [5].

Figure 2: U.S. Mars EDL aeroshells.

1.1 Background

Post-flight reconstruction of the EDL sequence has been conducted for every successful Mars mission to provide insight into the vehicle's trajectory and the atmospheric conditions it encountered during the descent. The data set of the past Mars missions has largely consisted of measurements from on-board accelerometers, gyroscopes, and radar altimeters, which were used for the estimation of the position, velocity, and attitude of the vehicles during the EDL timeline. Moreover, based on the sensed decelerations on the vehicle and the knowledge of the aerodynamic database, the atmospheric profiles encountered by these vehicles have been estimated.

Past Mars EDL reconstruction analyses have neglected measurement noise and uncertainty in the estimation models. The estimated trajectories and atmosphere from flight data have also not been applied to reduce the uncertainties in the engineering models used during design. Trajectory analyses for the recent MSL mission seen in Refs. [6] and [7] show the many uncertainties inherent in the EDL sequence.

In particular, the aerodynamic coefficients of the vehicles and the knowledge of the Martian atmosphere contain large uncertainties that in turn propagate into uncertainties in EDL performance. The following section will summarize the issues with these uncertainties and describe possible ways in which uncertainty quantification may remedy the situation.

1.1.1 Aerodynamic Uncertainty

1.1.1.1 Static Aerodynamic Coefficients

One of the major sources of uncertainties lie in the knowledge of the aerodynamic coefficients of the vehicle. Table 1 lists the static aerodynamic coefficient uncertainties for some recent Mars EDL vehicles [8, 9, 10]. As can be seen from the table, although the shape of the EDL vehicle has remained the same for all past U.S. missions, there is still high uncertainty in the aerodynamic performance of the vehicle, which in turn leads to increased design conservatism and potentially higher entry vehicle mass.

Table 1: Static Aerodynamic Coefficient Uncertainty for Selected Mars EDL Vehicles.

MPF	C_A	C_N	C_m	C_n	C_l
Mach $\geq$ 12*	$\pm$2%	$\pm$0.01	$\pm$0.003	N/A	N/A
Mach $\leq$ 8*	$\pm$10%	$\pm$0.01	$\pm$0.005	N/A	N/A
MER	C_A	C_N	C_m	C_n	C_l
Mach $\geq$ 10*	$\pm$3%	$\pm$0.01	$\pm$0.003	N/A	N/A
Mach $\leq$ 5*	$\pm$10%	$\pm$0.01	$\pm$0.005	N/A	N/A
Phoenix†	C_A	C_N, C_Y	C_m	C_n	C_l
Mach $\geq$ 10*	$\pm$3%	$\pm$0.01	$\pm$0.002, $\pm$20%	$\pm$0.002, $\pm$20%	1.24×10^{-6}
Mach $\leq$ 5*	$\pm$10%	$\pm$0.01	$\pm$0.005, $\pm$20%	$\pm$0.005, $\pm$20%	1.24×10^{-6}
MSL†	C_A	C_N, C_Y	C_m	C_n	C_l
Mach $\geq$ 10*	$\pm$3%	$\pm$0.01, $\pm$10%	$\pm$0.006, $\pm$20%	$\pm$0.003, $\pm$20%	0.000326
Mach $\leq$ 5*	$\pm$10%	$\pm$0.01, $\pm$10%	$\pm$0.005, $\pm$20%	$\pm$0.005, $\pm$20%	0.0004

*Uncertainty values are linearly blended between regimes.
†Uncertainty model consists of an adder and then a multiplier [9].
Gaussian distribution is assumed for the uncertainties listed above.

The uncertainties in the aerodynamic coefficients exist due to the various methods used to generate the aerodynamic database for a vehicle. As the work of Edquist et

al. [8] shows, the data are compiled from methods such as Computational Fluid Dynamics (CFD) tools that solve the Navier-Stokes equations and experimental data from ballistic range and wind tunnels.

Due to the various sources that account for the data, the uncertainties are often based on sensitivity studies using computational tools, past experience and engineering judgment, and experimental test calibration data. Uncertainty quantification using Mars flight data would definitely be an improvement over the disparate techniques of Earth-based uncertainty quantification; however, past EDL flight reconstructions have not performed aerodynamic uncertainty assessment.

Reconstruction of aerodynamic coefficients from previous flight data shows that there remains a potential gap between the state-of-the-art computational tools, like the CFD tool LAURA, and actual aerodynamic performance. Figure 3, where lift (C_L) and drag (C_D) coefficient reconstructed from Viking 1's on-board pressure transducer and LAURA predictions, show there are some disagreements between current modeling tools and flight data collected in the past [11]. The lift and drag coefficients predicted by the CFD tool are 3% to 5% below the measured data, and Edquist [11] goes on to test many possibilities for the discrepancy, such as angle of attack reconstruction error, center-of-gravity location offset, and off-nominal atmospheric density. Unfortunately, none of these hypotheses can completely explain the discrepancy. It should be noted that the flight data from Viking does not contain error bars and hence one cannot determine if the discrepancy is due to measurement or modeling errors; still, this disagreement underscores the need for improved analysis of Mars EDL flight data in order to reconstruct parameters of interest, such as aerodynamics, with estimated uncertainties so that such discrepancies can be mitigated and current engineering models and tools can be improved.

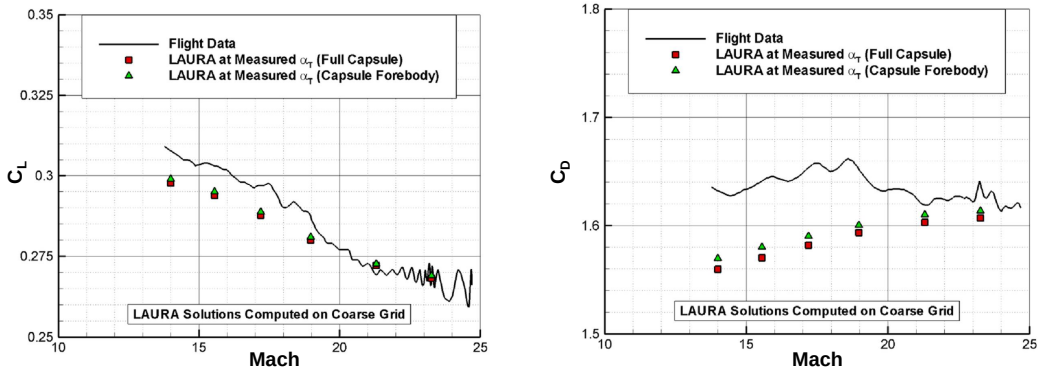

(a) Lift Coefficient [11]

(b) Drag Coefficient [11]

Figure 3: Comparison of Viking 1 reconstructed aerodynamics and CFD predictions at measured angle of attack.

1.1.1.2 Dynamic Aerodynamic Coefficients

Mars entry vehicles have been blunt bodies and these geometries display oscillatory behavior in some flow regimes leading to unstable pitching motion in some instances [12]. Figure 4 displays the signs of dynamic instability in blunt bodies through the angle of attack history of MPF and Phoenix spacecraft [2, 13]. Depending on the flight trajectory and vehicle orientation, these instabilities may occur just prior to maximum dynamic pressure and reach their peak in the mid to low supersonic flow regime [14]. Prediction of this phenomenon in early analytical work on the topic in the 1950's [15, 16] have been now supplemented by experimental and numerical analyses.

Experimental methods for characterizing dynamic stability have utilized wind tunnels and ballistic range facilities to determine aerodynamic coefficient like the pitch damping sum $(C_{m_q} + C_{m_{\dot{\alpha}}})$ [14]. Each of the experimental techniques have their own drawbacks, as listed by Ref. [14], and brings with them their own set of uncertainties, whether it is due to the data reduction method or assumptions made during testing. For example, Fig. 5(a) shows the reconstructed pitch damping sum from the same ballistic range data set by two independent parameter estimation tools

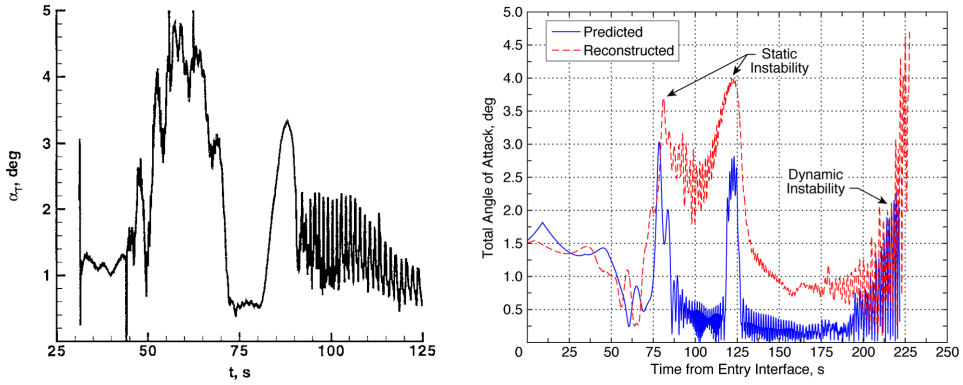

(a) Pathfinder [13] (b) Phoenix [2]

Figure 4: Pitching oscillation seen in the reconstructed angle of attack of Mars EDL spacecraft.

(CADRA and ADFDAS) [17]. There is little agreement in the two estimated sets of coefficients, especially near angle of attacks near zero. Such uncertainty between two tested and independent codes underscores the current lack of certainty in the knowledge of dynamic aerodynamic coefficients.

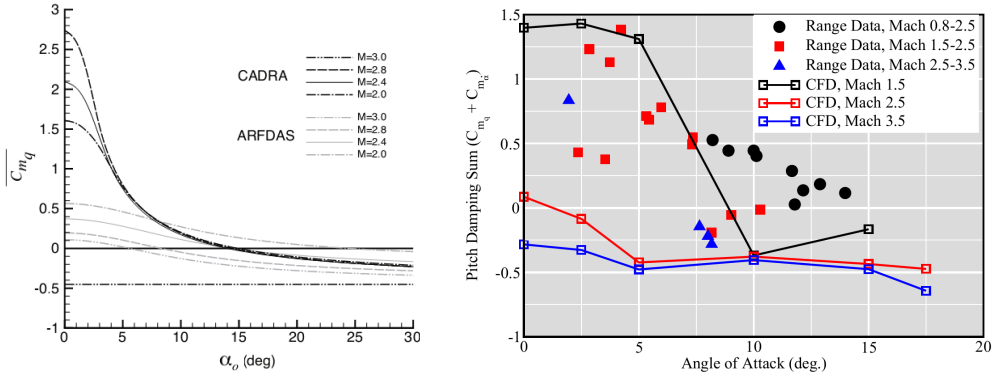

(a) MSL Ballistic Range Estimate [17] (b) MER CFD-based Results [18]

Figure 5: Uncertainties in dynamic aerodynamic coefficients demonstrated by disparity in the pitch damping sum reconstruction.

Numerical methods of computing dynamic aerodynamic coefficients using state-of-the-art CFD tools have not given much clarity to the issue. Typically, CFD-based dynamic analysis of blunt bodies involves perturbing a vehicle's attitude and then numerically computing time-accurate solutions using deforming grids [19]. However,

as seen in Fig. 5(b), CFD based results show little agreement with experimental results [18].

As can be clearly seen from Fig. 5, little agreement between numerical simulations and experimental data reduction techniques leaves large uncertainties in the knowledge of the dynamic stability parameters. Analysis of flight data for dynamic aerodynamic coefficient reconstruction can vastly improve the knowledge and the uncertainty quantification of these parameters. Additionally, accurate reconstruction of the dynamic coefficients can even verify and validate the performance of the state-of-the-art CFD tools, further improving design tools for future spacecraft.

1.1.2 Atmospheric Uncertainty

Another major contributor to Mars EDL design is atmospheric uncertainty (see Fig. 6). Large variations in the atmosphere due to the seasons, the amount of dust particles, and other weather-related events make the prediction of freestream density, pressure, and temperature very uncertain. For example, looking at Fig. 6(a), one can see large variations in density from the nominal prediction. Similar uncertainty in the atmospheric profile knowledge exists for other Mars atmosphere models like winds [20, 21, 22, 23]. The uncertainties in the atmospheric profile can manifest themselves as uncertainties in the spacecraft trajectory, as seen in the various landing footprint predictions for MSL based on different atmospheric model predictions (see Fig. 6(b)).

Reconstructing the atmosphere from flight data and then quantifying the uncertainties can improve atmospheric modeling. For Mars, information from orbiters, such as the Mars Global Surveyor, have provided data to characterize the top of the atmosphere with somewhat high certainty [24], but the characteristics of the atmosphere under 90 km altitude relies heavily on the in-situ data from the six entry missions (excluding MSL whose data has not been fully processed into global models

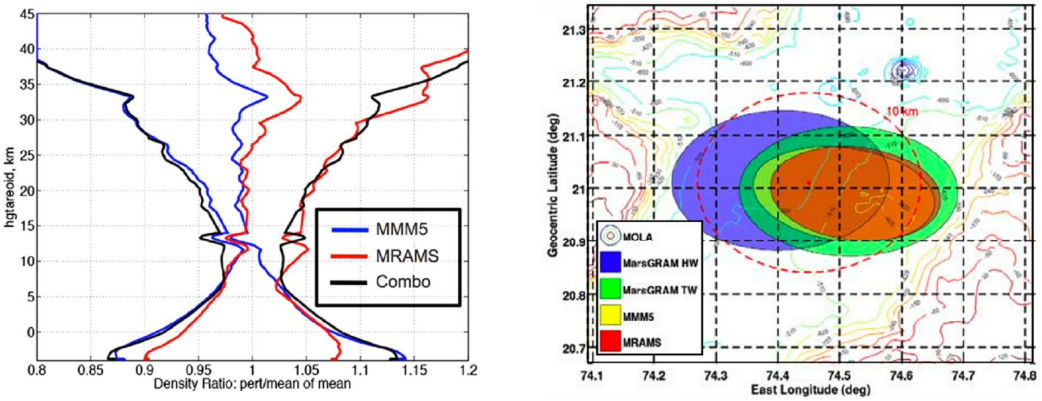

(a) Density uncertainties for MSL [4].

(b) MSL footprints for different atmosphere models [23].

Figure 6: Atmospheric uncertainty's effect on EDL vehicle design.

at the time of writing of this thesis) [24, 25]. Hence, the design of EDL trajectories rely on diverse modeling techniques, like global circulation models, mesoscale models, and large eddy simulations. These methods do not always agree, which adds to the overall uncertainty [21, 22, 25].

Moreover, the possible existence of highly variable density and wind shear regions in the atmosphere add to the overall uncertainty. Shuttle-derived atmospheric models of Earth showed these regions where density changed by as much as ±60% [26, 27]. These regions have been theorized to exist on Mars, where they may be caused by gravitational waves in the thin atmosphere [4]. Such variability in atmospheric conditions could constrain the design of EDL vehicles [25]. Thus, it is easy to see how reconstruction of flight data to estimate atmospheric properties can be valuable in maturing current atmospheric modeling tools, especially for the lower altitude regions.

1.1.3 Typical Mars EDL Vehicle Instrumentation

Although EDL flight data reconstruction provides a valuable tool to quantify aerodynamic and atmospheric uncertainties, on-board instrumentation has provided little information to separate the effects of the two uncertainties. Table 2 summarizes the various measurements taken during the EDL phase by past U.S. Mars missions.

Table 2: EDL-related measurements taken by U.S. Martian missions.

Measurements	Vikings[a]	Pathfinder[b]	MERs[c]	Phoenix[d]	MSL[e]
Accelerometer	X	X	X	X	X
Thee-axis gyroscope	X		X	X	X
Radar altimeter[g]	X	X	X	X	X
TPS Recession					X
Pressure (during EDL)	X	X[f]			X
Temperature (during EDL)	X	X			X

Notes: [a] [29, 30] [b] [31, 32, 33] [c] [34, 35] [d] [2, 36] [e] [3, 37]
[f] Pathfinder only took pressure measurements during subsonic parachute descent.
[g] Usually takes measurements during the last few stages of EDL.

Ref. [28] provides a more in-depth discussion of the various sensors used for other planetary EDL missions, including missions to Venus and Jupiter.

As can be seen in Table 2, most of the past EDL missions have only inertial measurement unit (IMU) instruments, such as accelerometer and gyroscope, during the hypersonic phases of EDL. Although these sensors provide a great estimate of position and velocity when integrated using schemes like those used for strap-down guidance systems [38], these measurements do not allow for simultaneous reconstruction of atmosphere and aerodynamic parameters . Usually aerodynamic knowledge is assumed to be known in order to reconstruct atmospheric parameters [39]. This leads to a confounding of aerodynamic and atmospheric uncertainties.

One solution to the confounding of the uncertainties is to have some means of observing freestream atmospheric conditions. Flush atmospheric data systems (FADS), consisting of pressure transducers on the aeroshell, can collect surface pressure data during the entry and help in the estimation of the aeroshell pressure distribution. In turn, freestream atmospheric parameters, like density and pressure, can be inversely estimated from the measured surface pressure distribution and a prediction of the surface pressure distribution based on the aerodynamic database [40, 41]. Although aerodynamic knowledge is needed for the initial prediction, the reconstruction process

does not ignore the uncertainty in these parameters. Instead, the known aerodynamics only provide an initial guess which is improved upon by the measured data that then leads to the updated atmospheric parameter estimates. Thus, aerodynamic uncertainty is not confounded with the atmospheric uncertainty. Section 2.2.1 discusses how the aerodynamic and atmospheric uncertainties are kept separate by using FADS data. Past use of FADS for re-entry and high speed applications is summarized below.

One of the first use of FADS were on the Viking landers [29, 42, 43]. The FADS sensors were arranged in an annular fashion with one port at the predicted stagnation point, as seen in Fig. 7 [42, 43]. However, the data from these spacecraft had significant noise and were in general unintelligible [29].

The Shuttle Entry Air Data System (SEADS) program used a flush-mounted air data system on the shuttle's nose [44] with the port configuration (shown in Fig. 7(a)) arranged in a cruciform shape. This configuration was derived using heuristic methods dependent on engineering judgment [40, 44]. Designers used error analysis to determine the minimum number of pressure ports and the ports were arranged in a cruciform manner to capture changes in the pitch and yaw plane. However, the cruciform configuration is only optimal if the trajectory has either angle of attack-only motion or sideslip angle-only motion. This configuration is non-optimal in terms of observability if both sideslip angle and angle of attack are non-zero at the same time. Since the SEADS configuration was an optimization of a point in the trajectory, it was not robust to variations from the nominal trajectory.

High-Angle-of-Attack Flush AirData Sensing (HI-FADS) systems have been used for aerodynamic test vehicles and conceptual studies for munitions guidance. The configurations were derived by adding annular arrays of pressure ports across the forebody of the vehicle, as seen in Fig. 7(b). Similar to SEADS, these applications did not use physics-based optimization routines to select the transducer locations; instead, it was hoped that adding more ports at different radial and angular directions would

capture the entire pressure distribution and allow for the estimation of the freestream condition [45].

The air data system for the proposed Aeroassist Flight Experiment (AFE) (shown in Fig. 7(d)) was based on physics-based optimization. Deshpande et al. [46] used a gradient-based estimator and a genetic algorithm (GA) to optimize the distribution of the sensors in order to decrease the effect of normally distributed random noise from the pressure transducers. The residuals between the estimated parameters and their true values were then combined in a single-objective function for the optimization routines. However, the study only considered reconstruction of a single trajectory point. As such, the reconstruction process that serves as the objective function for the optimization problem is expected to converge to a single trajectory state, similar to a situation in wind tunnel testing, but unlike the case of EDL reconstruction where the trajectory states are variable.

MSL also carried a set of FADS transducers, which was known as the Mars Entry Atmospheric Data System (MEADS). The MEADS science objective was to reconstruct dynamic pressure to within 2% and angle of attack and sideslip angle to within 0.5 deg. when the dynamic pressure is greater than 850 Pa [37].[1] Although the transducers that were used for MEADS could sample at high rates, due to memory constraints, both pressure and temperature data were saved at an effective sampling rate of 8 Hz [37].

To accomplish this, the MEADS sensors were arranged in a cruciform configuration around the forebody of the aeroshell (see Fig. 7(e)). The locations were based on the predicted pressure distribution on the aeroshell for a point in the trajectory where sideslip angle is small; however, no quantitative optimization procedure was

[1]The original specifications also included the objective of estimating freestream Mach number (M_∞) to within ± 0.1, but that requirement was dropped since Mach number calculation necessitates an accurate knowledge of the speed of sound, which is not observable with the FADS measurements without additional assumptions [48].

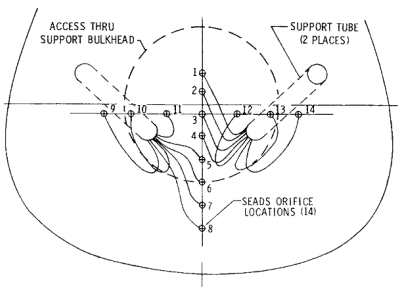

(a) SEADS [44]

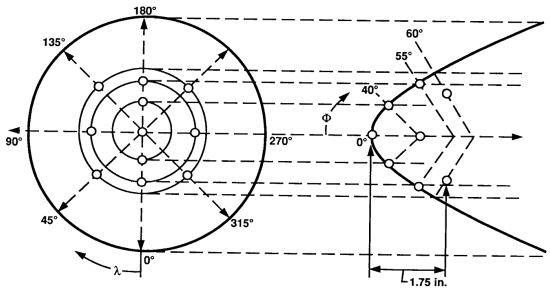

(b) HI-FADS [45]

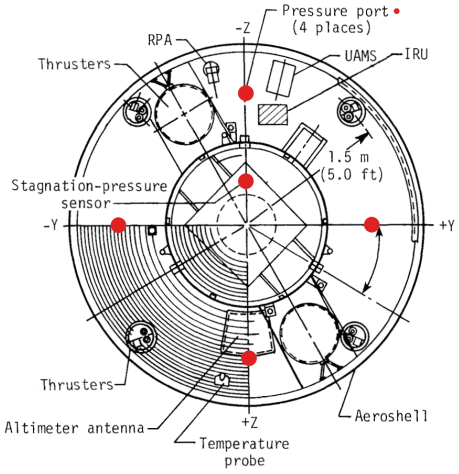

(c) Viking [43]

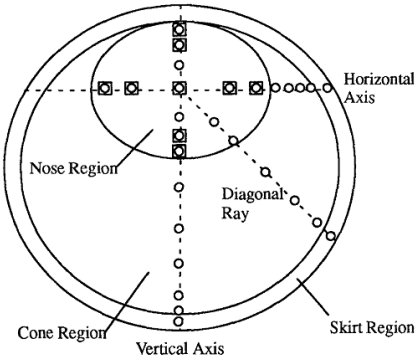

(d) AFE [46]

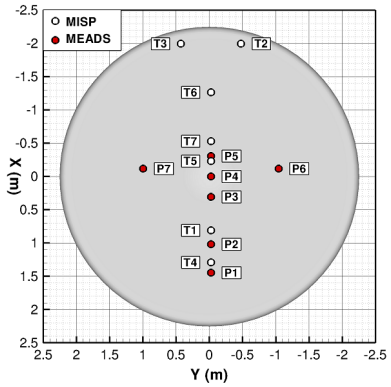

(e) MEADS [47]

Figure 7: Layouts of various FADS configurations.

conducted in the selection of the transducer locations. Based on the nominal trajectory, stagnation pressure was around P1 and P2, while P6 and P7 were the most sensitive to changes in the sideslip angle. All ports helped in the reconstruction of

the angle of attack history. However, in reality with off-nominal trajectory conditions the configuration is non-optimal [49]. Unlike the Viking FADS sensors, the MEADS sensors on MSL went through a rigorous calibration and measurement error characterization [50, 51].

1.2 Past Work in EDL Reconstruction

1.2.1 Overview of Reconstruction Techniques

Estimation is a technique of deducing the values of a process from the effects of the process; simply, it is inferring the independent variables from the dependent variables with a limited knowledge of the function that maps one type of variable to the other [52]. In Eq. (1), $\mathbf{x}$ signifies the state (the independent variable of interest), f is some mapping function, and $\mathbf{y}$ stands for the made observation. If $\mathbf{x}$ is given and $\mathbf{y}$ is desired, this situation is the direct problem; on the other hand, if $\mathbf{y}$ is known and $\mathbf{x}$ is desired, it is the inverse estimation (or estimation) problem. Sometimes little is known about f itself, which then is also a system identification problem [53]. Measurement, process, and random noises also enter the inverse analysis and system identification problem, further complicating the estimation.

$$\mathbf{y} = f(\mathbf{x}) \tag{1}$$

For experimental and flight data reconstruction applications, this process typically involves estimating parameters of interest from sensor measurements. Three issues need to be considered for inverse analysis: solution existence, uniqueness, and instability of the problem [53].

- For flight data analysis, sometimes the data may not fit the model used in the estimation process, which leads to non-existence of solution; usually these issues are dealt by improving model knowledge.

- Often times, the measurement quantity is not directly the parameter of interest,

and hence there is an issue of *observability*, which is the condition of whether or not states can be estimated from the observation. Less than perfect observability of data are usually the cause of non-unique solutions. It is also possible that the observation is not exactly the state of interest, but can be interpreted by using the dynamics of the system being studied (e.g. using accelerometer data to estimate position and velocity).

- One of the biggest hurdles to inverse estimation is that the problem is generally sensitive to small changes and can become divergent and unstable. For flight data reconstruction, where the process equations are highly non-linear, ill-conditioning of the data can be very detrimental to the estimation process.

With the above mentioned constraints, it is important to look at two classifications of the estimation problem. If a quantity of interest is time-invariant or slowly time varying, the reconstruction is often characterized as a *parameter estimation problem*. Eq. 1 is an example of parameter estimation, where the parameter $\mathbf{x}$ is being estimated from the observation $\mathbf{y}$. However, if quantities change significantly with time, one also has to use a dynamic equation in addition to a measurement equation and such reconstruction is termed as *state estimation problem* [54]. The process of conducting parameter estimation and state estimation is usually different because time-invariance can be used to make assumptions that can change the estimation process. On the other hand, state estimation methods can become parameter estimation techniques by assuming that the dynamic equation is zero [52].

Three parameters of interest to the EDL flight data reconstruction are the vehicle trajectory, atmospheric properties during the flight, and vehicle aerodynamics. Atmospheric properties and aerodynamic coefficient reconstruction methods are typically classified within parameter estimation, which involves least-squares and maximum likelihood type of estimators. Trajectory reconstruction involves dynamical system and is classified as a state estimation problem, in which typical methods include

Wiener filter, Kalman filters, and Batch filters [55]. [2] The following sections will give a brief overview of the reconstruction techniques typically used for Mars EDL flight data set.

1.2.2 Trajectory Reconstruction

Trajectory reconstruction is usually a requisite that enables scientific investigations for most instrumented planetary missions. An accurate trajectory reconstruction in turn aids in atmospheric investigations and maintaining telecommunication links. Typical EDL reconstruction techniques have consisted of direct integration of the measurements to produce position and velocity history (deterministic trajectory reconstruction) or have used statistical filters to combine multiple types of data to reconstruct the trajectory (statistical trajectory reconstruction). The following sections focuses on trajectory reconstruction techniques for Mars EDL vehicles, while Ref. [28] can be consulted for detailed descriptions of trajectory reconstructions for non-Mars EDL vehicles.

1.2.2.1 Deterministic Trajectory Reconstructions of Mars EDL Vehicles

Due to the limited choice of on-board sensors on Mars EDL vehicles, the reconstruction techniques have been mostly limited to deterministic estimation methods. These estimation techniques are similar to strap-down reconstruction methods, where the inertial measurements are integrated using the non-linear equations of motion without considering the measurement uncertainty in the estimation process [38]. Results from deterministic Mars EDL trajectory reconstructions can be found in the literature for Viking 1 and 2 [29, 43], Mars Pathfinder [31], Mars Exploration Rovers [34], and Phoenix [2, 36]. Deterministic trajectory reconstruction has also been used as the first step for atmospheric reconstruction that relies solely on accelerometer data.

[2] Note that although state estimation techniques have many more wrinkles than parameter estimation techniques, in the end all of the state estimation filters could be looked-upon as least-squares or maximum likelihood estimators.

These techniques are explained in more detail in Section 1.2.3 and Appendix A.

Deterministic reconstructions do not consider measurement and process uncertainties during estimation, and thus are unable to quantify the uncertainty of the estimated parameters without using external uncertainty quantification techniques, such as Monte Carlo analysis. Deterministic reconstruction methods are relatively simple and have a long heritage in the field; however, often the analyst has to make assumptions about the dynamics, like perfect knowledge of the aerodynamics or ignoring the effect of random noise in the accelerometer measurements, which can lead to filter divergence. A classic situation could be seen in Fig. 8, which shows altitude reconstruction for Mars Pathfinder based on accelerometer only measurements using a deterministic filter and then accelerometer measurements blended with radar altimeter data using a statistical filter [56]. One can easily see an improvement in the estimation when the statistical filter is able to use uncertainty statistics of the two data types to decide what is the best estimate of the altitude.

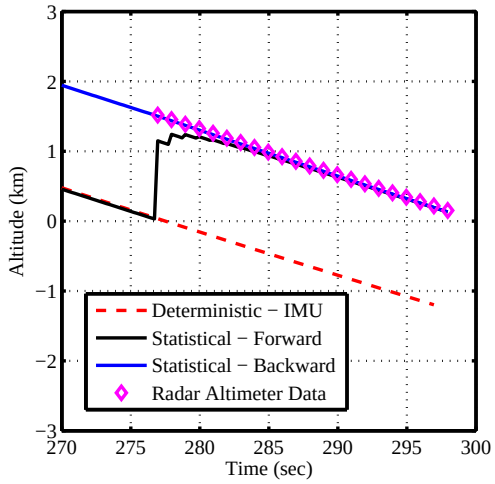

Figure 8: Effect of blending different data types on the estimate of altitude for Mars Pathfinder.

1.2.2.2 Statistical Trajectory Reconstructions of Mars EDL Vehicles

A few of the past EDL trajectory reconstruction efforts have utilized statistical estimation techniques, where the method of choice has been the simple Kalman Filter (KF). Kalman filtering was first utilized for Mars EDL reconstruction for Viking 1 and 2 by Euler et al. [30], who integrated the equations of motion using the IMU data and then used the radar altimeter and terminal landing Doppler data to correct the estimate of the trajectory. Although the Viking probes sampled the atmosphere during EDL using pressure probes, Euler's work did not include the pressure measurements within the trajectory estimation procedure; thus, a statistical estimation of both the trajectory and the atmosphere was not conducted at that point.

KF was also used for the Mars Pathfinder reconstruction by Spencer et al. [31], who also used radar altimeter data to correct a nominal trajectory based on the integration of IMU data. Spencer et al. also utilized a smoothing algorithm to combine the trajectory reconstruction from forward and backward runs of the data, but used this procedure with only the translational equations of motion. Since MPF did not have on-board gyros, angular parameter calculations assumed *a priori* knowledge of the vehicle's aerodynamics.

Extended Kalman Filter (EKF) has also been applied to the Mars Pathfinder [57, 28], MER [58], Phoenix [59], and MSL [60] data sets. Many of these studies used IMU and radar altimeter data as measurements instead of integrating them directly, and so measurement noise statistics were used by the reconstruction tool to determine the best estimate of the state. The work in this thesis is a continuation of those studies.

1.2.3 Atmosphere Reconstruction

Without pressure measurements during EDL, freestream density, and other atmospheric properties have been estimated using the definition of the axial force coefficient, the reconstructed velocity of the vehicle, and the on-board sensed accelerations

while assuming perfect knowledge of the aerodynamic coefficients. The pressure profile is then estimated using the hydrostatic equation. Seiff [39, 61] proposed such deterministic methods as early as the 1960's. These classical methods are described in greater detail in Appendix A. Atmospheric reconstructions of Mars missions using such techniques exist in the literature for the Viking missions [62, 63], Mars Pathfinder [31, 32, 64], MERs [35], and Phoenix [2, 65].

Withers et. al. [64] notes that the largest source of error in atmospheric reconstruction using the classical methods has been the uncertainty in the vehicle's attitude, which, in turn, affects the estimate of the aerodynamic coefficients used in the reconstruction. Withers presents several ways of estimating the attitude from purely accelerometer data, but the results show a great sensitivity to the assumptions made.

The problem with such estimation techniques is the confounding between the atmospheric and aerodynamic uncertainties. Measurement of the pressure distribution on the aeroshell provides information to estimate freestream atmospheric conditions independent of the IMU data and can be used to separate the two sources of uncertainty. As noted in Table 2, three of the past Mars missions before MSL, the two Viking missions and Pathfinder, had on-board pressure transducers. Pathfinder only took measurements after the parachute deployment [32], so that data cannot be used to reconstruct the atmosphere during the hypersonic EDL phase without additional approximations, such as those underlying the hydrostatic equation. Viking 1 and 2 [62], on the other hand, did take pressure measurements during the hypersonic phase of EDL, but the pressure measurements were not directly used in the trajectory estimation [63, 43].

On the other hand, pressure data have been used with statistical estimators for non-Mars EDL flight reconstructions. The Shuttle Entry Air Data System (SEADS) program of the 1980's used a flush-mounted air data system to estimate the pressure distribution across the Space Shuttle forebody during entry [66, 40, 41, 67, 68].

MSL's pressure data system is in large part based on the SEADS concept. The SEADS project was able reconstruct the freestream conditions during the Shuttle entry successfully and verified its results with simulation and wind tunnel data. However, reconstructions based on SEADS data did not blend the inertial measurements with the pressure distribution data; instead, an iterative, least-squares filter was used in conjunction with a database of pressure distributions on the vehicle forebody to inversely estimate the aerodynamic parameters that could create the pressure measurements at the transducers [40, 41]. Thus, the potential coupling between trajectory and atmospheric uncertainties were not considered by that analysis. Appendix B summarizes the algorithms that have been used in the past to reconstruct atmospheric parameters from FADS data sets.

There are also other measurements and sensors, like radio occultation, mass spectrometer, and gas chromatograph, that can improve the estimation of atmospheric properties besides in-situ FADS data. Ref. [28] provides a list of Earth-based and in-situ sensors that have been used to obtain atmospheric information for several planetary bodies. For example, Doppler tracking that records the Doppler shift of a radio wave from a spacecraft to determine its trajectory has been used in Mars science applications to determine wind profiles during EDL [69, 70]. Although these measurement types provide an independent source of atmospheric information, they have not been utilized in the past during trajectory and atmosphere reconstruction of EDL vehicles. Often, the uncertainty in the non-FADS and non-IMU measurements are large and they do not significantly improve the observability of the parameters of interest.

1.3 Application to Vehicle Design

The previous section discussed how specific reconstruction products, like trajectory, atmospheric properties, and aerodynamic coefficients, have been estimated from EDL

vehicle measurements. These products are often valuable since one can use them to characterize the performance of current spacecraft. For example, the Phoenix trajectory and atmospheric reconstruction helped explain why the spacecraft landed relatively far from its expected landing location [2]. At other times, the reconstruction products are helpful in achieving science goals, such as characterizing the atmosphere of a planetary body, as was the case with the Viking atmospheric reconstruction [63].

However, very rarely is EDL flight data reconstruction used as feedback to improve the design tools or engineering analysis methods. Since Mars-like atmosphere is hard to replicate on Earth, EDL flight data are often the best source of information to validate, verify, and improve state-of-the-art design tools.

1.3.1 Optimization of Flush Atmospheric Data System Layout

As mentioned earlier in Section 1.1.3, use of FADS sensors for entry applications has become more prevalent. However, the methods for FADS design and sensor arrangement still remain rudimentary. In spite of observations that different port configurations can vastly affect the effectiveness of the estimation [71], past FADS sensors have always been placed in symmetrical annular or cruciform patterns based on engineering judgment rather than computationally-based rationale. FADS configurations are also often designed for fixed points in the trajectory, e.g. the sensor configuration is designed for Mach 5 and angle of attack of 2 deg., even though variations from the nominal condition leave these configurations suboptimal for the inverse estimation of parameters. Bandwidth limits on on-board sensors for planetary entry missions make it crucial to make FADS configurations as efficient and optimized as possible in order to capture important pressure measurements under a range of conditions.

A thorough review of literature has shown only one past study that has considered a computationally-based optimization for FADS sensor placement for EDL

applications. This study was conducted in the early 1990's in support of the Pressure Distribution/Air Data System (PD/ADS) experiment that was proposed to be included in the Aeroassist Flight Experiment (AFE), which was later canceled. Deshpande et al. [46] used a gradient-based estimator and a genetic algorithm (GA) to optimize the distribution of the PD/ADS sensors in order to decrease the effect of normally distributed random noise of the pressure transducers. The AFE geometry and one of the optimized, sensor location results by Deshpande et. al. is shown in Fig. 9.

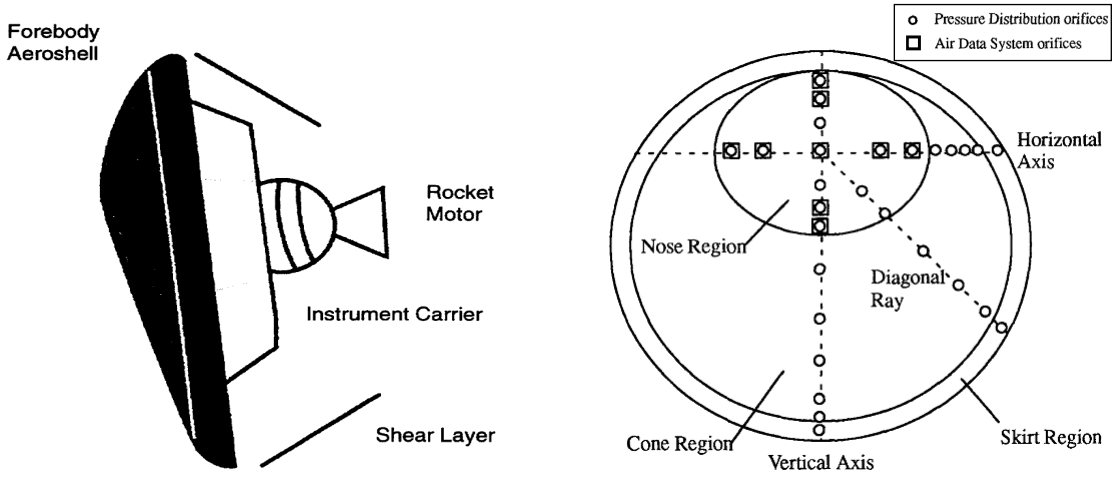

(a) AFE Geometry [72] (b) PD/ADS location optimization [46]

Figure 9: Aeroassist flight experiment pressure sensor optimization.

Deshpande et al. used modified Newtonian theory for the predicted pressure model and a non-statistically weighted, batch-type filter to estimate air data parameters, such as dynamic pressure, angle of attack, and sideslip angle. The residuals between the estimated parameters and their known, true values were then used in a single-objective function for the optimization routines, but the optimization was only conducted for a fixed trajectory point (one Mach number, one angle of attack, and one sideslip angle) instead of over a full vehicle trajectory. All of these points left the optimization results narrowly applicable, since slight off-nominal trajectory behavior would mean that the sensor ports were in off-optimal positions. A design

methodology which includes a statistical filter that uses measurement uncertainty information in the estimation process, a higher-fidelity pressure distribution model, and optimization at more that one trajectory point can create a sensor configuration that is more robust to off-nominal EDL trajectories and is more widely applicable.

1.3.2 Engineering Model Improvement for EDL Design

During current EDL vehicle design, large margins are often applied to mitigate design characteristics that are highly uncertain. As mentioned earlier, aerodynamics and atmospheric properties are especially uncertain parameters of the EDL design process. Evaluation of flight data could improve the predictions of state-of-the-art aerodynamics and atmospheric parameter prediction tools, allowing for design margins to be reduced and possibly boosting the performance of EDL vehicles.

Development of the aerodynamic database for a new spacecraft is a crucial process during vehicle design. Typically, this process involves CFD solutions, wind tunnel and ballistic range tests, and even Earth-based flight tests [73, 74]. Several examples of aerodynamic database development for Earth and Mars EDL vehicles can be found in the literature [9, 13, 17, 44, 75, 76, 77, 78]. However, rarely has actual flight data from Mars has been used as part of an aerodynamic database update. Considering the difficulties in simulating Mars-like conditions on Earth and also the constraints of wind tunnel and Earth-based flight testing, flight data from actual Mars EDL vehicles would be the best way to verify actual flight performance and improve designs for future missions. Aerodynamic reconstruction from Viking BLDT program [79], the Space Shuttle aerodynamic coefficient characterization studies [80], and the recent development of aerodynamics for the Ares I vehicle [74] elucidates ways in which such an update to an aerodynamic database could be performed. These Earth-based tests have advantages over actual Mars EDL flight data, namely an independent and more accurate characterization of atmospheric properties. In addition, the estimation

methodology and process these programs used could also be applied to Mars EDL vehicles.

Atmospheric models used for conceptual design of EDL vehicles are often based on computationally-fast surrogates of general circulation models. General circulation models solve differential equations that resolve mass, momentum, and energy transport in an atmosphere similar to how CFD solves for flow along an aerodynamic surface, but Global Reference Atmospheric Models (GRAM) simulate the results of the differential equations using parametrization that realistically captures the temperature, pressure, density, and winds of an atmosphere without actually solving the differential equations. As a consequence, GRAM models are orders of magnitude faster than global circulation models [81]. GRAM models are largely based on surrogate models of the global circulation models, but often adjustments are made to these parametrization using flight data. Early Mars-GRAM models had modifications made due to Mariner 9 orbiter and Viking probes data [81, 82] while some recent Mars-GRAM models have been validated with Mars Global Surveyor, Odyssey, and Mars Reconnaissance Orbiter data taken during aerobraking operations [24, 83]. However, the information is sparse compared to what is required for a GRAM model to be solely based on in-situ data, so GRAM models continue to be based on global circulation models and other physics-based simulations. Reconstruction products from EDL flight-data, especially using statistical estimation techniques, can provide GRAM model developers with good estimates of atmospheric properties with associated estimated uncertainties along an entire vertical profile of the atmosphere. These data can serve as anchors for GRAM models and improve the accuracy and resolution of atmospheric prediction tools in the design of future EDL vehicles.

1.4 Summary of Contributions

From the previous sections, one can note the many uncertainties that exist in the design process for Mars EDL vehicles. Much of this conservatism can be ameliorated by mitigating the deficiencies of past flight data reconstruction techniques. This thesis proposes a methodology that utilizes the sparse, disparate Mars EDL data set to reconstruct flight characteristics of Mars EDL vehicles, thereby improving upon the current techniques of uncertainty quantification for EDL trajectory, aerodynamics, and atmospheric estimation while also advancing EDL vehicle design. This goal is achieved through the following contributions.

Systematic development of a comprehensive methodology for parameter reconstruction and uncertainty quantification that blend dissimilar EDL data: The work presented in this research shows a methodology to conduct EDL reconstruction of parameters of interest, such as trajectory, vehicle aerodynamic coefficients, and atmospheric profiles. The methodology simultaneously utilizes disparate EDL data, such as accelerometer measurements, on-board gyroscopic rates, radar altimeter data, and pressure measurements from on-board transducers, in the reconstruction process and uses the uncertainty in the measurements and the initial conditions to determine the resulting uncertainties of the estimated parameters. Several statistical estimation algorithms are applied in this methodology. Statistical estimation techniques evaluated here include the Extended Kalman filter, Unscented Kalman filter, and Adaptive filter. Additionally, the methodology is augmented to allow measurement uncertainty quantification by estimating systematic and random error in the data set. This methodology is demonstrated using simulated data and the flight data set of the Mars Science Laboratory.

Demonstration of a design methodology for future atmospheric data systems: A new design algorithm for Mars EDL FADS instrumentation is developed that leverages the aforementioned reconstruction and uncertainty quantification

methodology to create guidelines for placement of sensors on EDL vehicles. On-board pressure measurements provided by FADS improve vehicle attitude and atmospheric estimation. The resulting designs using the optimization algorithm maximize the observability of the estimated parameters. The design process is tested for Mars EDL trajectories and potential sensor requirements for future instrumentation packages are also developed.

Investigation of the effects of the statistical reconstruction methodology on vehicle design through improved engineering models: The products derived from applying the reconstruction methodology to flight data can be applied to reduce design conservatism present in EDL conceptual design. The thesis considers and quantifies the improvement possible from the use of flight data on future EDL vehicle systems and discusses steps to increase the maturity of current design tools. Based on analysis of the statistical estimation framework developed in this thesis flight data needs are identified to reduce current vehicle design margins.

1.5 Outline for the Thesis

The remainder of this thesis proposal is divided into six chapters.

- Chapter II summarizes the estimation techniques that are being proposed to form a part of a statistical-based estimation methodology for Mars EDL flight data. The chapter introduces the estimation reconstruction methodology and lists the associated process and measurement equations needed for EDL reconstruction. Additionally, the estimation algorithms, taken from existing estimation theory literature, are summarized and the process of dealing with numerical ill-conditioning and process uncertainties are explained.

- Chapter III demonstrates the statistical-based estimation methodology using simulated Mars EDL data set. Different Mars EDL trajectories are used to create a simulated data set and the various estimators are applied to this data.

Since the truth information is known, the estimators performance is characterized relative to the actual states.

- Chapter IV demonstrates the statistical-based estimation method using actual flight data, specifically the data returned by the Mars Science Laboratory. Although the true performance of the vehicle remains unknown, the estimation results of the various methods are compared with each other and independent reconstruction efforts. This situation typifies the most realistic application the estimation methodology, since tuning of the various estimation techniques have to be determined *a priori*.

- Chapter V describes an application of the estimation methodology for vehicle design, specifically the design of a flush atmospheric data system. The optimal placement of these sensors has not been extensively explored in the literature previously and the estimation methodology serves as good optimization tool to determine the best placement and configuration for these sensors on EDL spacecraft.

- Chapter VI considers the application of the reconstruction methodology and its results for the maturation of engineering tools used for EDL conceptual design. Some specific issues being addressed include how reconstruction of flight data can be used to reduce EDL system margins and boost performance of future missions.

- Chapter VII summarizes the contributions by this thesis, discusses guidelines for what type of estimation algorithm is preferred for Mars EDL reconstruction, and lists lessons learned and future work.

CHAPTER II

ESTIMATION METHODOLOGY

The methodology used for reconstructing Mars EDL vehicle flight parameters involves taking EDL sensor measurements and using an estimation method to reconstruct the vehicle trajectory, atmospheric profile, and aerodynamic coefficients. The estimator is guided by the process equations, which describe the system dynamics of the problem, and the measurement equations of the various data types being used to inversely estimate the parameters of interest. The process equations are of the form shown in Eq. 2a, where the function f is a non-linear dynamic equation of the state vector, $\mathbf{x}$, and in the case of EDL trajectories are the equations of motion described in the next section (Eq. 3). The state noise (also called the process noise) vector is defined as $\mathbf{w}$, which is *usually* assumed to be a time-varying, Gaussian white noise. The measurement ($\mathbf{y}$) equation (Eq. 2b) also has a nonlinear function of the state vector (in this case represented by h) and a measurement noise vector ($\mathbf{v}$) that is also a time-varying, Gaussian white noise. The Gaussian distribution assumption is common to many types of estimation methods, although there is no requirement for it from the perspective of estimation and information theory.

$$\dot{\mathbf{x}} = f\left(t, \mathbf{x}, \mathbf{w}\left(t\right)\right) \tag{2a}$$

$$\mathbf{y} = h\left(t, \mathbf{x}, \mathbf{v}\left(t\right)\right) \tag{2b}$$

The following sections will describe the process equations and measurement equations needed for EDL parameter reconstruction, leading to the description of the specific statistical estimators used in this analysis.

2.1 Process Equations

2.1.1 Trajectory and Atmosphere Dynamical Equations

The estimators need dynamic equations of motion, as seen in Eqs. (3), to propagate the estimate of the states in time. For entry, descent, and landing applications, the parameters of interest include the vehicle's position, velocity, and attitude. The states can be augmented to include time-varying atmospheric states. An equation of motion must be presented for every state vector element so that the estimator can use initial solutions to create a nominal estimate of the state at a given time.

$$\dot{r} = V \sin\gamma \tag{3a}$$

$$\dot{\phi} = \frac{V \cos\gamma \sin\psi}{r} \tag{3b}$$

$$\dot{\theta} = \frac{V \cos\gamma \cos\psi}{r \cos\phi} \tag{3c}$$

$$\dot{V} = \frac{F_T}{m} - g \sin\gamma + \omega^2 r \cos\phi \left(\sin\gamma \cos\phi - \cos\gamma \sin\phi \sin\psi\right) \tag{3d}$$

$$\begin{aligned}\dot{\gamma} = \frac{1}{V}\Bigg[&\frac{F_N \cos\nu}{m} - g\cos\gamma + \frac{V^2}{r}\cos\gamma + 2\omega V \cos\phi\cos\psi \\ &+\omega^2 r \cos\phi \left(\cos\gamma\cos\phi + \sin\gamma\sin\phi\sin\psi\right)\Big]\end{aligned} \tag{3e}$$

$$\begin{aligned}\dot{\psi} = \frac{1}{V}\Bigg[&\frac{F_N \sin\nu}{m\cos\gamma} - \frac{V^2}{r}\cos\gamma\cos\psi\tan\phi + 2\omega V\left(\tan\gamma\cos\phi\sin\psi - \sin\phi\right) \\ &-\frac{\omega^2 r}{\cos\gamma}\sin\phi\cos\phi\cos\psi\Bigg]\end{aligned} \tag{3f}$$

$$\dot{p_\infty} = -\rho_\infty g V \sin\gamma \tag{3g}$$

$$\dot{\rho_\infty} = -\frac{\rho_\infty^2 g V \sin\gamma}{p_\infty} \tag{3h}$$

$$\begin{bmatrix}\dot{q}_0\\ \dot{q}_1\\ \dot{q}_2\\ \dot{q}_3\end{bmatrix} = \frac{1}{2}\begin{bmatrix}-q_1 & -q_2 & -q_3\\ q_0 & -q_3 & q_2\\ q_3 & q_0 & -q_1\\ -q_2 & q_1 & q_0\end{bmatrix}\left[\begin{bmatrix}\omega_x\\ \omega_y\\ \omega_z\end{bmatrix} - \frac{1}{r}R_{v,b}\begin{bmatrix}V\cos\gamma\cos\psi\\ -V\cos\gamma\sin\psi\\ -V\cos\gamma\cos\psi\tan\phi\end{bmatrix}\right] \tag{3i}$$

The equations of motions have been adapted from several sources [84, 85, 50]. The states consist of the vehicle's position, velocity, attitude, freestream pressure

(p_∞), and freesteam density (ρ_∞). The position is in terms of planet-centric radius (r), latitude (ϕ), and longitude (θ), while the velocity (V), flight path angle (γ), and heading angle (ψ) are defined relative to the planet surface and are based on the vehicle-carried local horizontal frame [84]. The heading angle is defined in the horizontal plane where due East is 0° and due North is 90°. The attitude states are given in terms of the quaternion (q_0, q_1, q_2, q_3) that defines the orientation between the vehicle-carried local horizontal frame and the body frame [86, 85].

The intermediate states and parameters needed to define the equations of motion include the planetary rotation rate (ω) and the rotation matrix ($R_{v,b}$), which is solely a function of the quaternion and defines the rotation from the local horizontal frame to the body frame [85]. Other intermediate states include the angular rates in the body frame, ω_x, ω_y, and ω_z, which come from the on-board gyroscopes, while g is the altitude-dependent gravitational acceleration (assumed here to be based on a spherical mass distribution). F_N and F_T represent the normal (lift) and tangential (drag) forces in the body axis and lift modulation is modeled in the equations using a bank angle (ν). The dynamical equations for the freestream pressure and density are derived from the hydrostatic equation and the perfect gas law and the derivation is described in Refs. [56] and [50]. Eqs. (3g) and (3h) use an isothermal assumption that is valid over small changes in the altitude. Since the freestream pressure and density rate equations are used as process equations and are propagated over small time steps, this assumption is reasonable. Note that the process noise chosen for the reconstruction process is tuned to compensate for potential issues with these equations.

The process equations used here are not exactly the same equations in the trajectory program that generates the simulated data which are used to evaluate the performance of the estimation methodology. Thus, there is a process uncertainty between how the simulated data are generated and how the estimator predicts the

values of the states. In a simulation, one can modify the estimator's process equations to match the trajectory program's dynamics, but in the case of real data, the simulation models are never perfect. Thus, the differences in the dynamics between the program and this estimation methodology provides a test of the unmodeled uncertainties expected in the actual data.

2.1.2 Improvement in the Process Equations

Past EDL reconstructions have had process equations similar to the ones shown in Eqs. (3) [87, 50, 88]. However, a big distinction between those sets of equations and Eqs. (3) is that the velocity propagation equations are a function of aerodynamic quantities that are found using the aerodynamic database and the current estimate of the state vector. Traditionally for EDL reconstruction, the velocity propagation equations have been a function of the sensed accelerations [50], which made accelerations part of the *process* rather than *measurements* used by the estimators. This distinction is important since for normal Mars EDL data sets, making accelerometers as part of the process would only leave FADS data and radar data as *measurements*. The times when FADS and radar altimeter data are available often do not overlap during EDL and since statistical filters are discrete-time estimators (i.e. estimated states are only available at epochs with measurements), the traditional approach leaves large chunks of times without an actual state estimate.

In the process equations provided here, accelerations are treated as *measurements* and since this data are available from entry interface to touchdown there are no gaps in the state estimate. Additionally, another advantage of these process equations is that accelerometer data and FADS data are both sensitive to freestream density, making the atmospheric quantity observable through two independent data sources. Thus, atmospheric and aerodynamic uncertainties are not confounded in

regions where both IMU and FADS data are available. Although a simple innovation, this last point makes this statistical estimation methodology an improvement over other EDL methods in the past. Not only are trajectory and atmospheric states estimated concurrently by statistical estimators, but one has now two independent sources of data at the same time to make atmospheric quantities observable.

2.2 Measurement Equations

Measurement equations are used by the statistical estimator to predict the measurement value based on the current estimate of the state. The actual measurements can then be compared with the predicted measurements, and the state can be appropriately updated. Most of the statistical estimators used in this work are based on linear filter theory, so the estimator assumes that the measurements are a linear function of the state vector plus a measurement error ($\mathbf{v}$) as described in Eq. 2b. For most measurement types, h is a non-linear function of the state vector, but using a first-order Taylor series expansion, Eq. (2b) can be linearized about a point (the nominal estimate of the state, $\bar{\mathbf{x}}$) as shown in Eq. (4), where $\tilde{\mathbf{x}}$ is the deviation in state from $\mathbf{x}$.

$$\mathbf{y}_i = h_i(\bar{\mathbf{x}}) + \left[\partial h/\partial \mathbf{x}\right]_{\mathbf{x}=\bar{\mathbf{x}}} \tilde{\mathbf{x}} + \mathbf{v}_i \tag{4}$$

A measurement sensitivity (Jacobian) matrix (H), shown in Eq. (5), is defined as

$$H = \begin{bmatrix} \partial h_1/\partial \mathbf{x} \\ . \\ \partial h_n/\partial \mathbf{x} \end{bmatrix}_{\mathbf{x}=\bar{\mathbf{x}}} \tag{5}$$

The measurement sensitivity equations have to be developed for every measurement type included in the estimation process. Christian et al. discusses the development of the sensitivity matrix for accelerometer and radar altimeter measurements [87]. More detailed expressions for the measurement sensitivity equations pertaining to accelerometer and radar altimeter measurements can be found in the works of Karlgaard

et al. [50] and Jaswinski et al. [89] The measurement equations of the FADS-type sensors are presented here.

2.2.1 Flush Atmospheric Data System

For pressure port data, a measurement equation has to predict static pressure value at a specific transducer and the equation is a function of three parameters: total angle of attack (α_t), freestream Mach number (M_∞), and the orientation of the transducer on the aeroshell, which are given in terms clock angle (ζ) and cone angle (η) [56]. The definition of the clock and cone angles with respect to the geometry of an entry body can be seen in Fig. 10 [90, 91].

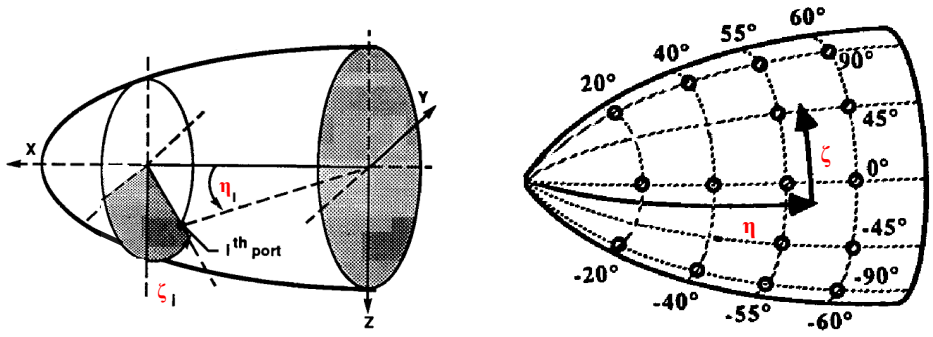

(a) Orientation angles definition [90] (b) Angle sign convention [91]

Figure 10: Definition of clock and cone angles.

During the hypersonic EDL phase, the velocity of the vehicle is large with respect to the wind velocity, so the planet-relative velocity can be used to calculate the angle of attack (α) and angle of sideslip (β) (Eqs. (6)). The two orientation angles can then be combined into a total angle of attack (also shown in Eqs. (6) - (9)), where u, v, and w are velocity components in the body axis.

$$\alpha = \tan^{-1} w/u \tag{6}$$

$$\beta = \sin^{-1} v/V \tag{7}$$

$$\alpha_t = \cos^{-1} (\cos\alpha \cos\beta) \tag{8}$$

$$M_\infty = V/a = V/\sqrt{kP_\infty/\rho_\infty} \tag{9}$$

Table 3: C_p values for ballistic range model at $M_\infty = 0.6$ and $\eta = 14$ deg.

Total angle	Clock angle, ζ (deg.)					
of attack (deg.)	0	5	10	15	20	25
0	1.096745	1.096747	1.096749	1.09675	1.096752	1.096754
5	1.096761	1.096763	1.096764	1.096766	1.096768	1.096770
10	1.096772	1.096774	1.096776	1.096778	1.096779	1.096781
15	1.096780	1.096781	1.096783	1.096785	1.096786	1.096788
20	1.096783	1.096784	1.096786	1.096788	1.096789	1.096791
25	1.096781	1.096783	1.096784	1.096786	1.096788	1.096789
30	1.096775	1.096777	1.096778	1.096780	1.096782	1.096783
35	1.096765	1.096767	1.096768	1.096770	1.096771	1.096773
40	1.096750	1.096752	1.096753	1.096755	1.096756	1.096758
45	1.096731	1.096733	1.096734	1.096736	1.096737	1.096739

As seen in Eq. (6), the velocity magnitude and the speed of sound (a), which is a function of the freestream pressure and density that are part of the state vector and the specific heat ratio (k) of the gas, can be used to calculate the local Mach number. Since the locations of the pressure measurement orifices are known, the pressure coefficient (C_p) at each orifice can then be found from tables created from the vehicle aerodynamic database. A small segment of such a database is shown in Table 3 [56]. After the pressure coefficient is found, the pressure at each surface location can be predicted using the vehicle velocity and density.

Besides inertial measurement unit data, atmospheric data system measurements are the only other on-board EDL sensor that make freestream atmospheric parameters observable. Using both types of data in a statistical estimator allows one to estimate independently atmospheric and aerodynamic quantities. Aerodynamic knowledge (in the form of the C_p distribution) is needed for the initial prediction of the atmospheric data measurement; however, the estimator also considers the uncertainty in the measurement, uncertainty in the nominal estimate of the atmospheric state, and the residual between the true and predicted measurement value to create the best

estimate of the atmospheric parameters. Hence, the uncertainty in the aerodynamic database does not translate fully into the uncertainty of the atmospheric parameter estimate. So unlike the classical methods of atmospheric reconstruction using solely IMU data (see Appendix A), the aerodynamic and atmospheric uncertainties can be differentiated. It is true that the initial prediction of the measurement, which is based on an assumed aerodynamic database, still affects the estimate of the atmospheric states, but uncertainties are not completely confounded as would be the case if only IMU data were used for the atmospheric reconstruction.

Since the measurement prediction equation (h) for the atmospheric data system is not analytical, the measurement Jacobian matrix (H) is numerically calculated. Numerical ill-conditioning can arise based on the step size (δh) used to perturb the pressure prediction equations. This problem can be alleviated if complex differentiation is used for the Jacobian calculation. Equation 10 shows the definition of complex differentiation. The process has been shown to have a truncation error of $O(\delta h^2)$ [92].

$$\frac{\partial h}{\partial \mathbf{x}} = \lim_{\delta h \to 0} \frac{\mathrm{Im}\left[h(\mathbf{x} + j\delta h)\right]}{\delta h} \approx \frac{\mathrm{Im}\left[h(\mathbf{x} + j\delta h)\right]}{\delta h} \tag{10}$$

2.3 Aerodynamic Calculations

The aerodynamic coefficients of the vehicle can be reconstructed after trajectory and atmospheric states have been estimated. As seen in Eq. 11a, aerodynamic force coefficients - in this case the axial force coefficient (C_A) - can be reconstructed from the axial acceleration measurements ($a_{x,b}$) and the estimated freestream density (ρ_∞) and velocity (V_∞) values. With the trajectory and atmosphere estimation process complete, one can also calculate the aerodynamic uncertainty using the known atmospheric uncertainties and measurement uncertainties and hence separately quantify aerodynamic and atmospheric uncertainties. The uncertainty in the estimate of the aerodynamic force coefficients (σ_{C_A}) can be calculated by applying the chain rule to

Eq. 11a) and using the already calculated uncertainties of the estimator's state vector as seen in Eq. 11b.

$$C_A = \frac{2ma_{x,b}}{\rho_\infty V_\infty^2 S} \tag{11a}$$

$$\sigma_{C_A} = \frac{2ma_{x,b}}{\rho_\infty V_\infty^2 S}\left(\frac{\sigma_{a_{x,b}}}{a_{x,b}} - \frac{\sigma_{V_\infty}}{V_\infty} - \frac{\sigma_{\rho_\infty}}{\rho_\infty}\right) \tag{11b}$$

2.4 Statistical Estimators

The Mars EDL data set considered for analysis here consists of accelerometers, rate gyroscopes, radar altimeters, and port pressure sensors. The estimation method in Fig. 11 can consist of deterministic or statistical estimators. All of these cases involve starting the reconstruction process from an initial condition and then propagating this condition to the time the next measurement is available, where the estimated states are updated using the measurement value. Three types of statistical estimators have been considered in this methodology: Extended Kalman Filter (EKF), Unscented Kalman Filter (UKF), and Adaptive filter. EKF has been the standard in the reconstruction field, whereas UKF has been recently introduced. Adaptive filters have been used in orbital determination problems and have been shown to be robust to situations where the *a priori* knowledge of process and measurement noises are lacking. The following section describes the algorithm for these three methods.

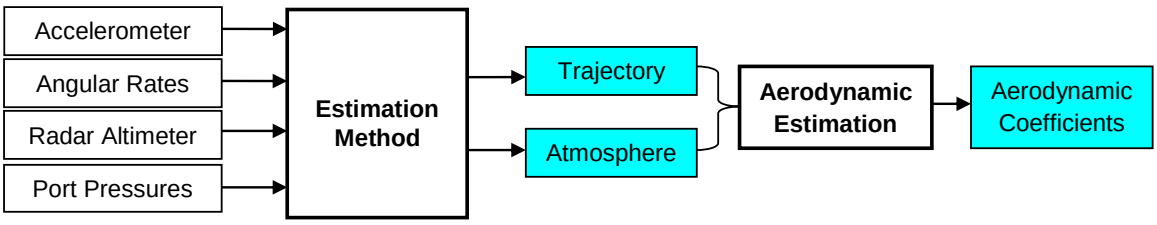

Figure 11: Flow diagram of the overall reconstruction methodology for Mars EDL flight parameters.

2.4.1 Extended Kalman Filter

EKF is a well-known modification of the linear Kalman filter and the algorithm is summarized below [93, 94]:

1. Initialize the state vector and the state covariance matrix at time $t_{k-1} = t_0$ and let $k = 1$, where k is an index of the epoch when a measurement is first available.

2. Read in the measurement at time t_k.

3. Calculate a nominal state ($\hat{\mathbf{x}}_k^-$) at time t_k by integrating the non-linear equations of motions (Eqs. (3)) with $\hat{\mathbf{x}}_{k-1}^+$ as the initial condition.

4. Calculate the nominal state covariance matrix ($\hat{P}_k^-$) by integrating the Riccati equations (Eq. (12a)).

5. Calculate the measurement residual vector ($\mathbf{y}_k$), the measurement sensitivity matrix (H_k), and the Kalman gain (K_k) using the nominal state and state covariance (Eq. (12b)).

6. Calculate the best estimate of the state ($\hat{\mathbf{x}}_k^+$) and state covariance ($\hat{P}_k^+$) using Eqs. (12c) and (12d).

7. Increment counter k and go back to step 2 until measurements at all times have been processed.

$$\dot{P} = AP + PA^T + BQB^T \tag{12a}$$

$$K_k = \hat{P}_k^- H_k^T \left(H_k \hat{P}_k^- H_k^T + R_k \right)^{-1} \tag{12b}$$

$$\hat{\mathbf{x}}_k^+ = \hat{\mathbf{x}}_k^- + K_k \left(\mathbf{y}_k - h(\hat{\mathbf{x}}_k^-) \right) \tag{12c}$$

$$\hat{P}_k^+ = (I - K_k H_K) \hat{P}_k^- (I - K_k H_k)^T + K_k R_k K_k^T \tag{12d}$$

A is the Jacobian of the equations of motion with respect to the state vector (i.e. $\partial\dot{\mathbf{x}}/\partial\mathbf{x}$), B is the Jacobian of the equations of state with respect to the state noise (also called process noise) vector (i.e. $\partial\dot{\mathbf{x}}/\partial\mathbf{w}$), and I is the $n \times n$ identity matrix, where is n is the number of states. The measurement covariance matrix ($R = E(\mathbf{v}\mathbf{v}^T)$) is defined at time k and information from pre-flight sensor calibration information is typically used for this matrix. The process noise covariance ($Q = E(\mathbf{w}\mathbf{w}^T)$) is typically based on experimentation or pre-flight modeling errors.

For Mars EDL trajectory reconstruction, these two matrices have the largest uncertainties. EKF assumes *a priori* knowledge of the R and Q noise matrices; however, for Mars EDL applications, R matrix is likely to involve IMUs and radar altimeters with *a priori* unknown bias, scaling, and random noise, and Q matrix is likely to include *a priori* unknown aerodynamic and atmospheric uncertainties. The lack of a good estimate for these statistics can corrupt the trajectory reconstruction and lead to filter divergence.

2.4.2 Unscented Kalman Filter

Instead of using a linearized approximation to update the state and covariance matrix, the UKF is based on the idea that a transformation of a probability distribution can be approximated with multiple direct evaluations of an arbitrary nonlinear function [95]. Just like the EKF, the UKF assumes that the state variables are Gaussian distributions in which the state estimates are the means and the state uncertainties are the standard deviations of the distributions.

The UKF propagates a set of specially chosen state vectors called sigma points to characterize the transformation of the state probability distribution. The definition of the sigma points and how they are propagated in time are shown in Eqs. 13 [95, 96], where n is the number of elements in the state space and λ_u, α_u, β_u, and κ_u are user

defined tuning constants. κ_u is 0 or $3-n$, $u=2$ when $\mathbf{x}$ is Gaussian, $\alpha_u \approx 1\times10^{-3}$, and $\lambda \approx \alpha_u^2(n+\kappa_u)-n$ [95, 97]. W is the weights for the $(2n+1)$ sigma points and h is the nonlinear transformation. The superscript "b" indicates the state and covariance pre-transformation and the superscript "a" indicates values post-transformation.

$$\mathbf{x}^{(0)} = \bar{\mathbf{x}} \tag{13a}$$

$$\mathbf{x}^{(i)} = \bar{\mathbf{x}} + \tilde{\mathbf{x}}^{(i)} \quad i=1,\ldots,2n \tag{13b}$$

$$\tilde{\mathbf{x}}^{(i)} = \left((n+\lambda_u)\,P\right)_i^T \quad i=1,\ldots,n \tag{13c}$$

$$\tilde{\mathbf{x}}^{(n+i)} = -\left((n+\lambda_u)\,P\right)_i^T \quad i=1,\ldots,n \tag{13d}$$

$$W_{mean}^{(0)} = \frac{\lambda_u}{n+\lambda_u} \tag{13e}$$

$$W_{covariance}^{(0)} = W_{mean}^{(0)} + 1 - \alpha_u^2 + \beta_u \tag{13f}$$

$$W^{(i)} = \frac{1}{2\,(n+\lambda_u)} \quad i=1,\ldots,n \tag{13g}$$

$$\mathbf{x}^{a(i)} = h\left(\mathbf{x}^{b(i)}\right) \tag{13h}$$

$$\bar{\mathbf{x}}^a = \sum_{i=0}^{2n} W^{(i)}\mathbf{x}^{a(i)} \tag{13i}$$

$$P^a = \sum_{i=0}^{2n} W^{(i)}\left(\mathbf{x}^{a(i)}-\bar{\mathbf{x}}^a\right)\left(\mathbf{x}^{a(i)}-\bar{\mathbf{x}}^a\right)^T + Q_{k-1} \tag{13j}$$

A new set of sigma points need to be calculated from $\hat{\mathbf{x}}_k^-$ for the measurement equations. The predicted measurement for each sigma point ($\hat{\mathbf{y}}_k^{(i)}$) and the estimate of the mean value for the predicted measurement ($\hat{\mathbf{y}}_k$) can be calculated using Eqs. 14. The predicted measurement covariance (P_y) and the cross covariance between the estimated state and measurement (P_{xy}) are used for the Kalman gain and state update steps [95, 96, 97].

$$P_y = \sum_{i=0}^{2n} W^{(i)} \left(\hat{\mathbf{y}}_k^{(i)} - \hat{\mathbf{y}}_k\right) \left(\hat{\mathbf{y}}_k^{(i)} - \hat{\mathbf{y}}_k\right)^T + R_k \tag{14a}$$

$$P_{xy} = \sum_{i=0}^{2n} W^{(i)} \left(\hat{\mathbf{x}}_k^{(i)} - \hat{\mathbf{x}}_k\right) \left(\hat{\mathbf{y}}_k^{(i)} - \hat{\mathbf{y}}_k\right)^T + R_k \tag{14b}$$

$$K_k = P_{xy} P_y^{-1} \tag{14c}$$

$$\hat{\mathbf{x}}_k^+ = \hat{\mathbf{x}}_k^- + K_k \left(\mathbf{y}_k - \hat{\mathbf{y}}_k\right) \tag{14d}$$

$$\hat{P}_k^+ = \hat{P}_k^- - K_k P_y K_k^T \tag{14e}$$

Unlike the EKF, UKF does not require the calculation of Jacobians and other derivative terms that are often computationally difficult and are sources of numerical ill-conditioning. Additionally, it should be noted that other derivative-free filters, such as the divided-difference filters, are essentially variants of the UKF with minor differences in the tuning parameters for selecting the sigma points [98].

For a multidimensional estimation problem, as is the case with EDL reconstruction, κ_u can be negative. In these cases, it is possible that the predicted covariance will not be positive semi-definite. In this case, Ref. [95] recommends a modification to the predicted measurement covariance equation (Eq. 14a). The modification simply consists of excluding the first sigma point from the covariance calculation and is shown in Eq. 15.

$$P_y = \sum_{i=1}^{2n} W^{(i)} \left(\hat{\mathbf{y}}_k^{(i)} - \hat{\mathbf{y}}_k\right) \left(\hat{\mathbf{y}}_k^{(i)} - \hat{\mathbf{y}}_k\right)^T + R_k \tag{15}$$

2.4.3 Adaptive Filtering

As mentioned earlier, adaptive filtering is used when one does not have *a priori* accurate knowledge of the measurement and process noise. Unlike linear, discrete, stochastic problems where the best linear, minimum variance, unbiased estimate of the state is given by the Kalman filter, no optimal estimator is known for a case

when the process noise and measurement noise parameters are unknown [99]. The approach used in this paper is the covariance matching or noise-adaptive technique and is summarized in Eqs. (16)-(22) [99, 100].

$$\mathbf{w}_j = \hat{\mathbf{x}}_j - \bar{\mathbf{x}}_j \quad j = 1, \ldots, N \tag{16}$$

$$\hat{\mathbf{w}} = \frac{1}{N} \sum_{j=1}^{N} \mathbf{w}_j \tag{17}$$

$$\hat{Q} = \frac{1}{N-1} \sum_{j=1}^{N} B \left[\left(\mathbf{w}_j - \hat{\mathbf{w}} \right) \left(\mathbf{w}_j - \hat{\mathbf{w}} \right)^T - \left(\frac{N-1}{N} \right) \left(\bar{P}_j^* - \hat{P}_j \right) \right] B^T \tag{18}$$

$$\bar{P}_j^* = \int_{t_{j-1}}^{t_j} \left(AP + PA^T \right) dt \tag{19}$$

$$\mathbf{v}_i = \mathbf{y}_i - h\left(\bar{\mathbf{x}}_i \right) \quad i = 1, \ldots, L \tag{20}$$

$$\hat{\mathbf{v}} = \frac{1}{L} \sum_{i=1}^{L} \mathbf{v}_i \tag{21}$$

$$\hat{R} = \frac{1}{L-1} \sum_{i=1}^{L} \left(\left(\mathbf{v}_i - \hat{\mathbf{v}} \right) \left(\mathbf{v}_i - \hat{\mathbf{v}} \right)^T - \left(\frac{L-1}{L} \right) H_i \bar{P}_i H_i^T \right) \tag{22}$$

Since the exact process and measurement noise are unknown (together with the true states), empirically derived quantities serve as surrogates to estimate the process and measurement noise. The empirically derived quantities $\mathbf{w}$ and $\mathbf{v}$ are approximations of the actual state noise and measurement noise vectors. Using these quantities, one can estimate Q and R as shown in Eqs. (16)-(22). Information from the last N state estimates are used to calculate $\mathbf{w}$, while information from the last L measurement points are used to calculate $\mathbf{v}$.

The values for the various state and covariance updates are found from the EKF. The state noise vector's batch size N does not need to be the same as the measurement noise vector's batch size L. It should be noted that for at least the first N and L state an *a priori* estimate of Q and R is used for the measurement update steps in the EKF. Thus, the batch sizes are tuning terms that need to be determined empirically: small

batch sizes would mean that the filter can begin adapting quickly in the reconstruction process, but a small sample size also means that the estimated statistics, Q and R, are not representative according to the central limit theorem.

For the specific case of Mars EDL trajectory reconstruction, Q can give information about the aerodynamic coefficient uncertainties or the atmospheric property uncertainties on the day-of-the-flight. The measurement noise uncertainties, R, can also give valuable information about the sensor calibration.

2.4.4 Statistical Smoothing

The reconstruction can start from the atmospheric entry (forward pass) or a projected landing location (backwards pass). The forward pass starts its estimate from an initial state and covariance that is found independent of the trajectory reconstruction process and the reconstruction is conducted in a chronological manner. The backwards pass has the advantage of starting at a smaller uncertainty value as it begins from the end of the forward estimate. The forward and backward pass estimates (denoted by the subscripts f and b respectively) can be combined using the Fraser-Potter smoothing solution [101], which is shown in Eqs. 23. It is advantageous to combine both the forward and backward estimates in finding an optimal estimate of the trajectory [50]. The forward pass estimate at time k uses the measurement data from entry to k, while the backward pass estimate at k uses the measurement data from landing time to k. The combined smoothed estimate at time k will then use measurement data at all times to create the estimate at k and is similar to a batch least-squares solution [102].

$$\hat{P}_k = \left[\hat{P}_{f,k}^{-1} + \hat{P}_{b,k}^{-1}\right]^{-1} \tag{23a}$$

$$\hat{\mathbf{x}}_k = \hat{P}_k \left[\hat{P}_{f,k}^{-1}\hat{\mathbf{x}}_{f,k} + \hat{P}_{b,k}^{-1}\hat{\mathbf{x}}_{b,k}\right]^{-1} \tag{23b}$$

2.4.5 Filter Tuning

The choice of the process and measurement noise statistics can have a significant effect on the performance of the statistical filter [103]. Tuning of filters is typically used to deal with ill-conditioning in the problem and is equivalent to regularization techniques in parameter estimation where a penalty function is added to improve the conditioning of the problem [53]. The selection process of the parameters is commonly known in the literature as *filter tuning* and it usually consists of a trial-and-error method of changing process and measurement noise statistics until a desirable result is met. The trial-and-error process is time consuming, relies on engineering judgment of the filter designer rather than some physical value, and is often non-unique. The designer could use statistical sample consistency checks to ensure that the filter is *consistent.* This involves three criteria [104]:

1. State errors should be unbiased ($E[\tilde{\mathbf{x}}] = 0$) and their covariance should be compatible with the state covariance (P)

2. The measurement residual (or innovation) should also be unbiased and be compatible with the measurement covariance (R)

3. The measurement residual should be random, white noise (i.e. uncorrelated in time)

For every filter used in this methodology, checks were made to ensure that the state residuals being calculated did not have a bias and that the estimated state covariance bounded the residuals. Similar checks were made for the measurement residuals as well. Additionally, it was ensured that the measurement noise residuals had a Gaussian distribution, which was the distribution that was assumed implicitly by all three filters.

However, the theory behind the Kalman filter only assures us that the above consistency checks will be true for linear problems [105]; there are no assurances

that the state covariance will represent the actual state error statistics for non-linear problems. Conversely, using consistency checks to design a filter does not guarantee a minimum state estimation error, which is the goal of the state estimation procedure in the first place [106].

Filter tuning can also be recast as a minimization problem [55, 106]. The objective function is to minimize state deviation error over time and the parameters of the optimization process are the process and measurement noise statistics. The process noise statistic consists of the contents of the process noise covariance (Q) and the measurement noise statistic similarly consists of the contents of the measurement noise covariance (R). Often the measurement noise can be calculated during sensor testing and calibration, so R is known and can be excluded from the filter tuning problem. Additionally, the usually unknown process noise covariance is a symmetric matrix, so if there are n states and Q is $n \times n$, then there are only $n(n+1)/2$ unique elements in the Q matrix. Since the off-diagonal elements of the matrix are cross correlations that are difficult to interpret physically, the minimization parameters can be reduced to only the n elements in the diagonal of the Q matrix (i.e. $q_{1,1}, q_{2,2}, \ldots, q_{n,n}$) [106].

Powell [106] and Oshman [107] suggest a minimization problem for filter tuning where the objective is to optimize the deviation of the state estimate from known truth values. Equation 24 shows the objective function (J) as function of process noise covariance elements, error between the true and estimated states ($\mathbf{e}$), and the number of measurement points (G) at which times the filter estimates a state. Non-dominated Sorting Genetic Algorithm-II [108] (NSGA-II) is used as the optimization routine, since the filter tuning process is inherently non-unique and multi-modal, which a stochastic search algorithm like NSGA-II can handle very well. The optimization routine is defined in more detail in Section 5.1.2.

$$J\left(q_{1,1}, q_{2,2}, \ldots, q_{n,n}\right) = \left[\frac{1}{G}\sum_{t_i=t_0}^{t_{final}} \mathbf{e}_i^T \mathbf{e}_i\right]^{\frac{1}{2}} \tag{24}$$

When true states are not known, filter tuning can be performed on simulated data similar to the true states and then the tuned parameters can be applied to the unknown truth case. Additionally, the RMS of the measurement residuals can serve as a surrogate for $\mathbf{e}$ in Eq. 24 [106]. Part of this thesis work is to demonstrate the EDL reconstruction methodology on actual flight data from the Mars Science Laboratory, in which case the true states are unknown. Thus, the effect of filter tuning based on simulated data or the measurement residual approach can be demonstrated during the reconstruction of that data set.

2.5 Summary

Typical atmospheric entry data set are sparse and often leave parameters of interest directly unobservable. This chapter presents an estimation methodology that can directly reconstruct EDL trajectory and atmospheric parameters and also estimate aerodynamic quantities using the reconstruction products while processing a realistic set of disparate data typically measured by EDL missions. The three main parts of the methodology presented are the process equations, measurements equations, and filter algorithms.

The process equations give a nominal estimate of the dynamics of the system and the specific equations presented here captured changes in the vehicle's position, velocity, attitude, and sensed atmospheric parameters. The equations are unique from past EDL reconstruction methodologies since the velocity propagation equations are a function of aerodynamic coefficients instead of measured accelerations, allowing IMU data to be treated as *measurements* in the estimation methodology and providing two independent observations of atmospheric density when IMU data are combined with FADS data.

The measurement equations provide nominal estimates of the sensor data and are critical for the estimator to translate information gained from measurements to

update the state estimate. The FADS data measurement equation is presented and the process of using trajectory and atmospheric estimates for aerodynamic estimates is also studied.

Finally, the algorithm for the three statistical filters - EKF, UKF, and Adaptive filter - are presented and the nuances between each estimator in terms of state uncertainty propagation and process noise handling were explained. The EKF is the standard non-linear filter popular in EDL and other state estimation fields, but UKF and Adaptive filter are believed to be more adept at handling non-linearity in the system dynamics, which is the point of concern for Mars EDL applications where there are large non-linear uncertainties introduced by the atmosphere and aerodynamics. Additionally, methods of combining different estimates using statistical smoothing or methods of characterizing process noise for the EKF using filter tuning are discussed.

The methodology developed in this chapter is tested in the next two chapters using simulated data set where the truth is known and flight data set. The methodology also serves as the tool for improved methods in sensor and vehicle design covered in later chapters.

CHAPTER III

SIMULATED DATA RECONSTRUCTION

The estimation methodology for EDL trajectory, atmosphere, and aerodynamic parameters described in the last section is demonstrated using simulated Mars EDL data sets in this section. Each estimation method is tested with simulated data set and the performance of the estimators is quantified by looking at the difference between the estimated quantities and the known, true states. In the next chapter, the estimation methodology will also be applied to an actual flight data set - Mars Science Laboratory - and the reconstruction between the different estimators will be compared.

The organization of this chapter is as follows. The simulated data set used to test the estimation methodology is introduced in Sec. 3.1 along with the initial state and process noise information. Next, Secs. 3.2 and 3.3 focus on the estimation performance of the EKF, UKF, and Adaptive filter with the simulated nominal and perturbed data set. Finally, the reconstruction performance of all three filters in the estimation performance are compared in Sec. 3.4.

3.1 Simulated Data Set

3.1.1 True Trajectory

Mars EDL data sets are simulated in this study to demonstrate the effectiveness of a statistical reconstruction methodology that incorporates disparate data types and estimates trajectory, atmospheric parameters, and aerodynamic coefficients. The NASA-developed Program to Optimize Simulated Trajectories II (POST2) [109] is used to generate two Mars EDL trajectories which are shown in Figs. 12 and 13. The trajectory is for a 2.65 m, 70 deg. sphere-cone with the same geometry and

specifications as the Mars Exploration Rovers (MER) and Phoenix entry vehicles. Two types of trajectories were simulated to test the estimation methodology. One is a nominal EDL trajectory while the other is a dispersed case of the nominal trajectory with perturbations to the vehicle's aerodynamic database, planetary atmosphere, and winds. These trajectories represent the truth data.

3.1.2 Sensor Measurements

The POST2 outputs are used to generate IMU (accelerometer and gyro rates), radar altimeter (when the altitude is less than 10 km), and pressure transducer data (when the dynamic pressure, q_∞, is greater than 850 Pa.). Random Gaussian noise is applied to the simulated data to model measurement noise and create a data set for analysis (see Fig. 14). The uncertainty of the noise is based on past Mars EDL instrumentation specifications as shown in Table 4.

Table 4: Measurement noise uncertainties for the simulated data set.

Measurement	3σ uncertainty (normal)	Sample rate (Hz.)
Three-axis sensed acceleration	100 μg-RMS[a]	25
Three-axis angular rate	0.03 deg/hour-RMS[b]	-
Radar altimeter altitude	0.3 m[a]	1
Pressure transducers	1% reading/transducer[c]	4

Notes: [a] [57] [b] [36] [c] [37]

The data sample rate used for reconstruction was chosen after a sensitivity study of the root-mean-square (RMS) of the error in the estimate of some parameters of interest, which are shown in Fig. 15. Although both the IMU and FADS data were available at higher sample rates, it was found that the error does not decrease significantly if the sample rate is increased from 25 Hz for the IMU data and 4 Hz for the FADS data.

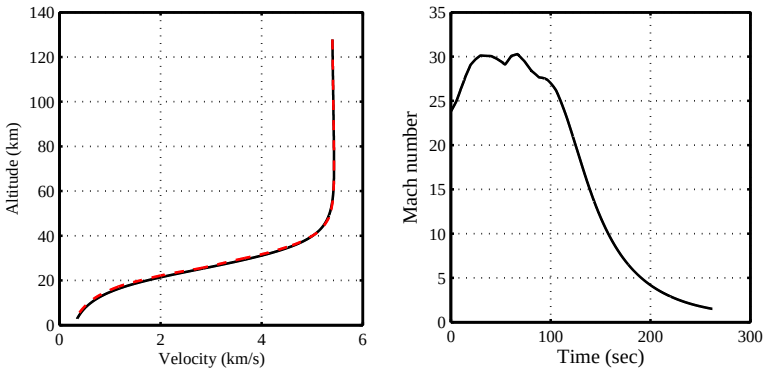

(a) Velocity vs. altitude

(b) Mach number

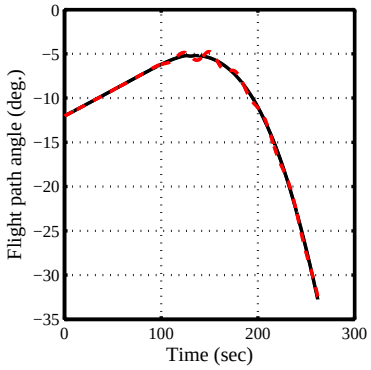

(c) Flight path angle

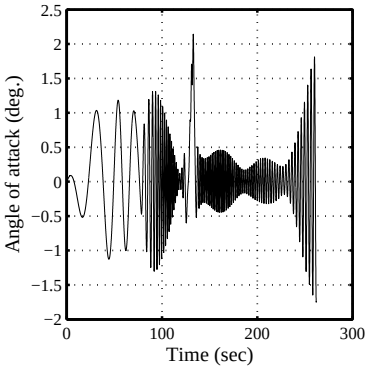

(d) Angle of attack

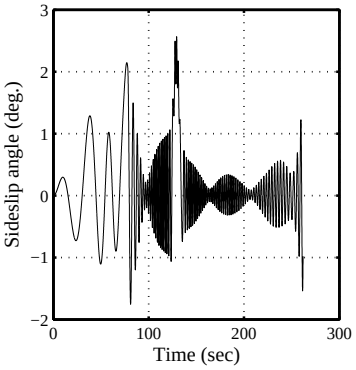

(e) Sideslip angle

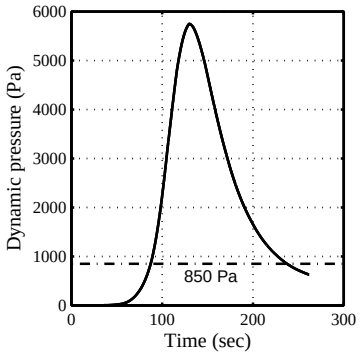

(f) Dynamic pressure

Figure 12: Reference trajectories used as the truth to verify reconstruction performance of this methodology.

3.1.3 Initial States and Process Noise Uncertainties

The reconstruction process for both data sets begins with the same initial conditions and initial covariance values. The initial uncertainties in the state variables are listed in Table 5 and are based on the initial conditions at entry interface from recent Mars

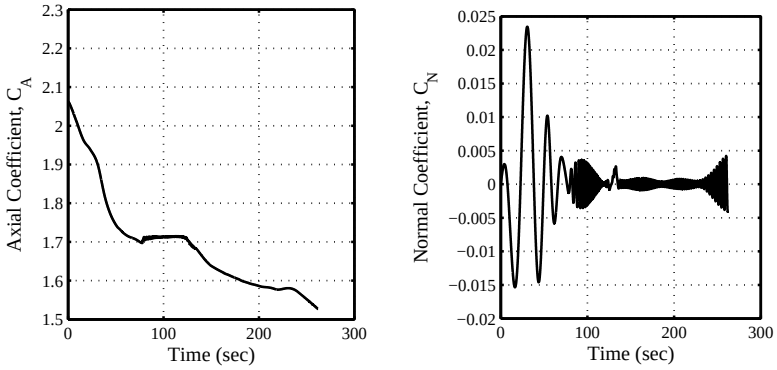

(a) Axial force coefficient (b) Normal force coefficient

Figure 13: Reference aerodynamic coefficients used as the truth to verify reconstruction performance of this methodology.

missions. The initial state covariance matrix is calculated from these values.

The process noise covariance is calculated using the uncertainty information given in Table 6. Process noise improves the estimator's ability to reconstruct parameters from noisy data and to model uncertainties in the process equations [89, 93, 94, 96]. Kinematic equations that describe the propagation of the position states are well-known and hence there is no process noise modeled for these equations. The velocity equations of motion, however, have uncertainties from the aerodynamics, atmospheric parameters, and other unknown model errors and hence have process noise states associated with them. The attitude states also have uncertainty, but since the equations are strongly related to the measured gyroscope rates, the process noise for the quaternion propagation equations are the same as the measurement noise of the angular rate sensors. The high process noises for freestream pressure and density demonstrate the relatively high uncertainty in the process equations so that the estimator is biased towards the more certain measurements from the accelerometer and FADS transducers.

The process noise uncertainties are tuning parameters for a filter and in this case the values were chosen using methods described in Sec. 2.4.5 to tune the EKF reconstruction using the nominal data set. The process noise could have been varied

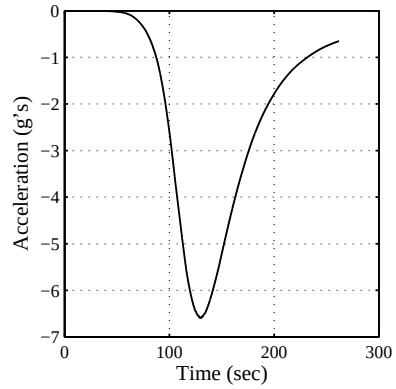

(a) Axial acc. ($a_{x,b}$)

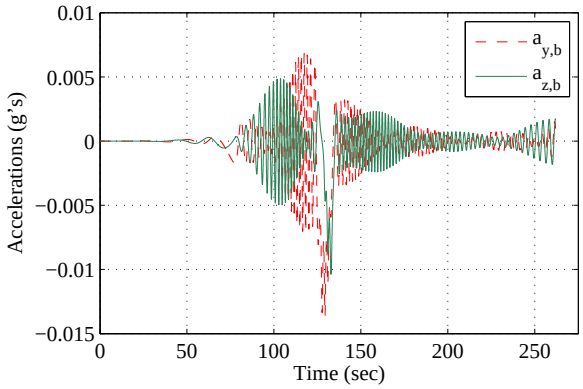

(b) Normal accelerations

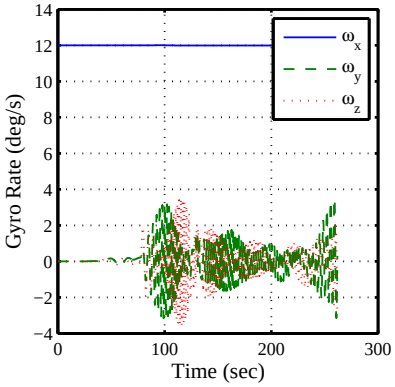

(c) Angular rates

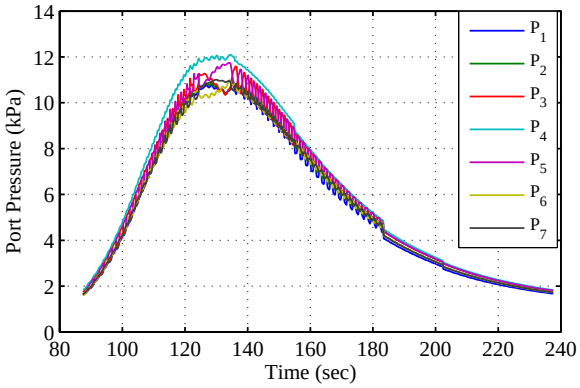

(d) Pressure transducers

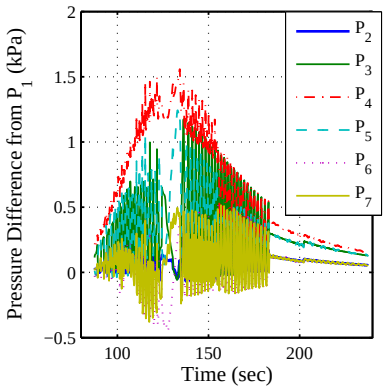

(e) Difference compared to P_1

Figure 14: Example of the simulated data used for the reconstruction.

for the UKF reconstructions and the dispersed data set reconstructions; however, the noise was kept constant for all of the reconstructions to test the robustness of the methodology. When an actual flight data set is analyzed, the truth information will be unknown; in that case, the tuned parameters from the simulated data set should

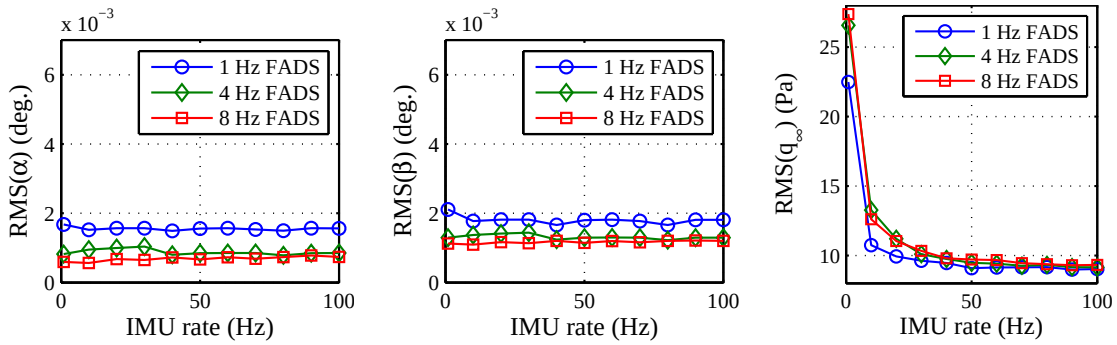

(a) Angle of attack (b) Sideslip angle (c) Dynamic pressure

Figure 15: Effect of sample rate of IMU and FADS data on the estimated parameter residual from the truth.

Table 5: Initial state uncertainties used for the reconstruction process.

State	3σ uncertainty (normal)
Radius (planet-centric) [57]	5100 m
Latitude (planet-centric) [57]	0.12 deg.
Longitude [57]	0.03 deg.
Velocity (relative) [36]	2.9 m/s
Flight path angle (relative) [57]	0.06 deg.
Heading angle (relative) [57]	0.06 deg.
Euler angles (related to the quaternion)	0.03 deg./angle
Freestream pressure	$10p_{\infty,0}$
Freestream density	$10\rho_{\infty,0}$

Table 6: Process noise uncertainties used for the reconstruction process.

State	3σ uncertainty (normal)
Radius (planet-centric)	-
Latitude (planet-centric)	-
Longitude	-
Velocity (relative)	0.003 m/s
Flight path angle (relative)	0.0825 deg.
Heading angle (relative)	0.0825 deg.
Quaternion	Based on angular rate measurement noise
Freestream pressure	$0.3p_{\infty}$
Freestream density	$0.3\rho_{\infty}$

be used to define the filter tuning parameters.

3.2 Nominal Data Set Reconstruction

3.2.1 EKF and UKF

3.2.1.1 Trajectory and Atmospheric Reconstruction

Trajectory parameters, such as planet-centric radius and planet-relative velocity, are the first step in the reconstruction process. The percent deviation from the truth for the trajectory parameters can be seen in Fig. 16. Both the EKF and the UKF do a good job of estimating the radius (within 0.2%) and the velocity, although the UKF estimate's residual magnitude is lower than the EKF estimate's residual. Note that the radius and its uncertainty estimation improve significantly with the introduction of radar altimeter measurement around 220 seconds.

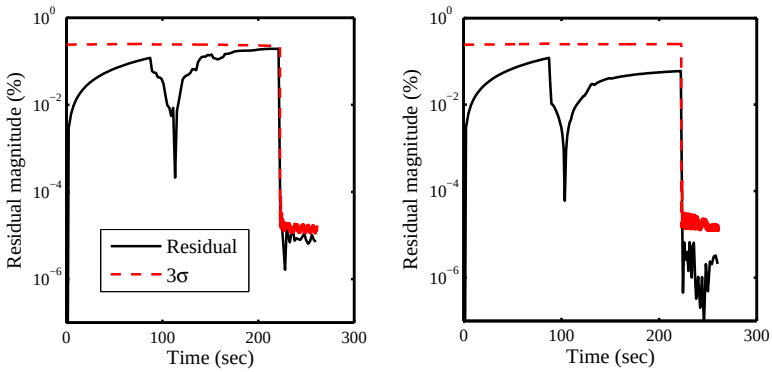

(a) Radius (EKF) (b) Radius (UKF)

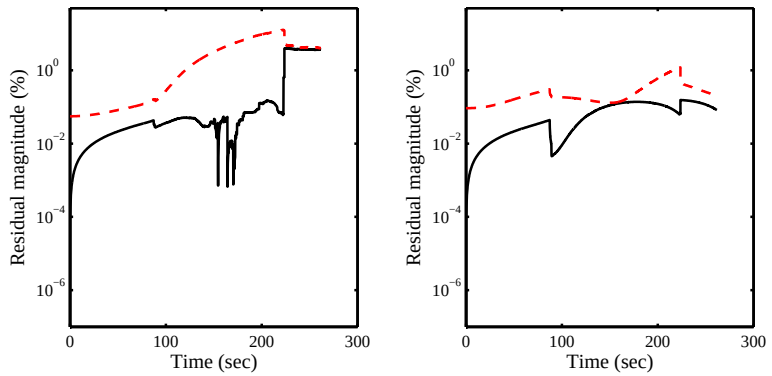

(c) Velocity (EKF) (d) Velocity (UKF)

Figure 16: Nominal simulated data set trajectory estimation using EKF and UKF.

The trajectory and atmospheric parameters in the estimation state vector are

used to generate estimates for the angle of attack, sideslip angle, Mach number, and dynamic pressure, which are shown in Fig. 17.

Recall from Sec. 1.1.3 that MSL had some defined objectives for the estimation of angle of attack, sideslip angle, and dynamic pressure (and initially for Mach number). For the most part, it appears that the trajectory and atmospheric parameters are reconstructed close to the MSL objectives, especially in the region where FADS data are available. The Mach number estimate does stray from the original objective bounds for both the EKF and UKF, but the UKF estimate's residual is lower than the EKF estimate's residual during the time FADS data are available. The original science goals were to reconstruct M_∞ within ± 0.1 of the truth, while the science goals for the other parameters were less stringent (e.g. α and β reconstruction goal is to estimate within ± 0.5 deg.). The Mach number value is dependent on the calculated speed of sound, which in turn relies on the estimated freestream pressure and density. These parameters are estimated using the FADS data that peak around the time period (Fig. 14(d)) when the Mach number is outside the objective bounds. The FADS data have simulated noises that are percentage of the nominal measurement and the data are noisiest in this region. This non-linearity manifests itself in the reconstructed freestream atmospheric parameters, speed of sound, and Mach number.

The estimated uncertainties presented are the 99.7% (3σ) confidence interval since the states are assumed to be Gaussian distributions and the residual between the estimated states and the truth fall within these confidence bands. Due to a lack of the true uncertainty values, it is hard to determine if the UKF provides a better estimate of uncertainties than the EKF, as predicted in the literature.

Quantifying uncertainties of the POST2 simulated data set using techniques such as Monte Carlo analysis and linear covariance analysis may be a possible solution to quantify the true uncertainty values; however, Monte Carlo analysis would only capture initial state uncertainty and process noise (i.e. atmospheric and aerodynamic

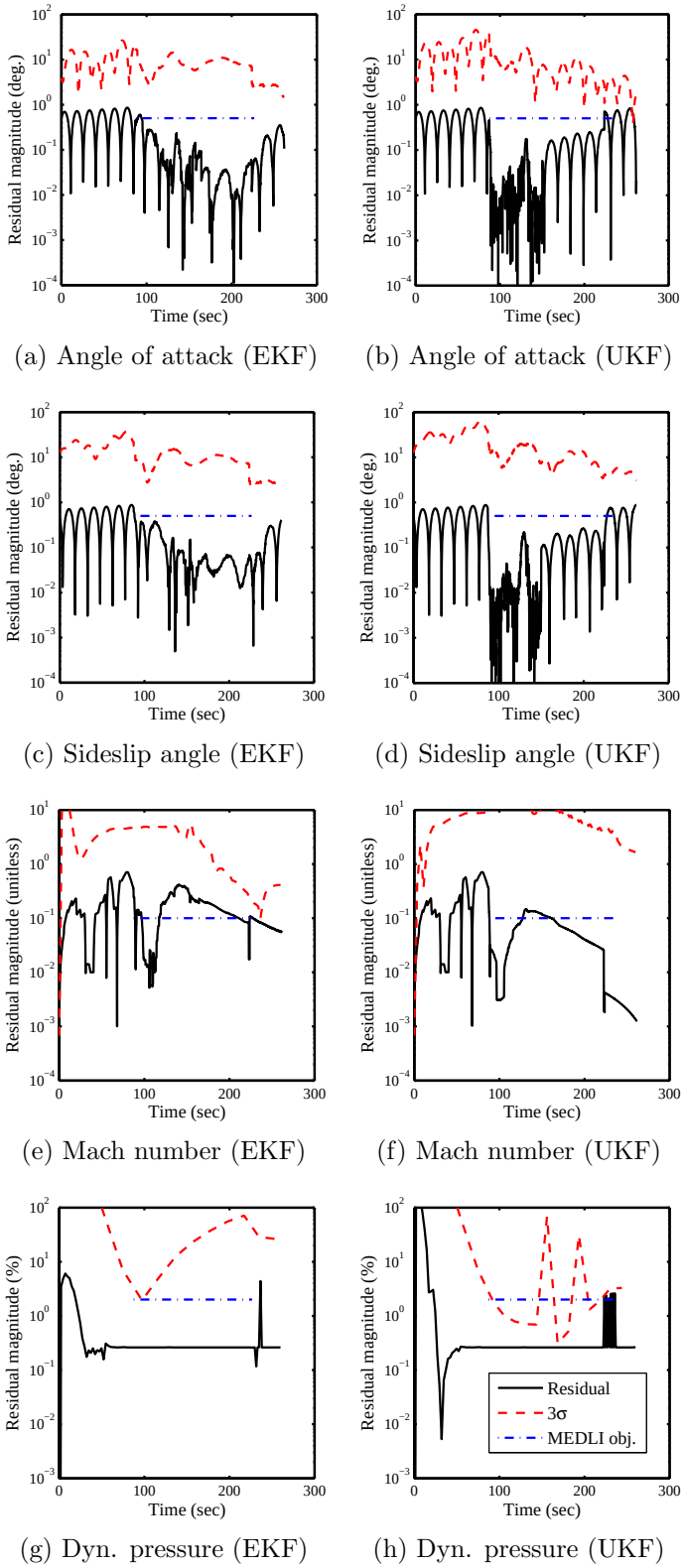

(a) Angle of attack (EKF) (b) Angle of attack (UKF)

(c) Sideslip angle (EKF) (d) Sideslip angle (UKF)

(e) Mach number (EKF) (f) Mach number (UKF)

(g) Dyn. pressure (EKF) (h) Dyn. pressure (UKF)

Figure 17: EKF and UKF estimate of the angle of attack, sideslip angle, Mach number, and dynamic pressure using the nominal simulated data set.

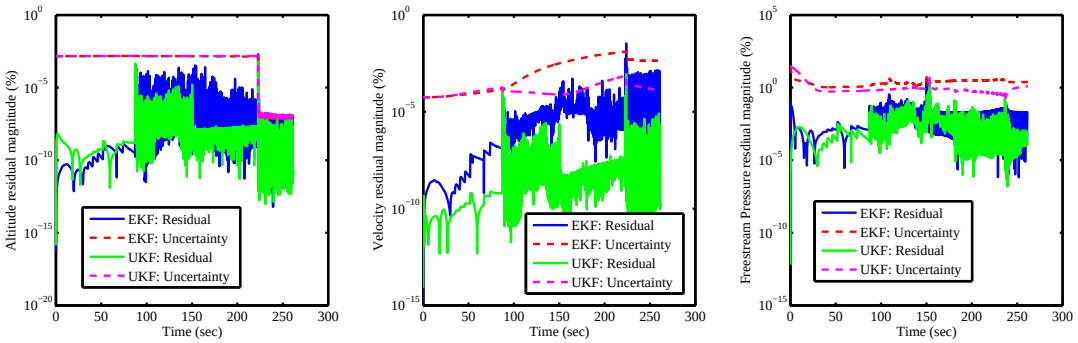

(a) Altitude (b) Velocity (c) Freestream pressure

Figure 18: Comparison of measurement residuals between EKF and UKF using the nominal simulated data set.

uncertainties) and fail to capture the uncertainty in the measurements themselves or the phenomenon of the filter improving its state estimate with every measurement that becomes available. Thus, the Monte Carlo or linear covariance analysis-based uncertainties will be different from the estimated uncertainties from the filter. Instead of comparing estimated and true uncertainties, a more appropriate check for the filter performance is comparing the residuals during measurement update (i.e. Eq. (12c) and not residual from the true states) and the estimated uncertainties. If the residuals lie within the bounds of the uncertainties then the filters are consistent [104]. Additionally, lower residuals would support the hypothesis that a filter is performing well. Figure 18 shows the measurement residuals of the radius, velocity, and freestream pressure for the EKF and UKF using the nominal data set. One sees that both filters are consistent, but the UKF slightly outperforms the EFK both in the lower residual values and tighter confidence bounds.

3.2.1.2 Aerodynamic Coefficients Reconstruction

Figure 19 shows the reconstructed aerodynamic force coefficients for the time span that FADS data were simulated since the freestream pressure and density are observable without any assumptions about the atmosphere for only this time period. The reconstructed axial force coefficient appears to be very close to the truth, as the

coefficient's deviation for both the EKF and UKF estimates mostly lie within ± 0.02 during the time period of interest. However, the true normal force coefficient (C_N) has a very small value (Fig. 13(a)), which raises a numerical issue as neither method estimates C_N to the same percentage accuracy as they estimate the axial force coefficient (C_A). Although the residuals for C_A and C_N are of the same order of magnitude, the residual for C_N is only one order of magnitude lower than its nominal value. The estimates for C_A and C_N are both accurate demonstrated by their low residuals, but the C_A estimate is better when considering the relative percentage accuracy.

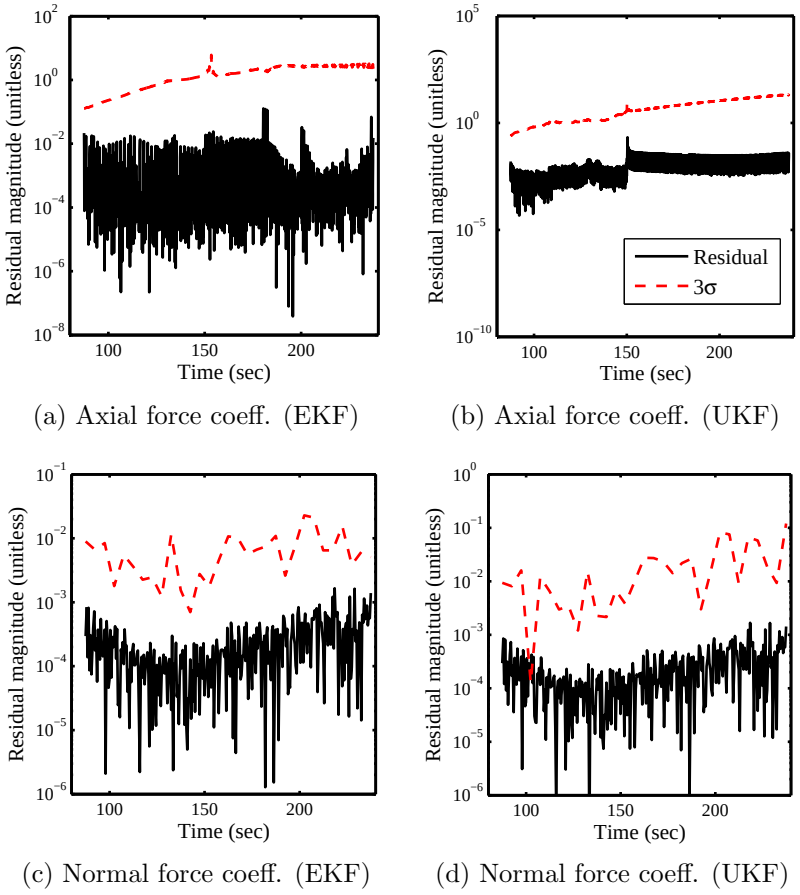

(a) Axial force coeff. (EKF)

(b) Axial force coeff. (UKF)

(c) Normal force coeff. (EKF)

(d) Normal force coeff. (UKF)

Figure 19: EKF and UKF aerodynamic coefficient estimation using the nominal simulated data set.

The 3σ bounds show that the C_A and C_N uncertainty estimates are approximately 1 and 1×10^{-2}. For nominal C_A values of about 1, an error band of 1 may be adequate,

but for nominal C_N values that are of the order 1×10^{-3}, an error band of 1×10^{-2} is large.

3.2.2 Adaptive Filter

3.2.2.1 Tuning of the Adaptive Filter

Most statistical filters have tuning parameters that have to be determined by the analyst to ensure that the filter maintains consistency and does not diverge. For EKFs, the tuning parameters are usually process noise, which the analyst determines experimentally or by using an optimization procedure [106]. An Adaptive filter with the covariance matching technique takes this subjectivity out of the equation by using the state and measurement residual statistics to calculate process or measurement noise and thus ensure consistency. However, since sample statistics are substituted for true (but unknown) statistics of the problem, there is still some subjectivity left in the choice of the sample size used for the noise covariance calculation. Too large of a sample size will ignore sudden changes in the process dynamics, while too small of a sample size will not be consistent with the central limit theorem and produce oscillatory results. This is similar to the situation of using a moving average filter with a variable sample window.

Myers [99] recommends using a fading memory weighting factor to emphasize recent samples in the statistical calculation. However, this introduces another subjective tuning parameter for the analyst to choose. Experimentally this filter has been found to be useful for situations when there is a sudden shift in dynamics, such as a vehicle maneuver. For the simulated EDL data set used for this study, there are no such sudden maneuvers; thus, the fading memory filter was not utilized.

In this investigation, the batch sample size, N, is the only tuning parameter and it is found experimentally, as seen in Fig. 20. The filter was run for several N-values, and it was found that $N = 10$ provides uncertainty values indistinguishable from uncertainties calculated with larger N-values. Note that for a sample size of $N = 5$,

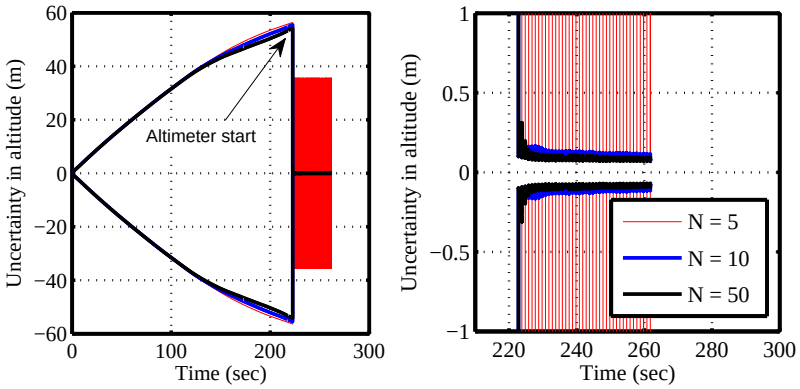

(a) Altitude (b) Altitude Zoomed-in

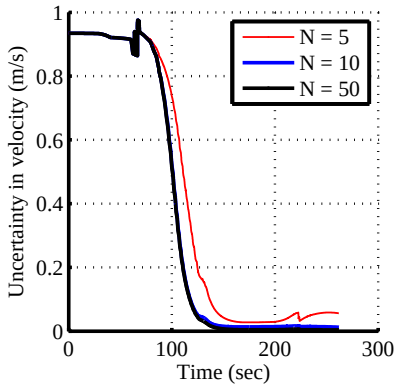

(c) Velocity

Figure 20: Effect of the Adaptive filter batch size on uncertainty calculation.

the uncertainty values could become very oscillatory for certain states like altitude, especially during the terminal descent region where a highly certain altimeter data and relatively less certain accelerometer data are available. With a small sample size, the uncertainty oscillates between the altitude estimate from these two data sources.

3.2.2.2 Sensitivity of Adaptive Measurement Noise Calculation

The Adaptive filter equations introduced in Chapter 2 showed how to adapt both process and measurement noise covariances. However, past Mars EDL reconstruction investigations have noticed that process noise uncertainty is the major contributor for an estimator's performance [110]. This can be observed in Figs. 21 where one sees

that process noise adaptation is the main factor in improving the estimator's performance. The use of measurement noise adaptation does not improve the estimation performance significantly at all. Hence, for simplicity, in this study only the process noise is computed by the Adaptive filter, while the measurement noise is assumed to be known *a priori* based on pre-flight sensor calibration information.

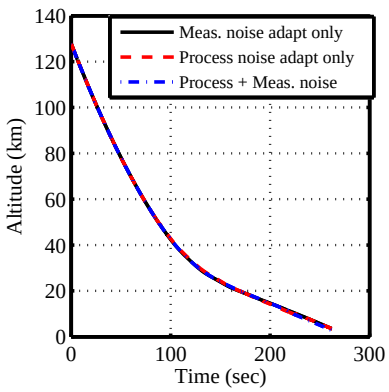

(a) Altitude

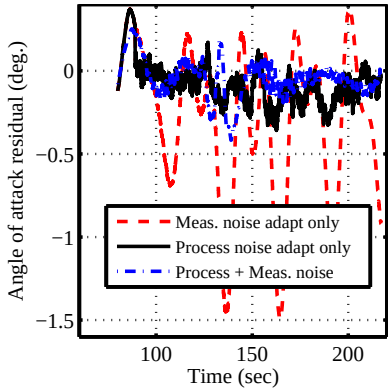

(b) Angle of attack error

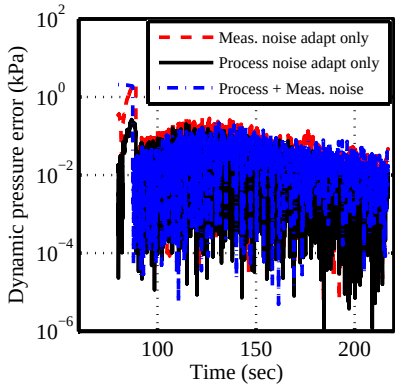

(c) Dynamic pressure error

Figure 21: Effect of calculating the measurement noise covariance adaptively for a simulated Mars EDL data set.

3.2.2.3 Trajectory Reconstruction

As discussed in Chapter 2, the Adaptive filter is an adaptation to the EKF, where most of the EKF equations are used for state propagation and measurement update, but the calculations of the noise matrices are done by the filter directly rather than the use of *a priori*-determined values. The Adaptive filter is used to reconstruct the

nominal data set and Figs. 22 and 23 compares the reconstructed trajectory using the Adaptive filtering technique to the actual data. One can see that there is a close agreement between the estimated and actual quantities. The maximum error in altitude is approximately 150 m and the maximum velocity error is about 0.5 m/s throughout an EDL sequence that lasts around 275 seconds. The effect of the relatively low uncertainty radar altimeter data is clearly visible in the altitude plots where the residual of the error reduces significantly when that data are introduced. This is very similar to actual Mars EDL cases when radar altimeter data available during terminal landing greatly reduce the altitude error relative to that derived from accelerometer only data [87, 56].

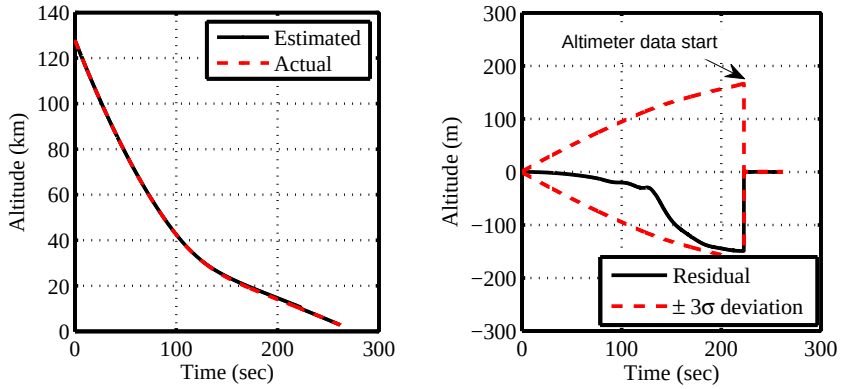

(a) Altitude (b) Error in altitude

Figure 22: Estimated position using Adaptive filter ($N = 10$) and the nominal simulated data set.

3.2.2.4 Atmosphere, Aerodynamics, and other Derived Quantities

Since the state vector also included atmospheric states, atmospheric parameters of interest are directly estimated by the filter. Additionally, derived states, such as angle of attack, sideslip angle, and dynamic pressure can be calculated using a combination of the estimated state vector. These reconstructed states are shown in Figs. 24 and 25.

Figs. 24 and 25 have labels identifying the region when pressure transducer measurements were available. FADS sensors, which measure the pressure distribution

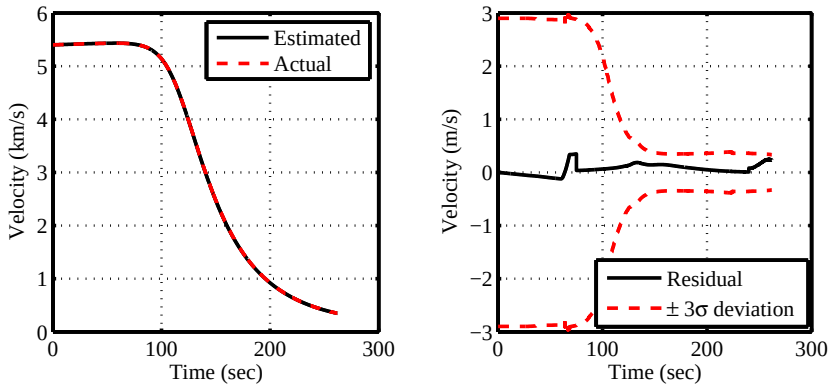

(a) Velocity (b) Error in velocity

Figure 23: Estimated velocity using Adaptive filter ($N = 10$) and the nominal simulated data set.

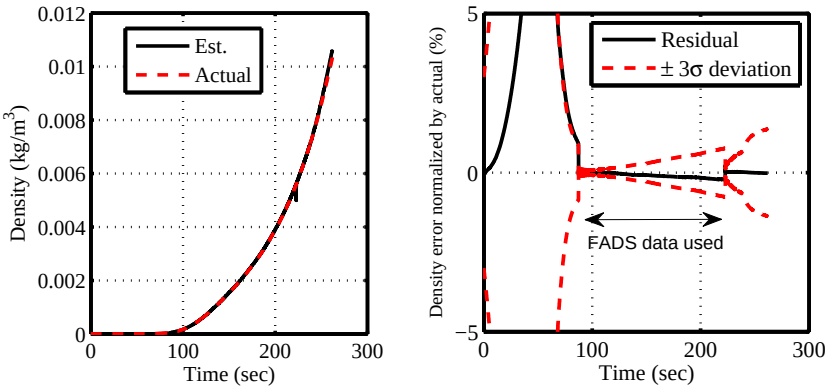

(a) Freestream density (b) Error in freestream density

Figure 24: Estimated atmospheric density using Adaptive filter ($N = 10$) and the nominal simulated data set.

on the aeroshell during entry, allow the estimation of density and pressure without relying solely on accelerometer data. This additional source of information improves the estimation of quantities like angle of attack and dynamic pressure.

Figure 26 shows the estimated axial force coefficient compared to the actual aerodynamic coefficient value. One can see that introduction of FADS data immediately improves the estimation accuracy.

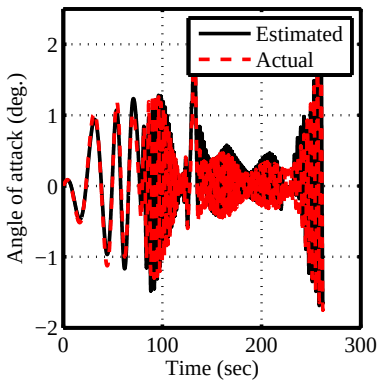

(a) Angle of attack

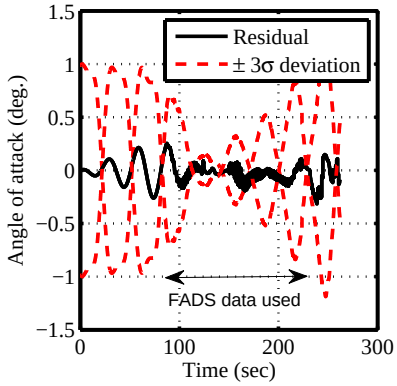

(b) Error in angle of attack

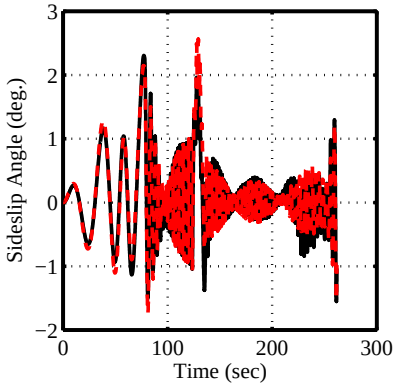

(c) Sideslip angle

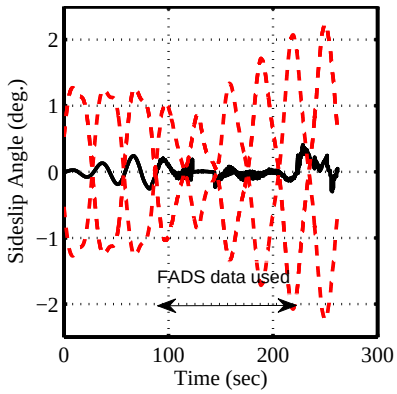

(d) Error in sideslip angle

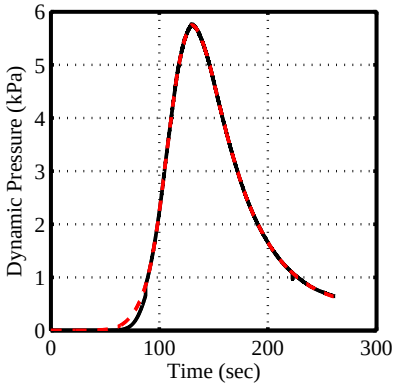

(e) Dynamic pressure

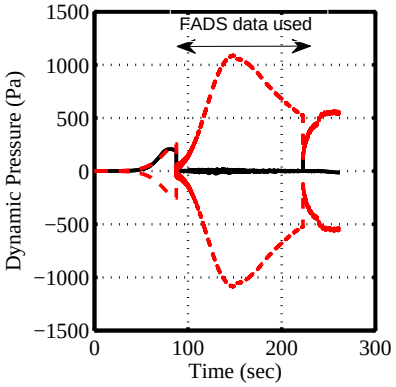

(f) Error in dynamic pressure

Figure 25: Derived quantities using Adaptive filter ($N = 10$) estimation results and the nominal simulated data set.

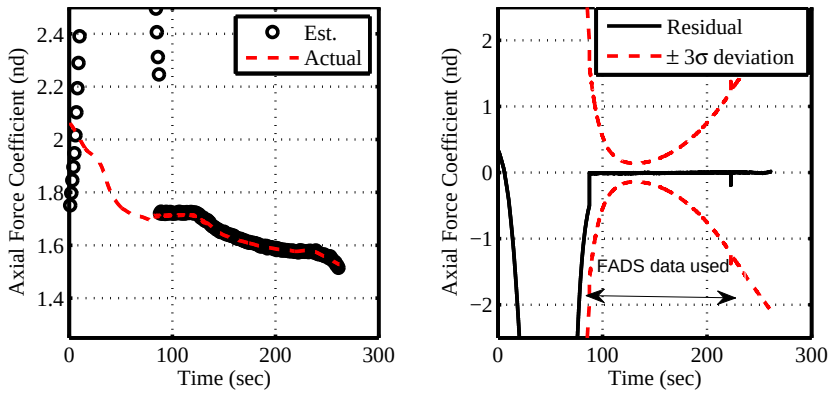

(a) Axial force coefficient (b) Axial force coefficient error

Figure 26: Derived aerodynamic parameter using Adaptive filter ($N = 10$) estimation results and the nominal simulated data set.

3.3 Dispersed Data Set Reconstruction

3.3.1 EKF and UKF

3.3.1.1 Trajectory and Atmospheric Reconstruction

The percent deviation from the truth for the trajectory parameters can be seen in Fig. 27. Once again, both the EKF and the UKF estimate the radius and the velocity accurately, although the UKF estimate's residual magnitude is lower than the EKF estimate's residual for radius and velocity.

The estimates of the derived parameters, specifically angle of attack, sideslip angle, Mach number, and dynamic pressure, using the dispersed simulated data set are shown in Fig. 28.

Compared to the reconstructed parameters from the nominal data set, the deviations of the estimates from the truth appear to be larger and noisier, which could be reflecting the perturbations in aerodynamics and atmosphere modeled in this trajectory or that the process noise is not tuned for this data set. Once again, the estimated angle of attack, sideslip angle and dynamic pressure meet the MSL science objectives for the most part, while the estimated Mach number (Figs. 28(e) and 28(f)) strays from the original MSL objective. The rationale for this deviation is similar to what

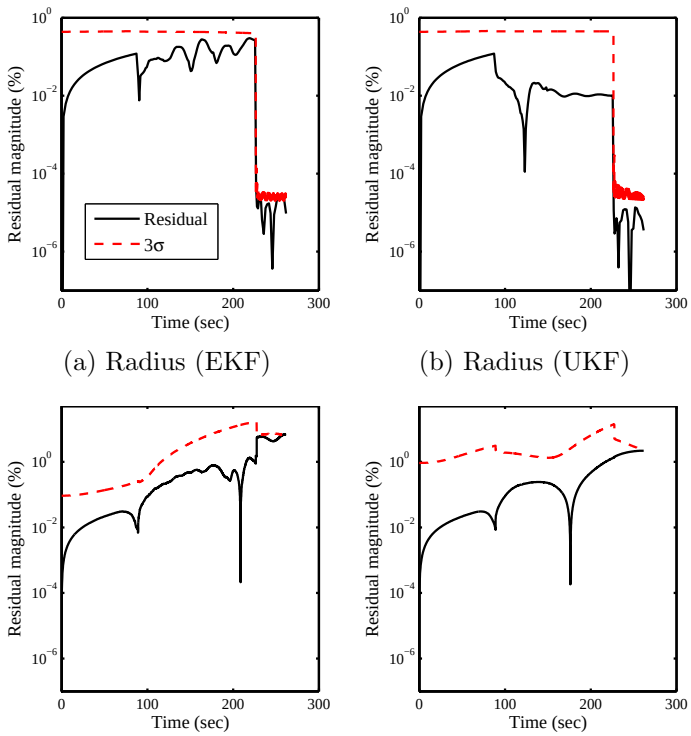

(a) Radius (EKF) (b) Radius (UKF)

(c) Velocity (EKF) (d) Velocity (UKF)

Figure 27: EKF and UKF trajectory estimation using the dispersed simulated data set.

was previously stated in Sec. 3.2. Note that in this case even the true Mach number profile shows significant variation in this region (Fig. 12(b)). This highly non-linear behavior affects the estimation performance of this parameter.

3.3.1.2 Aerodynamic Coefficients Reconstruction

The reconstructed aerodynamic force coefficients for the dispersed data set are shown in Fig 29. The small values for the normal coefficient again raise the same numerical issues previously discussed.

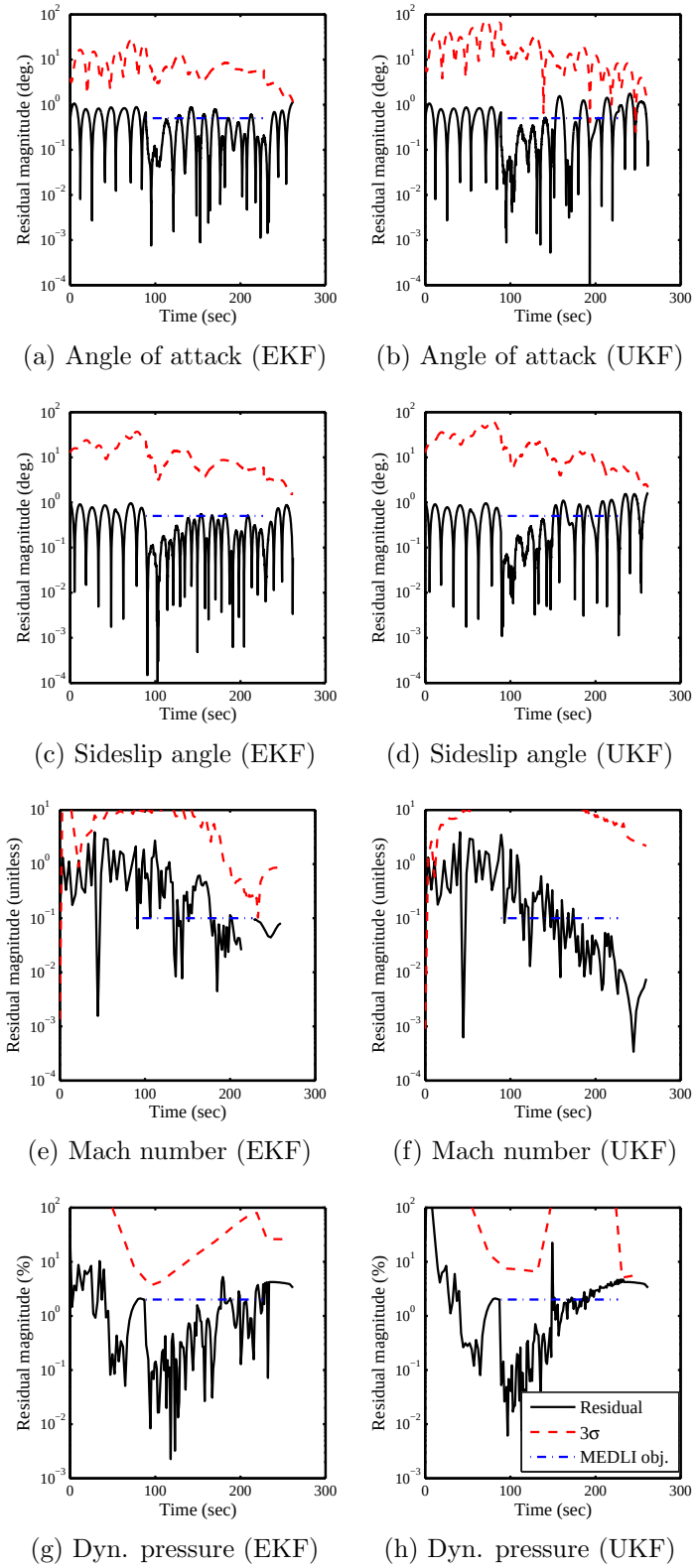

(a) Angle of attack (EKF) (b) Angle of attack (UKF)

(c) Sideslip angle (EKF) (d) Sideslip angle (UKF)

(e) Mach number (EKF) (f) Mach number (UKF)

(g) Dyn. pressure (EKF) (h) Dyn. pressure (UKF)

Figure 28: EKF and UKF estimate of the angle of attack, sideslip angle, Mach number, and dynamic pressure using the dispersed simulated data set.

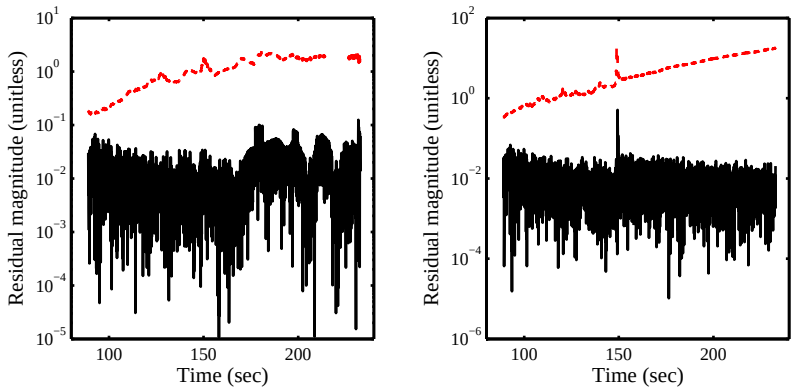

(a) Axial force coeff. (EKF)

(b) Axial force coeff. (UKF)

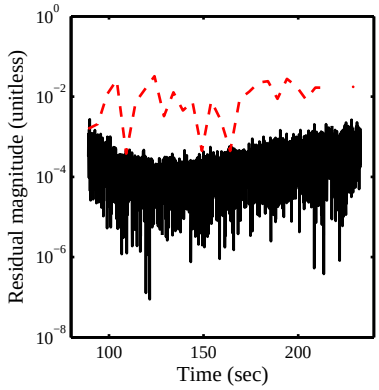

(c) Normal force coeff. (EKF)

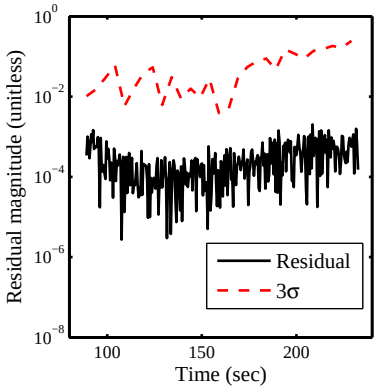

(d) Normal force coeff. (UKF)

Figure 29: EKF and UKF aerodynamic coefficient estimation using the dispersed simulated data.

3.3.2 Adaptive Filter

3.3.2.1 Trajectory Reconstruction

Figures 30 and 31 show the reconstructed trajectory for the dispersed data set using the Adaptive filtering technique. Once again, one can see that there is a close agreement between the estimated and actual quantities and the effect of the relatively low uncertainty radar altimeter data is again easily visible in the altitude plots. Upon comparing the estimated altitude and velocity uncertainty between the nominal (Figs. 22 and 23) and dispersed cases, one sees that the dispersed cases have larger uncertainties. This trend is similar to what was seen between the nominal and dispersed data set reconstruction using the EKF and UKF. The larger uncertainties

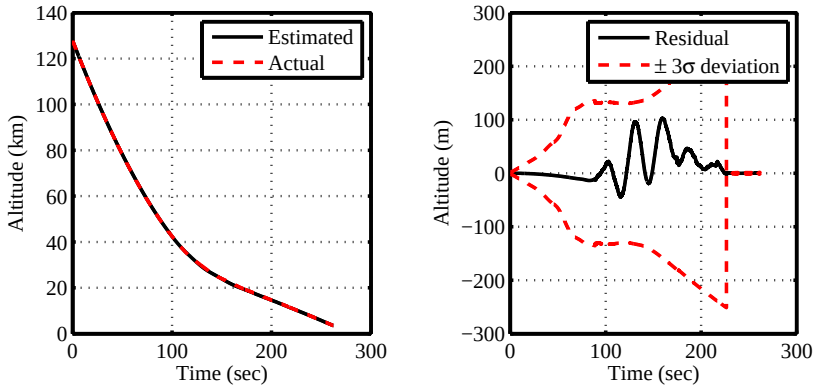

(a) Altitude (b) Error in altitude

Figure 30: Estimated position using Adaptive filter ($N = 10$) and the dispersed simulated data set.

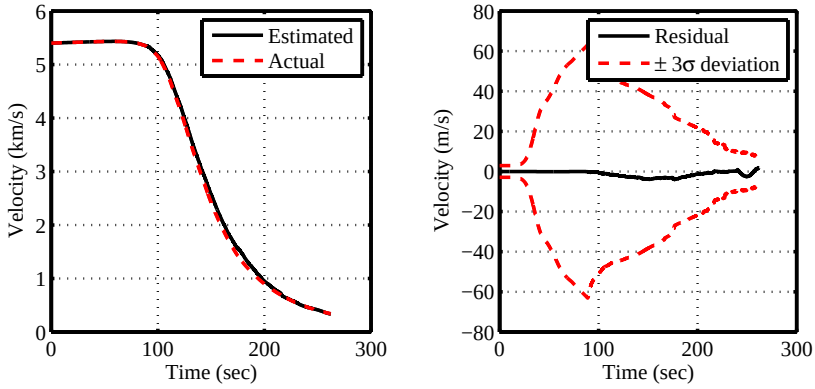

(a) Velocity (b) Error in velocity

Figure 31: Estimated velocity using Adaptive filter ($N = 10$) and the dispersed simulated data set.

can be attributed to the atmospheric and aerodynamic perturbations in the data set.

3.3.2.2 Atmosphere, Aerodynamics, and other Derived Quantities

The reconstructed freestream density for the dispersed data is shown in Fig. 32, and the derived angle of attack, sideslip angle, and dynamic pressure histories are shown in Fig. 33. The region where FADS data was used can be easily inferred from the graphs of the residual of the reconstruction, since there is a sharp drop-off in the reconstructed residual and uncertainties. Once again, this is consistent with the reconstruction behavior seen with the EKF and UKF albeit with the Adaptive filter

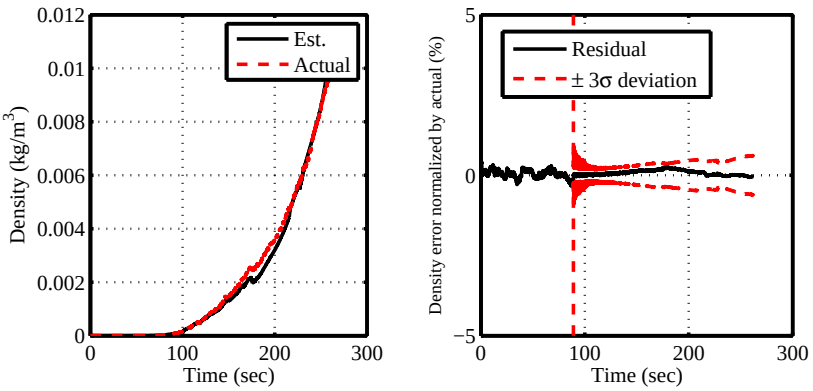

(a) Freestream density (b) Error in freestream density

Figure 32: Estimated atmospheric density using Adaptive filter ($N = 10$) and the dispersed simulated data set.

reconstruction yielding smaller uncertainty values in general.

Finally, the estimated axial force coefficient reconstruction is seen in Fig. 34. Similar to the case for the reconstruction results of the nominal data set, the axial coefficient residual is small but the uncertainties are rather large except in the region where both FADS and IMU data were available. This underscores the importance of blending these two different measurements and emphasizes the gain in model uncertainty quantification by using such techniques.

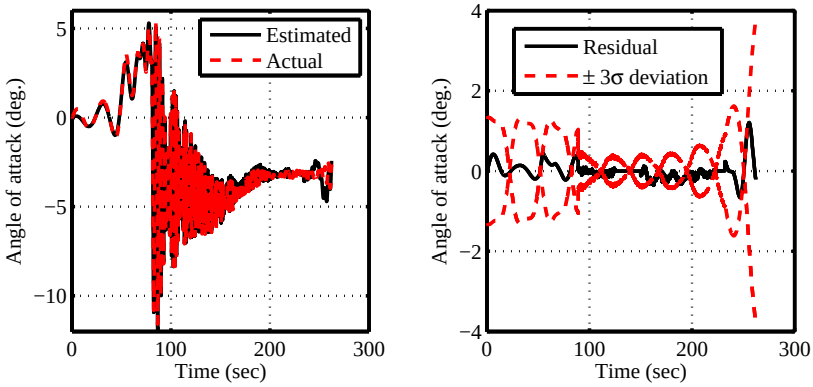

(a) Angle of attack

(b) Error in angle of attack

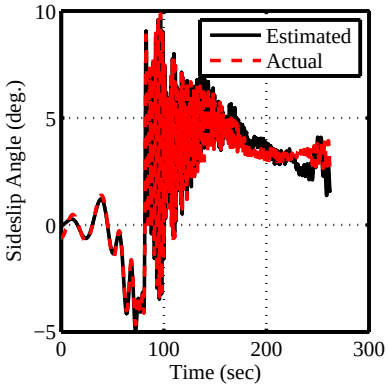

(c) Sideslip angle

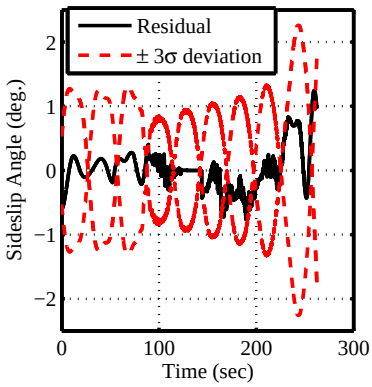

(d) Error in sideslip angle

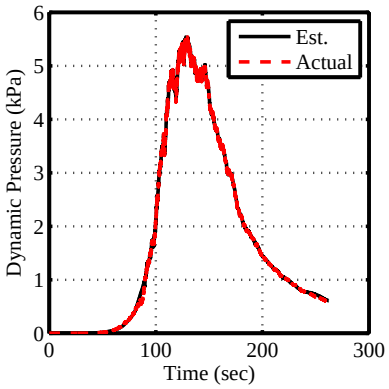

(e) Dynamic pressure

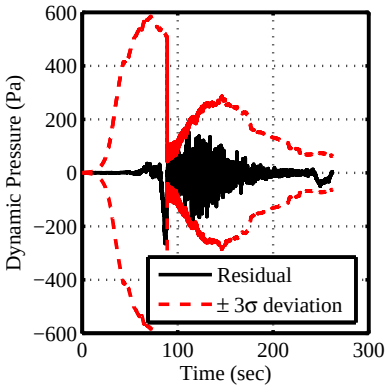

(f) Error in dynamic pressure

Figure 33: Derived quantities using Adaptive filter ($N = 10$) estimation results and the dispersed simulated data set.

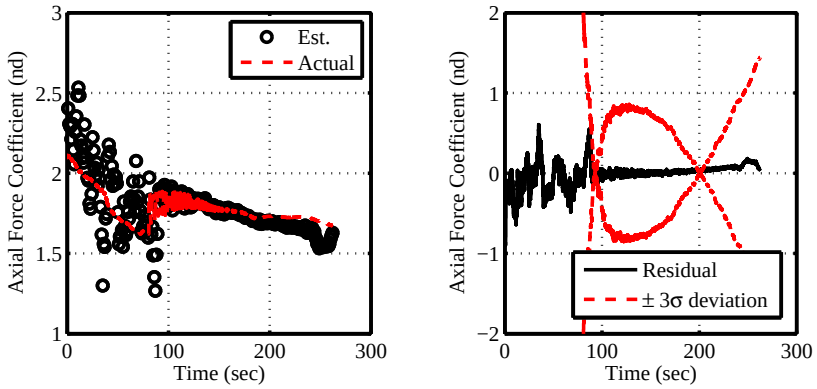

(a) Axial force coefficient (b) Axial force coefficient error

Figure 34: Derived aerodynamic parameter using Adaptive filter ($N = 10$) estimation results and the dispersed simulated data set.

3.4 Comparison of Estimation Performance

3.4.1 State Estimation Results

Tables 7 and 8 shows a comparison of the state estimation results between EKF, UKF, and the Adaptive filter using the simulated data set. The table shows the root-mean-square error from a sample of trajectory, atmospheric, and aerodynamic quantities that were estimated by all three filters.

Table 7: Comparison of RMS error in estimates for EKF, UKF, and Adaptive filter for the nominal simulated data set.

State	Adaptive	EKF	UKF
Radius (m)	297.4	3558	1553
Density (% actual)[a,b]	1.121	6.244	2.116
Angle of attack (deg.)[a]	0.082	0.192	0.145
Sideslip angle (deg.)[a]	0.112	0.211	0.140
Dyn. press. (% max)[a,c]	0.081	0.670	0.283
Axial force coefficient[a]	0.005	0.017	0.006

[a]RMS of the residual where FADS data are available.
[b]Normalized by actual density
[c]Normalized by max. pressure

The benefit of using Adaptive filtering is apparent when its estimation results are

Table 8: Comparison of RMS error in estimates for EKF, UKF, and Adaptive filter for the dispersed simulated data set.

State	Adaptive	EKF	UKF
Radius (m)	509.3	4550	1193
Density (% actual)[a,b]	2.301	10.90	3.675
Angle of attack (deg.)[a]	0.120	0.570	0.334
Sideslip angle (deg.)[a]	0.218	0.506	0.242
Dyn. press. (% max)[a,c]	0.205	0.784	0.463
Axial force coefficient[a]	0.014	0.022	0.018

[a]RMS of the residual where FADS data are available.
[b]Normalized by actual density
[c]Normalized by max. pressure

compared with results from other statistical filters with more empirically-driven process noise. The Adaptive filter shows an order of magnitude improvement in estimation capability for almost all estimated states. The improvement is more discernible when one considers the estimation performance for atmospheric and aerodynamic quantities when both IMU and FADS data were available. These quantities usually have large uncertainties associated with them for Mars EDL and the Adaptive filter shows that it can estimate these states with high accuracy albeit in a simulated setting. After the Adaptive filter, the UKF has the next smallest residual although the EKF residual is not that far off from the UKF residuals for some parameters.

Looking only at the state estimation results, if the truth information for the states were not known, it seems that either Adaptive filter or UKF is acceptable for reconstruction. Both outperform the EKF for the most part and additionally the EKF will be expected to have divergence issues if the reconstruction is conducted over a long time period due to non-linearity errors and higher order terms accumulating. However, both the Adaptive filter and the UKF are computationally intensive. The Adaptive filter requires the computational overhead of tracking the last N or L state error values to compute the noise matrices at any given time. The UKF requires $2n+1$ sigma points be propagated in time instead of just the propagation of the state

vector in the EKF. Of course, if the filters are used on data off-line from the actual event, which is the case for the off-line reconstruction of EDL performance, then the computational issues are negligible.

3.4.2 Uncertainty Estimation Results

However, the biggest improvement shown by the Adaptive filter is in the uncertainty estimation of these parameters as seen in Figs. 35. Looking at the radius and velocity 3σ uncertainty bounds, the Adaptive filter uncertainty estimates are lot tighter that the EKF and UKF estimated ones. Unfortunately, there are no true uncertainty bounds to compare these estimates to, as was the case for the state estimates, but one can interpret from the results that the tighter confidence bounds are an indication of greater precision in the estimate of the Adaptive filter.

More importantly, since the Adaptive filter formulation used in this investigation computed process noise, one can also look at some model error terms such as atmospheric and aerodynamic uncertainties. Figs. 35(c) and 35(d) show the estimated uncertainties in the freestream density and axial force coefficient. Both types of estimated uncertainties are shown for the region where both IMU and FADS data were available and the Adaptive filter estimate for both types of states are tightly bound in this region, especially when compared to the results of other statistical filters. For comparison, Fig. 35(d) also shows what the predicted uncertainty in the axial force coefficient would be from the aerodynamic database (as summarized in Table 1). The Adaptive filter estimate is very close to the predicted uncertainties and the tight confidence bounds raises hope that reconstruction of actual flight data using Adaptive filters will give realistic confidence bounds for estimated force coefficient and possibly allow for the maturation of current aerodynamic error models. One can similarly improve atmospheric models (such as those shown earlier in Figs. 6(a)) using Adaptive filter estimate of atmospheric properties.

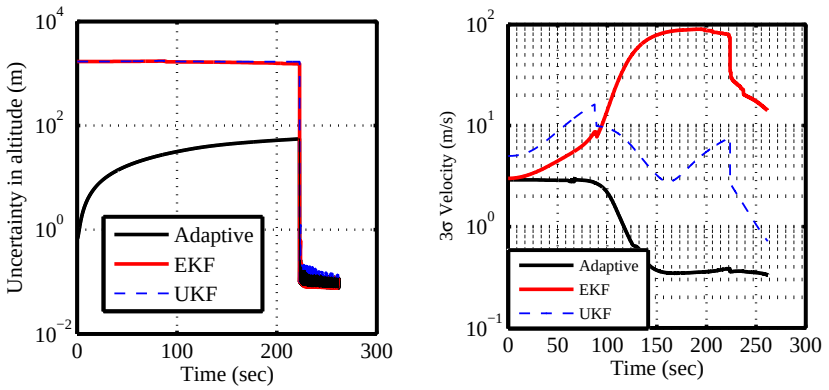

(a) Radius (b) Velocity

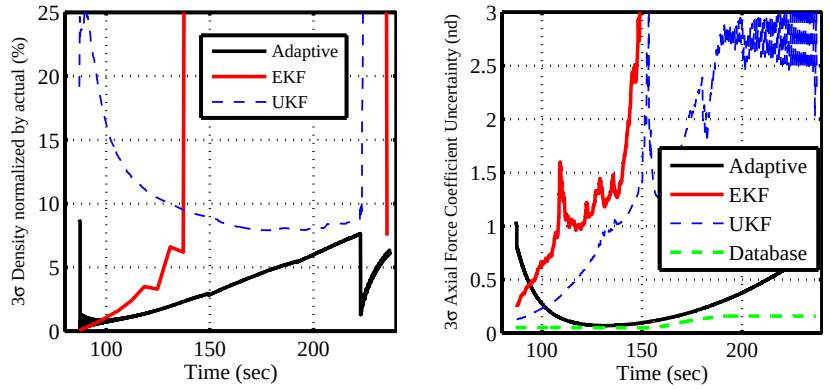

(c) Freestream Density (d) Axial force coefficient

Figure 35: State uncertainty quantification comparison between EKF, UKF, and Adaptive filter using the nominal simulated data set.

The vast difference in state and uncertainty estimation capabilities of the Adaptive filter and the more traditional EKF and UKF is in the computation of process noise on-line. For example, Fig. 36 shows the process noise of velocity for all three filter. The process noise used for the EKF and UKF to have non-divergent solutions was chosen to be uniform using auto-tuning techniques found in Ref. [106]. On the other hand, the adaptively calculated process noise varied over time and allowed the filter to have the appropriate level of noise necessary to maintain consistency and accuracy in the state estimation without significantly increasing the state uncertainty. The result is a more accurate state estimation with tighter confidence bounds.

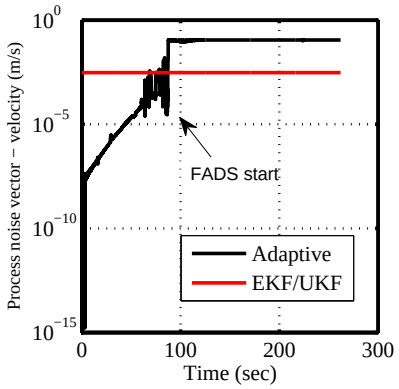

Figure 36: Process noise comparison for velocity between EKF, UKF, and Adaptive filter using the nominal simulated data set.

3.4.3 Computational Effort Comparisons

The prior sections compare the reconstruction performance of the three filters. A similar assessment can be made for the computation effort required by each filter.

EKF propagates the best state and covariance estimate from one measurement point to the next and requires the calculation of Jacobian matrices. For the process equations used in this problem, these Jacobians were calculated analytically for the most part and hence the normally computationally expensive calculation of Jacobians using numerical methods was mostly avoided. So the reconstruction of a 200-400 s Mars EDL trajectory using EKF took of the order of 5 minutes using a 3.4 GHz Intel i7 processor. Note that the codes were written in MATLAB and no special effort was made to optimize the run-time speed of the reconstruction code since this was not a real-time application.

The Adaptive filter uses the structure of EKF but also involves the calculation of the process and measurement noise covariances. The noise covariance calculations need a larger storage requirement than the EKF to keep track of the last N and L number of residuals. These calculations added a few more minutes to the run-time, but in general the Adaptive filter was able to process a Mars EDL trajectory in under 10 minutes using the same computing resources used for the EKF.

UKF requires the propagation of $2n+1$ sigma points for both the state propagation and measurement update steps. So when a large number of state elements are being estimated, the computational burden of the sigma point propagation significantly increases the run-time for the UKF. For a typical Mars EDL data set, the UKF had a run-time of around 30 minutes.

In terms of complexity of setting-up the various filters, the EKF and UKF were very simple to implement based on their algorithms that are widely available in literature. The Adaptive filter implementation was a little bit more complicated due to the requirement of storing the last N and L state and measurement residuals. It should be noted though that the biggest challenge of setting-up the reconstruction tools was not how to implement the three filters but instead understanding how to implement the measurement models and what process equations to choose to best model the dynamics of the parameters of interest. The latter two tasks needed a lot of experimentation and the majority of the time of the analyst.

3.4.4 Extensibility of Filter Comparison Results

This chapter provided a comparison of performance for three statistical filters. However, only two simulated data sets were used in the demonstration. Although trends from the two simulated data set reconstructions were similar, one may wonder about the extensibility of these results. Without considering a large variety of trajectories to test these methods, one cannot make a conclusive statement that one filter has a better performance than another filter.

Nevertheless, in the limited subspace of entry, descent, and landing trajectories especially those for Mars, this chapter and other studies [56, 28, 59] have provided enough examples to support statements about the performance of EKF versus UKF. Adaptive filters have not been considered extensively for EDL reconstruction so more examples are needed to make definitive conclusions about that particular filter. But

the results of this chapter and the next chapter, where the filters are applied to an actual flight data set, at least provide three independent Mars EDL trajectories with which to make initial assessments of the three filters. Testing these three filters on other trajectories in the future is necessary to further corroborate and strengthen these initial assessments. Ultimately, however, it should be noted that although some filters were found to have better performance than other filters when applied to the data sets used in this chapter, the main conclusion from this study is to recommend the usage of all three filters in situations where the truth is unknown such as when using an actual flight data set.

3.5 Summary

Testing the estimation methodology with the simulated EDL data set allowed for the luxury of knowing the truth and being able to benchmark filter performance to it. All three filters were tested using the simulated data and all three methods reconstructed the trajectory, atmosphere, and aerodynamic coefficients with proficiency. However, when one compared the residual errors between the estimate and the true states, the EKF's performance was well off compared to the Adaptive filter and the UKF. The Adaptive filter specifically performed really well with lower residual state errors and tighter confidence bounds when compared to the two other filters. However, it should be noted that unlike true state values, the true uncertainty values are unknown. So a tighter confidence bounds is only being used as a hypothesis that the Adaptive filter quantifies uncertainty well. In situations where the truth is unknown, the analysis shows that both Adaptive filter and UKF should be used since they have similar state error residuals and according to literature the UKF also performs well in uncertainty estimation.

CHAPTER IV

FLIGHT DATA RECONSTRUCTION: MSL

In the last chapter, the estimation methodology was tested with simulated data sets where the truth was known. However, in most practical applications of the methodology, the truth will not be known and comparisons can only be made with independent reconstructions using the same data. In this chapter, flight data of an EDL vehicle is analyzed, and the performance of all three filters is compared. The EDL flight data are from the Mars Science Laboratory, which successfully landed on Mars on Aug. 5, 2012. The vehicle landed at the near-equatorial Gale Crater that is at an altitude of about -4.5 km [111]. This chapter will present the data that were collected on-board and summarize the results of the trajectory, atmosphere, and aerodynamic reconstruction using the estimation methodology.

4.1 On-board Data

The data collected on-board MSL consisted of IMU observations (3-axis accelerometers and 3-axis gyroscopes), radar altimeter data, and MEADS measurements. Entry interface (EI) occurred at Spacecraft Clock Time (SCLK) of 397501714.953130 s and data was first collected at SCLK of 397501174.997338 s [112, 60]. The data presented below have been adjusted from SCLK to an epoch where entry interface is zero.

4.1.1 Inertial Measurement Unit Data

The raw data collected on-board MSL consisted of δV and $\delta\theta$ measurements that were converted into accelerations and angular rates using finite differencing. The nominal sampling rate of the data was 200 Hz. Although the vehicle contained two sets of IMUs, only data from IMU-A were used during EDL by the flight controller. The

reference frame for the IMU was different from typical flight dynamics convention of the body frame. The IMU frame, also referred to as the Descent Stage (DS) frame, had its positive z-direction outwards in the vehicle axial direction, while the x-direction is in the pitch plane. A negative 90 deg. rotation in the y-direction aligns the DS frame to the flight dynamics conventional body frame [112]. Figure 37 shows the unfiltered accelerations and angular rates in the vehicle body frame. The data were used in unfiltered form for reconstruction.

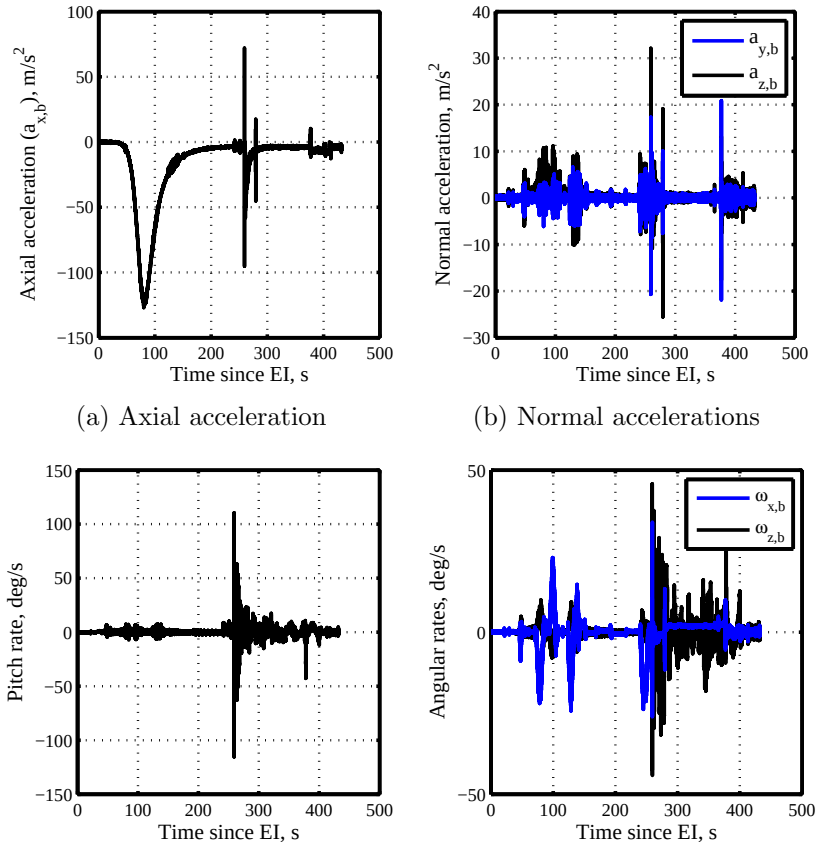

(a) Axial acceleration (b) Normal accelerations

(c) Pitch rate (d) Roll and Yaw rates

Figure 37: MSL inertial measurement unit data.

4.1.2 Terminal Descent Sensor - Radar Altimeter Data

The radar altimeter system took measurements during the terminal descent stage of the trajectory. The sensor suite consisted of several radar altimeter beams which

collected range and range rate information. These data were processed by the flight computer to calculate a slant range and slant velocity. The slant range information was used for the trajectory reconstruction. The unfiltered 20 Hz data and the down-sampled 1 Hz data are shown in Fig. 38 along with the slant range uncertainty calculated by the on-board flight software, which was used in the measurement noise covariance.

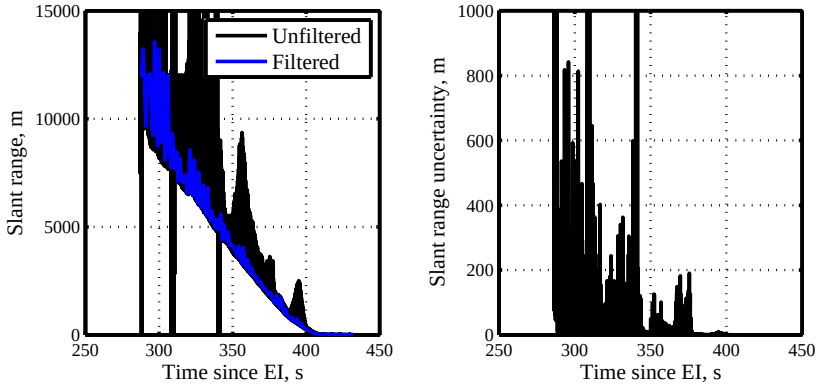

(a) Slant range (b) Slant range uncertainty

Figure 38: MSL terminal descent sensor slant range and uncertainty.

4.1.3 Mars Entry Atmospheric Data System

MEADS started collecting data from cruise stage separation at a nominal sampling rate of 8 Hz. The data were converted to engineering units using pre-flight and cruise-stage calibration information and an in-flight zero [60]. Data were collected until shortly before the parachute mortar fire; however, calibration of the MEADS data was only guaranteed when the dynamic pressure was greater than 850 Pa. For MSL, this range fell between 50 and 175 s after EI. Only data from this region is used for the analysis, although the data shown below in Fig. 39 are for all times after EI. The data were found to be close to the expected values and very little discrepancy was noticed in the initial analysis [60].

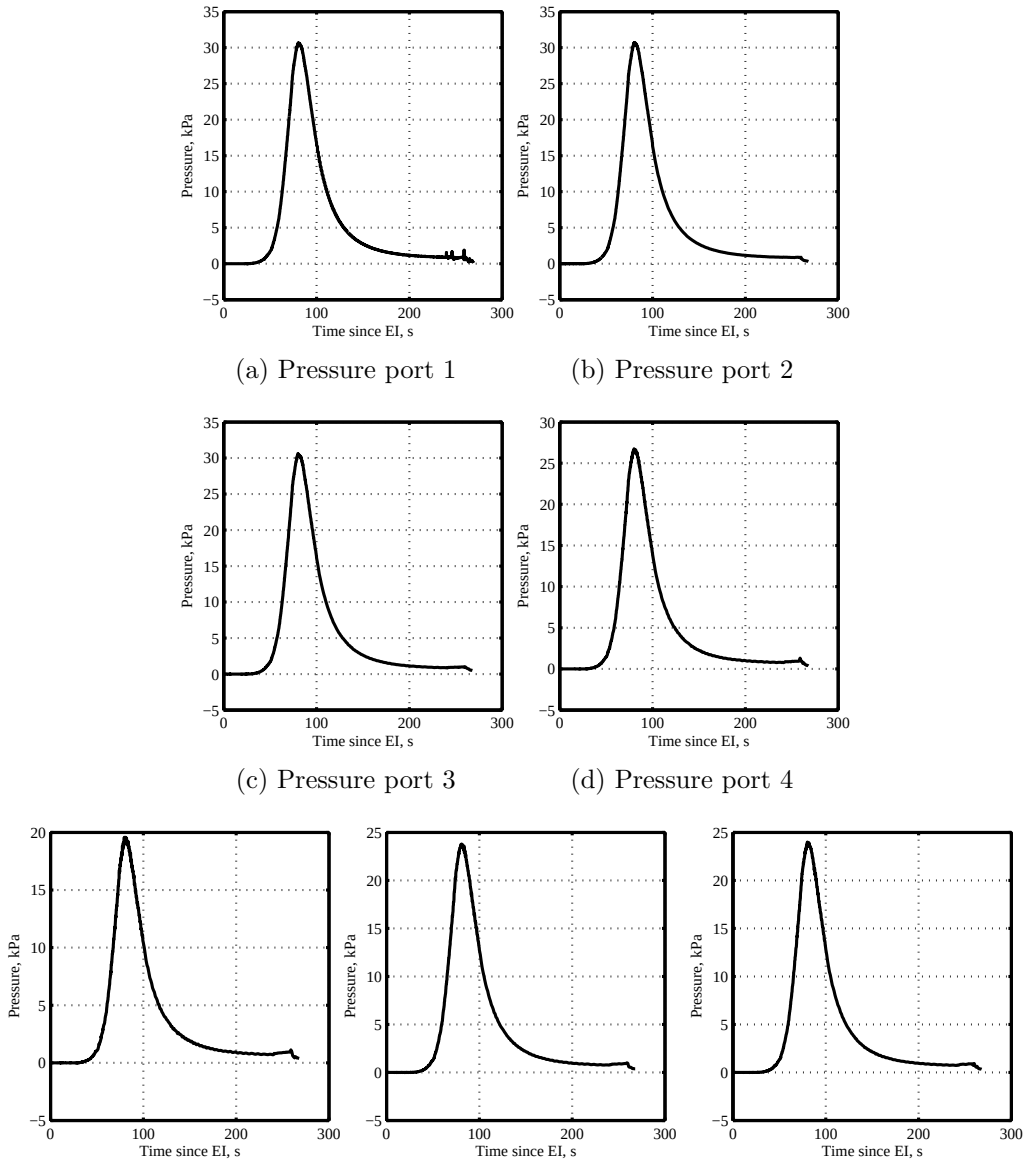

(a) Pressure port 1 (b) Pressure port 2

(c) Pressure port 3 (d) Pressure port 4

(e) Pressure port 5 (f) Pressure port 6 (g) Pressure port 7

Figure 39: MEADS data for pressure ports 1-7.

4.1.4 Initial Conditions

The reconstruction was conducted for a time period starting at the entry interface and ending with touchdown. However, the data needed for the reconstruction were available at many different epochs. For example, IMU and MEADS data were available from cruise stage separation, while radar altimeter data became first available late into the descent phase. Moreover, the initial state estimate was available at three

different epochs (EI - 9 min, 10 s; EI - 9 min; and EI) while the initial covariance was only available at EI - 9 min, 10 s. Thus, all of these values had to be brought to a standard starting epoch.

In order to find the initial conditions for all states and covariances at the entry interface, the statistical methodology was preceded by a deterministic reconstruction. The deterministic reconstruction used the IMU data to propagate the vehicle position, velocity, and attitude from EI - 9 min to touchdown. This process is similar to what was done for several past Mars EDL reconstructions [2, 31, 34]. This deterministic reconstruction was also the source of an initial estimate of freestream density and pressure. The initial freestream density prediction was found using the IMU data, assuming the perfect knowledge of aerodynamic parameters, while the initial freestream pressure was determined by integrating the hydrostatic equation with a surface pressure of 695 Pa (measured by MSL shortly after it reached the Martian surface) [60]. Although this procedure confounded aerodynamic and atmospheric uncertainties, one should note that the results from these deterministic reconstructions are only used to establish the *initial conditions* for freestream density and pressure at EI; afterward, a statistical estimation method is used for reconstruction based on both IMU and FADS data for atmosphere reconstruction, eliminating the need for *perfect* knowledge of the aerodynamic parameters.

The initial conditions for MSL's state vector are summarized in Tables 9 and 10. The initial covariance at EI was found using Monte Carlo simulation with an initial state and covariance known at EI - 9 min, 10 s.

Table 9: Initial Conditions for Mars Science Laboratory (at entry interface)

State	Condition	Standard Deviation (3σ)*
Radius (centric), m	3522200	32.0662
Latitude (centric), deg	-3.9186	0.000781
Longitude (East), deg	126.72	0.000367
Velocity (inertial), m/s	6083.3	0.026059
Flight-path angle (inertial), deg	-15.4892	0.000400
Azimuth angle (inertial), deg	93.2065	0.000268
Freestream pressure, Pa†	2.973×10^{-4}	$10P_{\infty,0}$
Freestream density, kg/m^3†	2.838×10^{-8}	$10\rho_{\infty,0}$

*Found with Monte Carlo simulation with known covariance at EI - 9 min
†Determined using a deterministic reconstruction

Table 10: Initial Conditions for Quaternions (at entry interface)

	$\mathbf{q}_{J,DS}$ (J2000 to DS)	$\mathbf{q}_{J,MCMF}$ (J2000 to MCMF)
Scalar	0.0018	0.9319
i	0.4011	0.1676
j	0.4059	0.2706
k	-0.8212	0.1739

Note: Initial Euler angle uncertainties assumed to be ± 0.2 deg

4.2 Customization of the Methodology

The realities of using a flight data set mean that the data are not always available in the format required by a generalized methodology. The methodology presented in Chapter 2 was adjusted accordingly based on the format of MSL's data. The data of the IMU were presented in a body-fixed reference frame called the "Descent Stage" frame. This frame is shown in Fig. 40 [112]. The IMU frame was related to the Descent Stage by the quaternion ($\mathbf{q}_{DS,IMU}$) given in Eq. (25). However, the Descent Stage is not the traditional flight-dynamics body-frame, so an extra rotation ($R_{DS,b}$) is needed to go from the descent stage to the flight-dynamics body frame, shown in Eq. (26).

$$\mathbf{q}_{DS,IMU} = \begin{bmatrix} 0.096566 & -0.370039 & 0.894064 & 0.233229 \end{bmatrix} \tag{25}$$

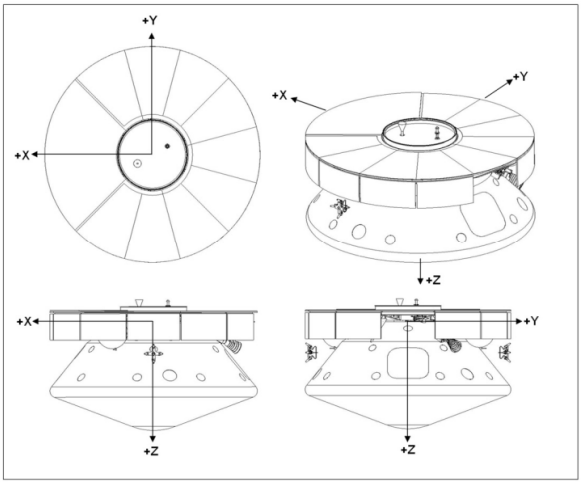

Figure 40: Notional representation of the Descent Stage coordinate system.

$$R_{DS,b} = \begin{bmatrix} 0 & 0 & 1 \\ 0 & 1 & 0 \\ -1 & 0 & 0 \end{bmatrix} \tag{26}$$

Additionally, the quaternion needed by the process equations in Chapter 2 and presented in Eq. (3) were to go from the local horizontal frame to the body frame, both of which are non-inertial frames. Hence, the dynamical equations had the quaternion rates component and a transport phenomena component (i.e. $V \cos\gamma \cos\psi$ component) to them. However, from Table 10, one has the entry interface values for the quaternions to go from J2000 to the Descent Stage and to go from J2000 to the Mars Centered Mars Fixed frame. Since J2000 is an inertial frame, one can find the quaternion from J2000 to Descent Stage ($\mathbf{q}_{J,DS}$) at any time using only the quaternion rate equation and the gyro rates (ω_x, ω_y, and ω_z), as shown in Eq. (27). Similarly, the quaternion from J2000 to the Mars Centered Mars Fixed frame ($\mathbf{q}_{J,MCMF}$) is a only a function of the simple quaternion rate equation and the rotation rate of the planet (ω), as shown in Eq. (28). Finally, the rotation matrix to go from the Mars Centered Mars Fixed frame to the local horizontal frame ($R_{MCMF,LH}$) is solely a function of

latitude (ϕ) and longitude (θ), as shown in Eq. (29). These quantities can be used to define the original quaternion used in the process equations of the generalized methodology, i.e. quaternion between local horizontal and body frames.

$$\begin{bmatrix} \dot{q}_{0,J,DS} \\ \dot{q}_{1,J,DS} \\ \dot{q}_{2,J,DS} \\ \dot{q}_{3,J,DS} \end{bmatrix} = \frac{1}{2} \begin{bmatrix} -q_{1,J,DS} & -q_{2,J,DS} & -q_{3,J,DS} \\ q_{0,J,DS} & -q_{3,J,DS} & q_{2,J,DS} \\ q_{3,J,DS} & q_{0,J,DS} & -q_{1,J,DS} \\ -q_{2,J,DS} & q_{1,J,DS} & q_{0,J,DS} \end{bmatrix} \begin{bmatrix} \omega_x \\ \omega_y \\ \omega_z \end{bmatrix} \tag{27}$$

$$\begin{bmatrix} \dot{q}_{0,J,MCMF} \\ \dot{q}_{1,J,MCMF} \\ \dot{q}_{2,J,MCMF} \\ \dot{q}_{3,J,MCMF} \end{bmatrix} = \frac{1}{2} \begin{bmatrix} -q_{1,J,MCMF} & -q_{2,J,MCMF} & -q_{3,J,MCMF} \\ q_{0,J,MCMF} & -q_{3,J,MCMF} & q_{2,J,MCMF} \\ q_{3,J,MCMF} & q_{0,J,MCMF} & -q_{1,J,MCMF} \\ -q_{2,J,MCMF} & q_{1,J,MCMF} & q_{0,J,MCMF} \end{bmatrix} \begin{bmatrix} 0 \\ 0 \\ \omega \end{bmatrix} \tag{28}$$

$$R_{MCMF,LH} = \begin{bmatrix} -\sin\phi & 0 & \cos\phi \\ 0 & 1 & 0 \\ -\cos\phi & 0 & -\sin\phi \end{bmatrix} \begin{bmatrix} \cos\theta & \sin\theta & 0 \\ -\sin\theta & \cos\theta & 0 \\ 0 & 0 & 1 \end{bmatrix} \tag{29}$$

4.3 Estimation Results

MSL flight data are reconstructed using EKF, UKF, and Adaptive filter to provide various *best* estimates of the spacecraft's trajectory, vehicle aerodynamics, and Mars' atmosphere during EDL. However, unlike Chapter 3, in lieu of knowledge about the true states all three reconstructions are equally plausible, so subjective comparisons between the reconstructions are made to ascertain estimation performance quality. Additionally, an independent, NASA-conducted reconstruction of the MSL data using the logic used on-board the flight software (FSW) [113] is provided where available for comparison with the three statistical estimations. The flight software reconstruction is largely a function of the IMU data.

4.3.1 Trajectory Reconstruction

The reconstructed trajectory for MSL is shown in Fig. 41 and the estimated uncertainties for the altitude and planet-relative velocity are shown in Fig. 42. Some major EDL events can be identified on the reconstructed profile and these have been labeled in the zoomed inset of the terminal descent phase (Fig. 41(b)). Parachute deployment occurs around 260 s after EI, resulting in an inflection point in the trajectory plot, while the heatshield jettisons approximately 20 s after the parachute deployment. The next set of major events happen quickly starting with the backshell separation at 375 s, then powered approach at 378 s, and lastly Sky Crane starting at 413 s. Finally, touchdown is sensed around 430 s (7 min, 10 s) after EI.

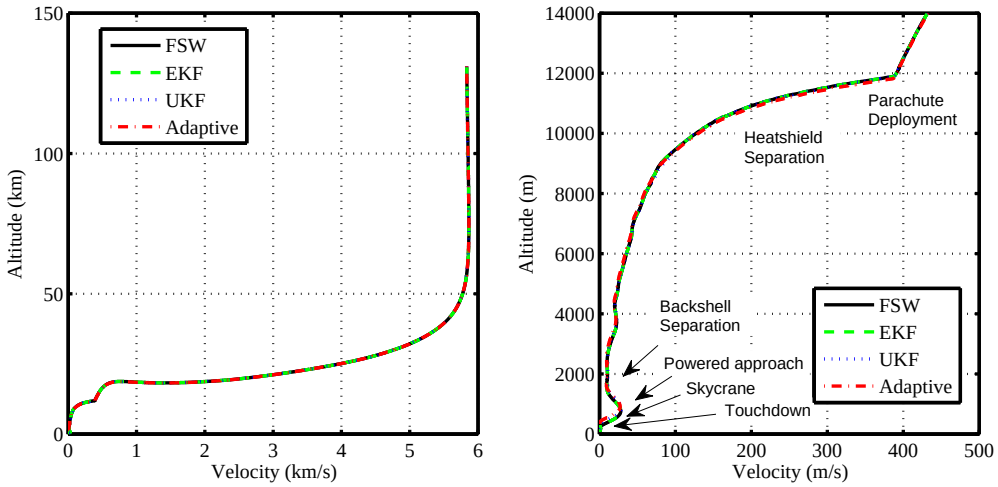

(a) Altitude vs. velocity (b) Terminal descent (zoom)

Figure 41: Reconstructed altitude and velocity history of MSL.

There is very little difference between the reconstructed altitude and velocity profiles of the three statistical estimators and the flight software. The flight software reconstruction is largely only a function of IMU data and is conducted deterministically. The fact that the FSW reconstruction matches so closely with the statistical estimations that also used other data types is a testament to the good quality of the IMU data, which greatly improved the performance of the trajectory reconstruction.

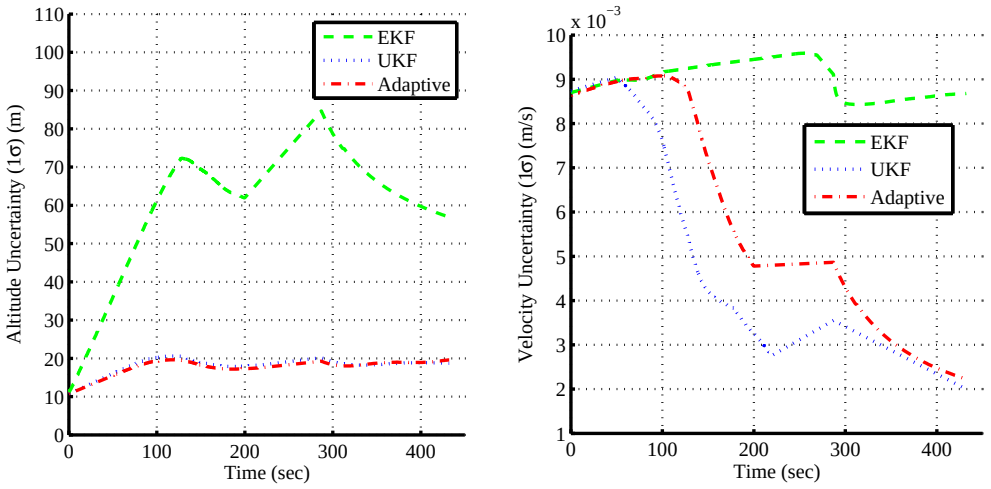

(a) Altitude uncertainty

(b) Velocity uncertainty

Figure 42: Reconstructed altitude and velocity uncertainties for MSL.

Other independent MSL data reconstructions have also noted the good quality of the IMU reconstruction [60, 114, 115].

The altitude and velocity uncertainty reconstructions (Fig. 42) show that in general EKF had larger estimated uncertainties than its other statistical estimation counterparts. The EKF altitude uncertainty shows the growth in uncertainty during the hypersonic flight regime through peak deceleration around 100 s, decrease in uncertainty in the region of bank angle reversals and hypersonic guidance, a slight growth in uncertainty during parachute deployment, and finally a steady decrease in altitude uncertainty after radar altimeter data are acquired. The UKF and Adaptive filter's estimated altitude uncertainties are not as dynamic as the EKF estimate. The differences in the behavior can be directly attributed to the handling of process noise. The EKF process noise is tuned using strategies described in Sec. 2.4.5 to account for the non-linearity in the dynamics that the first-order EKF equations cannot model well. The larger process noise also leads to larger estimated state uncertainties, as was shown in the simulated data results in Chapter 3. On the other hand, the UKF and Adaptive filter have higher order methods for modeling the non-linearity and process noise in the dynamics which keeps the estimate steady.

The velocity uncertainties are very small, when compared to past Mars missions. This is attributed to the excellent initial velocity estimate provided by the interplanetary navigation team (as was shown in Table 9) [116]. The EKF velocity uncertainty estimate does not decrease significantly from the initial estimate, but both the UKF and Adaptive estimates steadily decrease after the peak deceleration (around 100 s) and even further after radar altimeter data are acquired (near 300 s). Once again, the difference is due to the calculation of process noise. EKF has a slightly larger process noise that leads to slightly larger state uncertainty estimates. The UKF estimates smaller velocity uncertainties than the Adaptive filter in this case, but due to a lack of knowledge in the true state, it would be conjecture to attribute a physical rationale for this. Recall that with simulated data, the Adaptive filter actually had smaller uncertainties than the UKF.

The planet-relative flight path angle and azimuth angle histories are shown in Fig. 43. The time histories of these quantities are steady throughout the hypersonic and supersonic stages of flight, and show oscillations near the terminal descent portion when the Sky Crane was maneuvering. There is strong agreement between the reconstruction done by the three statistical estimators and the flight software estimate.

The time histories of the Euler angles - roll, pitch, and yaw - are shown in Fig. 44. Some crucial EDL events, such as bank reversals and heading alignment can be seen in these figures. The bank reversals are important since MSL was the first Mars EDL vehicle that used hypersonic guidance via bank angle modulation [3]. These modulations are visible on the roll and yaw angle history. Heading alignment prior to parachute deployment is also observed in the figures. The Euler angle plots have been restricted to shortly before parachute deployment, since these angles have little physical meaning after that point. Similar to the case for flight path and azimuth angles, there is strong agreement between the statistically-estimated quantities and

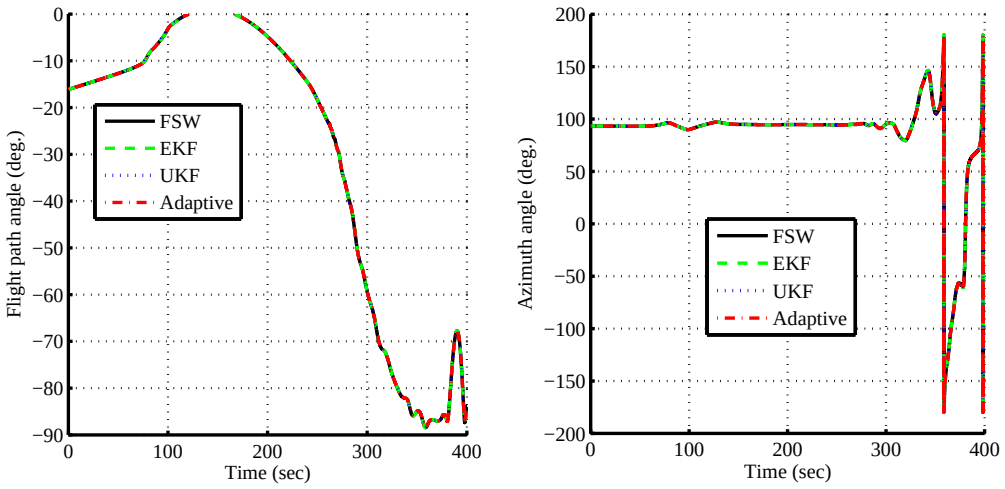

(a) Flight path angle

(b) Azimuth angle

Figure 43: Reconstructed flight path and azimuth angles for MSL.

the time history reconstructed by the flight software.

Angle of attack and sideslip angle histories are shown in Fig. 45. The time axes are restricted from entry interface to the point where MEADS data were no longer processed by the estimator for Figs. 45(a) and 45(b) to showcase the region where the orientation angle estimates were influenced by both IMU and FADS data. This region is also the only place in the reconstruction where aerodynamic and atmospheric uncertainties are not confounded since two independent measurements were used to estimate the angles.

Unlike the Euler angles, there are visible differences between the estimates derived by the three statistical estimators and the flight software. The angle of attack estimates for the Adaptive filter and UKF diverge slightly from the other estimates around 100 s and then there is a step increase seen around 135 s. Similar observations were made by other independent MSL reconstructions [10, 114]. The sideslip angle estimate has a difference that is more visible, since after 100 s the flight software and EKF estimates display a positive bias from zero, while the UKF and Adaptive filter estimates stay closer to zero but still display large oscillations. It is possible that the vehicle did indeed experience a non-zero sideslip angle, but a more likely explanation

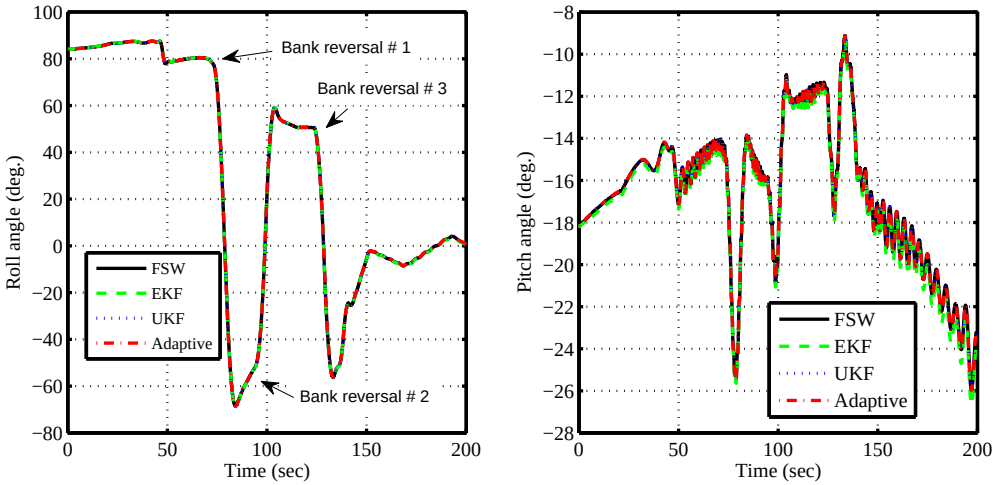

(a) Roll angle

(b) Pitch angle

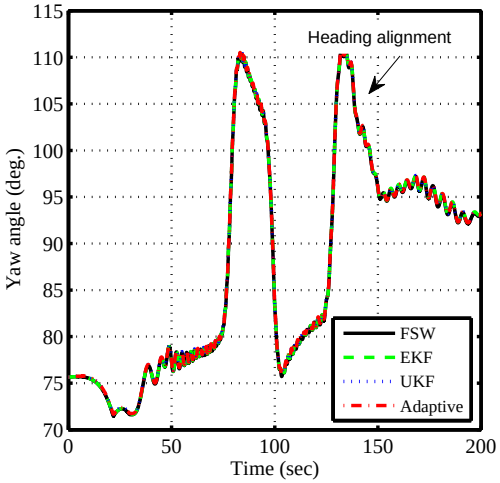

(c) Yaw angle

Figure 44: Reconstructed attitude history of MSL.

is a relatively significant cross wind component during this phase of flight that biases the IMU data [10, 115]. Since the methodology in this paper does not estimate winds and uses the planet-relative velocity instead of the wind-relative velocity for the angle calculations, a relatively strong wind may affect the accuracy of the angular estimates. The UKF and Adaptive filter are able to bias their result more towards FADS data that are theoretically not affected by the wind rather than the IMU data which are affected by the wind) and thus the filters' estimate sideslip angle closer to zero.

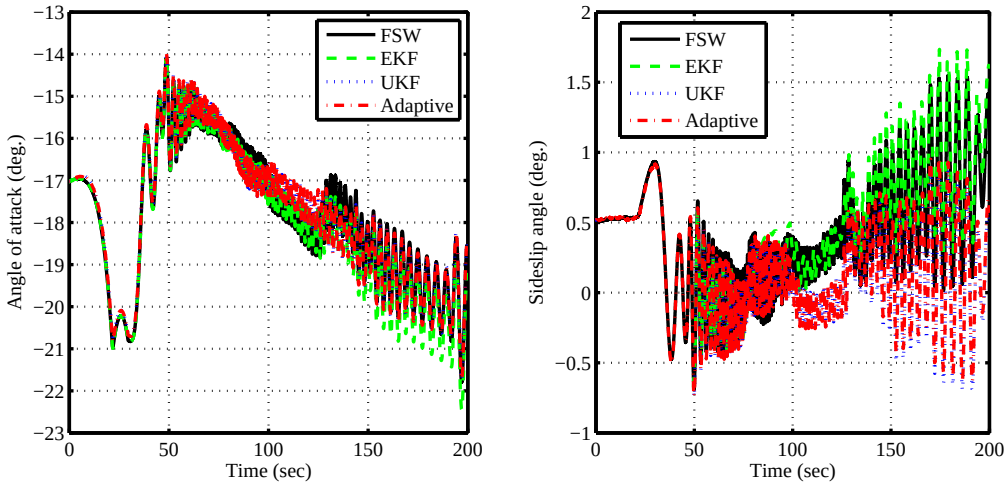

(a) Angle of attack (b) Sideslip angle

Figure 45: Reconstructed angle of attack and sideslip angle histories for MSL.

The angle of attack and sideslip angle uncertainties are shown in Fig. 46. One can see that the introduction of MEADS data to the estimators around 50 s drastically improves the uncertainty estimates in Figs. 45(a) and 45(b). The EKF seems to have a longer lag-time before the uncertainties of the two orientation angles settle to the level of the uncertainty estimates from the UKF and Adaptive filter. In general, one sees that the 1σ uncertainties for the angle of attack are of the order 0.2 deg. and the uncertainties for the sideslip angle are close to 0.1 deg.

The final landing location of MSL was available from post-flight communications between the rover and orbiting spacecraft [114]. This location and the reconstructed location using the estimation methodology are compared in Table 11. The 3σ uncertainty bounds of the reconstructed positions for all three estimates encompass the independently estimated location. The UKF and Adaptive filter have tighter bounds than the EKF, corroborating the expected outcomes when simulated data were analyzed by these estimators in Chapter 3.

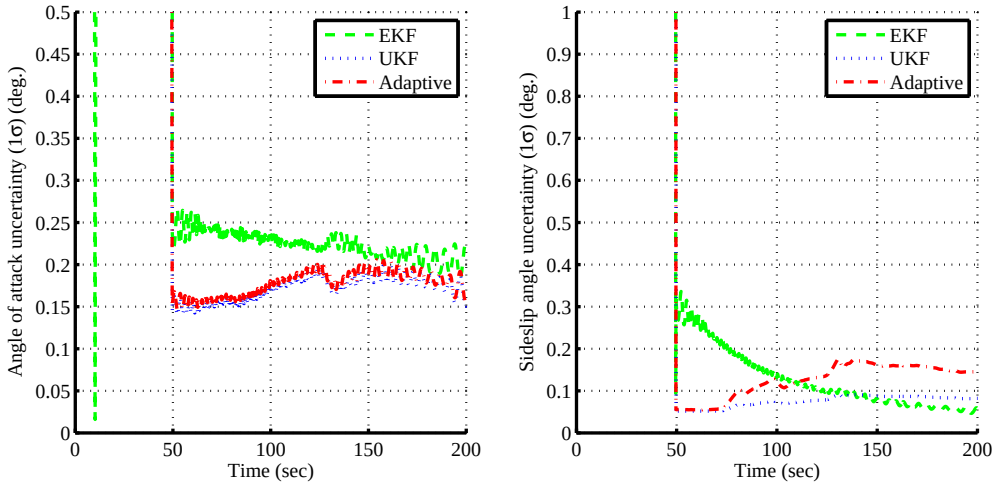

(a) Angle of attack (b) Sideslip angle

Figure 46: Reconstructed angle of attack and sideslip angle uncertainties for MSL.

Table 11: Final landing location of MSL

State	Orbit*	EKF	$3\sigma^{\dagger}$	UKF	$3\sigma^{\dagger}$	Adaptive	$3\sigma^{\dagger}$
Radius (km)	3391.13	3390.71	0.605	3391.30	0.195	3391.15	0.262
Lat. (deg)	-4.590	-4.632	0.075	-4.552	0.043	-4.557	0.045
Long. (deg)	137.442	137.394	0.0264	137.431	0.0129	137.438	0.0123

* Based on comm. between rover and orbiting satellites after landing [114].
† Assuming a normal distribution for the parameters.

4.3.2 Atmosphere Estimation

One of the unique features of the estimation methodology discussed in Chapter 2 is that atmospheric parameters are already included in the estimation state vector. Thus, there is no need to use the force coefficient equations or the hydrostatic equation to calculate atmospheric parameters.

Figure 47 shows the estimated atmospheric density history as well as the estimated uncertainty for the region where both IMU and FADS data were available. The value of the uncertainty generally increases with time as density increase. There is good agreement between the estimated states by the three statistical estimators, with the EKF having a slightly higher estimated uncertainty. The higher uncertainty for the EKF can be explained by the modeling of high process noise needed to avoid filter

divergence. The density and uncertainties are very smooth and do not display any large oscillations. This underscores the good quality of the IMU and FADS data as well as the near-nominal atmospheric profile encountered by MSL. One does not observe any large density variations akin to the potholes-in-the-sky that were studied during the design of MSL [25].

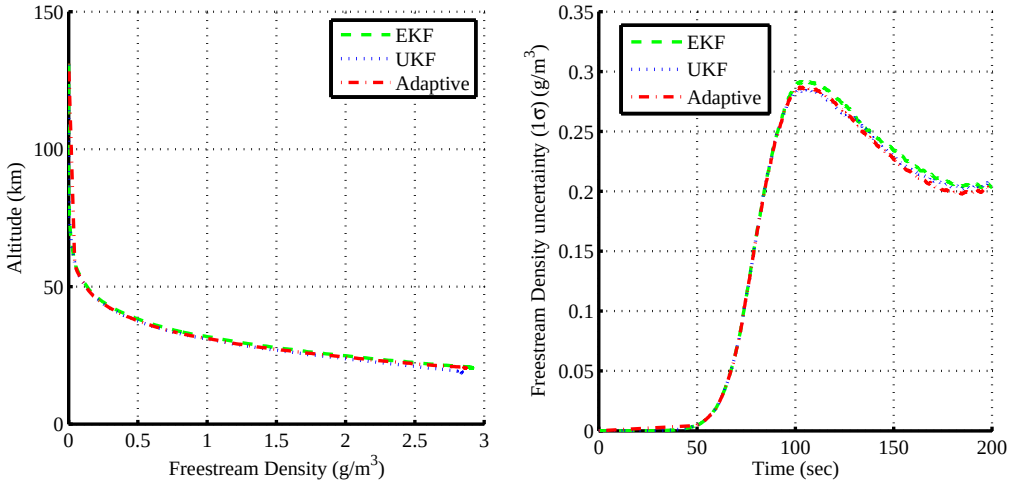

(a) Freestream density

(b) 1σ uncertainty

Figure 47: Reconstructed density for MSL when FADS data was used.

Freestream pressure, which is also an element of the state vector, is shown in Fig. 48 along with the estimated 1σ uncertainty. The values are once again shown for the time period where both IMU and FADS data were available. Similar to freestream density, all three estimates show good agreement in the estimated states, while the EKF uncertainty estimate is slightly off the uncertainties estimated by UKF and Adaptive filter. The agreement between the three estimators and the smoothness of the estimates once again is a result of the good quality of the data and the near-nominal environment.

The freestream temperature, which was calculated using the reconstructed density and pressure, is shown in Fig. 49 along with the estimated uncertainty.

The isothermal assumption for the hydrostatic equation and the perfect gas law were used to construct dynamical equations for freestream pressure and density in

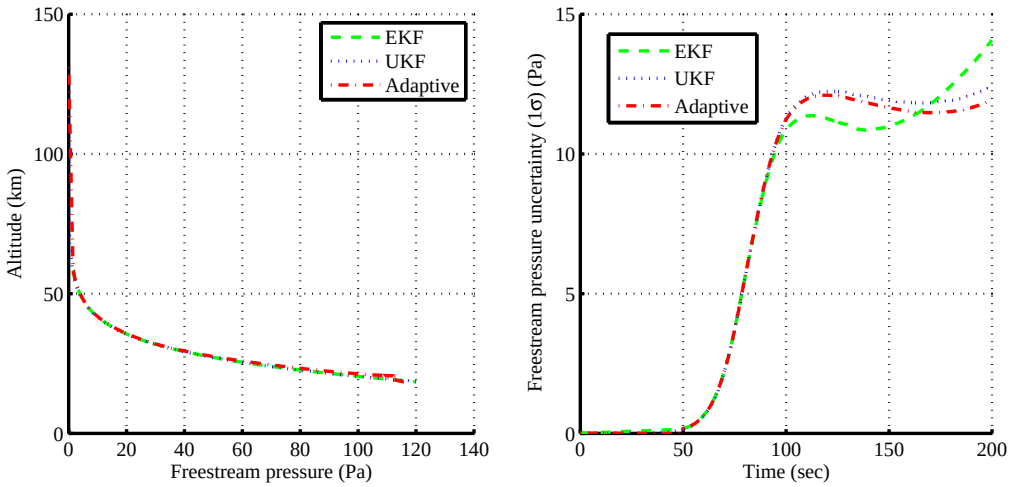

(a) Freestream pressure

(b) 1σ uncertainty

Figure 48: Reconstructed pressure for MSL when FADS data was used.

Chapter 2. The perfect gas law was also used here to reconstruct temperature from pressure and density. However, at the top of the atmosphere before FADS data are introduced, density is estimated using accelerometer data only and since there are not enough independent measurements of density and pressure, the estimated temperature remains constant (isothermal). Hence, the temperature profile in Fig. 49 is limited to the points where FADS data were available. The reconstructed uncertainties for temperature show similar trends as the uncertainties for other estimated atmospheric parameters. The EKF uncertainties are slightly larger and more oscillatory than the uncertainties estimated by the UKF and Adaptive filter.

The reconstructed dynamic pressure, Mach number, and their associated uncertainties are shown in Figs. 50 and 51. Dynamic pressure is calculated using the freestream pressure and planet-relative velocity, both quantities that are estimated by the methodology. Wind-relative velocity could be substituted for the planet-relative velocity for more accuracy, but the structure of this estimation methodology does not have means of estimating winds. Nevertheless, the reconstructed dynamic pressure and uncertainty agree well between the three estimators. Independent MSL reconstructions conducted by NASA also agree with these estimates [60]. Mach number

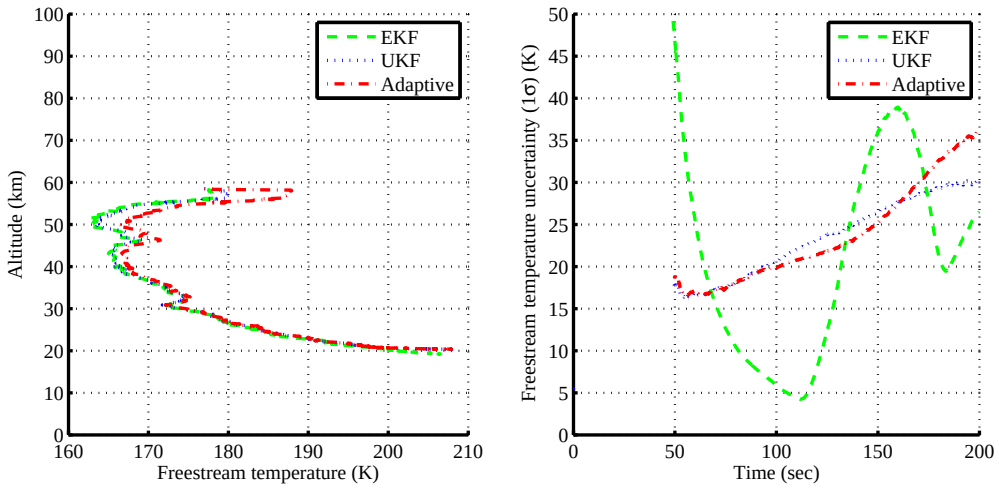

(a) Freestream temperature

(b) 1σ uncertainty

Figure 49: Reconstructed temperature for MSL when FADS data was used.

was calculated using the planet-relative velocity and speed of sound calculated from freestream density and pressure. However, the uncertainties in freestream pressure and density before FADS data are introduced are also present in the speed of sound calculation, making Mach number estimates in this region highly uncertain as seen in Fig. 51(b). It is interesting to note that although the estimates of Mach number from all three estimators agree very well with each other, the uncertainty estimated by the Adaptive filter decreases rapidly after FADS data are introduced around 50 s, but there is a lag before UKF and EKF estimates reach a lower level of uncertainty. This is a sign that the Adaptive filter, which calculates the process noise on-line, is more responsive to the lower level of uncertainty in atmospheric quantities once FADS data are introduced.

4.3.3 Aerodynamics Reconstruction

No aerodynamic parameters were directly estimated by the three filters. Nevertheless, one can use the estimated velocity and freestream density to derive the aerodynamic quantities using methods shown in Sec. 2.3. Figure. 52 shows the reconstructed axial force coefficient and its 1σ uncertainty, while Fig. 53 shows the estimates for

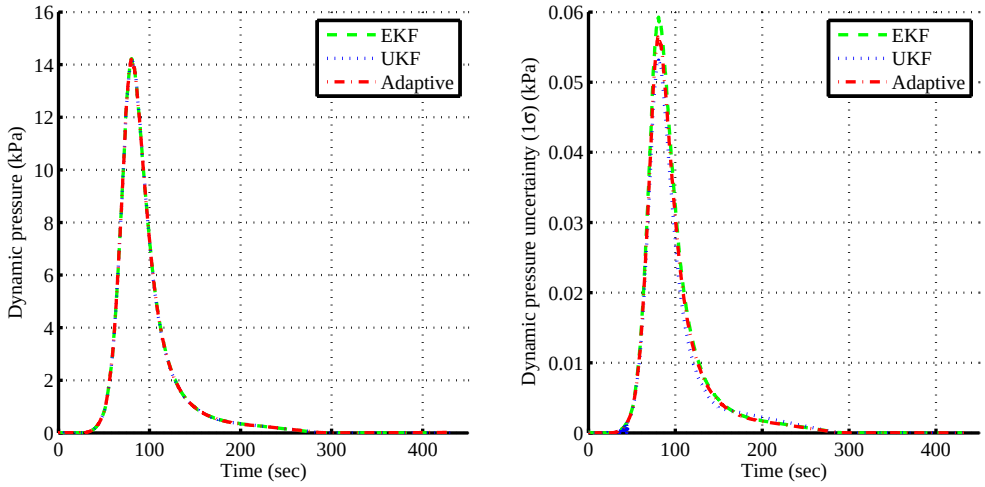

(a) Dynamic pressure (b) 1σ uncertainty

Figure 50: Reconstructed dynamic pressure and uncertainty for MSL.

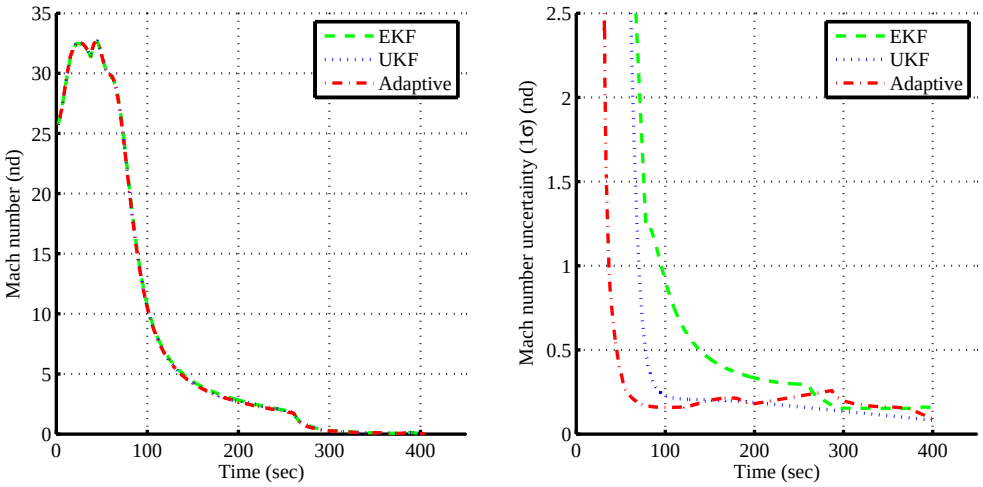

(a) Mach number (b) 1σ uncertainty

Figure 51: Reconstructed Mach number and its uncertainty for MSL.

the normal force coefficient. The figures have been restricted to the region where both IMU and FADS data were available. The pre-flight estimate of the two force coefficients are also shown for comparison.

The unfiltered form of the accelerometer data were used in the aerodynamic coefficient estimation, hence the reconstructed force coefficients are noisy. One could have used a filtered form of the IMU data, but since the unfiltered data were used by the estimators that same data were also used for the aerodynamic reconstruction.

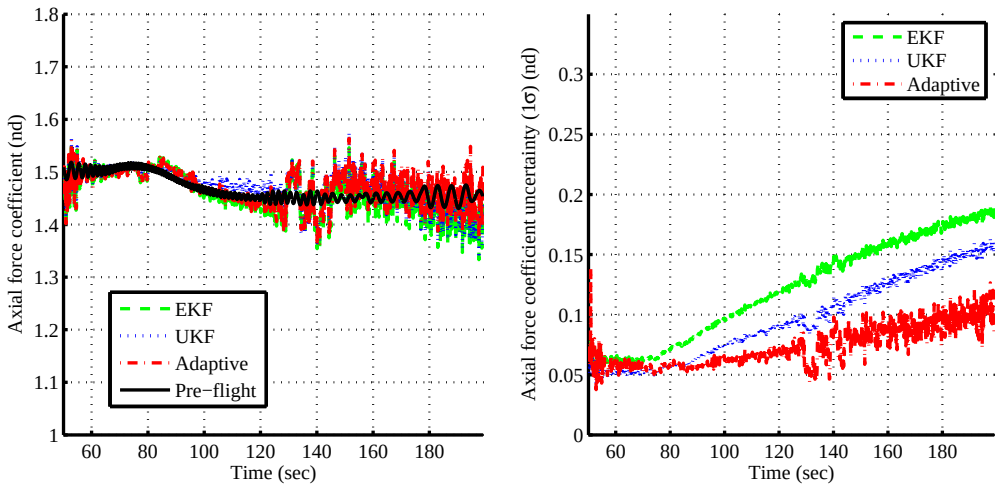

(a) Axial force coefficient (b) 1σ uncertainty

Figure 52: Reconstructed axial force coefficient and its uncertainty for MSL.

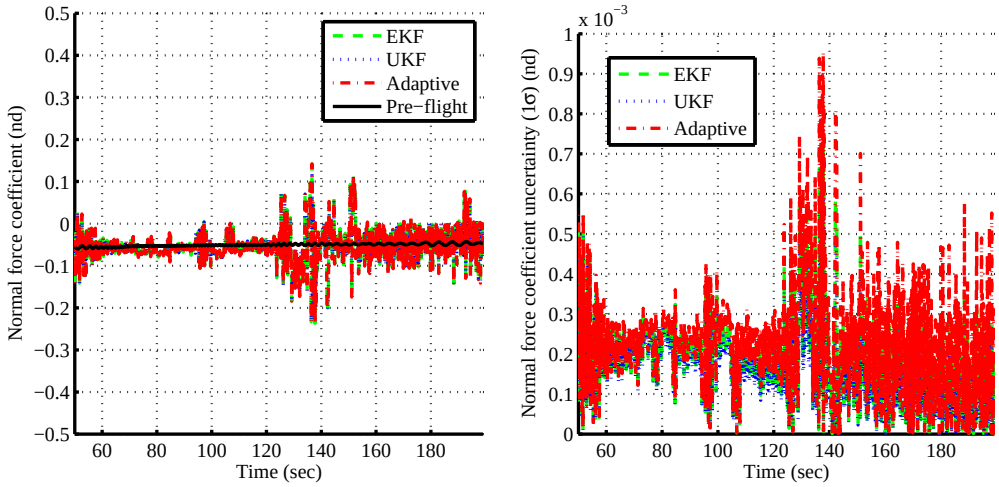

(a) Normal force coefficient (b) 1σ uncertainty

Figure 53: Reconstructed normal force coefficient and its uncertainty for MSL.

Additionally, both axial and normal force coefficients have an increase in noise after 130 s, which is a direct result of a step increase in noise in the actual sensed axial and normal force that is visible in Fig. 54. This time does not correlate to any specific EDL event, but happens shortly before heading alignment. Of course, this is also the time where the angle of attack and sideslip angles have off-nominal behaviors (see Fig. 45), so the increase in noise is probably directly related to the effect of the winds discussed earlier.

Overall, there is good agreement between the reconstructed force coefficients found by the three filters. The UKF estimate of the axial force coefficient is slightly more oscillatory than the EKF and Adaptive estimates between 100 and 130 s, but other than that all three estimates seem to overlap. The normal force coefficient estimate is extremely noisy for all three estimates, but the reconstructed values all show a negative mean bias around -0.05. Similar observations were noted in other independent MSL reconstructions [10, 114] as well, albeit with less noise since filtered-form of the IMU data were used in those cases. The axial force coefficient uncertainties show the familiar shape expected from simulated data reconstruction (Fig. 35(d)). The uncertainties are low when the FADS data are first introduced around 50 s, but slowly increase with time. The uncertainties also show the sign of the step increase in noise in the sensed force, since uncertainty estimates become more noisy after 130 s. There is no tell-tale shape in the normal force coefficient uncertainties, but all of the estimators have similar performance.

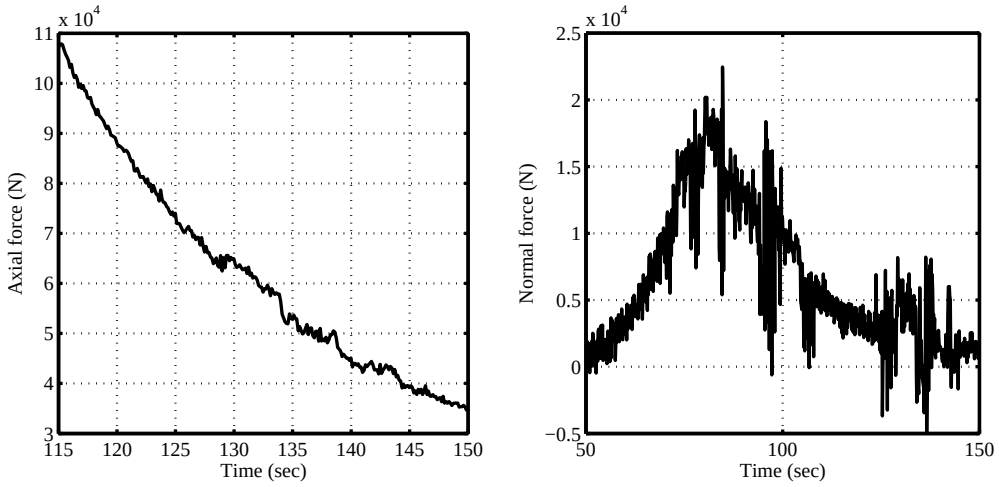

(a) Axial force (b) Normal force

Figure 54: Axial and normal forces sensed by the MSL IMU.

4.4 Summary

The Mars Science Laboratory mission demonstrated the first use of hypersonic guidance for Mars entry vehicles, and the aeroshell and supersonic parachute used by the spacecraft were the largest ever flown for Martian missions. Despite the challenges, the spacecraft safely landed on Aug. 5, 2012 in Gale Crater and relayed back inertial measurement unit data, radar altimeter measurements, and flush atmospheric data system pressure measurements that provide one of the most comprehensive data set for Mars entry vehicles.

The diversity of data from the mission makes MSL a very good test case for the statistical estimation methodology developed in Chapter 2. Although parts of the process equations had to be modified to make it applicable to this case, MSL flight data were reconstructed by three different statistical estimators with great success. Overall, there was great agreement between the estimated trajectory, atmosphere, and aerodynamics found by the three estimators and the estimates compared favorably when independent reconstruction results were available. The precise initial state conditions, great quality of the flight data, and the near-nominal trajectory of MSL led to very well-behaved reconstruction results. There was generally good agreement in the estimated uncertainties found by UKF and Adaptive filter, while the EKF uncertainties were generally higher than the ones found by the other filters. Since the process noise for the EKF is not tuned on-line, the noise is usually large to keep the filter from diverging which leads to relatively larger estimates of uncertainty. The UKF and Adaptive filter are able to better accommodate the non-linearity in the dynamics and are less affected by the process noise, leading to smaller uncertainties and tighter confidence bounds.

MSL had a near-nominal trajectory, but the one unexpected behavior was the larger-than-expected winds that led to larger than nominal angle of attack oscillations and non-zero sideslip angle in the supersonic regime. The reconstruction of

angle of attack and sideslip angle clearly captured this phenomenon. The FADS data were supposed to be non-susceptible to winds, while IMU data that measures sensed deceleration was susceptible to winds. The IMU-based flight software reconstruction both showed non-zero sideslip angles, while the UKF and Adaptive filter reconstructions showed sideslip angles with a mean of zero throughout the FADS data region. While the non-zero sideslip angle of the IMU-only flight software reconstruction is not unexpected, the EKF's non-zero sideslip angle is probably due to the filter's first-order state propagation equations and the way it handles process noise. While the UKF and Adaptive filter biased their estimates towards FADS data rather than IMU data in this regime and thus had near-zero sideslip angles, the EKF's process noise handling allowed the filter to be biased towards the high-rate, but wind-influenced IMU data, making the mean of the sideslip angle non-zero. This underscores the improvement in estimation capability possible as one moves from the more traditional EKF used in EDL reconstruction to higher-order filters like the UKF and Adaptive filter.

CHAPTER V

FADS DESIGN OPTIMIZATION

The narrative of the thesis has so far focused on the EDL performance reconstruction methodology and the results of this method when applied to simulated or actual flight data. However, the reconstruction methodology itself can be leveraged to improve vehicle design, especially the design of instrumentation on future missions. One specific area that has shown a gap in literature is the optimal placement of transducers in a flush atmospheric data system (FADS). As described before, FADS provide measurements of pressure on a vehicle's forebody during flight and in conjunction with inertial measurement unit (IMU) data enable the reconstruction of the vehicle's freestream conditions, angle of attack, and sideslip angle. Despite their increasingly prevalent use, the methods for FADS design and sensor arrangement remain rudimentary and are based on engineering judgment rather than computationally-based rationale. This is in spite of observations that different port configurations can vastly affect the effectiveness of the estimation [71].

This chapter will describe how the estimation methodology developed and demonstrated in the past chapters can be used for FADS optimization. The chapter places the FADS placement problem in the scope of a multi-objective optimization problem and tackles it in two different fashions. In the first method, the estimation methodology is directly used as an objective function and the optimization is dependent on the residual between the estimated states and the truth. In the other method, the concept of a lowest possible variance that can be estimated - known as the Cramér-Rao Lower Bound (CRLB) - is borrowed from estimation theory to find theoretically optimum FADS placement and improve the observability of the data. Using either

of these methods allows an EDL vehicle designer to move forward from selecting the best estimation methodology *post-flight* to deciding how to best arrange sensors to improve the yield of the estimation *pre-flight*.

5.1 Background

5.1.1 Past Optimization of Atmospheric Data Systems

As mentioned in Sec. 1.3.1, there has been limited work in the past to optimize the design atmospheric data systems in EDL vehicles. One of the few optimization studies for air data systems was conducted in the early 1990's in support of the Pressure Distribution/Air Data System (PD/ADS) experiment that was proposed to be included in the Aeroassist Flight Experiment (AFE), which was later canceled. In the study, Deshpande et al. [46] used a gradient-based estimator and a genetic algorithm (GA) to optimize the distribution of the PD/ADS sensors in order to decrease the effect of normally distributed random noise of the pressure transducers. Additionally, the work used modified Newtonian theory for the predicted pressure model and a batch-type reconstruction process to estimate air data parameters, such as dynamic pressure, angle-of-attack, and sideslip angle. The residuals between the estimated parameters and their known, true values were then used in a single-objective function for the optimization routines.

The work by Deshpande et al. only considered reconstruction of a single trajectory point (one Mach number, dynamic pressure, etc.). Such a situation can be imagined for a wind tunnel testing, where pressure transducers on a test object's forebody collect data while the object is kept at the same flow conditions for a fixed period of time. So the reconstruction process, which serves as the objective function for the optimization problem, is expected to converge to a single trajectory state, unlike the case of EDL reconstruction where the trajectory states keep changing. The focus of the current work is the optimization of sensor locations where the signal will change

with time. This topic has not been analyzed previously for atmospheric data systems.

Additionally, the EDL reconstruction process shown here uses a pressure distribution prediction model based on the aerodynamic database of the vehicle. This database incorporates data from higher fidelity models based on CFD and wind tunnel data and is expected to be more accurate than the modified Newtonian assumption used by Deshpande et al.

5.1.2 Multi-objective Sensor Placement Optimization

The FADS sensor configuration problem can be cast as a multi-objective optimization problem with the objective of placing sensors to accurately reconstruct parameters of interest in an inverse estimation process. Deshpande et al. [46] simplified this process by creating a single-objective optimization problem where they combined the multiple objectives of optimizing the reconstruction of dynamic pressure, angle-of-attack, and sideslip angle using weighting parameters. The use of these weighting parameters introduced subjectivity into the optimization process. Additionally, combining the three distinctive objective function values into a single objective function could lead to one of the objective functions dominating the design space due to larger magnitude of its values when compared to the other objectives. This scenario can hide optimal results for the non-dominant objective functions.

However, since that study, the field of multi-objective optimization has matured, and the concept of Pareto dominance can be coupled with different types of optimization techniques to enhance several objective functions concurrently without the necessity of weighting functions [117]. Pareto dominance allows one to find a set of optimal points that are an improvement over all other points in the design space [117]. The problem involves finding solutions that represent trade-offs among conflicting objective functions when multiple objective functions are involved. The concept of domination, as described in Eq. (30), occurs when a objective function parameter

vector $\mathbf{p}_1$ is better than another point $\mathbf{p}_2$ since the n-dimensional objective function vector $\mathbf{f}$ of $\mathbf{p}_1$ is no worse than the objective function vector of $\mathbf{p}_2$ and the function value $\mathbf{p}_1$ is strictly better that the function value of $\mathbf{p}_2$ along at least one dimension of the objective function [117]. All points that are non-dominated by any other point in the design space are members of the Pareto frontier.

$$\begin{aligned} \min \mathbf{f} &= \mathbf{f}(\mathbf{p}) \\ \forall i \in \{1, \cdots, n\} &: \mathbf{f}(\mathbf{p}_1)_i \leq \mathbf{f}(\mathbf{p}_2)_i \\ \exists j \in \{1, \cdots, n\} &: \mathbf{f}(\mathbf{p}_1)_j < \mathbf{f}(\mathbf{p}_2)_j \end{aligned} \tag{30}$$

The optimization technique used here and is the Non-dominated Sorting Genetic Algorithm II (NSGA-II) [108, 117]. NSGA-II is an evolutionary algorithm that can solve multi-modal problems such as the FADS sensor placement problem [49] better than traditional gradient-based methods that are often stuck in local minima. NSGA-II uses Pareto dominance to find the best representation of the Pareto frontier [117] and is considered a baseline technique in the field of multi-objective optimization [118].

The optimization algorithm consists of three basic steps: initialization, sorting, and reproduction (see Fig. 55). A randomly generated population of feasible port locations is initially generated and then the members are assigned different fronts based on the objective function values. A crowding distance in the objective function space between different design parameters is also calculated to ensure diversity in the frontiers. In successive iterations or generations, the optimizer uses an elitist technique to pair the most Pareto dominant parents to produce children using tournament selection, crossover, and mutation operations and the process is repeated for a user-defined period of time. Additionally, a continuous search space is implemented using modifications to the traditional mutation and crossover operators [119, 120]. It is expected that the final generation will be close to the theoretical Pareto frontier [108].

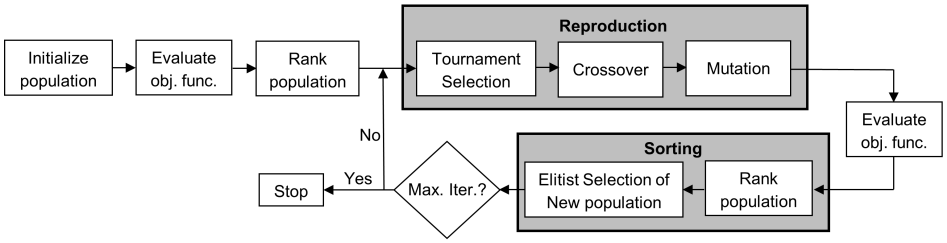

Figure 55: Flow diagram of Non-dominated Sorting Genetic Algorithm II.

Since the sensor placement problem for atmospheric data systems has many non-unique solutions, it is expected to be multi-modal and can benefit from such a procedure. In this work, the concepts of Pareto dominance and evolutionary algorithms that can handle multi-objective optimization are combined with the EDL reconstruction process to demonstrate a methodology to optimize FADS instrumentation. Such a procedure can advance the work by Deshpande et al. and allow future designers to determine the optimal number and locations of sensors on vehicles and objects that use atmospheric data systems for measurement.

5.1.3 Simulated Data Set for Reconstruction

A simulated, Mars EDL data set is used as the basis for the sensor location optimization objective function. These true states are provided by the Program to Optimize Simulated Trajectories II (POST2) [109], which was used to generate a nominal EDL trajectory that is presented in Fig. 56. The trajectory is for a 4.5 m, 70-deg sphere-cone with the same geometry and specifications as the Mars Science Laboratory (MSL).

For the residual-based optimization, the POST2 outputs are used to generate IMU data, radar altimeter measurements (when the altitude is less than 10 km), and FADS data (when the dynamic pressure is greater than 850 Pa.) using the same measurement equations that are used in the estimator but with random noise added to the measurements. The 850 Pa limit mimics the time frame in which the MSL science objective is defined [37, 48]. The plots for angle of attack and sideslip angle are

only shown to 200 seconds since the vehicle reaches the 850 Pa limit around that time period. For the observability-based optimization, the truth data is used to calculate the CRLB directly and simulated measurements are not generated.

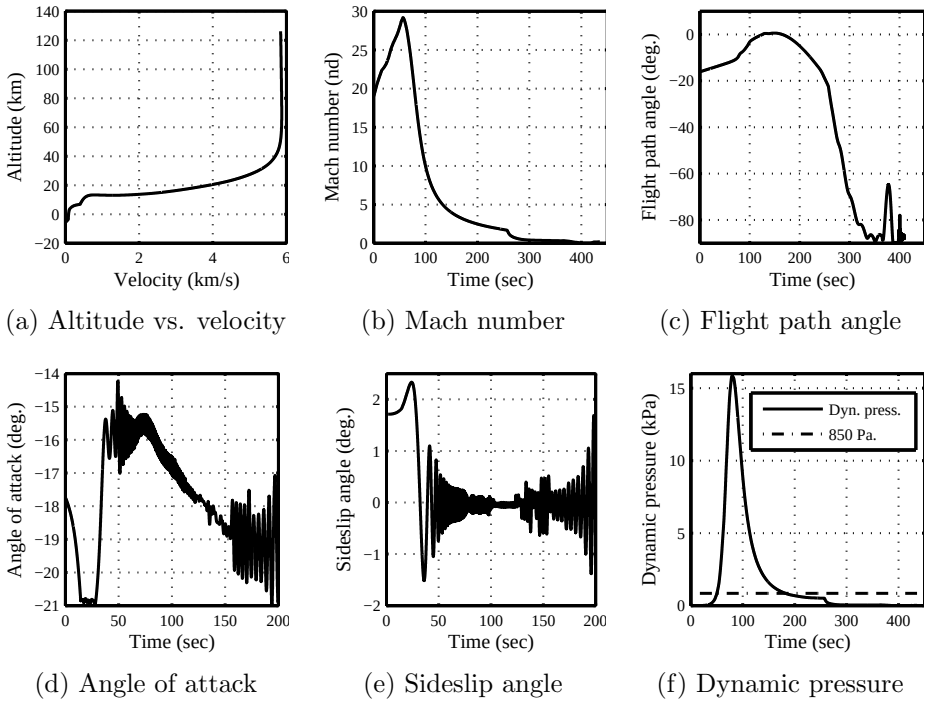

(a) Altitude vs. velocity (b) Mach number (c) Flight path angle

(d) Angle of attack (e) Sideslip angle (f) Dynamic pressure

Figure 56: Simulated trajectory used for creating the data set used for FADS optimization.

5.2 Residual-based Optimization Method

5.2.1 Cost Function

A major objective in optimizing the layout of the pressure-port system is to enhance the accuracy of the reconstruction process. The EKF is being used as the statistical estimator and it is assumed that the reconstructed parameters are supposed to be theoretically close to the true states based on the data set that is available since the EKF has been shown to reconstruct EDL parameters well in the last few chapters. Thus, the goal of the FADS layout optimization is to choose the number of transducers and the locations of the sensors so that the measurements themselves would be the *optimal data set* to reconstruct the flight parameters of interest.

The main parameters of interest are the dynamic pressure, angle-of-attack, and sideslip angle. The cost function (J) is represented by the residual between the estimated flight parameters and their true values. This is similar to what Deshpande et al. [46] used for the PD/ADS optimization; however, the subjectivity of the weighting parameters is removed from the optimization exercise. The cost functions for each parameter are combined into a vector that will be optimized using Pareto dominance. The residuals of the parameters are calculated at certain Mach numbers along the trajectory and the maximum residual is reported as the objective function value. The residuals are also normalized by the MSL science objective value, i.e. $\pm 2\%$ for q_∞ and 0.5 deg for α and β. Thus, an objective function value between 0 and 1 signifies that the port combinations produce data that can be reconstructed by the EKF to within MSL science objectives. The cost function is stated in Eqs. (31), where i is an index for the m-length Mach number vector over which the residuals are calculated. For this objective function $M_{\infty,i} = [14, 16, 18, 20, 24]$, which all fall within the nominal time frame the pressure data instrument operates.

$$\min J = [J_\alpha, \quad J_\beta, \quad J_{q_\infty}] \tag{31a}$$

$$J_\alpha = \max_{i=1}^{m} \left| \frac{\alpha_{\text{recon},i} - \alpha_{\text{true},i}}{\alpha_{\text{MSL objective}}} \right| \tag{31b}$$

$$J_\beta = \max_{i=1}^{m} \left| \frac{\beta_{\text{recon},i} - \beta_{\text{true},i}}{\beta_{\text{MSL objective}}} \right| \tag{31c}$$

$$J_{q_\infty} = \max_{i=1}^{m} \left| \frac{(q_{\infty,\text{recon},i} - q_{\infty,\text{true},i}) / q_{\infty,\text{true},i}}{q_{\infty,\text{MSL objective}}} \right| \tag{31d}$$

5.2.1.1 Constraints

Additionally, some geometric constraints were added to the problem. The port locations were restricted to within a 2 m radius on the forebody to restrict sensors on the vehicle shoulder and the ports had to be at least 0.125 m ($\approx$ 5 inches) apart. These constraints are representative of manufacturing constraints faced by real FADS sensor suites.

5.2.2 Effect of Random Noise

It should be noted that the objective function value depends on the random noise added to the various measurements. For the function evaluations here, the random seed used to generate the measurement noise was kept constant, which would mean that multiple function evaluations for the same configuration would yield the same exact objective function value; however, different random seeds for measurement noise would yield different results. In such cases, designers often use Monte Carlo analysis or linear covariance analysis to simulate the effect of random noise on the objective function value and then use a sample averaged mean objective function value for the optimization [106]. The effect of random measurement noise was simulated for this case by calculating the objective function value for one seven-port configuration with varying random seeds and is shown in Fig. 57.

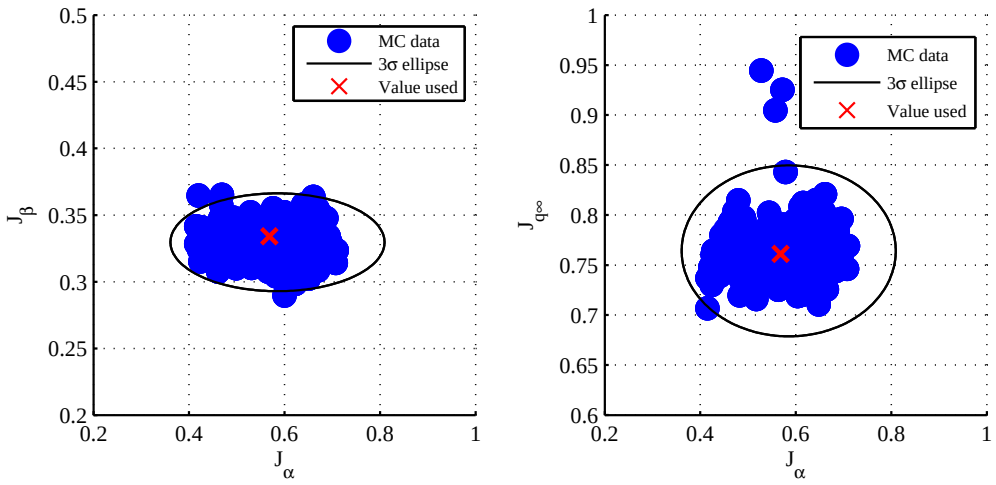

(a) J_α vs. J_β (b) J_α vs. $J_{q\infty}$

Figure 57: Effect of random measurement noise on the value of objective function for a single configuration.

The random noise does create some variation in the objective function value and should be considered by a designer of an atmospheric data system. However, for the optimization results shown here, the objective function evaluation was very time intensive and coupling a Monte Carlo analysis with it would have been even more

expensive. Additionally, the objective function value for the chosen measurement noise's random seed was very close to the mean value of the Monte Carlo-generated distribution in this case. So the random seed for the measurement noise was held constant and the objective function was calculated without using Monte Carlo analysis. The decision to keep the random seed for the noise constant for a computationally expensive objective function evaluation has some precedent in the literature [106].

5.2.3 Multi-modal Design Space

The main rationale for using an evolutionary algorithm, such as the GA, for optimization is the nonlinear, multi-modal nature of the design space. The objective function described in the earlier section meets this criterion, since the design space has several local optima. This is demonstrated in Fig. 58, where a gradient-based optimization routine (the MATLAB provided Sequential Quadratic Programming code within fmincon) is used to minimize just the J_α objective (Eq. (31b)) using different initial conditions. The GA-based optimized solution, which will be discussed in more detail in later sections, is also shown for comparison.

One can see in Figs. 58(a) and 58(b) that gradient-based optimizations are easily stuck in a local optimum despite varying the initial conditions; however, an evolutionary optimizer, such as the GA, can escape local minima due to the stochastic nature of the algorithm. This can eventually lead to a near optimum solution in a multi-modal design space as seen in Fig. 58(c). When the whole objective function vector is optimized to find the Pareto frontier and the number of ports in the configuration is varied, the design space is expected to become more complicated, thus strengthening the rationale for using an evolutionary optimization technique for this design problem.

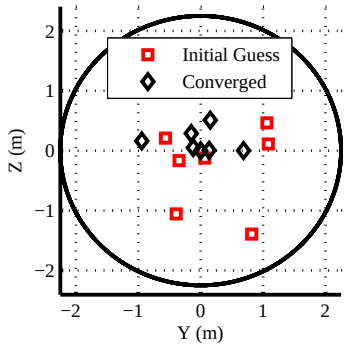

(a) Gradient optim. $J_\alpha = 0.8640$

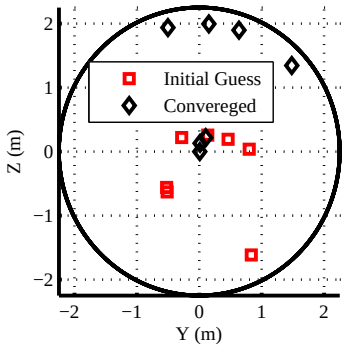

(b) Gradient optim. $J_\alpha = 0.6795$

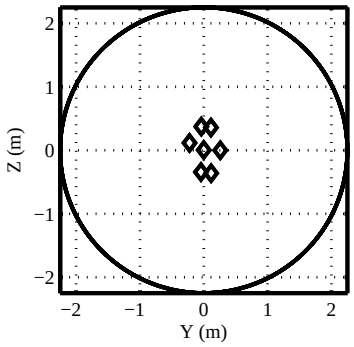

(c) Converged GA optim. $J_\alpha = 0.03397$

Figure 58: Optimal pressure-port locations using gradient-based optimization and GA-based optimization.

5.3 Residual-based Optimization Results

The main objective of the optimization methodology is to identify (1) minimum number of ports needed for accurate reconstruction and (2) the optimal location of the ports for each configuration. As two of the parameters of interest are orientation angles, the minimum number of ports studied are the two-port configurations, since angular value estimation requires at least two points of reference. For consistency with the MSL configuration, seven ports serves as the upper bound.

The study is broken into three steps. First, single-objective optimization is performed to identify the best configurations for systems for a given objective function and number of ports. Next, two-objective optimization is performed on each pair

of objective functions to study the trade-offs in the design space and visualize the Pareto frontier environment. Finally, all three objective functions are simultaneously optimized.

5.3.1 Single-objective Optimization

The optimizer is used to find optimal configurations that minimize each objective functions for two, three, four, five, six, and seven-port configurations. Convergence to the global minima cannot be guaranteed due to the stochastic nature of the optimizer; thus, each optimization is repeated at least 10 times using different random number seeds. Also, each optimization run is continued for at least 100 generations, as it was found that the minimization routine converged to the lowest possible function values by at least the 100th iteration. The maximum population size was limited to 32 members to limit number of function calls per generation; however, smaller population size leads to Pareto frontiers that are sparse.

Figure 59 shows the minimum objective function value found using single-objective optimization for a specific number of ports. Additionally, Table 12 summarizes the objective function vector for each of the single-objective optimization points noted in Fig. 59. Recall that the objective function values were normalized so that values between 0 and 1 signify that a configuration meets the minimum MSL objectives, so the values exceeding the MSL objectives are shown in bold. One sees that the optimal configuration for one objective function value often leads to unacceptable levels in the other objective functions. As a baseline, reconstruction of the simulated data set using the MSL configuration yielded $[J_\alpha, \quad J_\beta, \quad J_{q,\infty}] \quad = \quad [0.1657, \quad 0.0321, \quad 0.7876]$.

Figure 60 shows the optimum configuration for some of the single-objective results. The minimum dynamic pressure (Fig. 60(a)) result shows that the optimum configuration is to place the two ports in the stagnation region, similar to what MSL has done. Of course, the improvement in the pressure estimation comes at the cost

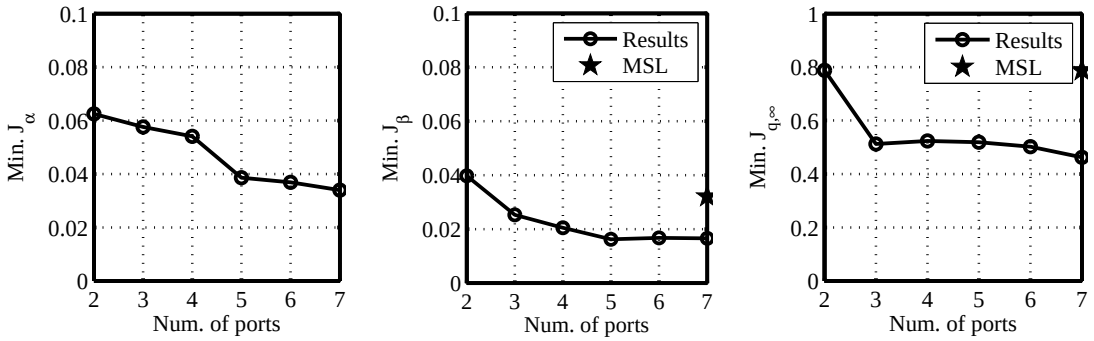

(a) α (b) β (c) q_∞

Figure 59: Results of single-objective optimization with MSL value also shown.

Table 12: Objective functions for single-objective optimization.

Obj.	2-port	3-port	4-port	5-port	6-port	7-port
			Minimum J_α solutions			
J_α	0.06246	0.05757	0.05408	0.03862	0.03687	0.03397
J_β	**2.217**	0.4953	0.24531	0.0486	0.052595	0.06094
$J_{q\infty}$	**1.033**	**1.0413**	0.75394	**1.059**	**1.102**	**1.0787**
			Minimum J_β solutions			
J_α	**6.366**	**2.932**	0.6574	0.1629	0.18525	0.1389
J_β	0.03976	0.02527	0.02052	0.01624	0.01673	0.01659
$J_{q\infty}$	**1.155**	**1.176**	**1.0378**	**1.0558**	0.9786	0.6746
			Minimum $J_{q\infty}$ solutions			
J_α	0.83212	0.1032	0.1072	0.1256	0.09104	0.082205
J_β	**1.701**	0.57362	0.096619	0.083149	0.072913	0.04621
$J_{q\infty}$	0.7877	0.5123	0.5237	0.5187	0.5023	0.4621

Note: Bold values exceed MSL's goals used for normalizing the function.

of worse sideslip angle and angle-of-attack detection. The minimum sideslip angle solution (Fig. 60(b)) spreads the four ports across the horizontal axis, but the ability to reconstruct dynamic pressure and angle-of-attack deteriorates. The seven-port minimum angle-of-attack result (Fig. 60(c)) is interesting as the configuration puts the pressure transducers on the spherical nose cap making the configuration sensitive to changes in the angle-of-attack, but also worsening the dynamic pressure reconstruction ability. Surprisingly, since the ports are spread around the spherical nose cap, there is some sideslip angle resolution. It is likely that the optimizer was trying to co-locate some of the sensors at the same spots but was prevented by the minimum

distance between sensors constraint.

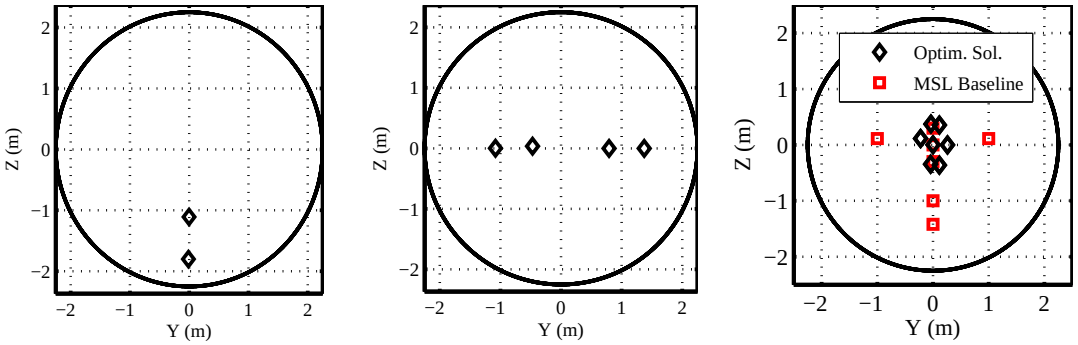

(a) Two-port min. $J_{q\infty}$ (b) Four-port min. J_β (c) Seven-port min. J_α

Figure 60: Optimized pressure-port configurations from single-objective optimization.

5.3.2 Two-objective Optimization

The results of the single-objective optimization showed that configurations that maximized the reconstruction capability of one parameter penalized the estimation of the other parameters. These trade-offs are visualized using Pareto frontiers developed from the results of two-objective optimization as seen in Figs. 61, 62, and 63. Zoomed insets of each pair of two-objective optimization are also provided.

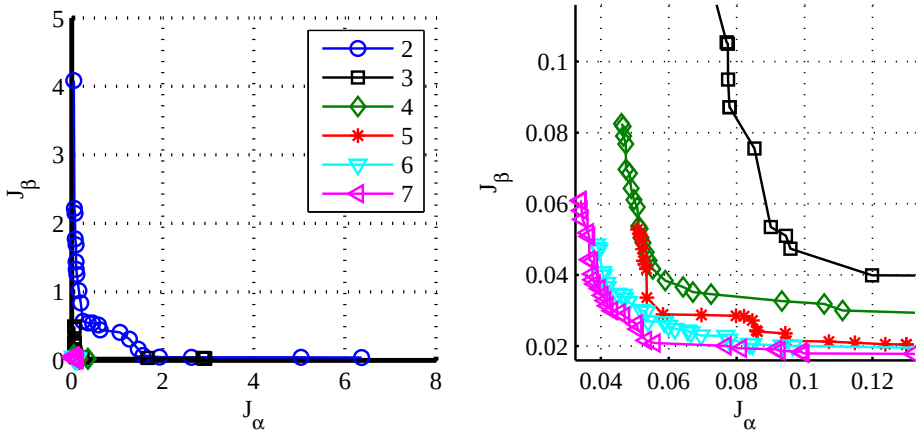

(a) J_β vs. J_α (b) Zoomed inset

Figure 61: Results of two-objective optimization for J_β vs. J_α.

It should be emphasized that although the Pareto frontiers of cases with different number of ports are plotted together in Figs. 61, 62, and 63, in reality each Pareto

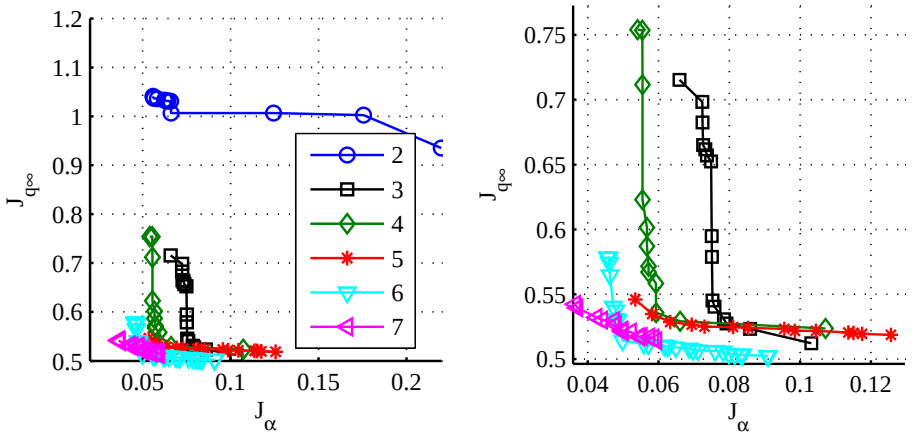

(a) $J_{q\infty}$ vs. J_α (b) Zoomed inset

Figure 62: Results of two-objective optimization for $J_{q\infty}$ vs. J_α.

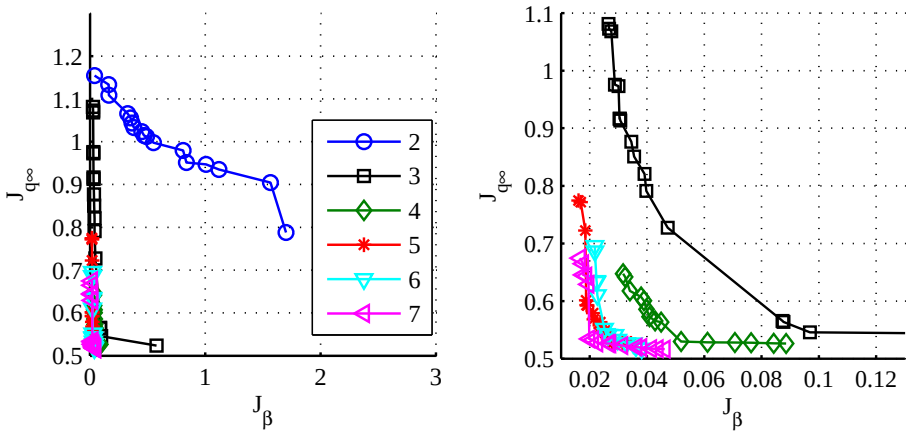

(a) $J_{q\infty}$ vs. J_β (b) Zoomed inset

Figure 63: Results of two-objective optimization for $J_{q\infty}$ vs. J_β.

frontier is a solution to a separate optimization problem with a separate design space. For example, there is no relation between the $J_\alpha - J_\beta$ Pareto frontier for the two-port case and the three-port case. One expects that as the number of ports increase the overall objective function values will decrease, but it is not as if the three-port case builds on the result of the two-port Pareto frontier case. Each optimization scenario is randomly initialized and the optimization procedures for different number of port cases do not share information with each other.

The Pareto frontiers in Figs. 61, 62, and 63 do coalesce onto each other as the

number of ports increase. This behavior signals a diminishing return type of behavior when the number of ports are increased. Upon inspection of the inset figures, it appears that when looking at α and β reconstruction performance, the six and the seven-port results are close to each other. There is little gained in adding an additional port to go from six to seven ports for this trade. Looking at the other two trades, the five-port solution appears to match the six and seven-port results in the β and q_∞ trade but remains far off from the six and seven-port results in the α and q_∞ trade. The diminishing return thus appears to be close to the six-port Pareto front. Recall that the MSL configuration yields $[J_\alpha, \quad J_\beta, \quad J_{q,\infty}] \quad = \quad [0.1657, \quad 0.0321, \quad 0.7876]$, which puts that configuration in the dominated solution space of the seven-port Pareto frontiers, albeit not too far off the front. Of course, it should be stressed that this observation is for the current objective function only and other formulations of the cost function might improve the ranking of the MSL configuration.

5.3.3 Three-objective Optimization

For the final optimization case, all three objective functions were minimized simultaneously by the NSGA-II optimizer. Figure 64 shows the optimization's results for the various number of port cases, with J_α as the x-axis, J_β as the y-axis, and $J_{q\infty}$ shown with color. Note that all of the points in the plots are part of 3-dimensional Pareto surfaces, whose two dimensions are shown on the x and y axes and the third dimension is represented with color. Additionally, the MSL baseline is also shown on the seven-port plot for comparison as a red diamond, even though it is not a Pareto-optimal solution according to the optimization and not on the Pareto surface.

Some representative seven-port cases from the Pareto-optimal solutions are shown in Fig. 65 and their objective function values are compared to the MSL configuration in Table 13. The MSL baseline is shown as squares and the optimized values are

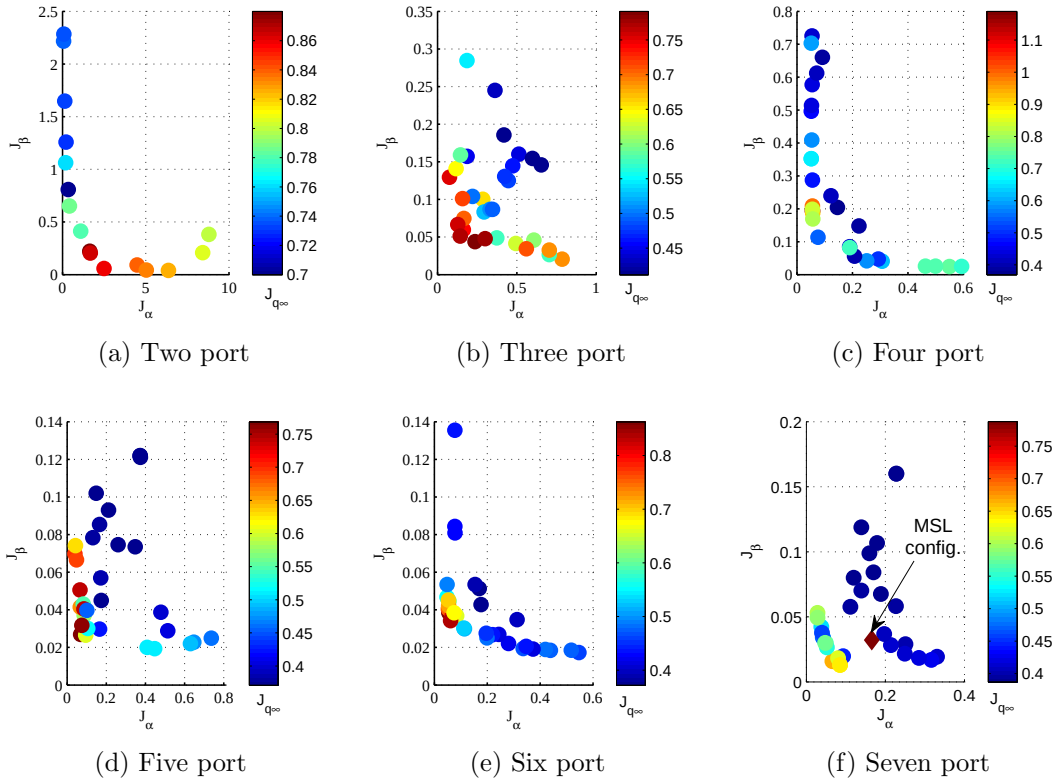

(a) Two port (b) Three port (c) Four port

(d) Five port (e) Six port (f) Seven port

Figure 64: Results of three-objective optimization.

shown as diamonds. The first case shows a configuration that improves the angle-of-attack and sideslip angle capabilities from MSL, but is worse off in estimating the dynamic pressure. The second figure is the opposite case, as dynamic pressure reconstruction ability improves due to extra ports near the stagnation point, but decreases angle-of-attack and sideslip angle estimation ability. The last configuration improves in all metrics, but the improvement is not as drastic in some parameters as in the first two cases. One can see that an optimization process can improve upon the MSL configuration and through a method, such as the one conducted in this paper, an atmospheric data system designer can decide which way he wants to move in the design space.

The three-objective optimization shows configurations which improves the estimation of all three parameters of interest. Thus, for an engineering solution, the designer

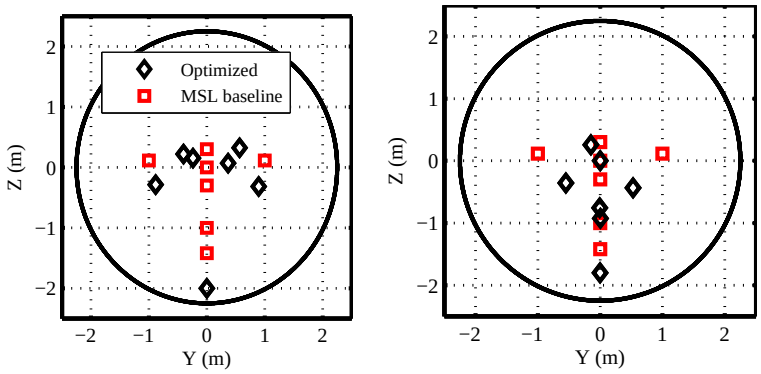

(a) Case 1: Lower J_α and J_β

(b) Case 2: Lower $J_{q\infty}$

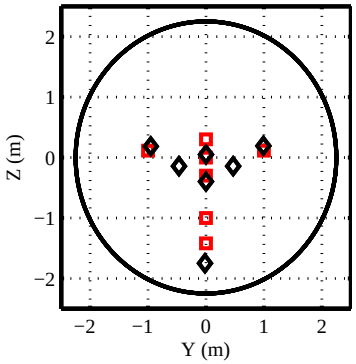

(c) Case 3: Lower J_α, J_β, and $J_{q\infty}$

Figure 65: Optimized pressure-port configurations from three-objective optimization.

Table 13: Comparison of seven-port representative cases with the MSL configuration.

Obj.	Case 1		Case 2		Case 3	
	Value	% Diff. MSL	Value	% Diff. MSL	Value	% Diff. MSL
J_α	0.06608	-60%	0.22787	+38%	0.09699	-41%
J_β	0.015924	-50%	0.16001	+398%	0.02791	-13%
$J_{q\infty}$	0.934463	+19%	0.541879	-31%	0.55450	-30%

does not need to conduct a single-objective or a two-objective optimization. In fact, the single-objective and two-objective optimization take a comparable about of time as the three-objective optimization; however, there is still a benefit in conducting the single and two-objective optimizations since they improve the understanding of the design space and helps the designer choose the appropriate configuration from the Pareto surface of the three-objective optimization.

5.3.4 Computational Effort

The NSGA-II based method found Pareto frontiers of near-optimum configurations in the multi-modal design space using a population size of 32 members, with each run propagated for 100 generations and then repeated 10 times, resulting in 32,000 function calls. On the other hand, a brute-force search, where each possible configuration was checked, would demand a significant more number of function calls. Figure 66(a) compares the numbers of function calls between the NSGA-II method and a brute-force method that searched all possible port locations within a 2 m radius with a grid resolution in the radial direction of 0.125 m and the angular direction of 60 deg. The resulting coarse grid is shown in Fig. 66(b). Deshpande et al. [46] did not provide any computational data for their method, and thus it is not included in this comparison.

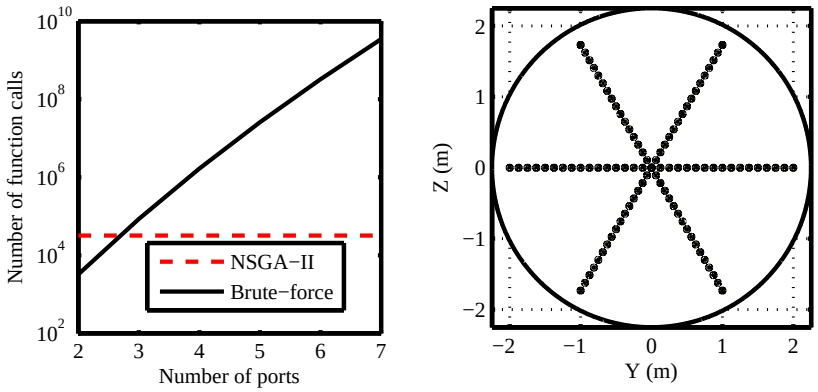

(a) Computational Comparison (b) Brute-force Search Grid

Figure 66: Comparison of computational effort between NSGA-II based method and brute-force search.

For a two-port comparison, Fig. 66(a) shows that the brute-force method is slightly better than the NSGA-II method, but the number of combinations searched by the brute-force method quickly makes the NSGA-II method the best choice as the number of ports being considered increases, even for a coarse search grid used in this comparison. One could use heuristics to reduce the number of function calls needed by

the brute-force method, but it is unlikely to improve the performance of the NSGA-II based method.

5.4 Observability-based Optimization Method

5.4.1 Observability and Cramér-Rao Lower Bound

Deshpande et al. [46] and the work in the previous section used the residual between the estimated parameters and the true parameters as the objective function for FADS optimization. Although a proper metric for sensor locations sensitivity during parameter estimation, the residual-based function is time intensive since an inverse parameter estimation process has to be conducted every time the function is evaluated. This also makes the objective function values dependent on the estimation method chosen.

An optimized sensor suite should be independent of what specific estimation method is used to process the observations leading to the concept of observability as a measure of how well the state vector can be deduced from the outputs [93]. Observability metrics can be found for linear, time-invariant systems using the observability Gramian, but are hard to calculate for nonlinear, time-varying systems [121], such as FADS sensors on a re-entry vehicle. The Cramér-Rao Lower Bound provides a useful substitute by defining the theoretical lower bound of the expected uncertainty for an estimation process. CRLB is independent of the estimation method and is defined as the inverse of the Fisher information matrix, which due to the Gauss-Markov Theorem results in a simple inequality as shown in Eq. (32). In this expression, P is the state covariance matrix, H is the measurement sensitivity matrix, and R is the measurement noise covariance.

$$P \geq \left(H^T R^{-1} H\right)^{-1} \tag{32}$$

If the measurement uncertainties are uncorrelated and can be represented by an identity matrix, the CRLB simplifies further to the expression in Eq. (33), which is

only a function of the Jacobian of the measurement equation with respect to the state vector (or H). For FADS, the measurement equation is the pressure measured by a transducer and this value is a function of the transducer location, trajectory states, and atmospheric conditions [56].

$$P_{\text{lowest}} = \left(H^T H\right)^{-1} \tag{33}$$

5.4.2 CRLB Sensitivity to Trajectory

Dynamic pressure (q_∞), angle of attack (α), and sideslip angle (β) are often the parameters of interest in FADS applications [44, 40, 46, 45] and were also the quantities for which MSL's science objectives were specified [37]. These terms serve as the state vector here, which means that H and the CRLB-calculated P will be calculated with respect to these parameters. If only the diagonal of P is considered, then one gets uncorrelated variance of each of the parameters of interest as seen in Eq. (34).

$$\left(H^T H\right)^{-1} = P_{\text{lowest}} = \begin{bmatrix} \hat{\sigma}_\alpha^2 & & \\ & \hat{\sigma}_\beta^2 & \\ & & \hat{\sigma}_{q_\infty}^2 \end{bmatrix} \tag{34}$$

FADS optimization will locate a sensor configuration that minimizes the non-normalized, standard deviation ($\hat{\sigma}$) - square-root of the variance - for each parameter of interest over the length of the trajectory. Due to multiple parameters of interest, the function is multi-objective and the optimum configurations will be part of Pareto frontiers. However, since the CRLB is calculated at a given trajectory condition, there will be a CRLB for every trajectory point. The CRLB values throughout the trajectory need to be combined into one objective function vector that describes a metric of observability for a given FADS configuration.

To decide how to combine the various CRLBs into one metric, a sensitivity study of the CRLB-based, parameter standard deviations was conducted. These standard deviation values were normalized by the MSL science objective values, i.e. 0.5 deg.

for angle of attack and sideslip angle and 2% of the actual dynamic pressure, to yield a normalized standard deviation (σ). NSGA-II was used to find Pareto frontiers at a few selected trajectory points for a seven-port configuration and the fronts' sensitivities to variations in trajectory were studied.

Figure 67 captures the Pareto frontier variation with Mach number. The range of the Pareto frontier decreases at certain Mach numbers - signifying an improvement in observability - but the trend is not based on an increase or decrease in Mach number. This is somewhat surprising since the flow regime actually changes from high, hypersonic speeds to low, supersonic speeds and one would assume that observability would change with the flow regime.

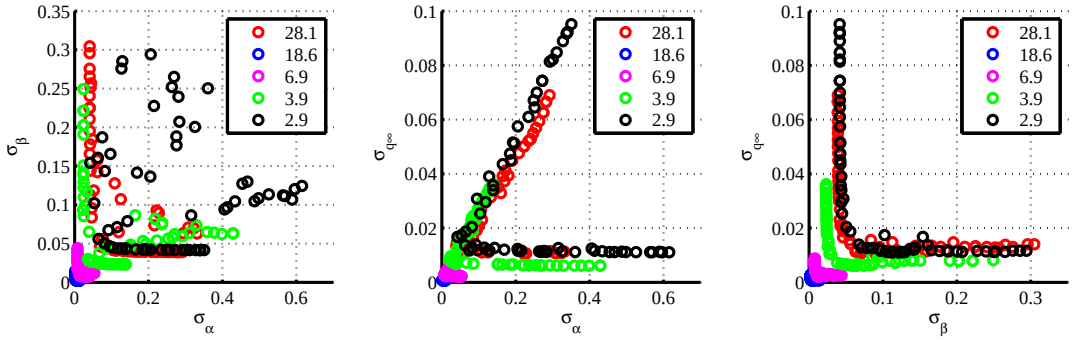

(a) σ_α vs. σ_β (b) σ_α vs. $\sigma_{q\infty}$ (c) σ_β vs. $\sigma_{q\infty}$

Figure 67: Sensitivity of CRLB to Mach number for the seven-port optimized configuration.

Instead, a stronger correlation is seen with dynamic pressure (Fig. 68), where higher dynamic pressure values lead to lower standard deviations and better observability. Due to CRLB's strong sensitivity to dynamic pressure, the metric used to aggregate CRLBs from various points in the trajectory should sample different dynamic pressure values to have a diversity of q_∞ conditions.

Angle of attack and sideslip angle also have an effect on the CRLB. Figure 69 displays the variation in Pareto frontiers at various sideslip angles for low q_∞ and high q_∞ conditions. Varying the sideslip angle slightly leads to a discernible change

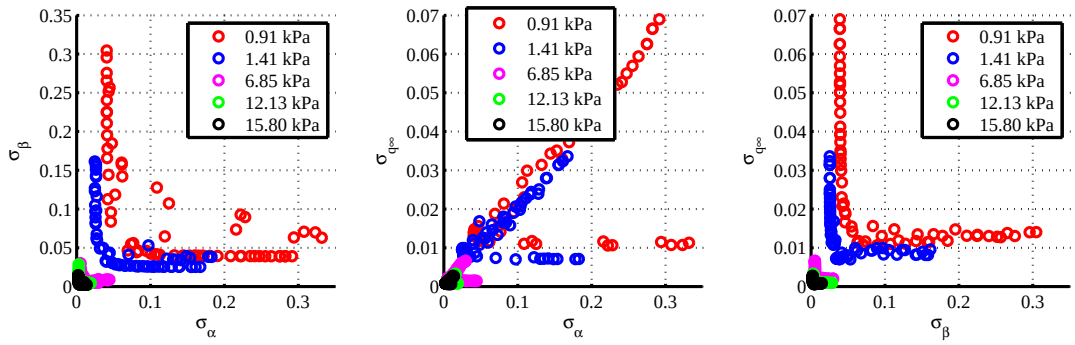

(a) σ_α vs. σ_β (b) σ_α vs. $\sigma_{q\infty}$ (c) σ_β vs. $\sigma_{q\infty}$

Figure 68: Sensitivity of CRLB to dynamic pressure for the seven-port optimized configuration.

in the Pareto frontier, suggesting that variations in this quantity should be captured in the aggregate metric. Variations in angle of attack displayed similar trends.

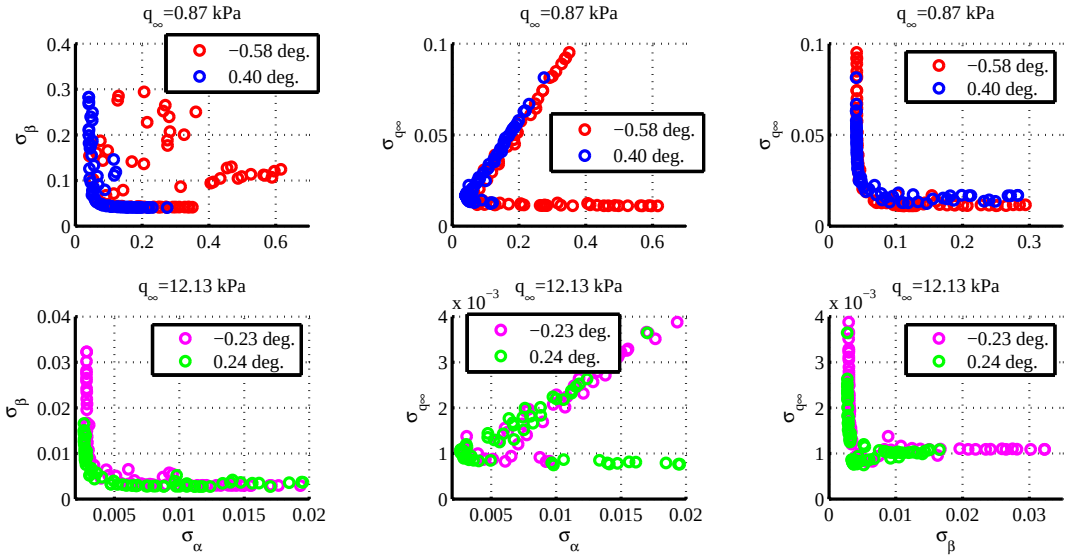

(a) σ_α vs. σ_β (b) σ_α vs. $\sigma_{q\infty}$ (c) σ_β vs. $\sigma_{q\infty}$

Figure 69: Sensitivity of CRLB to sideslip angle for the seven-port optimized configuration.

5.4.3 Objective Function Formulation

In this investigation, 20 sample locations from the test problem trajectory were selected for the aggregate objective function. These discrete trajectory states are shown

in Fig. 70 overlaid on the continuous trajectory. One can see that there has been equal distribution given to low and high dynamic pressure values and a variety of angle of attack and sideslip angles.

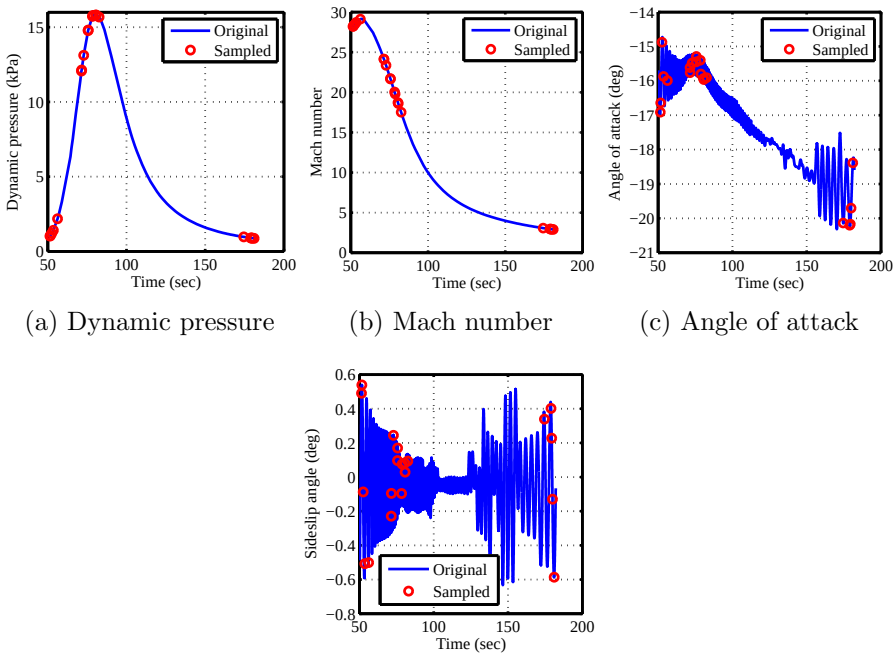

(a) Dynamic pressure (b) Mach number (c) Angle of attack

(d) Sideslip angle

Figure 70: Sampled trajectory points for the aggregate objective function.

Using these sampled points, the objective function $\mathbf{f}$ is defined in Eq. (35), while the optimization problem is defined in Eq. (36) where $\bar{}$ is the component-wise, arithmetic average of the objective functions. The inequality constraint in Eq. (36) is used to maintain a minimum spacing between the n port locations ($\mathbf{p}$) and this minimum distance $\mathrm{d_{min}}$ is chosen as 5 inches as was done for the residual-based optimization.

$$\mathbf{f}(\mathbf{p})_i = [\sigma_{\alpha,i}, \quad \sigma_{\beta,i}, \quad \sigma_{q\infty,i}]^T \quad \forall \quad i = \{1, \cdots, k\} \tag{35}$$

$$\begin{aligned} &\min \quad \bar{\mathbf{f}}(\mathbf{p}) \\ &\text{s.t.} \quad |\mathbf{p}_i - \mathbf{p}_j| \leq \mathrm{d_{min}} \quad \forall \quad i, j \in \{1, \cdots, n\} \end{aligned} \tag{36}$$

5.4.4 Implementation and Computational Effort

The NSGA-II method is an evolutionary algorithm so finding the true Pareto frontier is not guaranteed. The CRLB-based optimization was conducted with a population of 128 candidate configurations over 500 generations and this process was repeated 10 times. The final Pareto frontiers were found using the combined results. Experimentation showed that a population size of 128 provided a good distribution across the design space to capture the near-optimal Pareto frontier and that 500 generations were enough to reach a stable set of non-dominated points. This process required 640,000 function calls. These calls were made regardless of the type of configuration being optimized, i.e. a three-port or a seven-port situation had the same number of function calls. Additionally, the number of generations, population size, and number of repetitions were selected with conservatism to ensure that the optimization converged. It is possible that similar results could be achieved with far fewer function calls.

On the other hand, a brute-force search, where each possible configuration was checked, would demand a significantly larger number of function calls, especially as one increased the number of pressure transducers being optimized. This is described by Fig. 71 where the number of function calls using a Monte Carlo-like process on a representative grid of possible transducer locations and the CRLB-based, NSGA-II optimization process are compared. A smart culling process can reduce the grid size and the number of possible combinations to evaluate, but as shown in Fig. 71 even a coarser search grid size uses significantly more function calls compared to the NSGA-II optimization that uses a continuous search space.

In terms of computational speed, the CRLB-based objective function evaluation took around 10^{-3} s using a 3.4 GHz Intel i7 processor, with a slight increase in run time as the number of ports increased. On the other hand, the residual-based objective function took close to 25 s per run using the same hardware, underscoring

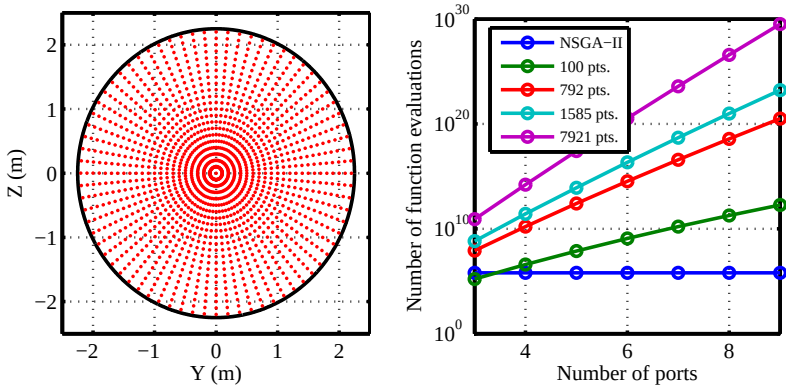

(a) Possible ports (1585 grid pts.) (b) Number of function calls

Figure 71: Function evaluation comparison between Monte Carlo-based search and the CRLB-based optimization method.

the improvement in speed if the CRLB-based function is used. Deshpande et al. [46] did not provide any computational data for comparison of their method.

5.5 Observability-based Optimization Results

5.5.1 Multi-objective Optimization Pareto Frontiers

The results of the CRLB-based FADS optimization are summarized in Fig. 72, which shows different views of the Pareto surface formed by the three-objective optimization. Pareto frontiers for three-port through nine-port configurations are shown. The two-port configuration did not provide a converged Pareto frontier in 500 generations and was excluded in this analysis.

Figure 72 shows that the Pareto frontiers come closer and closer to the origin as the number of ports increase. This is not surprising, since empirical evidence suggests that increasing the number of ports improves observability and leads to a lower objective function value. It also appears that the frontiers coalesce upon each other and not much is gained in observability after the six-port configuration. A six-port configuration thus appears to be the point of diminishing returns. The identification of the point of diminishing returns is investigated further later in this section.

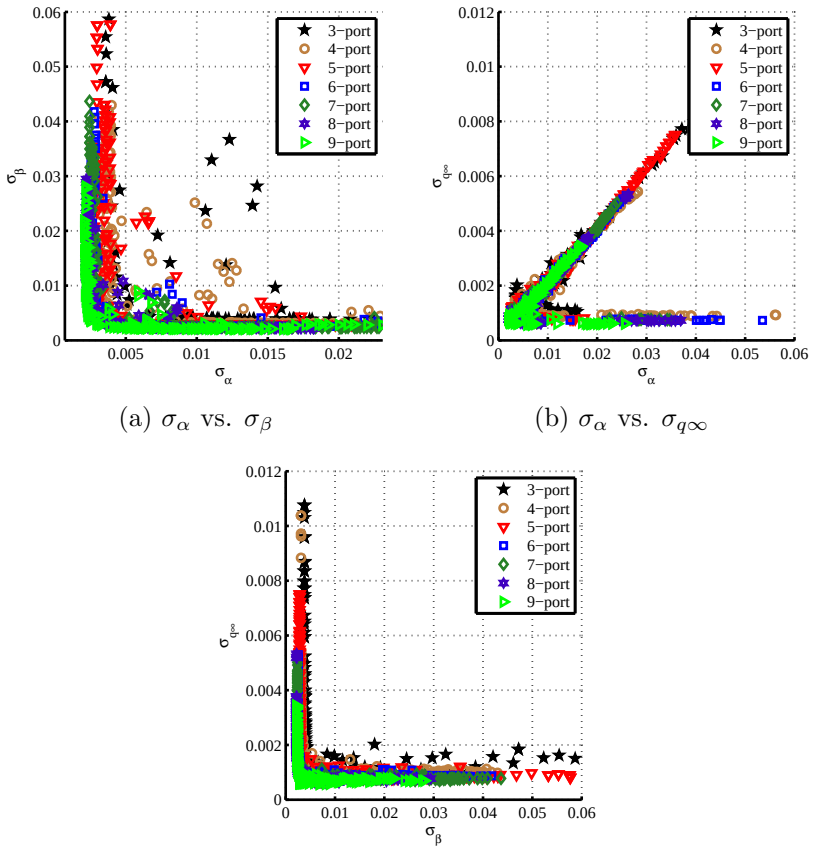

(a) σ_α vs. σ_β

(b) σ_α vs. $\sigma_{q\infty}$

(c) σ_β vs. $\sigma_{q\infty}$

Figure 72: Pareto frontiers from multi-objective optimization.

Some representative configurations from the Pareto frontier are shown in Fig. 73. Although there is a structure to the port configurations, there was no constraint for symmetry and thus the optimized configurations are non-symmetrical. The representative configurations chosen in Fig. 73 are for either minimum σ_α, σ_β, or $\sigma_{q\infty}$ and the layouts exhibit these qualities. Dynamic pressure observability is achieved by placing ports near the stagnation point, which for this trajectory was around $y = 0$ and $z =$ -1 m. Angle of attack observability is achieved by placing ports in the pitch plane on either side of the origin, while sideslip angle observability is maintained in a similar way except in the yaw plane. Numerical effects of the optimization are apparent in Fig. 73(b), where intuition would suggest that all of the ports would have $z = 0$, and Fig. 73(c), where all of ports don't have $y = 0$. Due to numerical noise, the

optimization may not capture these nuances very well.

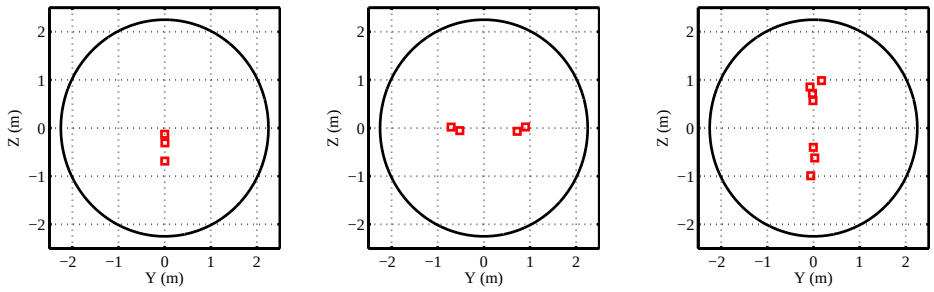

(a) Min. $\sigma_{q\infty}$ 3-port (b) Min. σ_{β} 4-port (c) Min. σ_{α} 7-port

Figure 73: Port configurations from some representative points of the Pareto frontiers.

Although single objective optimal results are interesting to study, designers are more interested in configurations that can achieve good performance in all of the objective functions. Every point of the Pareto frontier is a non-dominated solution and hence it is hard to pick one point over another; however, one can define an equally-weighted compromise point which is closest to the ideal solution. The definition of this compromise point may differ due to the type of weighting applied; however, the simplest such compromise point would come from a linear weighting scheme. Figure 74 explains the meaning of this linearized, equally-weighted compromise point on a nominal Pareto frontier.

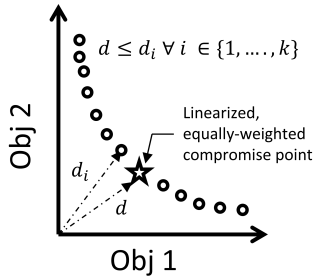

Figure 74: Definition of the linearized, equally-weighted compromise point of a Pareto frontier.

Using the linearized, equally-weighted compromise point as a benchmark of a good design, Fig. 75 shows some representative optimal configurations for various number of ports. Some broad design ideas can be gleaned from these configurations. It appears

that annular-like layouts - where ports are laid out in rings - are more preferred using this benchmark than cruciform layouts that were seen in some past configurations (Fig. 7). Additionally, many of these ports are concentrated near a ring of radius 0.5 m, which is near the area of a change in curvature as the aeroshell shape transitions from a spherical segment to the sharp cone. A change in curvature or geometry would make a port located in that region very sensitive to changes in the trajectory. Finally, all of the configurations have a port or two located near the stagnation point, suggesting that measuring pressure in this region improves observability of all of the parameters.

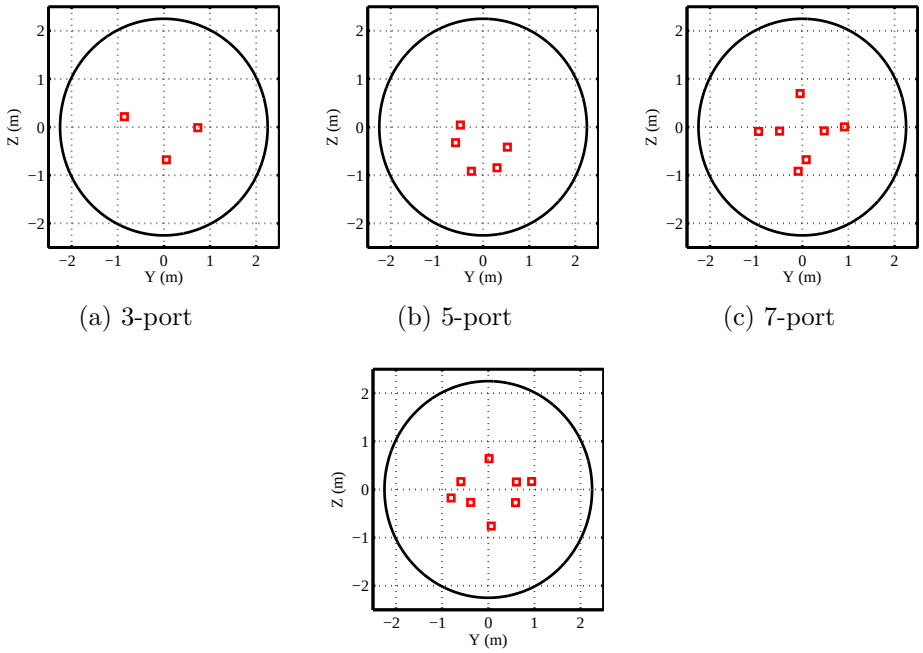

(a) 3-port (b) 5-port (c) 7-port

(d) 8-port

Figure 75: Port configurations of some of the linearized, equally-weighted compromise points of the Pareto frontiers.

Interestingly, some of the configurations shown could be simplified further. For example, the 7-port configuration in Fig. 75(c) shows two ports near $z = -1$. If these two ports are combined to create a 6-port configuration, the objective function values does not degrade significantly from the 7-port values. Thus, although numerical

optimization can quickly narrow down the design space to a list of good designs, it still leaves room for intuitive improvements by the designer.

The linearized, equally-weighted compromise point also allows one to visualize the point of diminishing returns. The diminishing point is apparent in Fig. 76, where the objective function values of the representative point of the Pareto frontier are plotted for different port configurations. If one is interested in only dynamic pressure reconstruction, a 5-port configuration seems to suffice as the point of diminishing returns. The Pareto contours in Figs. 72(b) and 72(c) that contain dynamic pressure dependency also support this assertion. However, when all of the parameters are considered together, one needs at least 6-ports to reach the point of diminishing returns, since the marginal return point is not reached for angle of attack and sideslip angle until this port configuration as seen in Fig. 76 and the Pareto frontier in Fig. 72(a).

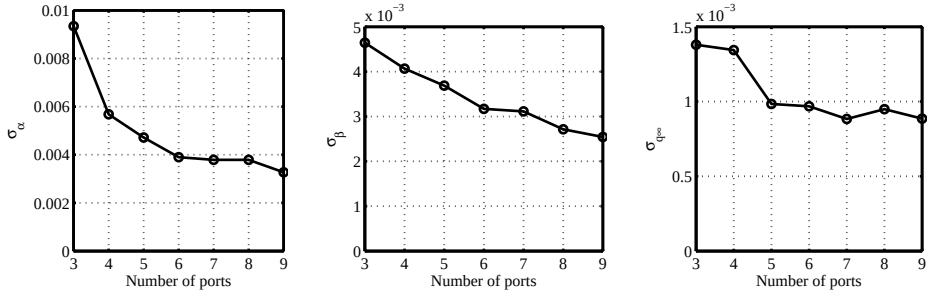

(a) Angle of attack (b) Sideslip angle (c) Dynamic pressure

Figure 76: Identification of the point of diminishing return for non-symmetric configurations using objective values of the linearized, equally-weighted compromise points.

5.5.2 Sensitivity to Pressure Models

The pressure model used to evaluate the objective function has a sensible effect on the optimization results. In Sec. 5.5.1, a Computational Fluid Dynamics (CFD) derived pressure distribution was used in the function evaluations. However, CFD results have some uncertainties associated with them. One can use the classical Newtonian model to represent the pressure distribution, as was done by Deshpande et al. [46].

Figure 77 captures the effect of using various pressure distributions by showing the Pareto frontiers for a 6-port configuration with the nominal CFD distribution, a CFD-based distribution perturbed randomly by 5%, and a Newtonian distribution.

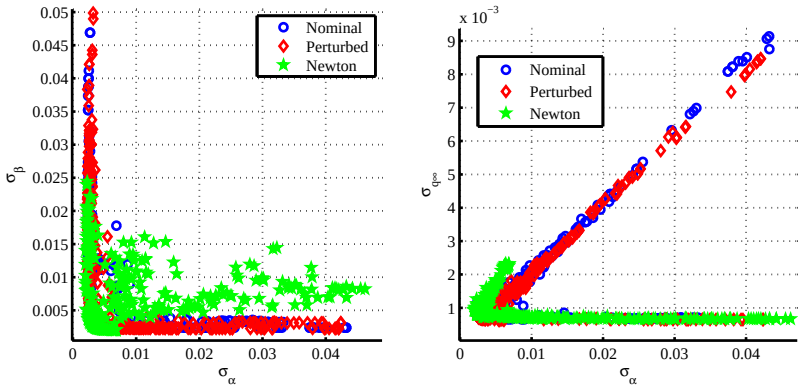

(a) σ_α vs. σ_β (b) σ_α vs. $\sigma_{q\infty}$

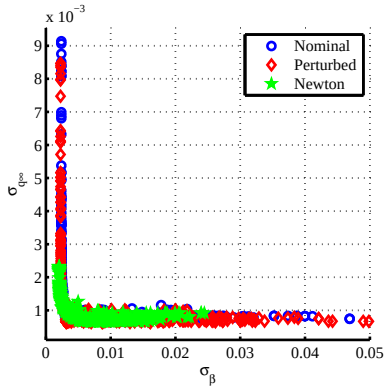

(c) σ_β vs. $\sigma_{q\infty}$

Figure 77: Comparison of Pareto frontiers for the 6-port configurations using various pressure models.

One does not see a major difference between the results of the two CFD-based optimizations, but the Newtonian distribution's Pareto frontier in the α-β slice appears less structured. Since the Newtonian distribution is based on a smooth function — $2\sin^2\theta$ — there are multiple port configurations that have similar objective function values and that makes the objective function space multi-modal.

Similar conclusions can be drawn when looking at the configurations described by the Pareto frontiers. Figure 78 shows the minimum σ_α configurations for the 6-port

case using different pressure models. As expected for a suite making angle of attack more observable, all three configurations have transducers that are located on the pitch plane and have sets of ports that are on either side of the origin to increase the sensitivity to changes in the angle of attack. Due to the accumulation of ports in two locations, it seems that if one was only interested in angle of attack reconstruction a 2-port solution could suffice. In reality, designers are interested in reconstructing more than one parameter and hence would not be interested in an optimal configuration for only one parameter.

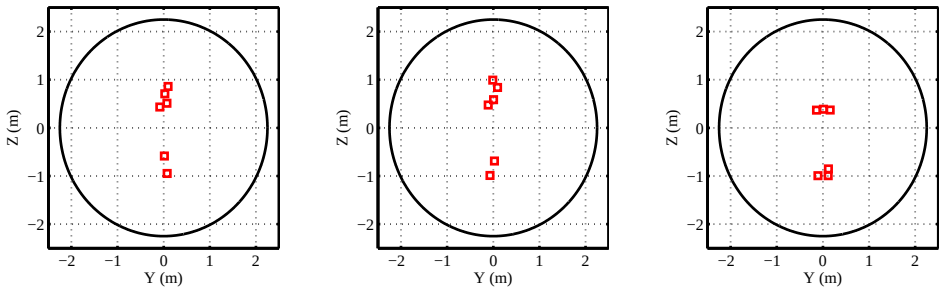

(a) Nominal (b) Perturbed (c) Newtonian

Figure 78: Optimal σ_α 6-port configuration using various pressure models.

The nominal and perturbed CFD-based configurations yield extremely similar results, while the Newtonian configuration is different. As the CFD-distribution is not as smooth as the Newtonian pressure distribution, the objective function space is less multi-modal and the configurations shown in Figs. 78(a) and 78(b) represent samples from a basin of attraction. The Newtonian distribution-based objective space is more multi-modal and vastly different looking configurations are represented in the Pareto frontiers.

This exercise underscores the need to use computational methods to optimize a FADS suite and to tailor it for the proper conditions. Simply relying on engineering judgment and pressure distribution predictions from one set of tools - the *modus operandi* of designing FADS configurations in the past - is not enough to design a robust sensor suite. The variations caused by using different pressure distributions

can be significant.

5.5.3 Sensitivity to Trajectory Perturbations

One of the main assertions of this comprehensive FADS placement optimization procedure is to make the chosen configuration robust and optimal over the entire trajectory. The effect of trajectory variations is clearly visible in Fig. 79 which shows the Pareto frontiers of a 6-port configurations using the nominal trajectory defined in Sec. 5.4.3 and another trajectory perturbed by 5% from the nominal. Even though the perturbation is small, the Pareto frontiers show a visible difference.

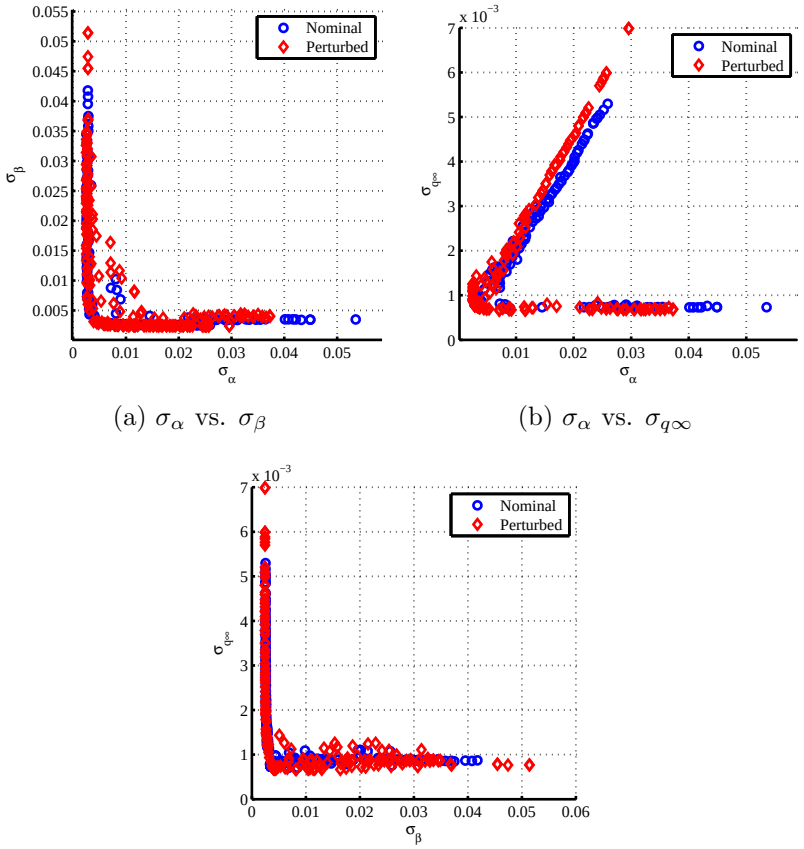

(a) σ_α vs. σ_β

(b) σ_α vs. $\sigma_{q\infty}$

(c) σ_β vs. $\sigma_{q\infty}$

Figure 79: Comparison of Pareto frontiers for the 6-port configurations using various trajectories.

The effect of trajectory variation is also apparent in the optimized FADS configurations for minimum $\sigma_{q\infty}$ shown in Fig. 80. As expected, the ports optimizing the

reconstruction of dynamic pressure are centered around the stagnation point. However, the slight difference between the optimal $\sigma_{q\infty}$ nominal (Fig. 80(a)) and perturbed (Fig. 80(b)) trajectory leads to a different looking port configuration. On the other hand, Fig. 80(c) shows a very different looking configuration that does not have the best $\sigma_{q\infty}$ value for either case but is still robust to the two different trajectories. This emphasizes the effect of trajectory perturbation and why FADS optimization should be performed across the entire trajectory and not at a single point of the trajectory. This way solutions that are robust to such perturbations can be found instead of optima based on point designs.

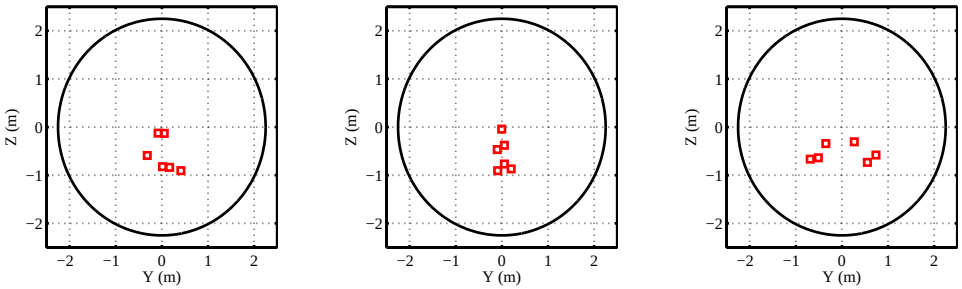

(a) Nominal (b) Perturbed (c) Robust

Figure 80: Optimal $\sigma_{q\infty}$ 6-port configuration using different trajectories.

5.5.4 Optimization with Symmetry Constraints

Past FADS sensors have had symmetric configurations (Fig. 7) and the FADS optimization study conducted by Deshpande et al. [46] explicitly set symmetry as a constraint. Due to the preference of symmetry in these past configurations, the optimization was also conducted with a symmetric constraint to look at how this affected the optimal configurations. The new objective function is shown in Eq. 37 and this optimization was repeated with various numbers of even-numbered pressure ports.

$$
\begin{aligned}
&\min \quad \bar{\mathbf{f}}(\mathbf{p}) \\
&\text{s.t.} \quad |\mathbf{p}_i - \mathbf{p}_j| \leq \mathrm{d}_{\min} \quad \forall \quad i,j \in \{1,\cdots,n\} \\
&\qquad \mathbf{p}_{i,y} = -\mathbf{p}_{j,y} \quad \forall \quad i \in \{1,\cdots,n/2\} \quad \text{and} \quad j = i + n/2 \\
&\qquad \mathbf{p}_{i,z} = \mathbf{p}_{j,z}
\end{aligned}
\tag{37}
$$

The Pareto frontiers of the design space are shown in Fig. 81. Once again, 2-port configurations were excluded due to their poor convergence in the optimization. The number of ports that serves as the point of diminishing returns may be determined using Fig. 82, which shows the objective function of the linearized, equally-weighted compromise points. For certain objectives, like sideslip angle, there seems to be little difference in objective value by increasing the number of ports and the point of diminishing returns appears to be at 4-port configurations. If one is interested in only sideslip angle reconstruction, a 4-port configuration could suffice. But overall, considering all of the objectives at once, it appears that 6-port configurations are the points of diminishing returns as the Pareto frontiers coalesce upon each other as the number of ports increase and only marginal improvement in the uncertainty is gained by increasing the number of ports.

The port configurations related to the linearized, equally-weighted compromise point of the Pareto frontiers are shown in Fig. 83.

There are some generalizing trends that can be observed when comparing the representative symmetric, linearized, equally-weighted compromise point configurations with their non-symmetric counterparts in Fig. 75. Similar to the situation with the non-symmetric cases, the optimal configurations appear to be annular rather than cruciform shaped. The ring of ports are in the region where the aeroshell shape transitions from a spherical segment to a cone. These design guides seem to reinforce lessons learned from the non-symmetric optimization. However, upon comparing their

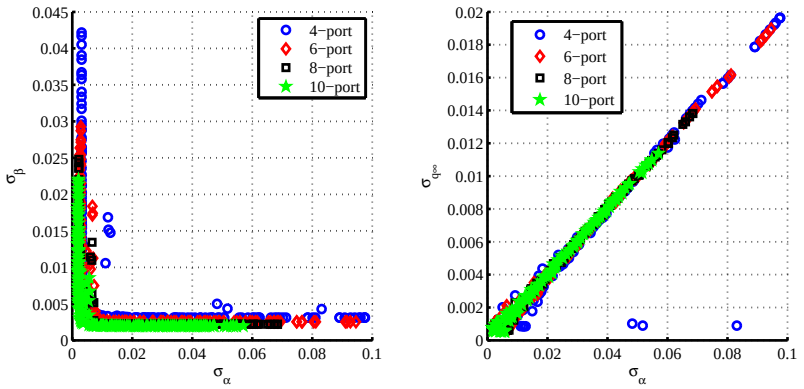

(a) σ_α vs. σ_β

(b) σ_α vs. $\sigma_{q\infty}$

(c) σ_β vs. $\sigma_{q\infty}$

Figure 81: Pareto frontiers from symmetric, multi-objective optimization for various port numbers.

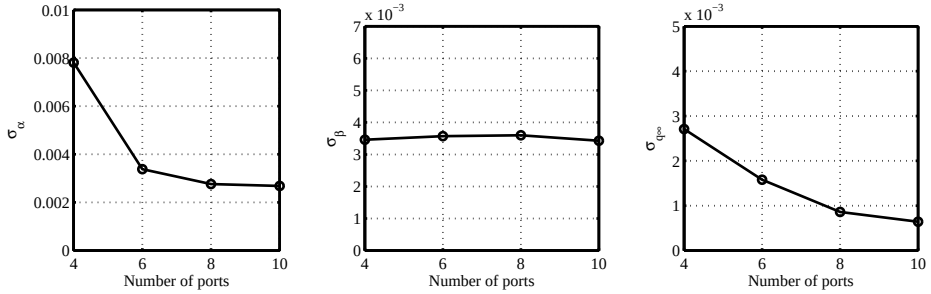

(a) Angle of attack

(b) Sideslip angle

(c) Dynamic pressure

Figure 82: The point of diminishing return of symmetric configurations found using objective function values of the linearized, equally-weighted compromise point.

respective objective function values, as shown in Table 14, the effect of the slight differences between the two optimizations are apparent. The table shows that although

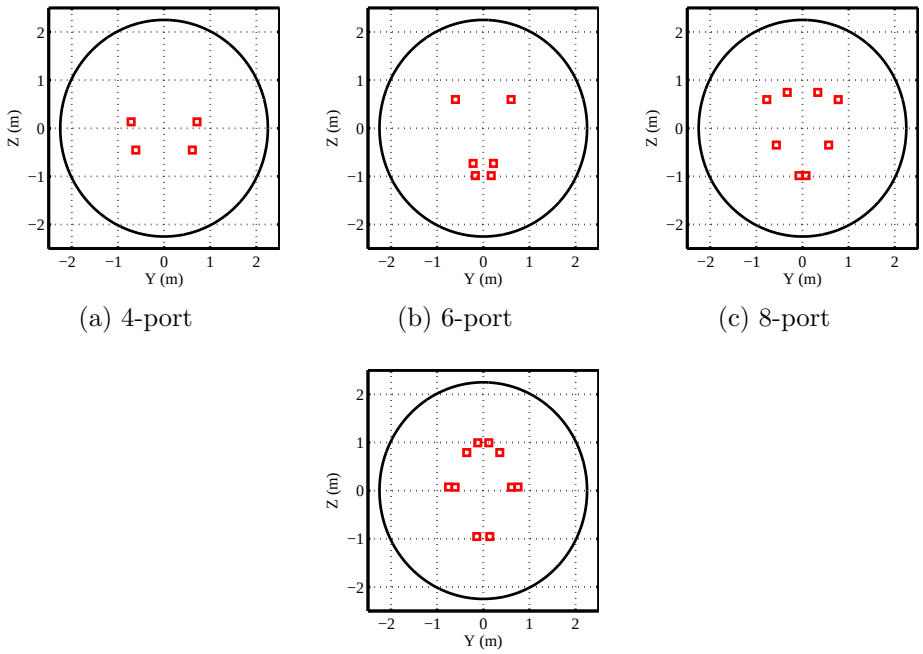

(a) 4-port (b) 6-port (c) 8-port

(d) 10-port

Figure 83: Configurations of the linearized, equally-weighted compromise points from symmetric optimization.

the symmetric constraint leads to slight improvements in some objective function values over the non-symmetric cases, there is always one objective function value where the symmetric case performs very poorly compared to its non-symmetric counterpart. It can be inferred then that symmetric constraints may hinder the observability of the sensor suite in some fashion over the non-symmetric constrained results.

Table 14: Comparison between non-symmetric and symmetric configurations using the linearized, equally-weighted compromise points.

Ports	Percent difference from non-symmetric values		
	$\%\sigma_\alpha$	$\%\sigma_\beta$	$\%\sigma_{q\infty}$
4	57.30	-14.92	11.37
6	-13.26	37.22	-5.31
8	-27.12	32.55	-11.95

5.5.5 Optimizing for Low Dynamic Pressure and Wind Speed Reconstruction

The observability of angle of attack, sideslip angle, and dynamic pressure were optimized by the objective function chosen in this study. However, wind speeds are also often important parameters of interest, and there are techniques that leverage FADS measurements and on-board IMU data to estimate these quantities [122]. Thus, the observability of wind speeds can also be a quantity that is added to the objective function. However, past studies have shown that the wind speed estimation is more a function of the IMU-based velocity reconstruction [50], so other changes to the objective function have to be also made to reflect this situation.

Another potential modification is to capture the effect of the measurement or sensor uncertainty in the objective function. Recall that for this objective function formulation the measurement noise covariance, R, was assumed to be an identity matrix. In actual sensors, the measurement uncertainty varies based on the flight regime or the dynamic pressure value and this can be reflected by varying R with the trajectory. In fact, FADS transducers are usually classified as either high dynamic pressure or low dynamic pressure sensors and engineers often design a port configuration for only one of these situations. For example, the MEADS suite that flew on MSL was only optimally calibrated for dynamic pressures above 850 Pa. although the transducers continued to take pressure measurements well below that limit. So one can optimize port configurations by including a varying R in the objective function and obtain results where one set of ports are optimized for high dynamic pressure regimes and another set is optimized for the low dynamic pressure regime.

5.6 Summary

The inclusion of FADS sensors can allow separation of aerodynamic and atmospheric uncertainties when combined with on-board IMU data; however, the past FADS have

not been optimized using a physics-based optimization routine. The methodology developed here introduces an optimization technique that can help designers plan the quantity and the locations of pressure transducers to reconstruct EDL flight parameters of interest, such as angle of attack, sideslip angle, and dynamic pressure.

One of the method presented uses the residual between the best estimated trajectory from a given data set and the true parameter values to optimize the location of the ports. Since the design space is multi-modal and multi-objective, an evolutionary algorithm that can handle multiple objective functions has been used to show results for single-objective, two-objective, and three-objective optimization results. Using a MSL-like trajectory as the test problem, these procedures give representative port configurations that improve reconstruction performance from the MSL baseline.

The other method uses the concept of observability to determine the optimum placement of sensors without considering the estimation method that will be used to analyze the data. Specifically, the Cramér-Rao Lower Bound is used to define the lowest possible standard deviation of the parameters of interest. The effect of the trajectory is considered in creating the objective function value, and it is found that dynamic pressure plays the most important role in the value of the Cramér-Rao-based uncertainties. An evolutionary optimization technique is again used to conduct the multi-objective optimization and Pareto frontiers are found for various port configurations. The optimization is conducted at first without any symmetrical constraints and then with symmetry enforced as constraint. In either case, it is found that a 6-port configuration is the point of diminishing return for the test problem. Hence adding an additional port after the 6th port has minimal gain.

These methods advance the state-of-the-art in sensor placement and design, specifically for atmospheric data system optimization, and introduce residual and non-residual based optimization methodologies that can be beneficial to the designer of future Mars EDL atmospheric data systems. The methodology can also be used to

find the design parameters that provide the optimized configuration of atmospheric data sensors without *a priori* weighting criterion. The optimization technique shown here together with the Pareto dominance concept allows a designer to locate most of the best configurations in a short period of time and thus allows for the optimal placement of sensors while also identifying trends useful in the design of future FADS instrumentation.

CHAPTER VI

IMPACT ON EDL VEHICLE DESIGN

Many different uncertainties facing EDL design were discussed in Chapter 1. These uncertainties lead to conservatism in design and ultimately to decreased potential performance. Of course, mission success is the ultimate goal and thus conservatism has remained in the design process. Mars EDL design has also suffered from a dearth of Mars-like test facilities on Earth, leading to few ways that uncertainties can be reduced in engineering design tools. However, with larger and more diverse types of data being collected during EDL, there is a possibility that techniques like the estimation methodology presented in this thesis and its reconstruction products can decrease the uncertainties inherent in engineering tools. This chapter looks at the impact of the estimation methodology on EDL tool maturation. Specifically, the chapter considers the maturation of aerodynamic databases and atmosphere modeling tools, since these two areas have some of the largest effects on uncertainties and margins for EDL vehicle design.

6.1 Aerodynamic Coefficients Modeling

Although the U.S. has been flying the same aeroshell shape to Mars since the 1970's, the uncertainties in the aerodynamic database have not been significantly reduced. Static aerodynamic coefficient uncertainties were shown in Table 1 in Chapter 1 and one observes that the uncertainties for various parameters have at best remained the same and in some instances have increased despite better modeling capabilities. This section considers the current methods of aerodynamic uncertainty modeling and provides recommendations on how the estimation methodology developed in this thesis along with future instrumented missions can lead to reductions in aerodynamic

database uncertainties.

6.1.1 Uncertainty Modeling for Aerodynamic Quantities

When the Viking aerodynamic database was created in the 1970's, very little CFD was used to determine the coefficients and the manner in which the uncertainties were defined are not well documented [123]. Interestingly, the dispersions for the Viking aerodynamics are smaller than what are used currently for 70-degree aeroshells for Mars EDL applications [17]. Instead, the current aerodynamic uncertainties owe their origins to work done for Mars Pathfinder and following missions.

Mars Pathfinder's aerodynamic database was a combination of data from CFD analysis and Viking-era ground test results [124]. The uncertainties were a function of the computational model uncertainties and measurement uncertainties of the Viking-era tests [124, 13]. Location of the sonic line, real gas effects, and other modeling assumptions led to compounding uncertainties on the aerodynamic database [13].

The Pathfinder aerodynamic database was further expanded for MER and Phoenix with detailed analysis for certain phenomena. Dynamic stability of the vehicle in supersonic condition, a situation difficult to model using current CFD tools, led to a reliance on ballistic range test data for pitch damping characterization [75] at a cost of significant uncertainty. The possibility of aerodynamic shape change due to ablation led to increase in uncertainties in rolling moment for Phoenix [8], a situation that was not even considered for the previous missions. Since Mars Science Laboratory was a non-spinning, lifting vehicle, the aerodynamic database development for this vehicle involved additional simulations that considered the effect of turbulent boundary layer on aerodynamic coefficients [17, 125]. Improved modeling of aerodynamic shape change due to ablation and effect of reaction control system interaction in aerodynamic coefficients also affected the uncertainties.

The lesson gained from the development of the aerodynamic database since the

Viking era is that although the general shape of the aeroshell that has been flown on Mars since the 1970's has been the same, newer computational and Earth-based experimental techniques have only reduced some forms of aerodynamic uncertainties. There remains unfulfilled promise in utilizing flight data to reduce the existing uncertainties in the aerodynamic database.

6.1.2 Updating Uncertainty Models with Flight Data

6.1.2.1 Opportunities to Update Uncertainty Models in the Past

Flight data have long provided opportunities to validate values and uncertainties in aerodynamic databases. Flight data have measurement uncertainties that can be resolved using available pre-flight calibration data and there are no issues regarding matching flight-relevant conditions that are faced with wind tunnel and ballistic range tests. However, sensors on-board EDL vehicles often do not directly measure quantities that have the largest uncertainties such as aerodynamic coefficients and the inference to go from what is measured to what is desired compounds additional uncertainties. The inability of past flight data to measure quantities with the largest uncertainties directly is one of the main reasons that aerodynamic database uncertainties have not decreased despite data from seven successful Mars missions.

Flight data from the Viking landers included both IMU and pressure measurements from the aeroshell using FADS sensors. One of the ports of the FADS configuration was strategically placed at the stagnation point (Fig. 7(c)) so that the aerodynamic coefficient reconstruction could be simplified to the formulas in Eqs. (38)- (40). However, there were no direct measurements of the atmospheric density (ρ_∞) or wind speeds (a component of V_∞) and the uncertainties in those values along with the measurement uncertainties of FADS and accelerometer did not provide enough uncertainty resolution to decrease the aerodynamic database uncertainties further.

$$C_A = \frac{C_{p,stag} m a_x}{p_{stag} S} \tag{38}$$

$$C_N = \frac{C_{p,stag} m \sqrt{a_y^2 + a_z^2}}{p_{stag} S} \tag{39}$$

$$C_{p,stag} = \frac{p_{stag}}{\frac{1}{2}\rho_\infty V_\infty^2 S} \tag{40}$$

Data from Pathfinder, MER, and Phoenix consisted of IMU measurements (as shown in Table 2 in Chapter 1), which by itself did not provide enough information to separate aerodynamic uncertainties from atmospheric uncertainties. In fact, Pathfinder only had accelerometer data, so even the attitude reconstruction of the vehicle was based on assumptions, adding additional uncertainty to the reconstructed aerodynamics [13]. Due to the large atmospheric uncertainties, aerodynamic uncertainties could not be determined at a level to warrant decreasing database uncertainties.

6.1.2.2 Past Difficulties in Aerodynamic Reconstruction with both FADS and IMU data

The addition of FADS sensors to IMU for MSL was intended to separate aerodynamic and atmospheric uncertainties [37]. Chapter 2 detailed the estimation methodology used to reconstruct trajectory, atmosphere, and aerodynamic coefficients concurrently using both FADS and IMU data. Refs. [60] and [126] describe other ways to reconstruct EDL parameters from FADS and IMU data sets. However, all of these methods use the FADS measurement equation presented in Sec. 2.2.1 as a way to bridge pressure values on the aeroshell to freestream values across the shock. Since the FADS measurement equation uses a CFD-based model for predicting surface pressure distribution, the uncertainties in the CFD model also translate into uncertainties in the estimated freestream and angular quantities [10]. Additionally, the measurement equation is also a function of Mach number, which is defined in Eq. (41). The

speed of sound (a) is in turn a function of freestream pressure and density while the freestream velocity is a function of the wind speed, all quantities that are not independently observed by sensors other than a FADS. Due to the lack of enough independent data, Mach number is extremely hard to estimate with low uncertainty, as was seen in Figs. 17, 28, and 51. Moreover, Karlgaard et al. [60] also show that Mach number is extremely hard to estimate using solely FADS data for $M_\infty \geq 3$. The large Mach number uncertainties increase the uncertainties of parameters estimated with the FADS data and do not provide enough justification to decrease aerodynamic uncertainties in the database.

$$M_\infty = V_\infty / a = \left(V - V_{wind}\right) / \sqrt{kP_\infty / \rho_\infty} \tag{41}$$

The difficulty of reconstructing Mach number also has parallels with other parameters like wind speed and freestream density that are needed for aerodynamic modeling. The estimation methodology developed in this thesis assumed that wind speed was negligible, but wind speed uncertainty is not negligible when one intends to decrease uncertainties in aerodynamic databases. Unfortunately, neither FADS measurements nor IMU data provide a way to separate wind speeds from inertial velocities in a non-unique manner. Ref. [50] refers to ways in which to estimate wind speeds within a statistical estimation framework, but wind speed estimation using that method can lead to non-unique answers and that certainly does not engender confidence in reducing aerodynamic coefficient uncertainties.

Additionally, although the methodology from Chap. 2 shows a way to estimate freestream density as a quantity by itself, in reality an estimation algorithm needs a very good estimate of velocity to separate freestream density from dynamic pressure, which is actually the quantity that is observed by FADS and IMU data. One can see this phenomena when one looks at the uncertainty in estimated dynamic pressure (such as in Fig. 25(f)) and the uncertainty of freestream pressure (in Fig. 24(b)). The

estimated dynamic pressure uncertainty is low throughout the trajectory compared to the density uncertainty, which only improves in the region where both FADS and IMU data are available and hence there is a very good estimate of dynamic pressure and velocity.

All of the above difficulties do not mean that aerodynamic quantities cannot be estimated with good certainty. Results from the MSL flight data set presented in Chapter 4 in Figs. 52 and 53 showed reconstructed aerodynamic coefficients and their uncertainties using the estimation methodology presented in this thesis. Independent MSL reconstructions from Ref. [10] agreed with these uncertainty estimates. Simulated data results in Chapter 3 showed that the estimation methodology with the current set of data may already quantify the aerodynamic uncertainties at the level of the aerodynamic database (see Fig. 35(d)). However, the current data collected on-board EDL vehicles still leaves high uncertainty in quantities like the speed of sound, wind speed, and freestream density, whose uncertainty creeps into the estimated aerodynamic coefficient uncertainties.

6.1.3 Improving Future Aerodynamic Uncertainty Quantification

One way in which uncertainties can be improved when FADS and IMU data are components of the data set is by optimizing the location of the FADS sensors. Chapter 5 provided methods of optimizing the placement of the FADS sensors for a residual-based approach where the accuracy of the estimate was the objective function or an observability-based approach where the uncertainty of the estimation process was the objective. Either approach can lead to a data set that produces smaller uncertainties for the estimated angle of attack, sideslip angle, and freestream quantities, fueling reductions in aerodynamic parameter uncertainties derived from these quantities. The optimization process also provides a framework to add estimation of other parameters with high uncertainties, such as wind speed, to the objective function. Thus,

certain FADS ports can be placed in locations that are most sensitive to wind speeds. This will lead to lower uncertainty on wind speed that will lower uncertainties on the derived aerodynamics.

Another way to improve the models is to directly measure the quantities that have high estimated uncertainties. One of the largest drivers of current aerodynamic uncertainty is the inability to separate freestream density uncertainty from the dynamic pressure uncertainty. Freestream density can be directly estimated using mass spectrometers and nephelometers, two types of instruments that have flown previously on planetary entry missions. Figure 84 shows schematics of mass spectrometers and nephelometers that have flown on past planetary entry missions.

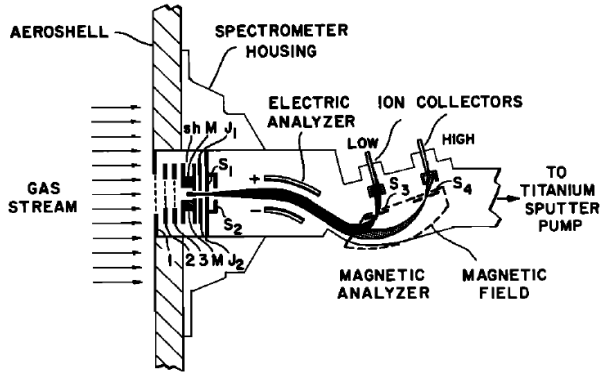

(a) Viking Mass Spectrometer [127]

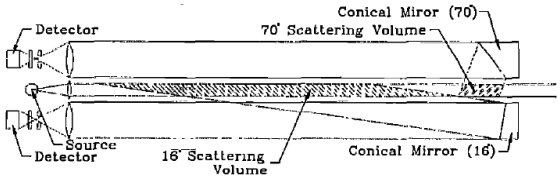

(b) Galileo Nephelometer [128]

Figure 84: Possible in-situ sensors for atmospheric density measurements.

Mass spectrometers ionize captured gas particles which then are transported to the mass analyzer using magnetic or electric fields. The instrument can calculate number density and molecular weight of the gas, which when combined leads to mass density of atmosphere. A nephelometer measures the light scattered by atmospheric

particles and leads to information like the particle size, phase, and number density of the atmosphere, which again can be combined to find the mass density of the atmosphere. Mass spectrometers have been widely used by early atmospheric probes to planetary bodies like Mars, Venus, Earth, Jupiter, and Titan [127, 129, 130, 131, 132, 133, 134, 135]. Nephelometers have also been used on multiple planetary bodies, but their use has not been as widespread as mass spectrometers [128, 136, 137]. In almost all cases, the mass spectrometers and nephelometers have been mounted on the side of the aeroshell and the instruments have been operated in many different flight regimes. Although the quality of the data from these past examples has not been great, with advances in instrumentation technology [137], one may expect a significant reduction in uncertainty of atmospheric density by directly measuring the quantity. Gains in density uncertainty quantification can translate into improved aerodynamic uncertainty quantification and improvements in the aerodynamic database.

Wind speed and Mach number uncertainties are the other large drivers of current aerodynamic uncertainties. Anemometers, which primarily are used to measure flow speed, can be combined with physics-based relations to measure winds and Mach number. Anemometers have not flown on past planetary entry missions and may not operate in hypersonic conditions. However, there has been some limited work to demonstrate supersonic flow anemometers, where a constant temperature hot wire is exposed to the flow and the change in resistance is converted to flow speed [138, 139, 140]. Reducing uncertainties in the supersonic regime is especially critical since one sees the highest uncertainties in the aerodynamics in this regime (see Table 1). Targeting instruments that directly measure atmospheric parameters for this regime can be extremely beneficial for future EDL design, since there are relatively large aerodynamic uncertainties that directly affect key EDL events like parachute deployment. Additionally, instruments like FADS are not as effective in this regime as they are currently construed. Direct measurement of the wind speed

and an estimate of the Mach number with improved uncertainties can lead to much improved uncertainty estimates of the aerodynamics and provide enough rationale for lowering current aerodynamic uncertainties.

The effect of these additional data sets on EDL reconstruction are demonstrated in Fig. 85. For this analysis, the nominal simulated data set from Chapter 3 is reevaluated using the estimation methodology and Adaptive filter with additional sensors that improve the accuracy of the freestream density and velocity. Table 15 summarizes the accuracy of the freestream density and velocity assumed for the analysis. The assumptions for the data accuracy are not based on actual sensor specifications of any current existing device; instead, accuracy values were selected to make the accuracy of these freestream quantities on par with other parameters with specific accuracy objectives. For example, MSL had a science objective to reconstruct dynamic pressure to within 2%. For this analysis, the two components of dynamic pressure - density and velocity - were simulated to be accurate within 1% using two new sources of data in addition to IMU and FADS.

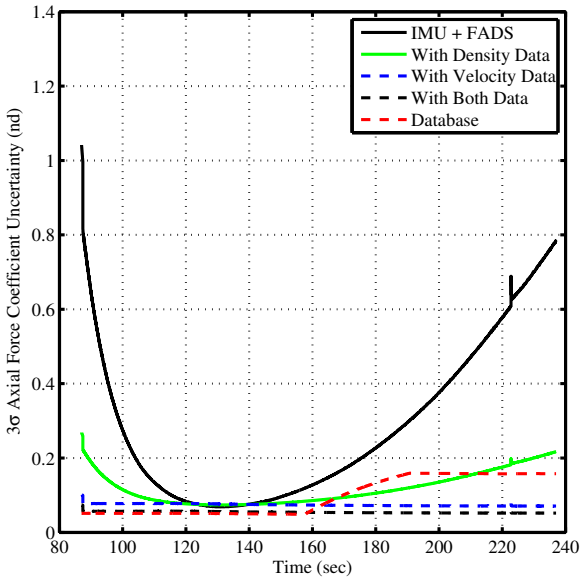

Figure 85: Effect on aerodynamic uncertainty quantification with augmented EDL data sets.

The results from Fig. 85 show that having a data set with direct and accurate

Table 15: Accuracy of data assumed for uncertainty quantification analysis.

Data Type	% Accuracy (3σ)
Freestream Density	1%
Freestream Velocity	1%

measurements of freestream density and velocity significantly improves uncertainty quantification. The density data could be provided by mass spectrometers or nephelometers, while the accuracy in the freestream velocity could be due to improvements in measuring wind speeds, speed of sound, or both. The analysis suggests that providing accurate observations of both of these parameters can reduce aerodynamic uncertainties even in the supersonic regime (near and after 200 s for this trajectory), an area where there are large uncertainties in the current aerodynamic database. The low dynamic pressure, supersonic regime is also an area where aerodynamic estimates based on current EDL FADS implementations have large uncertainties.

Of course, due to safety of the EDL vehicle adding several on-board sensors that are exposed to the flow might be unreasonable from a risk-management point of view. One possible solution that has been discussed recently after MSL's successful landing is to instrument the ballast weights that are discarded during EDL and then transmit data from these separate sounding probes. The ballast weights encounter similar atmospheric conditions as the main vehicle and directly measuring these atmospheric parameters may resolve the uncertainties plaguing aerodynamic modeling.

If the number of sensors providing measurements for a data set increase, using improved estimation methods for reconstruction becomes a necessity. The statistical estimation methodology provides a good framework to incorporate multiple, disparate data types and allows the estimate to be biased towards measurements with higher certainty. Additionally, it was seen in Chapter 3 that some higher-order methods suggested by the methodology, such as Unscented Kalman filter and Adaptive filters, show improvement in uncertainty quantification over lower-order estimators like

the Extended Kalman filter that are currently used in the EDL community. So direct measurements of parameters with high uncertainties combined with improved estimation methodologies such as the one developed in this thesis show promise of decreasing aerodynamic uncertainties in future engineering models.

6.2 Atmosphere Modeling

Atmospheric parameters have a large effect on the uncertainties of EDL vehicle performance as was shown in Fig. 6 in Chapter 1. In this section the state-of-the-art of atmospheric modeling for EDL design is discussed and consideration is given to how atmospheric reconstruction can improve future modeling efforts.

6.2.1 Current Atmospheric Modeling Techniques

The various models used to predict atmospheric conditions during EDL can be broadly divided into three categories: general circulation models, mesoscale models, and global reference models. Each model has a different level of fidelity and computational intensity, but should not be considered completely distinct since one type often relies on another type of model for the initial conditions.

General circulation models are finite difference tools that solve differential equations that describe meteorological phenomena. One can make a comparison to computational fluid dynamics to describe the mechanism of general circulation models and in fact many circulation models solve the Navier-Stokes equation as one of the governing equations. Since they are global in nature, the computational grids used by the circulation models are coarse and thus the models are not able to account for many phenomena at finer scales such as winds and large temperature inversions near the ground. Still, general circulation models give bulk parameter predictions and often serve to provide initial profiles for other tools. The most-used general circulation model for Mars EDL design is the NASA Ames Mars General Circulation Model (MGCM). The model has a long legacy and has been verified with several

lander data, such as measurements from Viking, Pathfinder, and MER, and orbiter observations from Mariner 9, Mars Global Surveyor, and Mars Reconnaissance Orbiter [141, 142, 143].

Recently, more focus has been given to the simulation of atmospheric properties near the Martian surface since orbiter instruments routinely give very good information about the upper atmosphere. General circulation models cannot simulate the active dynamics in this part of the atmosphere very well. Mesoscale models have tried to fill this gap. The differences between mesoscale models and general circulation models are in the way mesoscale models simulate turbulence for the boundary layer near the ground through large eddy simulations and deal with non-hydrostatic features of the atmosphere. Additionally, mesoscale models use nested grid schemes that improve the resolution of small scale atmospheric features. An example of a nested grid configuration is shown in Fig. 86 along with an example of the high-resolution atmospheric predictions from mesoscale modeling. Commonly used models of this class include the Mars Regional Atmospheric Modeling System (MRAMS) and the Mars Mesoscale Model 5 (MMM5). These models have been verified with flight data from Viking, Mars Pathfinder, and Phoenix and were used during the design phase of MSL [4, 22, 23, 144, 145, 146]. Although these models are better than the general circulation models in predicting smaller scale atmospheric features, both MRAMS and MMM5 need initial and boundary conditions that are provided by general circulation models like MGCM.

Global reference atmosphere models (GRAM) are engineering-level prediction tools that use databases of atmospheric simulation results found by general circulation models or mesoscale models. Parameterizations that realistically simulate the dynamics in pressure, temperature, and density without solving the Navier-Stokes equations make GRAMs computationally fast. The most commonly used GRAM for Mars EDL applications is Mars-GRAM that has been verified with flight data from

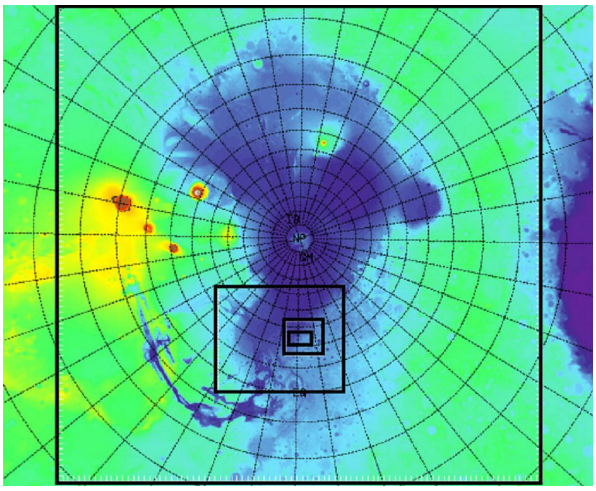

(a) Nested grids in MRAMS [4]

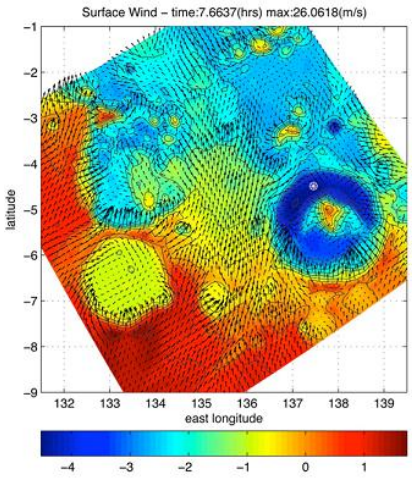

(b) Winds at Gale Crater using MMM5 [4]

Figure 86: Mesoscale model grid configuration and resulting high-resolution atmospheric predictions.

Mariner 9, Viking, Pathfinder, and recent orbiters [24, 83]. Despite the computational advantages associated with GRAMs, these models need some independent source of atmospheric data to make these predictions. Hence, these models are dependent on general circulation models, mesoscale models, or high-resolution flight data sets from on-board orbiters.

6.2.2 Current Procedures for Updating Models

The performance of atmospheric models for Mars are often verified against flight data from orbiters and probes; yet, the simulation parameters can be modified in non-unique ways to achieve similar results. Therefore, the adjustment of many of these parameters are done on an *ad hoc* basis, with trial-and-error and expert judgment used to match the flight data. Designers of general circulation models typically adjust parameters like the mean optical depth or sample the results at various frequencies to get consistent predictions [141]. Mesoscale models often ignore the first few days of simulation results for the atmosphere to "spin-up" properly and may need to adjust parameters for polar cap movement that is a large forcing function on the

environment [145, 146]. Although these adjustments lead to great agreement between the model results and flight data, these adjustments do not lead to accurate predictions of atmospheric conditions for future missions. Instead, fresh radio occultation data from orbiters, Earth-based observations, and in the rare cases measurements of the surface conditions are used to readjust the models for better performance in the future [4].

GRAMs also go through an adjustment process when new flight data are available for verification efforts. Since GRAM predictions are based on general circulation model and mesoscale models in the first place, adjustments in the high-fidelity models make their way into GRAM as well [82, 83]. However, additional adjustment factors are used to improve the match to the flight data. Mars-GRAM adjusts parameters such as the daily mean density and pressure that are used to bridge table look-up data from MGCS used for lower levels of the atmosphere and data from troposphere models used for the upper atmosphere [147]. Although these values have to satisfy some physical laws, such as the gas law and the hydrostatic equation, their values are not tied to directly observed quantities. Such adjustments make GRAM predictions very accurate and have low uncertainties for times when independent flight data are available (see Fig. 87), but do not provide any justification to believe that such accuracy is extensible for future missions.

The procedure for atmospheric modeling used during the design and landing site selection process for MSL represents the current state-of-the-art. A mixture of general circulation, mesoscale, and global reference atmosphere models were used to characterize the atmospheric environment and uncertainties for MSL's entry. MGCM was used to model the seasonal exchange of CO_2 that dominates the dynamics of Martian atmosphere [4]. Surface pressure predictions were made by reanalyzing the Mars Global Surveyor's Thermal Emission Spectrometer data set. The surface pressure predictions along with the MGCM-determined boundary conditions served as initial

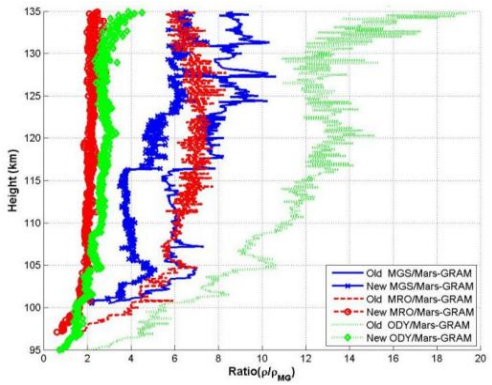

(a) 99th-percentile uncertainty bounds for density after adjustments [147]

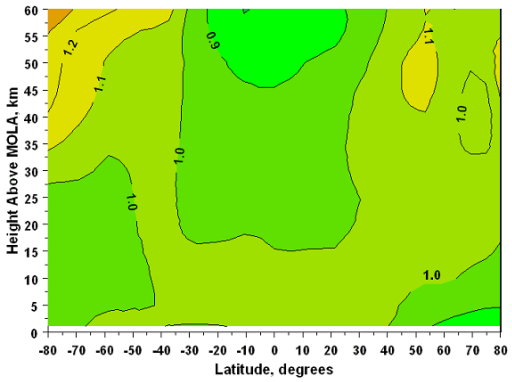

(b) Density ratio versus Global Surveyor data after adjustments [147]

Figure 87: Mars-GRAM predictions compared to flight data before and after adjustments.

conditions for MRAMS and MMM5, the two mesoscale models. Finally, the two mesoscale model results were turned into usable engineering data by using the framework of Mars-GRAM to quickly generate density and temperature profiles for use in EDL simulations [23, 25]. In addition, the Mars Climate Sounder on-board the Mars Reconnaissance Orbiter provided high-altitude vertical profiles of the atmosphere to test and tune the models. The mesoscale and general circulation models-derived atmospheric profiles allowed EDL designers to tune the entry system to meet design requirements. Ultimately, post-flight reconstructed atmospheric profiles from MSL were shown to be in great agreement with the pre-flight atmospheric predictions [60, 114].

6.2.3 Recommendation for Improving Future Models

Chapter 2 provided a procedure for reconstruction of atmospheric states and uncertainties from typical Mars EDL data and sample reconstruction products were shown in Chapters 3 and 4. Although, the reconstructed profiles from EDL data set can provide an accurate estimate of a vertical profile of the atmosphere at one epoch, the current atmospheric models do not gain much from an observation from one time point. Instead, the physics-based models, like the general circulation and mesoscale models, benefit more from data sets for large time periods over large swaths of a

planet. That type of data are most easily provided by orbiters rather than probes. Probe data is useful for validation exercises of models, but the tuning done to models to match probe flight data is not enough for accurate and highly certain predictions for future.

Ultimately, EDL reconstruction of atmospheric profiles by the estimation methodology does not seem to be the best way of maturing of state-of-the-art atmospheric models. Instead, continuous observations of atmospheric data, whether from orbiters or from ground stations, are the most beneficial way of improving atmospheric prediction tools. EDL atmospheric reconstructions using the estimation methodology can be valuable verification data for the updated models, but the extensibility of the models only occurs when the data are not limited to one epoch as is the case with EDL data.

6.3 Summary

One of the major motivations for the estimation methodology developed in this thesis is to improve uncertainty quantification of EDL parameters and feed-forward that information to improve EDL engineering models. The inability of current on-board sensors to directly observe many EDL parameters of interest has led to large uncertainties in some engineering models that has left conservatism in the design procedure. If the performance of future vehicles has to be improved, one needs to systematically reduce the uncertainties in current engineering tools.

Uncertainties in the aerodynamic database have a significant effect on EDL vehicle performance. Assumptions in modeling techniques such as CFD and Earth-based testing have left some of the uncertainties in the database. Past flight data have not remedied the situation, since several quantities that affect aerodynamic uncertainties are not directly observed. Introducing FADS to the typical EDL data sets

also have not improved the situation significantly since there are still other uncertainties and assumptions that are needed to process the new data type. Some possible solutions include optimizing the FADS sensor layout, the topic of Chapter 5, to target the estimation of uncertain parameters and improve the uncertainty modeling of most freestream and orientation angles so that these improvements feed-forward into the aerodynamic estimation. Additionally, directly measuring other uncertain parameters, such as freestream density, wind speed, and Mach number, through mass spectrometers, nephelometers, and anemometers can further reduce the overall uncertainty in the aerodynamics. Integrating in-situ measurement of these less observable parameters with the estimation methodology of this thesis can yield large gains in aerodynamic uncertainty quantification and improve the design of future EDL vehicles.

However, the results of the EDL estimation methodology is less likely to improve atmospheric modeling. The variable nature of atmospheres makes the estimation methodology and probe data in general not suitable for maturing atmospheric models. Instead, continuous observation of the atmosphere using on-ground meteorological stations and orbiters may be the best method of predicting atmospheric profiles with low uncertainties for future design.

CHAPTER VII

CONCLUSIONS AND FUTURE WORK

7.1 Summary of Contributions

This thesis has demonstrated a statistical estimation methodology for entry, descent, and landing parameters of interest that is also applied to improving current EDL vehicle design. The methodology was designed specifically for the estimation of vehicle trajectory, atmosphere, and aerodynamic parameters, which are simultaneously reconstructed by blending a disparate set of on-board data. The method was tested with simulated data and also applied to flight data from the Mars Science Laboratory mission. Additionally, the estimation methodology is applied to the optimization of flush atmospheric data systems and investigating the effect of improving engineering tools used in conceptual EDL design using products of the reconstruction methodology. A short summary of the academic contributions from this thesis is provided below and Table 16 shows the chapters associated with each contribution.

Table 16: Traceability of academic contributions.

Contribution	Ch. 2	Ch. 3	Ch. 4	Ch. 5	Ch. 6
Development of comprehensive methodology for parameter reconstruction and uncertainty quantification while blending dissimilar EDL data set	X	X	X		
Demonstration of design methodology for future atmospheric data systems				X	
Investigation of the effects of the statistical reconstruction methodology on vehicle design through improved engineering models		X	X		X

7.1.1 Comprehensive Methodology for Reconstruction and Uncertainty Quantification

As the crux of the thesis, the statistical estimation methodology developed in Chapter 2 creates a framework for estimating an EDL vehicle's trajectory, atmosphere, and aerodynamics from on-board data taken by most re-entry spacecraft. The methodology is an amalgamation of statistical techniques and improves upon the performance of currently accepted techniques used for EDL reconstruction.

One key component of this methodology is that the process equations use aerodynamic coefficients that are a function of the estimation state vector instead of sensed IMU acceleration for velocity state propagation. This distinguishes the current method from what is traditionally done for EDL reconstruction, but more importantly allows IMU accelerometer data to be treated as a measurement rather than a component of the process equations. Treating the accelerometer data as a measurement provides an additional data source besides FADS to sense freestream conditions.

Moreover, the methodology is one of the few EDL estimation methodologies that incorporates multiple data types together at the same time in a general manner. The current method blends accelerometer, gyroscope rates, FADS, and radar altimeter data, although the framework is suitable for other data types as well. Blending different data types allows the statistical estimator to bias the state estimates towards measurements with less uncertainty. Additionally, since the methodology is composed in a general manner, it is easily extensible to a wide range of estimation challenges.

Three different estimation techniques - EKF, UKF, and Adaptive filter - are available within this framework. Although EKF has been frequently used for non-linear filtering and sometimes for EDL reconstruction, UKF and Adaptive filter have not been commonly applied to EDL estimation. In fact, this thesis is the first application of an Adaptive filter for EDL reconstruction and the only application of UKF where the effect of the process noise has not been ignored. Each filter has its unique

strengths and when all three filters are available, an analyst is able to obtain a complete picture of EDL parameters. This is especially critical in situations where the truth is unknown, like most flight applications. Guidelines for choosing a certain filter are discussed in more detail in Sec. 7.2.

The estimation methodology has been validated using both simulated data and flight data. Chapter 3 presents estimation results when the methodology is applied to a nominal EDL data and a dispersed version of the nominal data with atmospheric and aerodynamic perturbations. The simulated data provide a proof-of-concept, since the true states are known. In both nominal and dispersed cases, all three filters had decent estimation performance with the Adaptive filter yielding the most accurate estimates. Since no true estimates of the uncertainties were available, the classification of the uncertainty estimation performance is based on the size of the confidence bounds. Based on this criterion, the UKF and Adaptive filters had the best performance since they displayed tighter confidence bounds than the EKF. The reconstruction methodology was also applied to the on-board Mars Science Laboratory data and the results were presented in Chapter 4. All three estimators had great agreement in the estimated trajectory, atmosphere, and aerodynamics although there were slight differences in the estimated uncertainties between the three filters.

The statistical estimation methodology combines aspects of many different numeric techniques to create a unified framework to estimate trajectory, atmosphere, and aerodynamic properties of EDL vehicles from on-board data. Although EDL reconstruction has been a topic of interest for a long time and several techniques have been applied to the problem in the past, the methodology presented in this thesis provides a comprehensive assessment that reconstructs most parameters of interest for EDL and provide statistics on the associated uncertainties while utilizing two or more data types as measurements to leverage the most information from the data set. The flexibility of the methodology also allows it to be applied to situations that lead

to improvements in current EDL vehicle design.

7.1.2 Design Methodology for Future Atmospheric Data Systems

One of the most straightforward ways the statistical estimation methodology can be applied is to optimize the design of the flush atmospheric data systems as shown in Chapter 5. FADS sensors are extremely useful for the EDL reconstruction process as they provide information about the vehicle's orientation and sensed freestream atmospheric properties. However, the design of past FADS layouts has been based on engineering judgment and heuristics. On occasions that the sensor layout has been optimized, the optimization was based on a point in the trajectory yielding a configuration that was not robust to other points of the trajectory or off-nominal conditions.

This thesis presents a new design algorithm for Mars EDL FADS instrumentation that leverages the statistical reconstruction and uncertainty quantification methodology to create guidelines for placement of sensors on EDL vehicles. The FADS instrumentation methodology presented here is the first attempt at casting the FADS sensor placement problem as multi-objective optimization problem. Results of the optimization lead to Pareto surfaces, presenting a designer with choices that fit a multitude of optimal criteria while only performing the optimization once. Two different philosophies are presented for FADS optimization.

The first approach is residual-based where the accuracy of the reconstruction conducted by a configuration drives the optimization. Simulated data are created for each configuration being tested and the estimation methodology is applied to reconstruct angle of attack, sideslip angle, and dynamic pressure. The residual between the estimated quantities and their true counterparts is quantified as an objective function, which is used by a multi-objective, non-dominated sorting Genetic Algorithm

find components of the Pareto surface. The objective function formulation is time-intensive, since an estimation must be conducted for each design parameter; however, keeping the estimation method in the loop allows the designer to optimize the sensors for best performance by the subsequent reconstruction effort.

The second approach is to maximize the observability of a configuration. The Cramér-Rao Lower Bound is used to quantify uncertainties of the estimation. This approach is less time intensive than the residual-based approach and the optimized results are also independent of any specific estimation technique. However, every point in the trajectory has an unique CRLB, so one must develop means to aggregate the various bounds in an appropriate manner.

Both approaches to FADS optimization provide designers with many candidate solutions and also yield important design trends for improving data quality. An important consequence of the optimizations was the identification of the point of diminishing returns. Bandwidth limits for on-board sensors on planetary entry missions make it crucial to make FADS configurations as efficient as possible in order to capture important measurements under a range of conditions.

7.1.3 Effects of the Statistical Reconstruction Methodology on Vehicle Design

One of the main goals of developing this estimation methodology is to improve uncertainty quantification of EDL parameters such that current engineering models can be improved. Aerodynamic parameters contain some of the largest uncertainties in EDL design so the effect of the estimation methodology on improving models for these quantities was studied.

Uncertainties in the current aerodynamic database stems from assumptions in modeling techniques and uncertain results of in Earth-based testing. The data set of past missions have not reduced many of these uncertainties since the parameters that have the largest uncertainties, such as freestream density, speed of sound, and wind

speeds, are not directly measured. Without these direct measurements, the estimation methodology cannot improve aerodynamic uncertainty significantly and cannot provide the rationale for reducing uncertainty in the current engineering models. However, improvement can be achieved by optimization of current sensors, such as FADS, to target the estimation of uncertain parameters and improve the uncertainty modeling of freestream and orientation angles in order to decrease uncertainty in the derived aerodynamic quantities. The most effective way to reduce aerodynamic uncertainty is to directly measure these uncertain quantities. Suggested sensors include mass spectrometers, nephelometers, and anemometers to reduce the uncertainty in the aerodynamics by directly measuring freestream density, wind speeds, and Mach number.

7.2 Filter Choice Recommendation

A major portion of this thesis consisted of applying three different statistical estimators for EDL reconstruction. EKF has been the standard of choice in non-linear filtering in many fields and Adaptive filtering has also been generally used since its initial introduction in the 1970's. UKF, developed in the late 1990's, has also been generally applied in non-linear filtering since computationally-intensive, Jacobian matrices do not have to be calculated. EDL reconstruction has largely been the purview of deterministic methods. When statistical estimation methods have been used, it has been largely EKF. Since three different methods were evaluated in this thesis using both simulated and actual flight data, recommendations are provided here about when to use a specific type of estimator. Although Wells also provides some guidelines in Ref. [28], the recommendations in this thesis, summarized in Table 17, are more comprehensive.

The most important requirement for an estimator is the accuracy of the estimated quantities. Chapter 3 tested the method with simulated data where the truth was

Table 17: Guidelines in choosing estimation methods for entry, descent, and landing reconstruction.

Description	EKF	UKF	Adaptive Filter
Accuracy of state estimate	●	●	●
Accuracy of uncertainty estimate	◐	●	●
Computational load & storage reqts.	◐	○	○
Low frequency of data	◐	●	●
Jacobian unavailable	○	●	○
Response to large deviations in dynamics	◐	●	●
A priori process and measurement noises unavailable	○	◐	●
Robustly stable to initial states and noises	◐	●	●
State parameter not directly observable	◐	◐	●

● Excellent
◐ Average
○ Below average

known and the estimate of MSL's landing location in Chapter 4 also had an independent, highly certain estimate. In these cases, all three estimators provided very accurate state estimates, as was summarized in Tables 7, 8, and 11. However, the EKF had larger estimated uncertainty bounds when compared with the UKF and Adaptive filter results. Although there was no truth data present to compare the estimated uncertainties, tighter uncertainty bounds indicate a more confident estimate and signify a better quality of uncertainty quantification.

One of the advantages of the EKF algorithm is that it is simple to implement as an on-line filter on a spacecraft. Modified forms of the EKF have been used in the past on-board vehicles as a navigation filter. On the other hand, UKF and Adaptive filter are harder to implement real-time. UKF requires propagation of the sigma points for state propagation and measurement updates, and the computational load increases linearly with the number of states being estimated. Adaptive filtering has large storage requirements as the last N states and covariances and the last L measurement residuals need to be stored for the process and measurement noise computations. The increased computational load of the UKF and the storage requirements of the

Adaptive filter make them poor candidates for real-time applications.

A common problem in past EDL missions have been the sparsity of data. Although recent missions, such as Phoenix and MSL, have high sample rates of IMU data, there are still some observations that are measured at low frequency. Figure 15 in Chapter 3 showed that EKF had a slight degradation in estimation performance at low sample rates. Since EKF uses a linearized version of the actual non-linear equations for covariance propagation, it requires frequent re-linearization to control the growth of non-linearity errors. Wells [28] also noticed a similar trend for the EKF. However, due to the use of sigma points that capture the non-linearity of the problem well, UKF appear to be more robust to lower sample rates of data. Adaptive filters, which use the same equations as the EKF for covariance propagation but also have adaptive process and measurement noises, are also less susceptible to filter divergence when the sample rate of data decreases.

The dynamics of a problem can make the equations of motion or measurement equations discontinuous or piece-wise continuous. In these instances, the Jacobian matrix will be undefined. UKF can still function in such situations, since the state, covariance, and measurement updates are conducted using sigma point propagation. However, the EKF and Adaptive filter need state and measurement sensitivity matrices. The derivative-free nature of the UKF makes it very attractive in situations with large discontinuities or dynamics with undefined partial derivatives. Adaptive filter, which still needs Jacobian matrices, can still perform well in situations with large deviations due to the adaptive nature of the process and measurement noise covariance. By adaptively calculating noise, the filter lessens the effect of the discontinuities and prevents divergence in the state and covariance estimates.

The Adaptive filter shines in situations where *a priori* state and measurement noise covariances are either unavailable or are not close to the actual values. The UKF can also be robust to bad initial estimates if enough sigma points are used, but has a

harder time converging to a solution where *a priori* noise statistics are unavailable. If the dynamics are modeled well by the process and measurement equations, UKF will still function in this situation. The EKF performs poorly in both scenarios, although if the process and measurement equations are close to the truth, the filter will still function.

Another criterion for evaluating the choice of filter is how well the estimator identifies quantities not directly-observable by observations. The aerodynamic coefficients, freestream density, and freestream pressure are good examples of quantities that can be indirectly inferred from IMU and FADS data, but are not directly measured. All three filters displayed good reconstruction performance whether simulated data (whose estimation results are summarized in Tables 7 and 8) or actual flight data (whose estimation results are summarized in Figs. 47, 48, 52, and 53) were used. The Adaptive filter performed the best, however, when both the state and uncertainty estimates are considered. For example, the axial force coefficient estimate in Fig. 35(d) is the only one with the parabolic shape seen in other independent aerodynamic reconstructions [10].

Overall, all three estimators have characteristics that make them the best choice in certain situations. The EKF tended to have more weaknesses when compared to UKF and Adaptive filter, but its simplicity makes it attractive for real-time or preliminary reconstruction of data. However, when computational time is not constrained, UKF and Adaptive filter both perform well with a slight edge to the Adaptive filter based on its better performance in the simulated data cases. For post-flight EDL reconstruction applications, all three filters could be appropriate choices with preference given to the UKF and Adaptive filter.

7.3 Future Work

This thesis presented a statistical estimation framework for incorporating disparate data types found on-board EDL vehicles and demonstrated how parameters of interest, such as trajectory, atmosphere, aerodynamic coefficients, and their associated uncertainties can be reconstructed from the data. The methodology utilized three statistical estimation methods and also demonstrated how the reconstructed products could be leveraged to improve future vehicle design, such as by sensor optimization or engineering tool maturation. The flexibility of the methodology easily lends itself for future augmentations, such improving uncertainty quantification through higher-order estimation methods, employing improved formulations for parameters with high uncertainties, and eventually making the estimation methodology feasible to be used as an on-board navigation filter.

7.3.1 Higher-order Estimation Methods for Uncertainty Quantification

The estimation methods utilized in this reconstruction as well as all past EDL statistical reconstructions have assumed that the state variables have normal distributions. When one considers the estimation of trajectory parameters, such as position or velocity, a normal distribution may be a justifiable assumption based on Monte Carlo simulations [5, 6, 124, 148]. However, there is no such justification for some other parameters of interest, such as wind speeds and aerodynamic coefficients. In fact, in many of these cases, uniform distribution or some other shape is a better assumption [6, 17].

Using EKF or the current form of the Adaptive filter does not allow one to consider non-Gaussian distributions. UKF is a higher-order filter in theory and the use of sigma points allows the filter to simulate the actual non-linear process without any assumptions about the Gaussian nature of the process. However, at the end the state propagation and measurement update stages, the sigma points are used to calculate

a mean and covariance that does assume a Gaussian process.

Instead, a possible method may be to have a multi-stage estimation algorithm that incorporates higher-order estimation methods for certain parameters to better document the non-Gaussian nature of the states. Possible higher-order estimation methods include the Second-Order Kalman filter and Particle filter [121, 96]. EKF, UKF, and Adaptive filter can be used in the first stage to update the trajectory estimates and then the more computationally-intensive and information demanding higher-order methods can use the new trajectory estimates for a smaller subset of estimation parameters, such as wind speeds, density, pressure, and aerodynamic coefficients. Such a process can even lead to better estimates of the uncertainties, since the parameter dynamics are not being forced into the form of a Gaussian process by the estimation methodology.

7.3.2 Improving Formulations for Uncertain Parameters

In order to estimate atmospheric states such as freestream density and pressure, the hydrostatic equation together with the perfect gas law were used to create atmospheric dynamical equations. This approach has been previously used in the literature [50], but in general the dynamic equations had several stringent assumptions associated with them and the process noises were relatively high to make the filter non-divergent when these dynamical equations were included. The high process noises suggest that the states might not be well modeled, but there is no easy recourse in order to estimate parameters like density and pressure that are more spatially evolving than dynamically evolving.

Instead, the estimation methodology may be recast from a pure state estimation problem to a mixed state and parameter estimation problem. Recall that in Chapter 1, a distinction was made between a parameter estimation problem (time-invariant estimation) and state estimation problem (time-varying estimation). A preliminary

estimate of a time-invariant quantity, such as atmospheric density, can be discretized by altitude. These individual densities at various increments can be thought of as control points that are updated by a parameter estimation methodology, while side-by-side the estimation methodology presented in this thesis can update time-varying states. There will be no need to create dynamical equations for parameters that are not time-varying and the estimation state vector can now include other uncertain time-invariant parameters like wind speed.

7.3.3 Application of the Sensor Placement Optimization to Other Disciplines

The sensor placement optimization method described in Chapter 5 was designed for atmospheric data system sensors, but is general enough to be applied to other disciplines as well. The field of sensor placement optimization has recently become very active and many studies have utilized evolutionary optimization techniques [149, 150, 151] to tackle multi-modal design spaces. However, in most instances the dynamics of the problem are vastly simplified to aid optimization speed and the uncertainties in the design space are not considered directly in the optimization. The observability-based technique described in this thesis is generalized enough to be a very attractive optimization option in cases where getting a robust solution that reduces the uncertainties in the design space is more important than simply finding an optimal but non-robust solution.

A good candidate for the application of this optimization method is the sensor placement of the thermocouples that were part of the MSL aeroshell instrumentation. Similar to the flush atmospheric data system sensors, the on-board thermocouples took in-situ measurements that were then used to reconstruct other parameters of interest, in this case surface heating and thermal protection system properties [152, 153]. The optimization method from Chapter 5 could be arapted to calculate the optimal locations of the thermocouples so that they would be most sensitive to changes

in surface heating and TPS material properties and provide the best data set for reconstruction for a given trajectory.

7.3.4 Optimization of EDL Trajectories to Benefit Science Output

The sensor optimization process could also be used to design trajectories that will maximize the observability for a given configuration of sensors. Mathematically, the sensor optimization method as currently construed will have to be slightly modified so that various trajectories will be the design parameters instead of sensor locations. However, the objective function can still be residuals of the reconstruction process or the observability of the sensors based on CRLB. The biggest issue in applying this methodology for trajectory shaping will be the best way to parameterize the trajectories for the optimization process. Simplistic parameterizations based on one or two trajectory qualities, such as the initial position and velocity, will allow a rapid exploration of the design space but not provide enough fidelity in the dynamics to find true global optima. Parameterizations using techniques such as collocation might provide ways to preserve fidelity of the dynamics during optimization without slowing down the process [154].

7.3.5 Simplification of the Atmospheric Data System Optimization Formulation

The objective function for the atmospheric data system optimization consists of angle of attack, sideslip angle, and dynamic pressure, which are all quantities that are dependent on the pressure distribution over the aeroshell. Hence, one can envision simplifying the three-objective optimization problem to a single objective optimization using some formulation that is solely a function of the pressure coefficient. However, it is not obvious what this formulation of the pressure coefficient should look like. A simple maximization or minimization of the pressure coefficient value does not lead a sensor configuration that best estimates angle of attack or sideslip angle. One can try

to place sensors in regions where the pressure coefficient changes rapidly, but it is not always obvious what parameter - angle of attack, sideslip angle, or dynamic pressure - is being helped with such placement. Thus, although there exists a potential for simplifying the multi-objective optimization problem using pressure coefficients, the proper formulation still requires work in the future.

7.3.6 Extension of Methodology for On-board Navigation Filter

One of the main goals of this thesis is to utilize estimation methodology products to improve future vehicle design. However, the estimation methodology itself could be looked upon as an improved navigation filter for a future EDL vehicle. The three estimation methods can be three independent voting filters that determine the state knowledge of the vehicle during re-entry. Of course, in the current formulation the estimation methodology is too unwieldy and computationally-intensive to be used on-line. But unlike batch filters, all of the filters used in this method are sequential and lend themselves as potential on-board filters with some modification and computational optimization. Moreover, if FADS systems are used on-board EDL vehicles, an estimation methodology such as the one presented in this thesis can incorporate that data with IMU and radar data for flight navigation instead of just using FADS for scientific investigations. The improved knowledge of angle of attack, sideslip angle, and freestream parameters that come with FADS data can vastly improve the performance and margins of guidance systems, both in hypersonic and supersonic regimes.

APPENDIX A

CLASSICAL ATMOSPHERIC ESTIMATION

Due to the lack of pressure measurements during the entry phase of vehicles, past atmospheric reconstructions have largely relied on a deterministic approach involving accelerometer measurements, reconstructed velocity estimates, and *a priori* knowledge of the aerodynamic coefficients of the entry body. This method of atmospheric estimation was first suggested by Seiff in 1963 [39] and has since matured in its implementation.

The reconstruction process uses the drag (C_D) or axial force (C_A) equation (shown in Eq. 42a) to estimate the freestream density (ρ_∞). Then the hydrostatic equation (Eq. 42b) is integrated to reconstruct the freestream pressure (P_∞). Finally, the freestream temperature (T_∞) can be estimated from the perfect gas equation of state (Eq. 42c) and the knowledge of freestream density, freestream pressure, and the gas constant (R) of the atmosphere, which depends in turn on the molecular weight of the atmosphere.

$$\rho_\infty = -\frac{2dV/dt}{V^2 C_D A/m} = -\frac{2a_x}{V^2 C_A A/m} \tag{42a}$$

$$dP = -g\rho dh \tag{42b}$$

$$T_\infty = \frac{p_\infty}{R\rho_\infty} \tag{42c}$$

The process of being able to use Eq. 42a to reconstruct freestream density comes after at least an initial attempt at trajectory reconstruction. Since accelerations from the inertial measurement unit (IMU) is already available, this data can be integrated to come up with a time history of the spacecraft's position and velocity. However, the

trajectory reconstruction only provides one of the two unknowns needed for density reconstruction; the drag or axial force coefficient history with respect to time has to be separately determined. Seiff [39] originally suggested that C_D could be held constant for the hypersonic regime when the body is doing a ballistic entry; however, later work has suggested that due to the large significance of angle of attack oscillation on the value of the drag/axial coefficient, it is important to calculate an angle of attack history to determine the correct force coefficient.

The most popular method has been using an aerodynamic database or table to calculate the angle of attack. Vehicle aerodynamic databases typically consist of tables of force and moment coefficients as a function of Mach number or velocity, Knudsen number, and total angle of attack. For hypersonic regime, drag coefficients are insensitive to Mach number [39] and if the vehicle is in continuum flow, Knudsen number effects are also low. Hence, aerodynamic coefficients can be approximated as a function of only the total angle of attack. Using the sensed accelerations (a_x, a_y, a_z), one can approximate a ratio of the axial and normal force (C_N) coefficient as shown in Eq. 43. [155]

$$\frac{C_N}{C_A} = \frac{\sqrt{a_y^2 + a_z^2}}{a_x} \tag{43a}$$

The force coefficient ratio together with the aerodynamic database information can then be used to fix a time history of the angle of attack. Next, the angle of attack history could then be used to calculate the appropriate drag or axial force coefficient from the aerodynamic database. Finally, with the known acceleration values, velocity estimate, and predicted aerodynamic coefficient information, the freestream density can be reconstructed using Eq. 42a.

The hydrostatic equation as shown in Eq. 42b makes the isothermal assumption to simplify the original barometric equilibrium equation to the form shown. The isothermal assumption suggests that changes in relative temperature with height is far less than changes in relative density with respect to height, which can be assumed

for most planetary atmospheres. [61, 156] With this in mind, the freestream pressure can be calculated by integrating the hydrostatic equation as shown in Eq. 44. The gravitational acceleration term (g) can be modeled as constant, varying with the square of the local radius (inverse squared law), or calculated with a high fidelity gravity model which is a function of the altitude and other state parameters, such as geodetic latitude. [157]

$$P_\infty = \int_{h_0}^{h} -g\rho dh \tag{44}$$

The reconstructed pressure value can be susceptible to wide variations based on the constant of integration chosen. If the integration is conducted from atmospheric entry and the pressure there is assumed to be zero but in actuality is a non-zero number, there will always exist a bias term. This can be especially troublesome for the thin, Martian atmosphere where even a small bias is relative a large issue. Thus, typically, the constant of integration is anchored to some independent pressure measurement, such as surface pressure measurements made by the vehicle after landing. One of the surprising benefits of the integration operation is that pressure estimation is more accurate than the density reconstruction. This is based on the fact that the quantity ρV is more accurately known than ρ, and this improves the pressure estimation. [39]

The freestream temperature calculations using Eq. 42c are straight-forward with known freestream density and pressure. The gas constant must be known and it can be estimated very well if on-board instruments include mass spectometers. [156] Moreover, sensitivity studies have found that the drag coefficient uncertainty may not have a huge effect on temperature estimation. Temperature is proportional to a ratio between an integration of C_D^{-1} over altitude and just C_D^{-1}. For blunt-bodies, C_D varies by only tens of percent during the entire re-entry sequence. Hence, there is a very little dependence between the force coefficient and temperature. [64] Freestream temperature calculations are however very much dependent on wind speeds, [36] and temperature measurements derived from accelerometer information has been shown

to be counter-intuitive at near sub-sonic speeds. [158].

The classical approach of using only accelerometer measurements to calculate atmospheric parameters is very popular in literature due to its simplicity, but has been shown to be sensitive to many types of errors, including uncertainties in accelerometer measurements, reconstructed velocity, entry angle, and frequency/sample rate of the data. [159] However, the most sensitive uncertainty is associated with the knowledge of the vehicle attitude and the resulting aerodynamic force on the body. Hence, the need of using a pressure measurement in addition to the accelerometer data for atmospheric reconstruction is imperative to remove the effect of aerodynamic uncertainty.

APPENDIX B

FADS DATA ATMOSPHERE ESTIMATION

Flush air data systems (FADS) have been utilized in the Viking missions, the Shuttle Air Data System (SEADS), and high angle of attack FADS (HI-FADS) [90, 160] aircraft on Earth. The analysts using air data systems are typically interested in four parameters: freestream pressure (P_∞), freestream density (ρ_∞), angle of attack (α), and sideslip angle (β). These four parameters are part of the air data state vector (x). Usually, the reconstruction process involves using an iterative, least-squares algorithm to estimate the four air data parameters from pressure data taken from the FADS sensors. The procedure assumes that the surface pressure at port i can be given by Eq. 45, which is a function of the total pressure (P_t), surface incidence angle (θ), and the pressure ratio (R) (defined in Eq. 46). [40, 161, 50] These quantities in turn are a function of the angle of attack, sideslip angle, and the port orientation angles (ζ and η) that were defined in Chapter 2.

$$P_i = P_t \left[(1 - R) \cos^2 \theta_i + R \right] \tag{45a}$$

$$\cos\theta_i = \cos\alpha \cos\beta \cos\eta_i + \sin\beta \sin\zeta_i \sin\eta_i + \sin\alpha \cos\beta \cos\zeta_i \sin\eta_i \tag{45b}$$

$$R = \frac{P_\infty}{P_t} = \begin{cases} \left[\frac{2}{(\gamma+1)M_\infty^2} \right]^{\gamma/(\gamma-1)} \left[\frac{2\gamma M_\infty^2 - (\gamma-1)}{\gamma+1} \right]^{1/(\gamma+1)} & \text{for} M_\infty > 1 \\ \left[1 + \frac{\gamma-1}{2} M_\infty^2 \right]^{-\gamma/(\gamma-1)} & \text{for} M_\infty \leq 1 \end{cases} \tag{46}$$

The iterative estimator tries to use a linearized version of the original non-linear function (f) shown in Eqs. 45 and 46 to minimize the difference between the actual measurement and the measurement value predicted by the estimated states. [45] The linearized measurement equation is described in Eq. 47, where the measurement

sensitivity matrix (H) is defined in the same way as in the prior sections.

$$P = f(x) + \frac{\partial f}{\partial x}\Delta x + \text{h.o.t.} \tag{47a}$$

$$y = P_{actual} - f(x) = H\Delta x \tag{47b}$$

Next, the famous weighted, least-square normal equation is used to solve for the estimated states using Eqs. 48. [93] The measurement noise covariance (R) serves as the weighting factor.

$$\Delta x = \left(H^T R^{-1} H\right)^{-1} H^T R^{-1} y \tag{48a}$$

$$\hat{x}^+ = \hat{x}^- + \Delta x \tag{48b}$$

This type of atmospheric reconstruction using FADS data has been referred to as the differential corrections algorithm [162] and has been shown to be effective for high angle of attack flight reconstruction applications. However, the methodology does not typically use any other type of sensor data in the parameter estimation problem. Improvements to the FADS reconstruction method have been suggested recently [163], but they do not typically involve utilizing other data types together with FADS. Very early, designers recognized that the FADS reconstruction problem is very multi-modal and the estimation methodology often provides non-unique results. Hence, work was done initially to identify under what situations the FADS data would lead to faulty estimated states. Since the FADS reconstruction procedure was based on least-squares regression methods, the χ^2 of the estimated parameter (or fits) were calculated to assess the *goodness-of-fit*. [164, 165, 160] Other efforts were made in improving the calibration information of the FADS sensor to improve the pressure reconstruction. [166] Some other enhancements involved using a stochastic, genetic algorithm instead of gradient-based algorithms (like the differential corrections approach) to reconstruct the air data parameters. [167] However, the biggest problem with all of these approaches was that assumptions were made about the trajectory

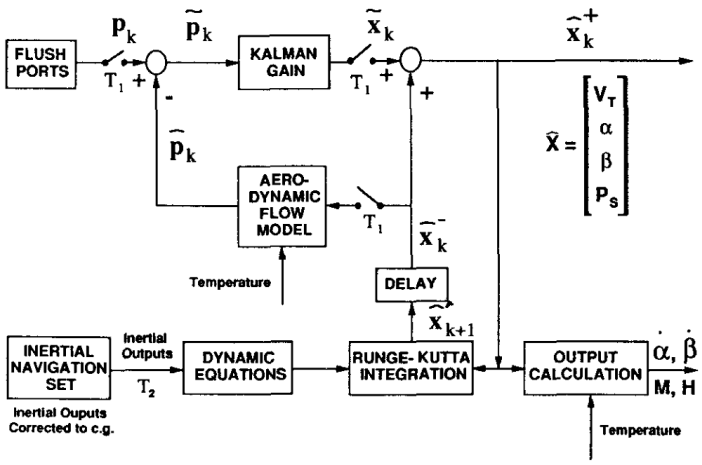

Figure 88: Hybrid air data estimation algorithm using IMU and FADS data.

states in order to cast the reconstruction as a parameter estimation problem; if IMU and other on-board sensors could be used with the FADS data in the estimation process, then assumptions about the flight's trajectory would not have to be made.

Kasich et. al. [91] suggests a hybrid approach where FADS measurements are blended together with inertial measurement unit (IMU) data in a Kalman filter. Figure 88 shows the flow diagram of the hybrid air data estimator, where the dynamic equations propagate the state variable that consist of angle of attack, sideslip angle, total pressure (called P_s in this case), and the dynamic pressure (related to true air speed (V_T)) using IMU data. The *Aerodynamic Flow Model* box uses equations similiar to Eqs. 45 and 46 to predict the flush port data as a function of the state vector. The Kalman filter then uses the residual between the predicted and actual FADS values to update the state vector. Although there is a loose coupling between the IMU and FADS data using this approach, the methodology does not attain the improvement in parameter and uncertainty estimation that a close coupling between the two types can bring.

There are a few studies in the past where a Kalman filter has been used to simultaneously estimate a vehicle's trajectory and atmosphere using both IMU and FADS

dataset. [50, 168, 169] The improvement in estimation capability shown by these studies serve as the motivation behind the reconstruction methodology presented in this thesis in Chapter 2. The methodology shown in this thesis attempts to improve parameter estimation and uncertainty quantification done by the simple Kalman filters in the past, and thus utilize the complete dataset from an EDL flight to accurately reconstruct the spacecraft's performance.

APPENDIX C

LIST OF PUBLICATIONS

C.1 Journal Articles

1. **Dutta, S.**, Braun R.D., Russell, R.P, Striepe, S.A., and Clark, I.G., "Comparison of Statistical Estimation Techniques for Mars Entry, Descent, and Landing Reconstruction," *Journal of Spacecraft and Rockets*, 2013, accessed May 24, 2013, doi:10.2514/1.A32462.

2. **Dutta, S.**, Braun R.D., and Karlgaard, C.D., "Atmospheric Data System Sensor Placement Optimization for Mars Entry, Descent, and Landing," *Journal of Spacecraft and Rockets*, 2013, accessed July 12, 2013, doi:10.2514/1.A32515.

3. **Dutta, S.**, Braun, R.D., and Karlgaard, C.D., "Uncertainty Quantification for Mars Entry, Descent, and Landing Reconstruction Using Adaptive Filtering," *Journal of Spacecraft and Rockets* (accepted for publication in September 2013).

4. **Dutta, S.** and Braun, R.D., "Cramér-Rao Lower Bound Optimization of Flush Atmospheric Data System Sensor Placement," *Journal of Spacecraft and Rockets* (submitted in September 2013).

5. **Dutta, S.** and Braun, R.D., "Statistical Entry, Descent, and Landing Performance Reconstruction of the Mars Science Laboratory," *Journal of Spacecraft and Rockets* (planned submission in February 2014).

C.2 Conference Proceedings

- Published Papers

1. **Dutta, S.** and Braun, R., "Mars Entry, Descent, and Landing Trajectory and Atmosphere Reconstruction," AIAA 2010-1210, *AIAA Aerospace Sciences Meeting*, Orlando, FL, 2010.

2. **Dutta, S.**, Clark, I.G., Russell, R.P, and Braun R.D., "Statistical Entry, Descent, and Landing Performance Reconstruction of the Mars Phoenix Lander," *International Planetary Probe Workshop*, Portsmouth, VA, 2011.

3. **Dutta, S.**, Braun R.D., Russell, R.P, Clark, I.G., and Striepe, S.A., "Comparison of Statistical Estimation Techniques for Mars Entry, Descent, and Landing Reconstruction from MEDLI- like Data Sources," AIAA 2012-400, *AIAA Aerospace Sciences Meeting*, Nashville, TN, 2012.

4. **Dutta, S.**, Mahzari, M., White, T., Braun, R.D., "Integrated Trajectory, Atmosphere, and Aerothermal Reconstruction Methodology Using the MEDLI Dataset," *International Planetary Probe Workshop,* Toulouse, France, 2012.

5. **Dutta, S.**, Braun R.D., and Karlgaard, C.D., "Atmospheric Data System Sensor Placement Optimization for Mars Entry, Descent, and Landing," AIAA 2012-4507, *AIAA Atmospheric Flight Mechanics Conference,* Minneapolis, MN, 2012.

6. **Dutta, S.**, Braun, R.D., and Karlgaard, C.D., "Uncertainty Quantification for Mars Entry, Descent, and Landing Reconstruction Using Adaptive Filtering," AIAA 2013-0026, *AIAA Aerospace Sciences Meeting*, Dallas, TX, 2013.

7. **Dutta, S.** and Braun, R.D., "Preliminary Statistical Trajectory and Atmosphere Reconstruction of MSL Entry, Descent, and Landing," AAS 13-309, *AAS/AIAA Space Flight Mechanics Meeting*, Kauai, HI, 2013.

8. **Dutta, S.** and Braun, R.D., "Cramér-Rao Lower Bound Optimization

of Flush Atmospheric Data System Sensor Placement," AIAA 2013-4502, *AIAA Atmospheric Flight Mechanics Conference*, Boston, MA, 2013.

- Accepted Submissions

  1. **Dutta, S.** and Braun, R.D., "Statistical Entry, Descent, and Landing Performance Reconstruction of the Mars Science Laboratory," *AIAA Atmospheric Flight Mechanics Conference*, National Harbor, MD, 2014 (accepted).

- Additional Publications

  1. Wells, G., **Dutta, S.**, Mattson, S., and Lisano, M., "Phoenix Location Determination using HiRISE Imagery," *International Planetary Probe Workshop*, Barcelona, Spain, 2010.
  2. **Dutta, S.**, Smith, B., Prabhu, D., Venkatapathy, E., "Mission Sizing and Trade Studies for Low Ballistic Coefficient Entry Systems to Venus," IEEE AC 134, *IEEE Aerospace Conference*, Big Sky, MT, 2012.
  3. **Dutta, S.**, Lantukh, D.V., Kosh, J.G., and Poston, M.J., "A Student Vision of the Future of U.S. Space Exploration," AIAA 2012-5315, *AIAA SPACE 2012 Conference*, Pasadena, CA, 2012.
  4. **Dutta, S.**, "Society and Aerospace Technology," *Aerospace America*, Vol. 50, No. 11, p. 38, 2012.
  5. **Dutta, S.**, Simonis, K.D., and Braun, R.D., "Analytically-derived Aerodynamic Force and Moment Coefficients of Resident Space Objects in Free-Molecular Flow," *AIAA Atmospheric Flight Mechanics Conference*, National Harbor, MD, 2014 (accepted).

REFERENCES

[1] Braun, R. D. and Manning, R. M., "Mars Exploration Entry, Descent, and Landing Challenges," *Journal of Spacecraft and Rockets*, Vol. 44, No. 2, 2007, pp. 310–323.

[2] Desai, P. N., Prince, J. L., Queen, E. M., Schoenenberger, M., Cruz, J. R., and Grover, M. R., "Entry, Descent, and Landing Performance of the Mars Phoenix Lander," *Journal of Spacecraft and Rockets*, Vol. 48, No. 5, 2011, pp. 798–808.

[3] Steltzner, A., Kipp, D., Chen, A., Burkhart, D., Guernsey, C., Mendeck, G., Mitcheltree, R., Powell, R., Rivellini, T., Martin, M. S., and Way, D., "Mars Science Laboratory Entry, Descent, and Landing System," IEEEAC 1497, *IEEE Aerospace Conference,* Big Sky, MT, 2006.

[4] Vasavada, A., Chen, A., Barnes, J., Burkhard, P., Canton, B., Dwyer-Cianciolo, A., Fergason, R., Hinson, D., Justh, H., Kass, D., Lewis, S., Mischna, M., Murphy, J., Rakfin, S., Tyler, D., and Withers, P., "Assessment of Environments for Mars Science Laboratory Entry, Descent, and Surface Operations," *Space Science Review*, Vol. 170, No. 1-4, 2012, pp. 793–835.

[5] Way, D., Powell, R., Chen, A., Stelzner, A., San Martin, M., Burkhard, P., and Mendeck, G., "Mars Science Laboratory: Entry, Descent, and Landing System Performance," IEEEAC 1467, *IEEE Aerospace Conference,* Big Sky, MT, 2007.

[6] Striepe, S., Way, D., Dwyer, a. M., and Balaram, J., "Mars Science Laboratory Simulations for Entry, Descent, and Landing," *Journal of Spacecraft and Rockets*, Vol. 43, No. 2, March 2006, pp. 311–323.

[7] Way, D., "On the Use of a Range Trigger for the Mars Science Laboratory Entry, Descent, and Landing," IEEE AC 1142, *IEEE Aerospace Conference,* Big Sky, MT, 2011.

[8] Edquist, K. T., Desai, P. N., and Schoenenberger, M., "Aerodynamics for the Mars Phoenix Entry Capsule," AIAA 2008-7219, *AIAA/AAS Astrodynamics Specialist Conference,* Honolulu, HI, 2008.

[9] Schoenenberger, M., Dyakonov, A. A., Buning, P., Scallion, W., and Van Norman, J., "Aerodynamic Challenges for the Mars Science Laboratory Entry, Descent and Landing," AIAA 2009-3914, *AIAA Thermophysics Conference,* San Antonio, TX, 2009.

[10] Schoenenberger, M., Van Norman, J., Dyakonov, A. A., Karlgaard, C., Way, D., and Kutty, P., "Assessment of the Reconstructed Aerodynamics of the Mars

Science Laboratory Entry Vehicle," AAS 13-306, *AAS/AIAA Space Flight Mechanics Conference, Kauai, HI*, 2013.

[11] Edquist, K., "Computations of Viking Lander Capsule Hypersonic Aerodynamics with Comparisons to Ground and Flight data," AIAA-2006-6137, *AIAA Atmospheric Flight Mechanics Conference and Exhibit,* Keystone, CO, 2006.

[12] Chapman, G. and Yates, L., "Dynamics of Planetary Probes: Design and Testing Issues," AIAA 1998-0797, *Aerospace Sciences Meeting,* Reno, NV, 1998.

[13] Gnoffo, P., Braun, R., Weilmuenster, K., Mitcheltree, R. A., Engelund, W. C., and Powell, R. W., "Prediction and Validation of Mars Pathfinder Hypersonic Aerodynamic Database," *Journal of Spacecraft and Rockets*, Vol. 36, No. 3, 1999, pp. 367–373.

[14] Kazemba, C., Braun, R., Clark, I., and Schoenenberger, M., "Survey of Blunt Body Dynamic Stability in Supersonic Flow," AIAA 2012-4509, *AIAA Atmospheric Flight Mechanics Conference,* Minneapolis, MN, 2012.

[15] Allen, J., "Motion of a Ballisticf Missile Angularly Misaligned with the Flight Path Upon Entering the Atmosphere and Its Effect Upon Aerodynamic Heating, Aerodynamic Loads, and Miss Distance," Tech. rep., NACA TN-4048, 1957.

[16] Tobak, M. and Allen, J., "Dynamic Stabiligy of Vehicles Traversing Ascending or Descending Paths Through the Atmosphere," Tech. rep., NACA TN-4275, 1958.

[17] Schoenenberger, M., Yates, L., and Hathaway, W., "Dynamic Stability Testing of the Mars Science Laboratory Entry Capsule," AIAA 2009-3917, *AIAA Thermophysics Conference,* San Antonio, TX, 2009.

[18] Murman, S. and Aftosmis, M., "Dynamic Analysis of Atmospheric-Entry Probes and Capsules," AIAA 2007-74, *AIAA Aerospace Sicneces Meeting,* Reno, NV, 2007.

[19] Stern, E., Gidzak, V., and Candler, G., "Estimation of Dynamic Stability Coefficients for Aerodynamic Decelerators Using CFD," AIAA 2012-3225, *AIAA Apllied Aerodynamics Conference,* New Orleans, LA, 2012.

[20] Desai, P. N., Blanchard, R. C., and Powell, R. W., "Entry trajectory and atmosphere reconstruction methodologies for the Mars Exploration Rover mission," *International Planetary Probe Workshop*, 2004.

[21] Justus, C. and Johnson, D., "Mars Global Reference Atmosphere Model, 2001 Version (Mars-GRAM 2001): Users Guide," Tech. rep., NASA TM-210961, 2001.

[22] Tyler, D., Barnes, J., and Haberle, R., "Simulation of surface meteorology at the Pathfinder and VL1 sites using a Mars mesoscale model," *Journal of Geophysical Research*, Vol. 107, No. E4, 2002, pp. 1–17.

[23] Chen, A., Vasavada, A., Cianciolo, A., Barnes, J., Tyler, D., Rafkin, S., Hinson, D., and Lewis, S., "Atmospheric Risk Assessment for the Mars Science Laboratory Entry, Descent, and Landing System," IEEEAC 1153, *IEEE Aerospace Conference,* Big Sky, MT, 2010.

[24] Justus, C., Duvall, A., and Johnson, J., "Mars-GRAM validation with Mars global surveyor data," *Advances in Space Research*, Vol. 34, 2004, pp. 1673–1676.

[25] Cianciolo, A., Way, D., and Powell, R., "Effects of Atmospheric Phenomena on Mars Science Laboratory Entry Performance," AIAA 2008-6427, *AIAA/AAS Astrodynamics Specialist Conference and Exhibit,* Honolulu, HI, 2008.

[26] Findlay, J., Kelly, G., and Troutman, P., "Final Report - Shuttle Derived Atmospheric Density Model Part 1," Tech. rep., NASA CR-17158, 1984.

[27] Findlay, J., Kelly, G., and Troutman, P., "Final Report - Shuttle Derived Atmospheric Density Model Part 2," Tech. rep., NASA CR-17158, 1984.

[28] Wells, G., *A Comparison of Multiple Techniques for the Reconstruction of Entry, Descent, and Landing Trajectories and Atmospheres*, Ph.D. thesis, Georgia Institute of Technology, 2011.

[29] Ingoldby, R., Michel, F., Flaherty, T., Doty, M., Preston, B., Villyard, K., and Steele, R., "Entry Data Analysis for Viking Landers 1 and 2," Tech. rep., NASA CR 159388, 1976.

[30] Euler, E., Adams, G., and Hopper, F., "Design and Reconstruction of the Viking Lander Descent Trajectories," *Journal of Guidance, Control, and Dynamics*, Vol. 1, No. 5, 1978, pp. 372–378.

[31] Spencer, D., Blanchard, R., Braun, R., Kallemeyn, P., and Thurman, S., "Mars Pathfinder Entry, Descent, and Landing Reconstruction," *Journal of Spacecraft and Rockets*, Vol. 36, No. 3, 1999, pp. 348–356.

[32] Schofield, J. T., Barnes, J., Crisp, D., Haberle, R., Larsen, S., Magalhaes, J., Murphy, J., Seiff, A., and Wilson, G., "The Mars Pathfinder Atmospheric Structure Investigation/Meteorology (ASI/MET) Experiment," *Science*, Vol. 278, No. 5344, Dec. 1997, pp. 1752–1758.

[33] Milos, F. S., Chen, Y., Thornton, J. M., and Astronautics, L. M., "Mars Pathnder Entry Temperature Data , Aerothermal Heating, and Heatshield Material Response," *Journal of Spacecraft and Rockets*, Vol. 36, No. 3, 1999, pp. 380–391.

[34] Blanchard, R. C., "Entry, Descent, and Landing Trajectory and Atmosphere Reconstruction for the Mars Exploration Rovers Missions A and B," Tech. rep., NASA-JPL Subcontract CCNS20568F, 2008.

[35] Withers, P. and Smith, M., "Atmospheric entry profiles from the Mars Exploration Rovers Spirit and Opportunity," *Icarus*, Vol. 185, No. 1, Nov. 2006, pp. 133–142.

[36] Blanchard, R. C. and Desai, P. N., "Mars Phoenix Entry , Descent , and Landing Trajectory and Atmosphere Reconstruction," *Journal of Spacecraft and Rockets*, Vol. 48, No. 5, 2011, pp. 809–821.

[37] Gazarik, M. J., Wright, M. J., Little, A., Cheatwood, F. M., Herath, J. A., Munk, M. M., Novak, F. J., and Martinez, E. R., "Overview of the MEDLI Project," IEEEAC 1510, *IEEE Aerospace Conference,* Big Sky, MT, 2008.

[38] Regan, F. J. and Anandakrishnan, S. M., *Dynamics of Atmospheric Re-Entry*, American Institute of Aeronautics and Astronautics, Reston, VA, 1993.

[39] Seiff, A., "Some Possibilities for Determining the Characteristics of the Atmospheres of Mars and Venus from Gas-Dynamic Behavior of a Probe Vehicle," Tech. rep., NASA TN D-1770, 1963.

[40] Pruett, C. D., Wolf, H., Heck, M. L., and Siemers, P. M., "Innovative Air Data System for the Space Shuttle Orbiter," *Journal of Spacecraft and Rockets*, Vol. 20, No. 1, 1983, pp. 61–69.

[41] Siemers, P., Wolf, H., and Flanagan, P. F., "Shuttle Entry Air Data System Concepts Applied to Space Shuttle Orbiter Flight Pressure Data to Determine Air Data - STS 1-4," AIAA 1983-0118, *AIAA Aerospace Sciences Meeting,* Reno, NV, 1983.

[42] Seiff, A., "The Viking Atmosphere Structure Experiment - Techniques, Instruments, and Expected Accuaracies," *Space Science Instrumentation*, Vol. 2, 1976, pp. 381–423.

[43] Blanchard, R. C. and Walberg, G. D., "Determination of the Hypersonic-Continnum/Rarefied-Flow Drag Coefficient of the Viking Lander Capsule 1 Aeroshell from Flight Data," Tech. rep., NASA TM 1793, 1980.

[44] Siemers, P. M. and Larson, T. J., "Space Shuttle Orbiter and Aerodynamic Testing," *Journal of Spacecraft*, Vol. 16, No. 4, 1979, pp. 223–231.

[45] Whitmore, S., Moes, T., and Larson, T., "High Angle-of-Attack Flush Airdata Sensing System," *Journal of Aircraft*, Vol. 29, No. 5, 1992, pp. 915–919.

[46] Deshpande, S., Kumar, R., Seywald, H., and Siemers, P., "Air data system optimization using a genetic algorithm," AIAA 1992-4466, *AIAA Guidance, Navigation, and Control Conference,* Hilton Head, SC, 1992.

[47] Edquist, K. T., Dyakonov, A. A., Wright, M. J., and Tang, C. Y., "Aerothermodynamic Design of the Mars Science Laboratory Heatshield," AIAA 2009-4075, *AIAA Thermophysics Conference,* San Antonio, TX, 2009.

[48] Schoenenberger, M., "Mars Entry Atmospheric Data System (MEADS) Reconstruction Overview," *MEDLI Flight Data Reconstruction TIM*, July 2012.

[49] Dutta, S., Braun, R., and Karlgaard, C., "Atmospheric Data System Sensor Placement Optimization for Mars Entry, Descent, and Landing," *Journal of Spacecraft and Rockets*, 2013, pp. (accepted for publication).

[50] Karlgaard, C. D., Beck, R. E., Keefe, S. A., Siemers, P. M., White, B. A., Engelund, W. C., and Munk, M. M., "Mars Entry Atmospheric Data System Modeling and Algorithm Development," AIAA 2009-3916, *AIAA Thermophysics Conference,* San Antonio, TX, 2009.

[51] Commo, S. and Parker, P., "Statistical Engineering Perspective on Planetary Entry, Descent, and Landing Research," *Quality Engineering*, Vol. 24, No. 2, 2012, pp. 306–316.

[52] Kamen, E. and Su, J., *Introduction to Optimal Estimation*, Springer Publications, London, UK, 1999.

[53] Aster, R., Borchers, B., and Thurber, C., *Parameter Estimation and Inverse Problems*, Elsevier, Waltham, MA, 2011.

[54] Bar-Shalom, Y., Li, X., and Kirubarajan, T., *Estimation with Applications to Tracking and Navigation*, John Wiley & Sons, Inc., New York, NY, 2001.

[55] Maybeck, P., *Stochastic Models, Estimation, and Control, Vol. 1*, Addison Wesley Longman, Reading, MA, 1989.

[56] Dutta, S. and Braun, R., "Mars Entry, Descent, and Landing Trajectory and Atmosphere Reconstruction," AIAA 2010-1210, *AIAA Aerospace Sciences Meeting,* Orlando, FL, 2010.

[57] Christian, J., Verges, A., and Braun, R., "Statistical Reconstruction of Mars Entry, Descent, and Landing Trajectories and Atmospheric Profiles," AIAA 2007-6192, *AIAA SPACE Conference and Exposition,* Long Beach, CA, 2007.

[58] Wells, G. and Braun, R. D., "Reconstruction of the Spirit Mars Exploration Rover Entry, Descent and Landing Performance," AA 3-2008-16, *International ARA Days Conference,* Arachon, France, 2008.

[59] Dutta, S., Clark, I., Russell, R., and Braun, R., "Statistical Entry, Descent, and Landing Performance Reconstruction of the Mars Phoenix Lander," *International Planetary Probe Workshop, Portsmouth, VA*, 2011.

[60] Karlgaard, C., Kutty, P., Schoenenberger, M., Shidner, J., and Munk, M., "Mars Entry Atmospheric Data System Trajectory Reconstruction Algorithms and Flight Results," AIAA 2013-0028*, 51st AIAA Aerospace Sciences Meeting, Grapevine, TX*, 2013.

[61] Seiff, A. and Reese Jr, D., "Use of Entry Vehicle Responses to Define the Properties of the Mars Atmosphere," *Advances in the Astronautical Sciences*, Vol. 19, 1965, pp. 419–445.

[62] Hopper, F., "Trajectory, Atmosphere, and Wind Reconstruction from Viking Measurement," AAS 75-068, *AIAA/AAS Astrodynamics Conference,* Nassau, Bahama, 1975.

[63] Seiff, A. and Kirk, D., "Structure of the Atmosphere of Mars in Summer at Mid-Latitudes," *Journal of Geophysical Research*, Vol. 82, No. 28, 1977, pp. 4364–4378.

[64] Withers, P., Towner, M., Hathi, B., and Zarnecki, J., "Analysis of entry accelerometer data: A case study of Mars Pathfinder," *Planetary and Space Science*, Vol. 51, No. 9-10, Aug. 2003, pp. 541–561.

[65] Withers, P. and Catling, D. C., "Observations of atmospheric tides on Mars at the season and latitude of the Phoenix atmospheric entry," *Geophysical Research Letters*, Vol. 37, No. 24, Dec. 2010, pp. 1–5.

[66] Bradley, P. F., Siemers, P. M., and Weilmuenster, K., "An Evaluation of Space Shuttle Orbiter Forward Fuselage Surface Pressures : Comparison with Wind Tunnel and Theoretical Predictions," AIAA 1983-119, *AIAA Aerospace Sciences Meeting,* Reno, NV, 1983.

[67] Henry, M., Wolf, H., and Siemers, P. M., "An Evaluation of Shuttle Entry Air Data System (SEADS) Flight Pressures: Comparisons with Wind Tunnell and Theoretical Predictions," AIAA 1988-2052, *AIAA Aerodynamic Testing Conference,* San Diego, CA, 1988.

[68] Wolf, H., Henry, M. W., and Siemers, P. M., "Shuttle Entry Air Data System (SEADS): Optmization of Preflight Algorithms based on Flight Results," AIAA 1988-2053, *AIAA Aerodynamic Testing Conference,* San Diego, CA, 1988.

[69] Michael, W., Tolson, R., Brenkle, J., Cain, D., Fjeldbo, G., Stelzried, C., Grossi, M., Shapiro, I., and Tyler, G., "The Viking Radio Science Investigations," *Journal of Geophysical Research*, Vol. 82, No. 8, 1977, pp. 4293–4295.

[70] Kornfeld, R. P., Bruvold, K. N., Morabito, D. D., Craig, L. E., Asmar, S. W., and Ilott, P. A., "Reconstruction of Entry , Descent, and Landing Communications for the Phoenix Mars Lander," *Journal of Spacecraft and Rockets*, Vol. 8, No. 5, 2011, pp. 1–46.

[71] Cobleight, B., Whitmore, S., Haering, J. E., Borrer, J., and Roback, V., "Flush Airdata Sensing System Calibration Procedures and Results for Blunt Forebodies," Tech. rep., NASA TP-1999-209012, 1999.

[72] Hollis, B., "Experimental and Computal Aerothermodynamics of a Mars Entry Vehicle," Tech. rep., NASA CR 201633, 1996.

[73] Parikh, P., Engelund, W., Armand, S., and Bittner, R., "Evaluation of a CFD Method for Aerodynamic Database Development using the Hyper-X Stack Configuration," AIAA 2004-5385, *Applied Aerodynamics Conference,* Providence, RI, 2004.

[74] Pamadi, B., Pei, J., Covell, P., Gumbert, C., Hanke, J., and Favaregh, N., "Aerodynamic Database Development for Liftoff/Transition and Ascent of the Ares I Vehicle," *Journal of Spacecraft and Rockets*, Vol. 49, No. 4, 2012, pp. 586–595.

[75] Schoenenberger, M., Hathaway, W., Yates, L., and Desai, P., "Ballistic Range Testing of the Mars Exploration Rover Entry Capsule," AIAA 2005-055, *AIAA Aerospace Sciences Meeting and Exhibit,* Reno, NV, 2005.

[76] Topper, B., Brown, T., Bukowski, E., Davis, B., Hall, R., Muller, P., Vong, T., and Brandon, F., "Feasibility of Determining Aerodynamic Coefficients for a NASA Apollo Body with the Use of Telemetry Data from Free Flight Range Testing," Tech. rep., ARL TR 4271, 2007.

[77] Brown, J., Bogdanoff, D., Yates, L., and Chapman, G., "Transonic Aerodynamics of a Lifting Orion Crew Capsule from Ballistic Range Data," *Journal of Spacecraft and Rockets*, Vol. 47, No. 1, 2010, pp. 36–47.

[78] O'Keefe, S. and Bose, D., "IRVE-II Post-Flight Trajectory Reconstruction," AIAA 2010-7515, *AIAA Atmospheric Flight Mechanics Conference,* Toronto, Canada, 2010.

[79] Moog, R. and Michel, F., "Ballon Launched Viking Decelerator Test Program - Summary Report," Tech. rep., NASA TR 37202359, 1973.

[80] Compton, H. R., Blanchard, R. C., and Walberg, G. D., "An Experiment for the Shuttle Aerodynamic Force Coefficient Determination from Inflight Dynamical and Atmospheric Measurements," AIAA 1978-0795, *AIAA Aerodynamic Testing Conference,* San Diego, CA, 1978.

[81] Justus, C., "Mars Global Reference Atmospheric Model for Mission Planning and Analysis," *Journal of Spacecraft*, Vol. 28, No. 2, 1991, pp. 216–221.

[82] Justus, C., James, B., and Johnson, D., "Recent and Planned Improvements in the Mars Global Reference Atmospheric Model (MARS-GRAM)," *Advances in Space Research*, Vol. 19, No. 8, 1997, pp. 1223–1231.

[83] Tolson, R., Keating, G., Zurek, R., Bougher, S., Justus, C., and Fritts, D., "Application of Accelerometer Data to Atmospheric Modeling During Mars Aerobraking Operations," *Journal of Spacecraft and Rockets*, Vol. 44, No. 6, 2007, pp. 1172–1179.

[84] Vinh, N., Busemann, A., and Culp, R., *Hypersonic and Planetary Entry Flight Mechanics*, The University of Michigan Press, Ann Arbor, MI, 1980.

[85] Kuipers, J., *Quaternions and Rotation Sequences*, Princeton University Press, Princeton, NJ, 1999.

[86] Etkin, B., *Dynamics of Atmospheric Flight*, Dover Publications, Meneola, NY, 2000.

[87] Christian, J. A., *Statistical Reconstruction of Mars Entry, Descent, and Landing Trajectories and Atmospheric Profiles*, Master's thesis, Georgia Institute of Technology, 2007.

[88] Wells, G., Dutta, S., Mattson, S., and Lisano, M., "Phoenix location determination using hirise imagery," *International Planetary Probe Workshop, Barcelona, Spain*, 2010.

[89] Jaswinski, A., *Stochastic Processes and Filtering Theory*, Academic Press, San Diego, CA, 1970.

[90] Whitmore, S., Moes, T., and Larson, T., "Preliminary Results From a Subsonic High Angle-of-Attack Flush Airdata Sensing (HI-FADS) System: Design, Calibration, and Flight Test Evaluation," Tech. rep., NASA TM 101713, 1990.

[91] Kasich, D. C. and Cheng, P. Y., "Flush Port / lnertially Blended Air Data Estimator," AIAA 1991-0670, *AIAA Aerospace Sciences Meeting,* Reno, NV, 1991.

[92] Martins, J. R. R. A., Kroo, I. M., and Alonso, J. J., "An Automated Method for Sensitivity Analysis using Complex Variables," AIAA 2000-0689, *AIAA Aerospace Sciences Meeting,* Reno, NV, 2000.

[93] Tapley, B. D., Schutz, B., and Born, G., *Statistical Orbit Determination*, Elsevier Academic Press, Burlington, MA, 2004.

[94] Zarchan, P. and Musoff, H., *Fundamentals of Kalman Filtering, A Practical Approach*, American Institute of Aeronautics and Astronautics, Reston, VA, 2000.

[95] Julier, S., Uhlmann, J., and Durrant-Whyte, H., "A new method for the nonlinear transformation of means and covariances in filters and estimators," *IEEE Transactions on Automatic Control*, Vol. 45, No. 3, March 2000, pp. 477–482.

[96] Simon, D., *Optimal State Estimation*, Wiley-Interscience Inc., Hoboken, NJ, 2006.

[97] Lee, D.-J. and Alfriend, K. T., "Sigma Point Filtering for Sequential Orbit Estimation and Prediction," *Journal of Spacecraft and Rockets*, Vol. 44, No. 2, March 2007, pp. 388–398.

[98] Norgaard, M., Poulsen, N. K., and Ravn, O., "New developments in state estimation for nonlinear systems," *Automatica*, Vol. 36, No. 11, Nov. 2000, pp. 1627–1638.

[99] Myers, K. and Tapley, B. D., "Adaptive sequential estimation with unknown noise statistics," *IEEE Transactions on Automatic Control*, Vol. 21, No. 4, 1976, pp. 520–523.

[100] Stengel, R., *Optimal Control and Estimation*, Dover Publications, New York, NY, 1994.

[101] Fraser, D. C. and Potter, J. E., "The Optimum Linear Smoother as a Combination of Two Optimum Linear Filters," *IEEE Transactions on Automatic Control*, Vol. August, No. 31, 1969, pp. 387–390.

[102] Bell, B., "The Iterated Kalman Smoother as a Gauss-Newton Method," *SIAM Journal on Optimization*, Vol. 4, No. 3, 1994, pp. 626–636.

[103] Gelb, A., *Applied Optimal Estimation*, MIT Press, Cambridge, MA, 1974.

[104] Bar-Shalom, Y. and Fortmann, T., *Tracking and Data Association*, Academic Press, Boston, MA, 1988.

[105] Kalman, R. E., "A New Approach to Linear Filtering and Prediction Problems," *Journal Of Basic Engineering*, Vol. 82, No. Series D, 1960, pp. 35–45.

[106] Powell, T., "Automated Tuning of an Extended Kalman Filter Using the Downhill Simplex Algorithm," *Journal of Guidance, Control, and Dynamics*, Vol. 25, No. 5, 2002, pp. 901–908.

[107] Oshman, Y. and Shaviv, I., "Optimal Tuning of a Kalman Filter Using Genetic Algorithm," AIAA 2000-4558*, AIAA Guidance, Navigation, and Control Conference,* Denver, CO, 2000.

[108] Deb, K., Pratap, A., Agarwal, S., and Meyarivan, T., "A Fast and Elitist Multiobjective Genetic Algorithm: NSGA-II," *IEEE Transactions on Evolutionary Computation*, Vol. 6, No. 2, 2002, pp. 182–197.

[109] Striepe, S., Powell, R., Desai, P., Queen, E., Brauer, G., Cornick, D., Olson, D., and Peterson, F., *Program To Optimize Simulated Trajectories (POST II), Vol. II: Utilization Manual,* Version 1.1.6.G, 2004.

[110] Dutta, S., Braun, R., Russell, R., Striepe, S., and Clark, I., "Comparison of Statistical Estimation Techniques for Mars Entry, Descent, and Landing Reconstruction," *Journal of Spacecraft and Rockets*, 2013, pp. (accepted for publication).

[111] Golombek, M. P., Grant, J., Kipp, D., and et. al., "Selection of the Mars Science Laboratory Landing Site," *Space Science Review*, July 2012.

[112] Essmiller, J., Brugarolas, P., and San Martin, M., "MSL EDL GN&C Reference Frames," MSL Reconstruction TIM, Sept. 2012.

[113] Serricchio, F. and San Martin, M., "Mars Science Laboratory Navigation Filter," International Planetary Probe Workshop 2013, *San Jose, CA*, 2013.

[114] Karlgaard, C., Kutty, P., Schoenenberger, M., and Shidner, J., "Mars Science Laboratory Entry, Descent, and Landing Trajectory and Atmosphere Reconstruction," AAS 13-307*, AAS/AIAA Space Flight Mechanics Conference, Kauai, HI*, 2013.

[115] Way, D. W., Davis, Jody, D., and Shidner, J. D., "Assessment of the Mars Science Laboratory Entry, Descent, and Landing Simulation," AAS 13-420*, AAS/AIAA Space Flight Mechanics Conference, Kauai, HI*, 2013.

[116] Martin-Mur, T., Kruizinga, G., and Wong, M., "Mars Science Laboratory Interplanetary Navigation Performance," AAS 13-232*, AAS/AIAA Space Flight Mechanics Conference, Kauai, HI*, 2013.

[117] Deb, K., *Multi-Objective Optimization using Evolutionary Algorithms*, John Wiley & Sons, Ltd., 2001.

[118] Reyes-Sierra, M. and Coello Coello, C. A., "Multi-Objective Particle Swarm Optimizers: A Survey of the State-of-the-Art," *International Journal of Computational Intelligence Research*, Vol. 2, No. 3, 2006, pp. 287–308.

[119] Deb, K. and Agarwal, R., "Simulated Binary Crossover for Continuous Search Space," *Complex Systems*, Vol. 9, 1995, pp. 115–148.

[120] Beyer, H.-G. and Deb, K., "On Self-Adaptive Features in Real-Parameter Evolutionary Algorithms," *IEEE Transactions in Evolutionary Computation*, Vol. 5, 2001, pp. 250–270.

[121] Crassidis, J. and Junkins, J., *Optimal Estimation of Dynamic Systems*, Chapman & Hall/CRC, 2004.

[122] Kelly, G. M., Findlay, J. T., and Compton, H. R., "Shuttle Subsonic Horizontal Wind Estimation," *Journal of Spacecraft*, Vol. 20, No. 4, 1983, pp. 390–397.

[123] Flaherty, T., "Aerodynamics Data Book," Tech. rep., *NASAT TR-3709014*, Martin Marietta Corporation, 1972.

[124] Braun, R. D., Powell, R. W., Engelund, W. C., Gnoffo, P. A., Weilmuenster, K. J., and Mitcheltree, R. A., "Mars Pathfinder Six-Degree-of-Freedom Entry Analysis," *Journal of Spacecraft and Rockets*, Vol. 32, No. 6, 1995, pp. 993–1000.

[125] Dyakonov, A. A., Schoenenberger, M., and Van Norman, J., "Hypersonic and Supersonic Static Aerodynamics of Mars Science Laboratory Entry Vehicle," AIAA 2012-2999*, 43rd Thermophysics Conference, New Orleans, LA*, 2012.

[126] Blanchard, R., Tolson, R., Lugo, R., and Huh, L., "Intertial Navigation Entry, Descent, and Landing Reconstruction Using Monte Carlo Techniques," AAS 13-308*, AAS/AIAA Space Flight Mechanics Conference,* Kauai, HI, 2013.

[127] Nier, A. and McElroy, M., "Composition and Structural of Mars' Upper Atmosphere Results From the Neural Mass Spectrometers Viking 1 and 2," *Journal of Geophysical Research*, Vol. 82, No. 28, 1977, pp. 4341–4349.

[128] Popp, J., Naughton, J., Papadopoulos, P., Venkatapathy, E., and Ragent, B., "Simulation of Galileo Probe Descent Through Jovian Clouds," AIAA 1999-0561, *37th AIAA Aerospace Sciences Meeting and Exhibit,* Reno, NV, 1999.

[129] Istomin, V., Grechnev, K., Ozerov, L., Slutskii, M., Pavlenko, V., and Tsvetkov, V., "Experiment to Measure the Atmospheric Composition of Mars on the Mars 6 Entry Capsule," *Cosmic Research*, Vol. 13, 1975, pp. 13–17.

[130] Avduevskii, V., Borodin, N., Burtsev, V., Malkov, Y., Marov, M., Morozov, S., Rozhdestvenskii, M., Romanov, R., Sokolov, S., Fokin, V., Cheremukhina, Z., and Shkirina, V., "Automatic Stations Venera 9 and Venera 10 - Functioning of Descent Vehicles and Measurements of Atmospheric Parameters," *Cosmic Research*, Vol. 14, 1976, pp. 577–586.

[131] Colin, L. and Hunten, D., "Pioneer Venus Experiment Descriptions," *Space Science Reviews*, Vol. 20, 1977, pp. 451–525.

[132] Seiff, A., "Entry-Probe Studies of the Atmosphere of Earth, Mars, and Venus: A Review," AIAA 1990-0765, *28th Aerospace Sciences Meeting,* Reno, NV, 1990.

[133] Young, R., Smith, M., and Sobeck, C., "Galileo Probe: In Situ Observations of Jupiter's Atmosphere," *Science*, Vol. 272, 1996, pp. 837–838.

[134] Seiff, A., Kirk, D., Knight, T., Mihalov, J., Blanchard, R., Young, R., Schubert, G., von Zahn, U., Lehmacher, G., Milos, F., and Wang, J., "Structure of the Atmosphere of Jupiter: Galileo Probe Measurements," *Science*, Vol. 272, 1996, pp. 844–845.

[135] Kazeminejad, B. and Atkinson, D., "The ESA-Huygens Probe Entry and Descent Trajectory Reconstruction," Tech. rep., European Space Agency Special Publication (ESA SP 544), 2004.

[136] Ragent, B., Privette, C., Avrin, P., Waring, J., Carlson, C., Knight, T., and Martin, J., "Galileo Probe Nephelometer Experiment," *Space Science Reviews*, Vol. 60, 1992, pp. 179–201.

[137] Banfield, D., Gierasch, P., and Dissly, R., "Planetary Descent Probes: Polarization Nephelometer and Hydrogen Ortho/Para Instruments," *IEEE Aersoapce Conference,* Big Sky, MT, 2005.

[138] Krause, L. and Fralick, G., "Miniature Drag Force Anemometers," Tech. rep., NASA TM X-3507, 1977.

[139] Smits, A. and Muck, K., "Constant temperature Hot-Wire Anemometer Practice in Supersonic Flows," *Experiments in Fluids*, Vol. 2, 1984, pp. 33–41.

[140] Richard, J. and Fralick, G., "Use of Drag Probe in Supersonic Flow," *AIAA Journal*, Vol. 34, No. 1, 1995, pp. 201–203.

[141] Haberle, R., Pollack, J., Barnes, J., Zurek, R., Leovy, C., Murphy, J., Lee, H., and Schaeffer, J., "Mars Atmospheric Dynamics as Simulated by the NASA Ames General Circulation Model: 1. The Zonal-Mean Circulation," *Journal of Geophysical Research*, Vol. 98, No. E2, 1993, pp. 3093–3123.

[142] Haberle, R., Joshi, M., Murphy, J., Barnes, J., Schofield, J., Wilson, G., Lopez-Valverde, M., Holligsworth, J., Bridger, A., and Schaeffer, J., "General circulation model simulations of the Mars Pathfinder atmospheric structure investigation/meteorological data," *Journal of Geophysical Research*, Vol. 104, No. E4, 1999, pp. 8957–8974.

[143] Haberle, R., Murphy, J., and Schaeffer, J., "Orbital change experiments with a Mars general circulation model," *Icarus*, Vol. 161, 2003, pp. 66–89.

[144] Rafkin, S., Haberle, R., and Michaels, T., "The Mars Regional Atmospheric Modeling System: Model Description and Selected Simulations," *Icarus*, Vol. 151, 2001, pp. 228–256.

[145] Tyler Jr., D., Barnes, J., and Skyllingstad, E., "Mesoscale and large-eddy simulation model studies of the Martian atmosphere in support of Phoenix," *Journal of Geophysical Research*, Vol. 113, No. E00A12, 2008, pp. 1–27.

[146] Tamparri, L., Barnes, J., Bonfiglio, E., Canton, B., Friedson, A., Ghosh, A., Grover, M., Kass, D., Martin, T., Mellon, M., Michaels, T., Murphy, J., Rafkin, S., Smith, M., Tsuyuki, G., Tyler Jr., D., and Wolff, M., "Expected atmospheric environment for the Phoenix landing season and location," *Journal of Geophysical Research*, Vol. 113, No. E00A20, 2008, pp. 1–18.

[147] Justh, H., Justus, C., and Ramey, H., "The Next Generation of Mars-GRAM and its Role in the Autonomous Aerobraking Development Plan," AAS 11-478*, AAS/AIAA Astrodynamics Specialists Conference,* Girdwood, AK, 2011.

[148] Prince, J. L., Desai, P., Queen, E. M., and Grover, M. R., "Entry, Descent, and Landing Operations Analysis for the Mars Phoenix Lander," *Journal of Spacecraft and Rockets*, Vol. 48, No. 5, 2012, pp. 756–764.

[149] Padula, S. L., Kincaid, R. K., and William, C., "Optimization Strategies for Sensor and Actuator Placement," Tech. rep., NASA TM 1999-209126, 1999.

[150] Furuya, H. and Haftka, R., "Combining Genetic and Deterministic Algorithms for Locating Actuators on Space Structures," *Journal of Spacecraft and Rockets*, Vol. 33, No. 3, 1996, pp. 422–427.

[151] Ngatchou, P., Fox, W., and El-Sharkawi, M., "Distributed sensor placement with sequential particle swarm optimization," *Proceedings 2005 IEEE Swarm Intelligence Symposium*, Ieee, 2005, pp. 385–388.

[152] Mahzari, M., Cozmuta, I., Clark, I., and Braun, R., "An Inverse Parameter Estimation Methodology for the Analysis of Aeroheating and Thermal Protection System Experimental Data," AIAA 2011-4027, *42nd AIAA Thermophysics Conference,* Honolulu, HI, 2011.

[153] Mahzari, M. and Braun, R., "Time-dependent Estimation of Mars Science Laboratory Surface Heating form Simulated MEDLI Data," AIAA 2012-2871, *AIAA Thermophysics Conference,* New Orleans, LA, 2012.

[154] Benson, D., Huntington, G., Thorvaldsen, T., and Rao, A., "Direct Trajectory Optimization and Costate Estimation via an Orthogonal Collocation Method," *Journal of Guidance, Control, and Dynamics*, Vol. 29, No. 6, 2006, pp. 1435–1440.

[155] Peterson, V., "A Technique for Determining Planetary Atmopshere Structure From Measured Accelerations of an Entry Vehicle," Tech. rep., NASA TN D-2669, 1965.

[156] Sommer, S., Boissevain, A., Yee, L., and Hedlund, R., "The Structure of an Atmosphere From On-board Measurements of Pressure, Temperature, and Acceleration," Tech. rep., NASA TN D-3933, 1967.

[157] Sofair, I., "Improved Method for Calculating Exact Geodetic Latitude and Altitude." *Journal of Guidance, Control, and Dynamics*, Vol. 20, No. 4, 1997, pp. 824–826.

[158] Withers, P., "Should We Believe Atmospheric Temperatures Measured by Entry Accelerometers Traveling at "Slow" Near-Sonic Speeds?" Tech. rep., NASA CP-2004–213456, 2005.

[159] Peterson, V., "Analysis of the Errors Associated with the Determination of Planetary Atmosphere Structure from Measured Accelerations of an Entry Vehicle," Tech. rep., NASA TR R-225, 1965.

[160] Whitmore, A. and Moes, R., "Measurement Uncertainty and Feasibility Study of a Flush Airdata System for a Hypersonic Flight Experiment," Tech. rep., NASA TM 4627, 1994.

[161] Beck, R., Karlgaard, C., and Keefe, S. O., "Mars Entry Atmospheric Data System Post-Flight Data Analysis Tool : Modeling and Sensitivity Updates," Tech. rep., AMA No. 7-20, Analytical Mechanics Associates, Hampton, VA, 2007.

[162] Anderson, M., Lawrence, W., and Lopez, J. L., "Robustness of the differential corrections algorithm in an air data estimation system," AIAA 1994-3608, *AIAA Guidance, Navigation and Control Conference,* Scottsdale, AZ, 1994.

[163] Nieden, P. and Olivier, H., "Determination of Atmospheric Densities from Reentry Flight Data," *Journal of Spacecraft and Rockets*, Vol. 44, No. 2, 2007, pp. 332–337.

[164] Whitemore, S., "Development of a Pneumatic High-Angle-of-Attack Flush Airdata Sensing (HI-FADS) System," Tech. rep., NASA TM 104241, 1991.

[165] Whitmore, S. and Moes, T., "Failure Detection and Fault Management Techniques for a Pneumatic High-Angle-of-Attack Flish Airdata Sensing (HI-FADS) System," Tech. rep., NASA TM 4335, 1992.

[166] Whitmore, S. and Moes, T., "The Effects of Pressure Sensor Acoustics on Airdata Derived from a High-Angle-of-Attack Flush Airdata Sensing (HI-FADS) System," Tech. rep., NASA TM 101736, 1991.

[167] Anderson, M. B., Lawrence, W. R., and Lopez, J. L., "Supplementing Gradient Search with Genetic Algorithm for Air Data Estimation System," AIAA 1994-1931, *AIAA Applied Aerodynamics Conference,* Colorado Springs, CO, 1994.

[168] Moes, T. and Whitmore, S., "A Preliminary Look at Techniques Used to Obtain Airdata From Flight at High Angles of Attack," Tech. rep., NASA TM 101729, 1990.

[169] Moes, T. and Whitmore, S., "Preliminary Results from an Airdata Enhancement Algorithm with Application to High-angle-of-attack Flights," Tech. rep., NASA TM 101737, 1991.